MASS SPECTROMETRIC METHODS DEVELOPMENT FOR IDENTIFICATION OF DRUG/HERBICIDE SUBSTANCES AND MUTAGENIC IMPURITIES, AND GAS-PHASE REACTIVITY STUDY OF PHENYLCARBYNE ANIONS

by

Erlu Feng

A Dissertation

Submitted to the Faculty of Purdue University

In Partial Fulfillment of the Requirements for the degree of

Doctor of Philosophy

Department of Chemistry

West Lafayette, Indiana

May 2022

THE PURDUE UNIVERSITY GRADUATE SCHOOL
STATEMENT OF COMMITTEE APPROVAL

Dr. Hilkka I. Kenttämaa, Chair

Department of Chemistry

Dr. Adam Wasserman

Department of Chemistry

Dr. Mingji Dai

Department of Chemistry

Dr. Gozdem Kilaz

School of Engineering Technology

Approved by:

Dr. Christine A. Hrycyna

To my parents, Jian Feng and Alice Zhao

To my girlfriend, Linrui Jin

This would never be achieved without your love and support.

ACKNOWLEDGMENTS

The first acknowledgement is given to my advisor, Prof. Hilkka I. Kenttämaa. I am greatly thankful for her guidance and advice throughout my PhD studies. All the time spending with her was meaningful and helpful. Mass spectrometry was a completely new field to me when I joined the group, but her experience in the mass spectrometric area helped me to be a good researcher in this field, and her passion also motivated me to follow her example. She also dedicated a lot to train me for improving my writing and presenting skills, and this will be precious treasure that will benefit me in my whole life.

I would like to thank my committee members: Prof. Adam Wasserman, Prof. Mingji Dai and Prof. Gozdem Kilaz. They gave me great support and useful advice, and without their help, I could not achieve what I have done in graduate school. I would like to thank Dr. John J. Nash for his help in quantum chemical calculations.

All the past and current group members in Kenttämaa Lab, who I enjoyed working with, are acknowledged. Particularly, I would like to thank Dr. Xin Ma, my best friend and mentor in this group, who cooperated with me in many projects. I would also like to especially thank the people who helped me in my research: Dr. Mckay Easton, Dr. Jacob Milton, Dr. Zaikuan Yu, Dr. Jeremy Manheim, Dr. Edouard Niyonsaba, Dr. Duanchen Ding, Yuyang Zhang, Judy Kuan-Yu Liu, Victoria Boulos, Wanru Li, Yue Fu, Caroline Rowell and Hanning Jiang.

Finally, I would like to be thankful to my girlfriend, Linrui Jin, for spending five years together with me and supporting me in my most difficult time. It is my fortune to meet her at Purdue. I would also like to express my gratitude to my parents. They raised me up, gave me the best education, and supported me to pursue a PhD at Purdue. Without their unconditional love, I would never become who I am today.

TABLE OF CONTENTS

LIST OF TABLES

LIST OF FIGURES

ABSTRACT

Mass spectrometry (MS) is a versatile analytical tool that is especially useful for identification of unknown compounds in mixtures when coupled with chromatography. In MS experiments, the analytes are ionized, separated based on their mass-to-charge (*m/z*) ratios, and detected. The molecular weight of the analyte can often be derived from the mass spectrum if stable molecular ions ($M^{\bullet+}$) or stable protonated/deprotonated analyte molecules ($[M+H]^+$ or $[M-H]^-$) are generated. Further, MS can also be used to obtain structural information for the ionized analytes via their fragmentation reactions. Tandem mass spectrometry (MS^n) experiments are powerful for the characterization of unknown compounds in mixtures without the need for coupling them with chromatography. In MS^n experiments, the analytes are ionized, the ions of interest are isolated and subjected to reactions, such as collision-activated dissociation (CAD) or ion-molecule reactions with neutral reagent molecules. The fragmentation pattern or the diagnostic ion-molecule reaction product ions can be utilized to elucidate the structures of the analytes. The fragment ions or diagnostic product ions can further be subjected to CAD to obtain more structural information. Besides analytical purposes, MS^n also provides a powerful tool for exploring the reactivities of reaction intermediates that are elusive, such as phenylcarbyne anions and phenylcarbene anions.

The research described in this dissertation mainly focuses on the development of MS^n methods based on diagnostic gas-phase ion-molecule reactions followed by CAD for (1) the characterization of differently substituted ureas and (2) the differentiation of sulfonate esters from their isomeric analogs, such as sulfite esters and sulfones. HPLC was coupled with the MS^n methods discussed above to demonstrate its usefulness in the identification of compounds in mixtures. Additionally, a gas-phase reactivity study on phenylcarbyne anions is discussed in this dissertation. The phenylcarbyne anions were generated by CAD of two nitrogen molecules from negatively charged phenyl tetrazole precursors. Their reactivities towards various reagents were explored and rationalized with the help of quantum chemical calculations.

CHAPTER 1. INTRODUCTION AND OVERVIEW

1.1 Introduction

Since its introduction by J. J. Thomson in 1913,[1] mass spectrometry has developed into a powerful analytical tool utilized in many fields, including pharmaceutical sciences,[2] biochemistry,[3,4] forensic sciences,[5] environmental science[6] and clinical chemistry.[7] In these fields, mass spectrometry has seen many applications, such as identification of unknown chemicals, determination of elemental compositions of compounds and structural characterization of previously unknown analytes.

The oldest MS ionization technique, electron ionization (EI), provides plenty of structural information for analytes via their fragment ions.[8] However, this approach often does not provide molecular weight information as the molecular ion is completely fragmented. To address this problem, many "softer" ionization methods, such as electrospray ionization[9,10] (ESI) and atmospheric pressure chemical ionization (APCI),[11,12] have been developed that enable the generation of a stable molecular ion ($M^{\bullet+}$) or protonated/deprotonated analyte ($[M+H]^+$ or $[M-H]^-$).[13,14] The molecular weight (MW) of the analyte can thus be deduced from the mass spectrum. On the other hand, these experiments do not usually provide structural information. In order to determine the structures of the ionized analytes, tandem mass spectrometry (MS^n) experiments are often conducted.[15] In the simplest MS^n experiment, MS^2, the analytes are ionized, the ions of interest are isolated and subjected to reactions. One commonly used reaction type is collision-activated dissociation (CAD),[16,17] wherein the isolated ions are accelerated, subjected to activating collisions with a gas (usually helium or nitrogen) and fragmented.[17] The CAD pattern (MS^2 spectrum) can be used to obtain structural information for the isolated ion.[18]

Although CAD can enable identification of unknown ionized compounds, it often requires access to authentic model compounds.[19,20] Even then, CAD often generates similar fragmentation patterns for isomeric ions.[21,22] In order to address this issue, gas-phase ion-molecule reactions have been developed as an alternative method for structural elucidation in MS^n experiments.[23] Instead of subjecting the isolated ions to energetic collisions, the ions of interest are allowed to react with reagent molecules to generate product ions.[23] With the selection of an appropriate reagent, diagnostic product ions can be generated and utilized to provide structural information for the

analyte.[24-29] If more structural information is desired, these diagnostic product ions can be subjected to CAD.[27-29] In these studies, quantum chemical calculations are usually employed to explore the mechanisms of the formation of the diagnostic product ions and fragment ions.[28,29] Additionally, coupling this analytical approach with chromatography enhances its practicality for complex mixture analysis.[28,29]

Gas-phase ion-molecule reactions occurring in tandem mass spectrometers also provide a powerful tool for the examination of the reactivity of many charged reaction intermediates, such as carbyne anions and carbene anions.[30,31] These intermediates are challenging to study in solution as they are extremely reactive and short-lived.[32-34] Many reactive intermediates have been generated and studied in this manner over the past decades.[35-38]

1.2 Overview

This dissertation is divided into six chapters. An overview of the dissertation is provided in Chapter 1. The fundamental principles of linear quadrupole ion trap mass spectrometry and high-performance liquid chromatography are discussed in Chapter 2. An introduction to quantum chemical calculations is provided in Chapter 3. In Chapter 4, a method based on gas-phase ion-molecule reactions followed by two steps of CAD is introduced for the characterization of protonated substituted ureas, which are commonly utilized as herbicides. In Chapter 5, the development of another analytical method is delineated for the differentiation of mutagenic sulfonate esters from their isomeric analogs – sulfite esters and sulfones. Also, this method is based on gas-phase ion-molecule reactions followed by CAD. In Chapter 6, a gas-phase reactivity study of phenylcarbyne anions is presented.

1.3 References

1. Thomson, J. J. Rays of positive electricity and their application to chemical analyses. Longmans, Green and Co.: London, 1913.

2. Petrović, M., Hernando, M.D., Díaz-Cruz, M.S. and Barceló, D., Liquid chromatography–tandem mass spectrometry for the analysis of pharmaceutical residues in environmental samples: a review. *J. Chrom. A* **2005**, *1067*, 1-14.

3. Bantscheff, M., Schirle, M., Sweetman, G., Rick, J. and Kuster, B., Quantitative mass spectrometry in proteomics: a critical review. *Anal. Bioanal. Chem.* **2007**, *389*, 1017-1031.

4. Bantscheff, M., Lemeer, S., Savitski, M.M. and Kuster, B., Quantitative mass spectrometry in proteomics: critical review update from 2007 to the present. *Anal. Bioanal. Chem.* **2012**, *404*, 939-965.

5. Benson, S., Lennard, C., Maynard, P. and Roux, C., Forensic applications of isotope ratio mass spectrometry—a review. *Forensic Sci. Int.* **2006**, *157*, 1-22.

6. Richardson, S.D., Environmental mass spectrometry: emerging contaminants and current issues. *Anal. Chem.* **2012**, *84*, 747-778.

7. Shushan, B., A review of clinical diagnostic applications of liquid chromatography – tandem mass spectrometry. *Mass Spectrom. Rev.* **2010**, *29*, 930-944.

8. Thomas, M. C.; Mitchell, T. W.; Blanksby, S. J. Ozonolysis of phospholipid double bonds during electrospray ionization: A new tool for structure determination. *J. Am. Chem. Soc.* **2006**, *128* (1), 58–59.

9. Whitehouse, C.M., Dreyer, R.N., Yamashita, M. and Fenn, J.B., Electrospray interface for liquid chromatographs and mass spectrometers. *Anal. Chem.* **1985**, *57*, 675-679.

10. Yamashita, M. and Fenn, J.B., Electrospray ion source. Another variation on the free-jet theme. *J. Phys. Chem.* **1984**, *88*, 4451-4459.

11. Carroll, D.I., Dzidic, I., Stillwell, R.N., Haegele, K.D. and Horning, E.C., Atmospheric pressure ionization mass spectrometry. Corona discharge ion source for use in a liquid chromatograph-mass spectrometer-computer analytical system. *Anal. Chem.* **1975**, *47*, 2369-2373.

12. Carroll, D.I., Dzidic, I., Stillwell, R.N., Horning, M.G. and Horning, E.C., Subpicogram detection system for gas phase analysis based upon atmospheric pressure ionization (API) mass spectrometry. *Anal. Chem.* **1974**, *46*, 706-710.

13. Owen, B.C., Gao, J., Borton, D.J., Amundson, L.M., Archibold, E.F., Tan, X., Azyat, K., Tykwinski, R., Gray, M. and Kenttämaa, H.I., Carbon disulfide reagent allows the characterization of nonpolar analytes by atmospheric pressure chemical ionization mass spectrometry. *Rapid Commun. Mass Spectrom.* **2011**, *25*, 1924-1928.

14. Horning, E.C., Horning, M.G., Carroll, D.I., Dzidic, I. and Stillwell, R.N., New picogram detection system based on a mass spectrometer with an external ionization source at atmospheric pressure. *Anal. Chem.* **1973**, *45*, 936-943.

15. Louris, J.N., Brodbelt-Lustig, J.S., Cooks, R.G., Glish, G.L., van Berkel, G.J. and McLuckey, S.A., Ion isolation and sequential stages of mass spectrometry in a quadrupole ion trap mass spectrometer. *Int. J. Mass Spectrom. Ion Processes* **1990**, *96*, 117-137.

16. McLuckey, S.A., Principles of collisional activation in analytical mass spectrometry. *J. Am. Soc. Mass Spectrom.* **1992**, *3*, 599-614.

17. Mayer, P.M. and Poon, C., The mechanisms of collisional activation of ions in mass spectrometry. *Mass Spectrom. Rev.* **2009**, *28*, 608-639.

18. Banoub, J., Delmas Jr., G.H., Joly, N., Mackenzie, G., Cachet, N., Benjelloun-Mlayah, B. and Delmas, M., A critique on the structural analysis of lignins and application of novel tandem mass spectrometric strategies to determine lignin sequencing. *J. Mass Spectrom.* **2015**, *50*, 5-48.

19. Grebe, S.K. and Singh, R.J., LC-MS/MS in the clinical laboratory–where to from here?. *The Clin. Biochem. Rev.* **2011**, *32*, 5-31.

20. Xiao, J.F., Zhou, B. and Ressom, H.W., Metabolite identification and quantitation in LC-MS/MS-based metabolomics. *Trends Anal. Chem.* **2012**, *32*, 1-14.

21. Kong, J.Y., Yu, Z., Easton, M.W., Niyonsaba, E., Ma, X., Yerabolu, R., Sheng, H., Jarrell, T.M., Zhang, Z., Ghosh, A.K. and Kenttämaa, H.I., Differentiating isomeric deprotonated glucuronide drug metabolites via ion/molecule reactions in tandem mass spectrometry. *Anal. Chem.* **2018**, *90*, 9426-9433.

22. Zhu, H., Ma, X., Kong, J.Y., Zhang, M. and Kenttämaa, H.I., Identification of carboxylate, phosphate, and phenoxide functionalities in deprotonated molecules related to drug metabolites via ion–molecule reactions with water and diethylhydroxyborane. *J. Am. Soc. Mass Spectrom.* **2017**, *28*, 2189-2200.

23. Liu, J.K.Y., Niyonsaba, E., Alzarieni, K.Z., Boulos, V.M., Yerabolu, R. and Kenttämaa, H.I., Determination of the compound class and functional groups in protonated analytes via diagnostic gas-phase ion-molecule reactions. *Mass Spectrom. Rev.* **2021**, mas.21727

24. Sheng, H., Williams, P.E., Tang, W., Zhang, M. and Kenttämaa, H.I., Identification of the sulfoxide functionality in protonated analytes via ion/molecule reactions in linear quadrupole ion trap mass spectrometry. *Analyst* **2014**, *139*, 4296-4302.

25. Sheng, H., Williams, P.E., Tang, W., Riedeman, J.S., Zhang, M. and Kenttämaa, H.I., Identification of the sulfone functionality in protonated analytes via ion/molecule reactions in a linear quadrupole ion trap mass spectrometer. *J. Org. Chem* **2014**, *79*, 2883-2889.

26. Watkins, M. A.; Price, J. M.; Winger, B. E.; Kenttämaa, H. I., Ion−molecule reactions for mass spectrometric identification of functional groups in protonated oxygen-containing monofunctional compounds. *Anal. Chem.* **2004,** *76*, 964–976.

27. Duan, P.; Fu, M.; Gillespie, T. A.; Winger, B. E.; Kenttämaa, H. I., Identification of aliphatic and aromatic tertiary N-oxide functionalities in protonated analytes via ion/molecule and dissociation reactions in an FT-ICR mass spectrometer. *J. Org. Chem.* **2009,** *74*, 1114–1123.

28. Feng, E.; Ma, X.; Kenttämaa, H. I., Characterization of protonated substituted ureas by using diagnostic gas-phase ion-molecule reactions followed by collision-activated dissociation in tandem mass spectrometry experiments. *Anal. Chem.* **2021,** *93*, 7851–7859.

29. Zhu, H.; Max, J. P.; Marcum, C. L.; Luo, H.; Abu-Omar, M. M.; Kenttämaa, H. I., identification of the phenol functionality in deprotonated monomeric and dimeric lignin degradation products via tandem mass spectrometry based on ion–molecule reactions with diethylmethoxyborane. *J. Am. Soc. Mass Spectrom.* **2016,** *27*, 1813–1823.

30. Hu, J., Hill, B.T. and Squires, R.R., New approach to carbene chemistry via distonic carbene ions. a case of spin-forbidden proton transfer and carbene− biradical tautomerism. *J. Am. Chem. Soc.* **1997**, *119*, 11699-11700.

31. Seburg, R.A., Hill, B.T., Jesinger, R.A. and Squires, R.R., The phenylcarbyne anion. *J. Am. Chem. Soc.* **1999**, *121*, 6310-6311.

32. Ruzsicska, B. P., Jodhan, A., Choi, H. K. J., Strausz, O. P. and Bell, T. N., Chemistry of carbynes: reaction of CF, CCl, and CBr with alkenes. *J. Am. Chem. Soc.* **1983**, *105*, 2489-2490.

33. LaFrancois, C. J. and Shevlin, P. B., Formation of both CCl and CF in the reaction of atomic carbon with chlorofluorocarbons. *J. Am. Chem. Soc.* **1994**, *116*, 9405-9406.

34. Wang, J., Ding, Y.H. and Sun, C.C., Cyanomethylidyne: A reactive carbyne radical. *ChemPhysChem* **2006**, *7*, 710-722.

35. Williams, P.E., Jankiewicz, B.J., Yang, L. and Kenttämaa, H.I., Properties and reactivity of gaseous distonic radical ions with aryl radical sites. *Chem. Rev.* **2013**, *113*, 6949-6985.

36. Ding, D., Feng, E., Kotha, R.R., Chapman, N.C., Jiang, H., Nash, J.J. and Kenttamaa, H., Spin-spin Coupling Controls the Gas-phase Reactivity of Aromatic σ-Type Triradicals. *Chem. Eur. J.* **2021**, *27*, 1-14

37. Jin, C., Feng, E., Ma, X., Tang, W., Sheng, H., Wittrig, A., Gao, J. and Kenttämaa, H.I., Reactivity of para-benzynes in solution and in the gas phase. *Tet. Lett.* **2021**, *74*, 1-3.

38. Ma, X., Feng, E., Jiang, H., Boulos, V.M., Gao, J., Nash, J.J. and Kenttämaa, H.I., Protonated ground-state singlet *meta*-pyridynes react from an excited triplet state. *J. Org. Chem.* **2021**, *86*, 3249-3260.

CHAPTER 2. INSTRUMENTATION – LINEAR QUADRUPOLE ION TRAP MASS SPECTROMETRY AND HIGH-PERFORMANCE LIQUID CHROMATOGRAPHY

2.1 Introduction to mass spectrometry

Mass spectrometry is a powerful analytical tool that has a wide range of applications in many fields, including pharmaceuticals,[1] biochemistry,[2,3] polymer science,[4] forensics,[5] environmental science[6] and clinical chemistry.[7] In these areas, mass spectrometry has seen many applications, such as identification of unknown compounds, determination of element compositions for compounds, structural characterization of compounds and their quantitation.

In a typical mass spectrometry experiment, three essential steps must occur: 1) Evaporation of the compounds in the sample and their ionization, 2) ion separation based on their mass-to-charge (*m/z*) ratios, and 3) ion detection. Various evaporation/ionization techniques have been developed for different types of compounds, including but not limited to heating combined with electron ionization (EI),[8] electrospray ionization (ESI),[9,10] atmospheric pressure chemical ionization (APCI),[11,12] matrix-assisted laser desorption/ionization (MALDI)[13] and desorption electrospray ionization (DESI).[14] Among the ionization techniques mentioned above, ESI and APCI are the two techniques utilized in all the experiments discussed in this dissertation. Their principles are introduced in detail in the following sections.

In order to separate the ions that were generated in the ion source, the ions must be transferred into a mass analyzer. In the mass analyzer, ions are separated according to their *m/z* ratios. Different categories of mass analyzers have been developed, including magnetic sector mass analyzers,[15] time of flight analyzers[16] and ion traps.[17-19] They separate the ions based on different principles. The most common types of ion traps include orbitraps,[17] Fourier transform ion cyclotron resonance ion traps[18] and linear quadrupole ion traps.[19] All experiments discussed in this dissertation were conducted using linear quadrupole ion trap mass spectrometers. The principles of these instruments are discussed in the following sections.

After the ion separation, the separated ions are either detected or subjected into tandem mass spectrometry (MS^n) experiments to obtain structural information or examine their reactivity in the gas phase. In order to characterize the structures of the ions, collision-activated dissociation (CAD) is usually employed. In CAD experiments, the ions of interest are isolated, accelerated and allowed

to collide with helium gas, which induces fragmentation.[20,21] Another approach to obtain structural information is via gas-phase ion-molecule reactions. In these experiments and also to study the gas-phase reactivity of ions, the ions are isolated just like for CAD experiments and then allowed to react with reagent molecules to generate product ions.[22-24] These product ions can further be subjected to ion-molecule reactions or CAD for their structural characterization.

2.2 Ionization methods

Evaporation and ionization of the compounds of interest are the first two steps of a mass spectrometry experiment. A broad range of ionization methods have been developed based on different experimental purposes. In this thesis, the principles and applications of electrospray ionization (ESI) and atmospheric pressure chemical ionization (APCI) are discussed as they were both utilized in the research described in this thesis.

2.2.1 Electrospray ionization (ESI)

ESI is considered as a 'soft' ionization technique because it only induces minor or no fragmentation to the generated ions.[25] ESI is typically utilized for ionizing polar molecules that have acidic sites suitable for deprotonation or basic sites suitable for protonation.[25,26] ESI is commonly employed for ionizing macromolecules, such as proteins and other biopolymers, to generate multiply charged ions and characterize their structures via further fragmentations.[27,28]

The process of evaporation and ionization of compounds in ESI experiments consists of three main steps, which are discussed below.[29,30]

1) Formation of charged droplets. The analyte is dissolved in a liquid, such as acetonitrile, methanol or water.[29,31] The analyte solution is transferred through a transfer capillary tube (Figure 2.1). A high voltage (± 2-5 kV) is applied to the capillary tube to induce an electric field.[26] As a result, the surface of the analyte solution is charged at the tip of the capillary tube, and an elongated cone of the solution is formed under the influence of the electric field. This cone is called Taylor cone.[31,32] At the tip of the Taylor cone, the charged liquid breaks from the cone and generates highly charged, small droplets (Figure 2.1).

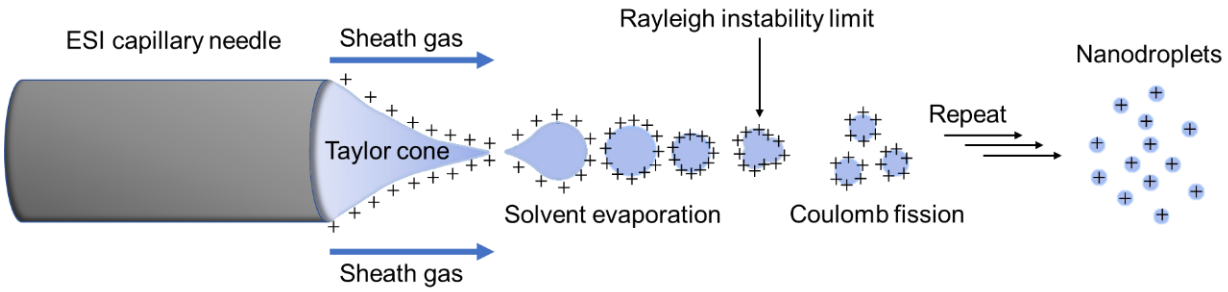

Figure 2.1. Illustration of the ESI process in the positive ion mode. Small droplets are formed from the Taylor cone. Solvent evaporate from the droplets until the Rayleigh instability limit is reached, and the Coulomb fission occurs. This process repeats until nanodroplets are generated.

2) Fission of the charged droplets. Dry sheath gas (usually N_2) is used to evaporate solvent from the charged droplets.[29] As a result, each droplet shrinks in size and its charge density increases until the Coulombic repulsion on the surface of the droplet surpasses its surface tension (Figure 2.1). This critical point is called Rayleigh instability limit.[33] At this point, the droplet undergoes Coulomb fission to yield numerous smaller droplets (Figure 2.1).[34] The process of evaporation and fission repeats several times until the generation of the nanodroplets, from which the ions are released.

3) Ion generation. All gaseous ions are produced from the above nanodroplets. Three ion release mechanisms have been proposed: *ion evaporation model (IEM)*, *charge residue model (CRM)* and *chain ejection model (CEM)*. *IEM* is generally believed to take place for small, singly charged ions.[30] In this model, the Rayleigh-charged nanodroplets induces a high electrostatic repulsion between the surface and the ion inside the droplet.[35,36] This results in the ejection of small ions from the droplet surface (Figure 2.2). *CRM*, on the other hand, best explains the release of large ions or multi-charged ions.[30] In this model, one nanodroplet only contains one analyte molecule.[37] With the assistance of the drying sheath gas, the solvent in the nanodroplet is eventually completely evaporated and the ion is released (Figure 2.2).[37] *CEM* describes the release of unfolded ionized proteins.[30] In this model, the long hydrophobic chain of the unfolded proteins protrudes outside the nanodroplet,[38] which reinforces the electrostatic repulsion between the charged solvent molecules and the charged proteins inside the nanodroplet. Under this circumstance, the unfolded protein is expelled from the nanodroplet to form a multiply charged protein (Figure 2.2).[38]

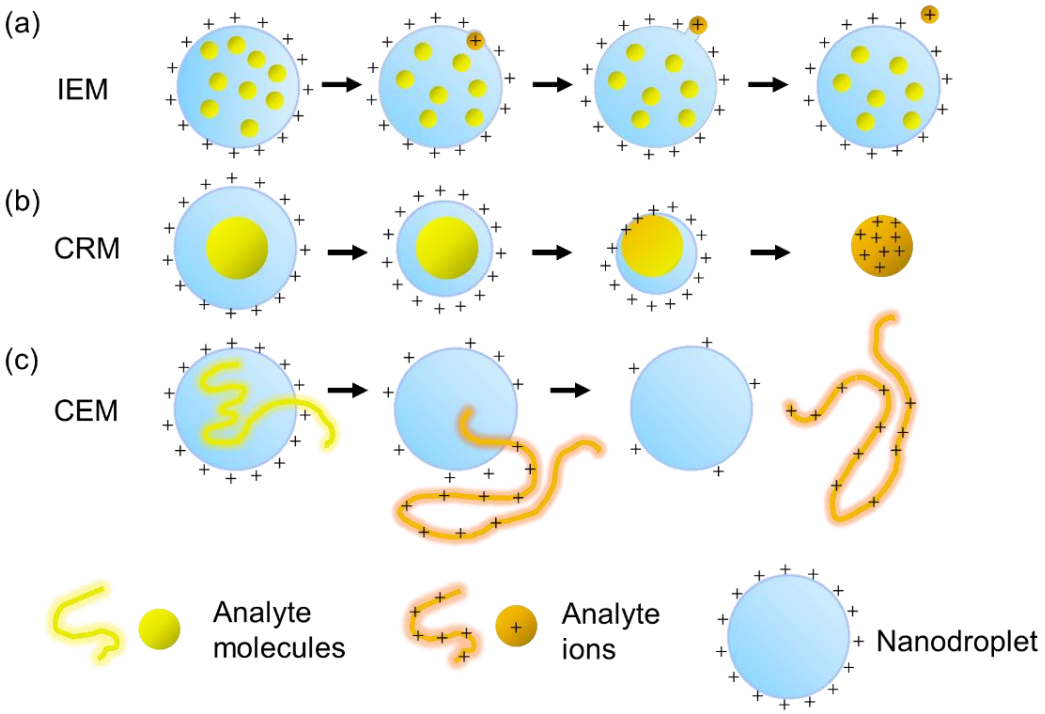

Figure 2.2. Illustrations of the ion generation from a positively charged nanodroplet via (a) ion evaporation model (IEM), (b) charge residue model (CRM) and (c) chain ejection model (CEM).[30]

2.2.2 Atmospheric pressure chemical ionization (APCI)

APCI is also a relatively 'soft' ionization technique but different from ESI, it is commonly utilized for ionization of both polar and nonpolar small molecules.[39] Also unlike ESI, most ions generated by APCI are singly charged.[40]

The process of APCI consists of two steps – evaporation and ionization. The analyte solution flows through a silica tube inside the APCI source and arrives to a spray nozzle located at the end of the tube (Figure 2.2). The solution is then mixed with a nebulizer gas (N_2), which disperses it into a fine mist of small droplets.[41,42] These droplets are directed by the nebulizer gas into a ceramic heater (150-450 ˚C), which generates a gas stream containing analyte, solvent and N_2 (Figure 2.2).[41]

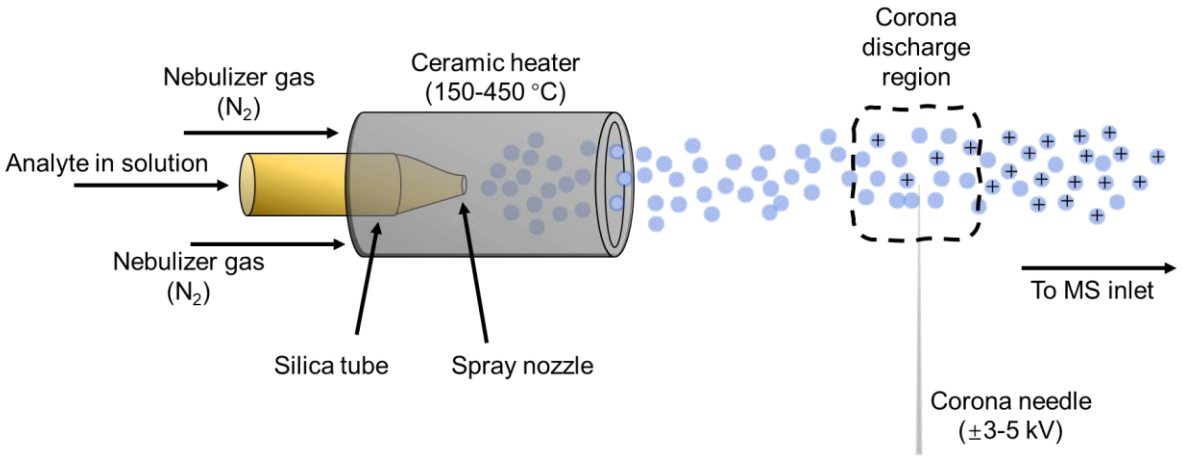

Figure 2.3. Illustration of the APCI process in the positive ion mode. Fine mist containing small droplets is formed at the spray nozzle. Ceramic heater generates a gas stream, which gas stream flows to the corona discharge region. Sheath gas molecules are ionized in this region, followed by the subsequent ionization of solvent and analyte molecules via their reactions with the ionized sheath gas molecules. The ionized analyte molecules are transferred into MS inlet.

The resulting gas stream flows into the ionization region, where a corona needle is located (Figure 2.2). A high voltage (± 3-5 kV) is applied on the corona needle to generate high energy electrons at the tip of the corona needle, which is called corona discharge (Figure 2.2).[43] As the gas stream travels into high voltage corona discharge, some of the nitrogen molecules collide with the high energy electrons and eject an electron to form the nitrogen molecular ions $N_2^{+\bullet}$. The nitrogen molecules are ionized first because nitrogen is the most abundant molecule in the gas stream. The solvent molecules are then ionized from the nitrogen molecular ions. The analyte molecules are finally ionized from the ionized solvent molecules upon a series of gas-phase ion-molecule reactions.[41,44] The ions that are generated are most commonly radical molecular cations ions of the analyte or protonated analytes. These two possibilities are discussed below.

Scheme 2.1 demonstrates the formation of the radical molecular cations of the analyte molecules via APCI.[45] These experiments involve dissolving the analyte in CS_2 solvent. After the formation of $N_2^{+\bullet}$ ion, $N_2^{+\bullet}$ abstracts an electron from a CS_2 molecule to generate a molecular ion $CS_2^{+\bullet}$. $CS_2^{+\bullet}$ then abstracts an electron from an analyte molecule (M) to generate the radical molecular cation $M^{+\bullet}$. The generation of the radical molecular cations requires that the molecular ion of the solvent is not a Brønsted acid. Otherwise, it may assist in the formation of protonated analytes.[46]

$$N_2 + e^- \longrightarrow N_2^{+\bullet} + 2e^-$$
$$N_2^{+\bullet} + CS_2 \longrightarrow CS_2^{+\bullet} + N_2$$
$$CS_2^{+\bullet} + M \longrightarrow CS_2 + M^{+\bullet}$$

Scheme 2.1. APCI mechanisms for the ionization of analyte molecules (M) to generate molecular radical cations ($M^{+\bullet}$). These ion-molecule reactions occur when the nebulizing gas (N_2), solvent (CS_2), and analyte (M) are present in the corona discharge region.

Scheme 2.2 illustrates the APCI mechanism for the formation of protonated analytes.[44] This process requires the protonated solvent to be a Brønsted acid.[46] Therefore, the analyte dissolved in water solvent is used as an example. Like Scheme 2.1, $N_2^{+\bullet}$ abstracts an electron from a water molecule to generate molecular ion $H_2O^{+\bullet}$. Next, $H_2O^{+\bullet}$ protonates surrounding water molecule to generate a hydronium cation (H_3O^+) and a hydroxyl radical ($HO^\bullet$). The hydronium cation adds with other water molecules to generate secondary clusters $(H_2O)_nH^+$. These clusters protonate analyte molecules (M) to generate the protonated analytes $[M + H]^+$.

$$N_2 + e^- \longrightarrow N_2^{+\bullet} + 2e^-$$
$$N_2^{+\bullet} + H_2O \longrightarrow H_2O^{+\bullet} + N_2$$
$$H_2O^{+\bullet} + H_2O \longrightarrow H_3O^+ + HO^\bullet$$
$$H_3O^+ + H_2O \longrightarrow (H_2O)_2H^+$$
$$(H_2O)_{n-1}H^+ + H_2O \longrightarrow (H_2O)_nH^+$$
$$(H_2O)_2H^+ + M \longrightarrow MH^+ + 2\,H_2O$$
$$(H_2O)_nH^+ + M \longrightarrow MH^+ + n\,H_2O$$

Scheme 2.2. APCI mechanisms that ionize analyte molecules (M) to form protonated analyte molecules (MH^+). These ion-molecule reactions occur when nebulizing gas (N_2), solvent (H_2O), and analyte (M) are present in the corona discharge region. The protonated solvents must be Brønsted acids.

2.3 Linear quadrupole ion trap mass spectrometry

In this research described in this dissertation, all mass spectrometry experiments were conducted using a Thermo Scientific™ LTQ linear quadrupole ion trap (LQIT) mass spectrometer. LQIT mass spectrometry was invented[47] in 2002 as an improvement to the conventional three-dimensional quadrupole ion trap (QIT).[48,49] Compared with the QIT, LQIT is an instrument with

a greater ion trapping efficiency , higher sensitivity and wider dynamic range.[47] LQIT has been extensively utilized for the analysis of small compounds,[50,51] proteins[52,53] and other biopolymers[54,55] since its invention.

The LQIT mass spectrometer utilized in this research consisted of three key regions: the atmospheric-pressure ionization (API) region, the ion optics region, and the ion trap and detector region. A schematic depicting the four regions is shown in Figure 2.4. In this section, the configurations and principles of these three regions are discussed.

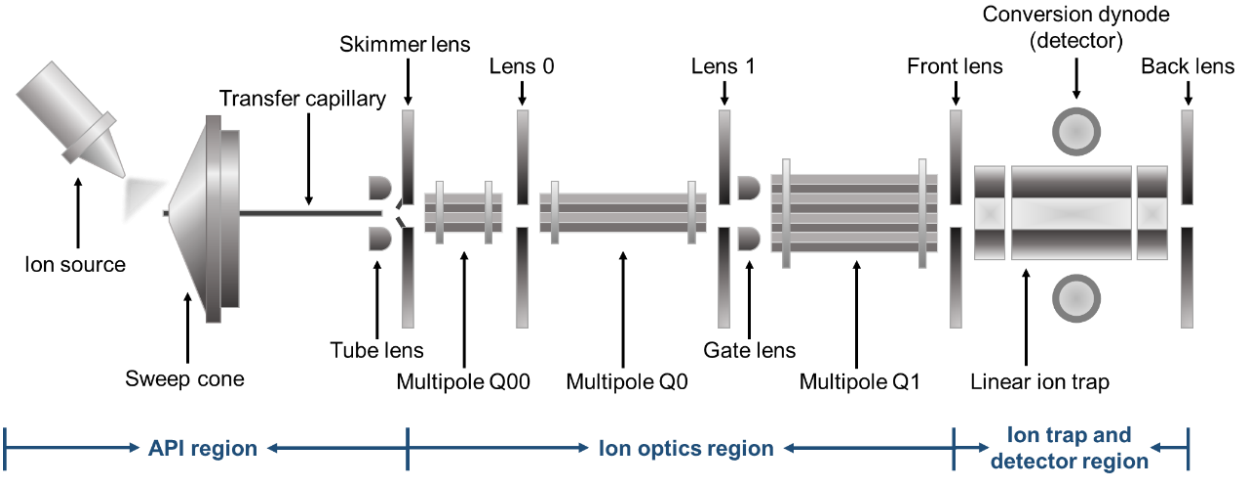

Figure 2.4. Schematic of the Thermo Scientific™ LTQ linear quadrupole ion trap (LQIT) mass spectrometer.

2.3.1 Atmospheric pressure ionization (API) region

The API region was composed of an ion source box (Ion Max™ API source housing) and an API stack (Figure 2.5). The ionization source, a corona discharge needle (if APCI is used) and a sweep cone were located in the ion source box operated at atmospheric pressure (~760 Torr). The API stack consisted of an ion transfer capillary tube, a tube lens and a skimmer lens (Figure 2.5). The pressure in the API stack was maintained at approximately 1 Torr by using two Edwards E2M30 rotary-vane mechanical pumps at an evacuation rate of 650 L/min. A convectron gauge monitored the pressure in the API stack.[47]

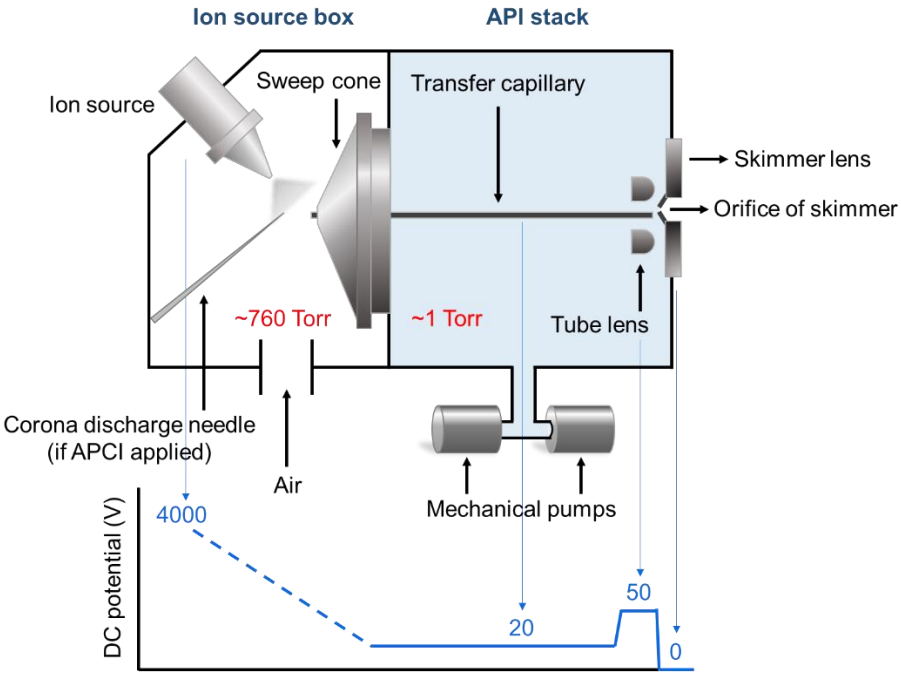

Figure 2.5. Schematic of the ion source box and the API stack region with typical pressure (red) and typical DC potential (blue) indicated for each section.

The positive ions generated in the ionization source were directed into the API stack due to the downhill pressure gradient (760 Torr to 1 Torr) and DC voltage gradient (± 3-5 kV to ± 0-60 V). The ions were then transmitted through the ion transfer capillary tube with a temperature of 50-350 °C. At the end of the ion transfer tube, the ions were decelerated and focused by the tube lens. A DC voltage (10-130 V) was applied to the tube lens to direct the ions through the orifice of the skimmer lens into the ion optics region. In order to prevent any neutral molecules entering the ion optics region, the orifice wass positioned offset from the radial center of the ion transfer tube.[47]

2.3.2 Ion optics region

Ion optics consisted of two square quadrupole ion guides (Q00 and Q0) and one cylindrical octupole ion guide (Q1).[47] Pressures in these three ion guides were reduced sequentially from Q00 to Q1, achieving a vacuum of ~0.5 Torr, ~10^{-3} Torr and ~10^{-5} Torr in Q00, Q0 and Q1, respectively (Figure 2.6). These pressures were maintained by an Leybold TW220/150/15S triple-inlet turbomolecular pump at an evacuation rate of 25 L/s, 300 L/s and 400 L/s, respectively. At the end

of each ion guide, a lens (lens 0, lens 1, gate lens and front lens) were used as vacuum baffles to divide regions with different pressure levels (Figure 2.6).

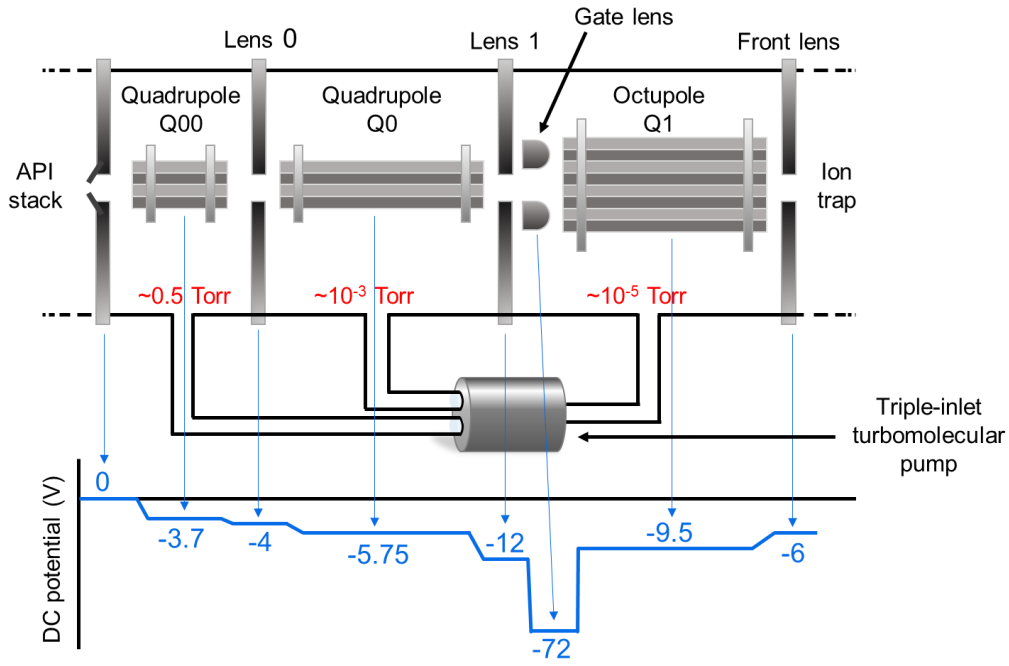

Figure 2.6. Schematic of the ion optics region with pressure (red) and typical DC potential (blue) indicated for each section.

From the API stack, three multipoles transmitted the ion beam into the ion trap. The trajectories of the ions must be restricted inside the multipoles in the radial direction (x- and y-directions) to prevent their collisions with the electrodes. In order to control the trajectories of the ions in the radial direction, a radio frequency (RF) voltage with the same amplitude and phase was applied to the opposing electrodes of the quadrupole (or octupole) and another RF voltage with same amplitude but 180° out-of-phase was applied to adjacent electrodes (Figure 2.7). The RF voltage on the opposing electrodes oscillates from positive to negative in a sine wave and the one on the adjacent electrodes oscillates from negative to positive simultaneously (Figure 2.7). The periodic electric field generated by the oscillating RF voltages[56] forces the ions into moving on a circle in the radial direction (Figure 2.7) without hitting the electrodes.

On the other hand, the ions had to be guided along the axial direction (z-direction) so that they can reach the ion trap. A DC voltage gradient was applied to each multipole and lens in order to provide ions additional kinetic energy and facilitate their movement along the axial direction

(Figure 2.6). With the combined effect of the DC and RF voltages, the ions adopt a circular oscillatory movement that resembles a corkscrew from the Q00 quadrupole ion guide toward the ion trap.

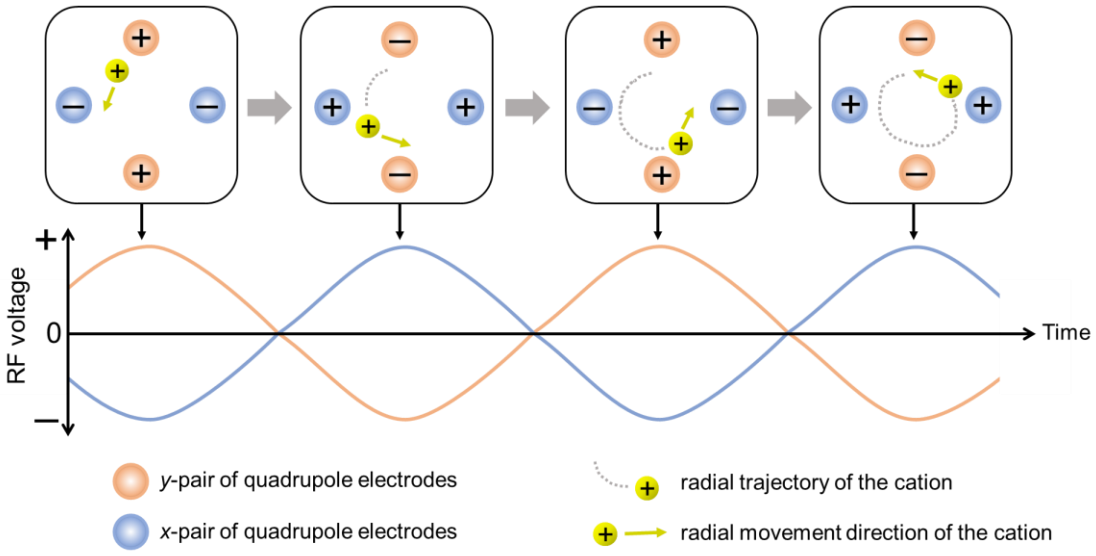

Figure 2.7. Illustration of the RF voltages applied to the electrodes of the quadrupoles/octupole in the ion optics, showing the oscillation of the RF voltage polarity as a function of time and the radial trajectory and movement of a cation at different points of time.

2.3.3 Ion trap region

After travelling through the ion optics region, the ions entered the ion trap region. The nominal pressure in this region was approximately 10^{-5} Torr, based on a reading on a Bayard-Alpert ion gauge.[47] However, due to the presence of helium buffer gas in the ion trap, the real pressure in the ion trap was about 0.002 Torr.[57] The pressure of helium in the ion trap could not be measured by the ion gauge because it cannot ionize helium molecules.[58]

The ion trap was composed of four parallel hyperbolic electrodes and was divided into three sections along the z-direction: front section, center section and back section (Figure 2.8).[47] The lengths of the front and back sections were 12 mm, and the length of the center section was 37 mm. Two slits (0.25 mm × 30 mm) were located on the two x-electrodes of the center section (Figure 2.8), which were utilized to eject ions from the ion trap into the two detectors. In the ion trap, the ions could be trapped, isolated, activated, and ejected. The principles of these events are discussed later in Section 2.4.

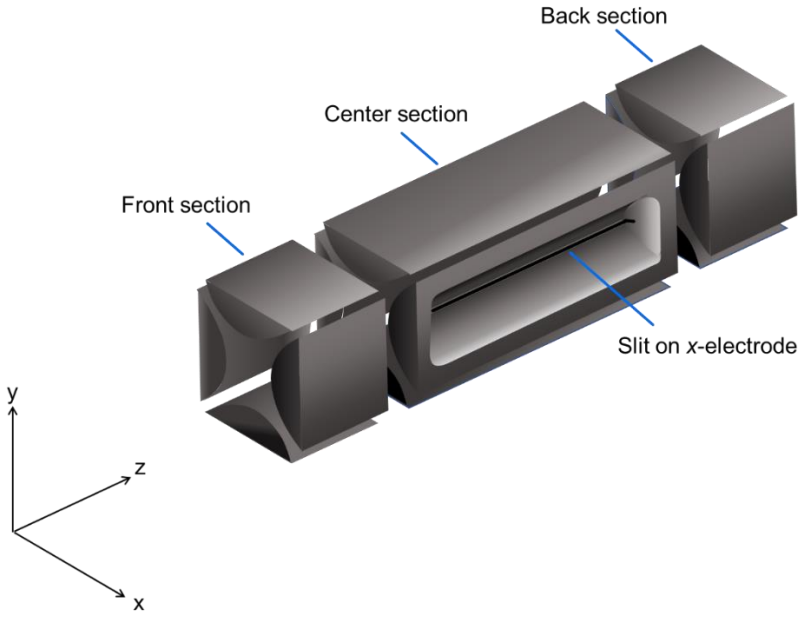

Figure 2.8. Schematic of the three sections of a linear quadrupole ion trap.

Two detectors were located on the opposite sides of the two x-electrodes. Each detector was composed of a conversion dynode and an electron multiplier (Figure 2.9).[47] A large attractive potential (± 15 kV) was applied to the dynode. As a result, after the ejection of ions through the two slits in the x-electrodes, the ion beam was directed towards the dynodes. When an ion strikes the curved metal surface of the dynode, one or few secondary particle(s) are produced. The strike of a cation produces electron(s) or anion(s) as secondary particle(s).[59] The strike of an anion, on the other hand, produces cation(s) as secondary particle(s).[59] A voltage gradient was applied between the dynode and the electron multiplier in order to accelerate the secondary particles into the electron multiplier.

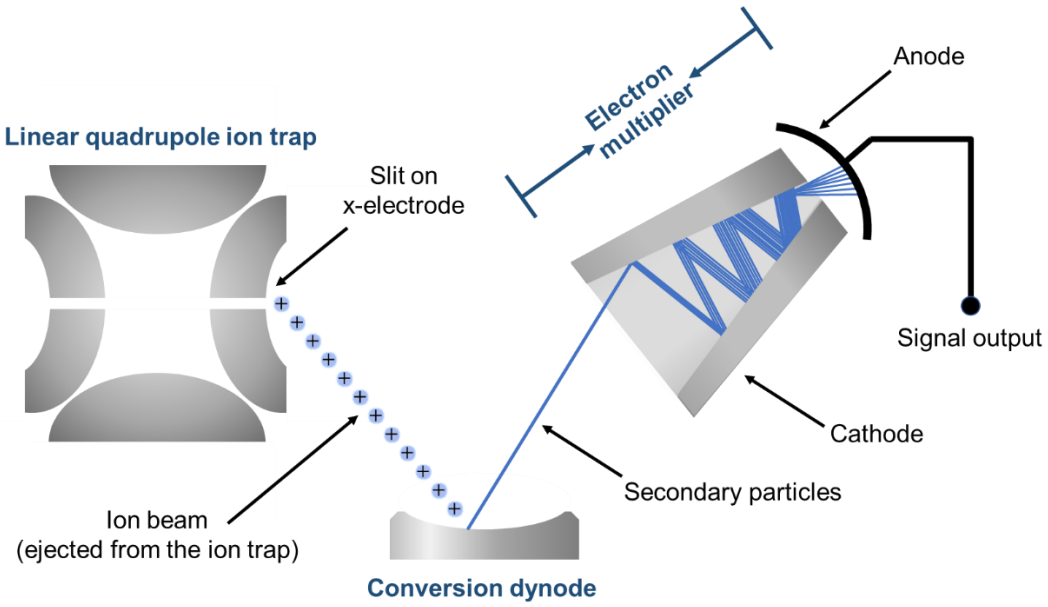

Figure 2.9. Simplified schematic of one of the detectors of the LQIT mass spectrometer. The detector was positioned on the opposite side of the x-electrode. Ions (shown here as cations) ejected from the ion trap struck the conversion dynode to produce secondary particles. These secondary particles were directed into the cathode of the electron multiplier to generate many more electrons upon consecutive collisions with the surface. The resulting electron cascade was collected by the anode and the amplitude of the current was measured.

An electron multiplier consisted of two parts: a funnel-shaped cathode and a cup-shaped anode.[47] The secondary particles from the dynode arrive at the cathode first and hit the inner wall of the cathode. This results in the generation of electrons that move deeper into the cathode due to the increasing positive potential gradient. During their movement toward the anode, the electrons hit the surface several times to produce more electrons. Eventually, a measurable electric current was generated at the cup-shaped anode. The amplitude of this current reflects the relative abundances of the ions that were ejected from the ion trap, as the amplitude is proportional to the number of the ions.

2.4 Ion behaviors in ion trap

2.4.1 Ion motion in LQIT

In the ion trap, RF and DC voltages were applied to the electrodes of the linear quadrupole ion trap to generate a three-dimensional electric field. The ions were restricted in the ion trap by

the electric field in the radial and axial directions. In the following two sections, the radial and axial motions of the trapped ions in are discussed in detail.

2.4.1.1 Radial motion

The combination of the RF and DC voltages applied on the four electrodes generates a quadrupolar electric field in the ion trap.[47] The electric potential ϕ_0 applied on the electrodes can be expressed as:[49,60]

$$\phi_0 = U - V cos\Omega t \qquad \text{Equation 2.1}$$

where U and V are the amplitudes of the DC and RF voltages applied to the electrodes, respectively. Ω is the angular frequency of the RF voltage, and t is time.

At the point x,y,z within the generated electric field, the potential ϕ can be expressed as:

$$\phi = \frac{\phi_0}{r_0^2}(\lambda x^2 + \sigma y^2 + \gamma z^2) \qquad \text{Equation 2.2}$$

where r_0 is the radius of the inscribed circle of the electrodes and λ, σ and γ are the weighing constants for x, y and z coordinates, respectively. For a linear quadrupole ion trap, $\lambda = -\sigma = 1$ and $\gamma = 0$.[60] Therefore, the potential at the point x,y,z can be expressed as:

$$\phi = \frac{\phi_0}{r_0^2}(x^2 - y^2) \qquad \text{Equation 2.3}$$

The electric field intensity in the x-direction (E_x) can be obtained by differentiating the potential ϕ to x as below:

$$E_x = -\frac{\partial \phi}{\partial x} = -2\frac{\phi_0}{r_0^2}x \qquad \text{Equation 2.4}$$

For an ion located at x,y,z, the force component in the x-direction (F_x) that the ion is subjected to can be expressed as:

$$F_x = ze \times E_x = -2ze\frac{\phi_0}{r_0^2}x \qquad \text{Equation 2.5}$$

where z is the number of the charges of the ion and e is the elemental charge. Substituting Equation 2.1 into Equation 2.5, Equation 2.6 is obtained:

$$F_x = -\frac{2ze}{r_0^2}(U - V cos\Omega t)x \qquad \text{Equation 2.6}$$

On the other hand, the force component in the x-direction (F_x) can also be expressed as:

$$F_x = ma_x = m\frac{d^2x}{dt^2} \qquad \text{Equation 2.7}$$

where m is the mass of the ion and a_x is the acceleration of the ion in the x-direction.

Combination of Equations 2.6 and 2.7 yields a linear second-order homogeneous differential equation of x as shown below.

$$m\frac{d^2x}{dt^2} = -\frac{2ze}{r_0^2}(U - Vcos\Omega t)x \qquad \text{Equation 2.8}$$

For y-direction, Equation 2.9 can be obtained with the same derivation process as Equation 2.8:

$$-m\frac{d^2y}{dt^2} = m\frac{d^2(-y)}{dt^2} = -\frac{2ze}{r_0^2}(U - Vcos\Omega t)(-y) \qquad \text{Equation 2.9}$$

Equations 2.8 and 2.9 can be further rearranged as follows:

$$\frac{d^2x}{dt^2} + \frac{2ze}{mr_0^2}(U - Vcos\Omega t)x = 0 \qquad \text{Equation 2.10}$$

$$\frac{d^2(-y)}{dt^2} + \frac{2ze}{mr_0^2}(U - Vcos\Omega t)x(-y) = 0 \qquad \text{Equation 2.11}$$

Equations 2.10 and 2.11 are in the same form as the Mathieu Equation[61] shown below:

$$\frac{d^2u}{d\xi^2} + u(a_u - 2q_u cos2\xi) = 0 \qquad \text{Equation 2.12}$$

where u represents x or $-y$, and ξ is a dimensionless parameter equal to $\frac{\Omega t}{2}$ for Equations 2.10 and 2.11. a_u and q_u are called the trapping parameters.[49] When they reside in a specific region called the Mathieu Stability region,[60] the Mathieu Equation has a stable solution, which means that the ions have stable trajectories in the ion trap.

Substitution of $\xi = \frac{\Omega t}{2}$ into Equation 2.12 yields:

$$m\frac{d^2u}{dt^2} + \frac{\Omega^2}{4}(a_u - 2q_u cos\Omega t)u = 0 \qquad \text{Equation 2.13}$$

Combining Equation 2.13 with Equations 2.10 and 2.11, the trapping parameters in the x- and y-directions are obtained as shown below:

$$a_u = a_x = -a_y = \frac{8zeU}{mr_0^2\Omega^2} \qquad \text{Equation 2.14}$$

$$q_u = q_x = -q_y = -\frac{4zeV}{mr_0^2\Omega^2} \qquad \text{Equation 2.15}$$

As mentioned above, for an ion to have a stable trajectory in the ion trap requires that its a_u and q_u values fall within the Mathieu Stability region. The diagram shown in Figure 2.10 is called the Mathieu Stability Diagram.[61] Ions with stable trajectories have *a* and *q* values located in the overlapping region in Figure 2.10.

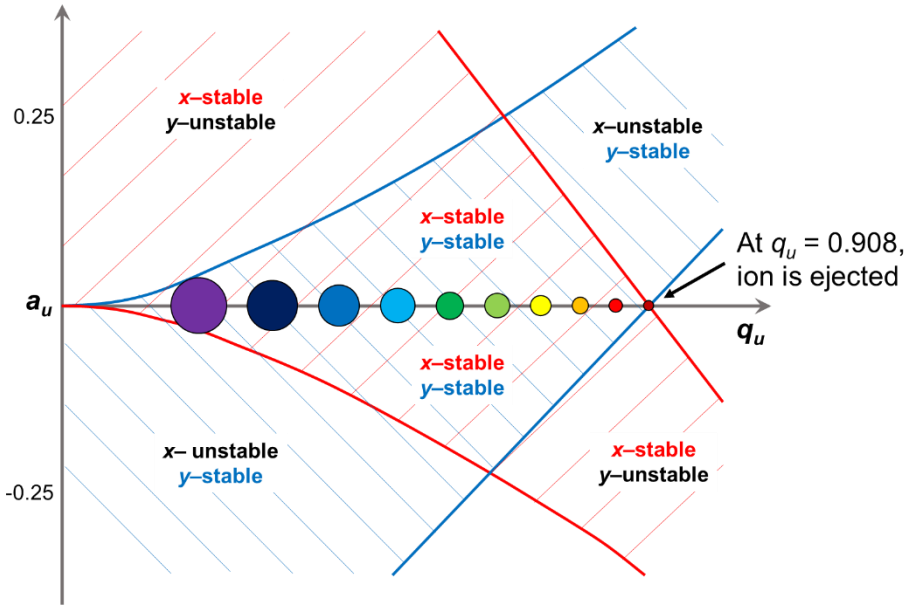

Figure 2.10. Mathieu Stability Diagram for a linear quadrupole ion trap. The colored circles represent ions with different *q* values. The sizes of the circles represent the *m/z* ratios of the ions. Ions with *a* and *q* values inside the overlapping region (both *x*- and *y*-stable) have stable trajectories in both *x*- and *y*-direction.

In LQIT, the DC voltage is usually set to zero, which causes a_u to be zero. As shown in Figure 2.10, at $a_u = 0$, q_u ranges from 0 to 0.908 for trapped ions whose q value is in the stability region. The wide range of q_u values in the stability region enables the trapping of ions with a wide range of *m/z* values.

Besides the ion motions mentioned above, each ion also has a specific secular motion whose frequency ω_u can be described as:

$$\omega_u = \frac{\beta_u \Omega}{2} \qquad \text{Equation 2.16}$$

where β_u is a coefficient that can be calculated from a_u and q_u. Under the circumstance that $a_u < 0.2$ and $q_u < 0.4$, β_u can be approximated as:

$$\beta_u = \sqrt{a_u + \frac{q_u^2}{2}} \qquad \text{Equation 2.17}$$

In LQIT, β_u ranges from 0 to 1, so the maximum value of ω_u is $\Omega/2$, which is the half of the angular frequency of the RF voltage.

2.4.1.2 Axial motion

Different DC voltages are applied to the different sections of the ion trap to trap ions in the axial direction.[47] Typical DC voltages when trapping positive ions are illustrated in Figure 2.11 (for negative ions, the polarities are reversed). The DC voltages applied to the front and back sections are both greater than the DC voltage applied to the center section. A DC potential well is hence created, which restrict the axial motion of the ions within the center section. As the slits on the x-electrodes reside in the center section, the potential well improves the efficiency of the ion ejection through the slits.[47,62]

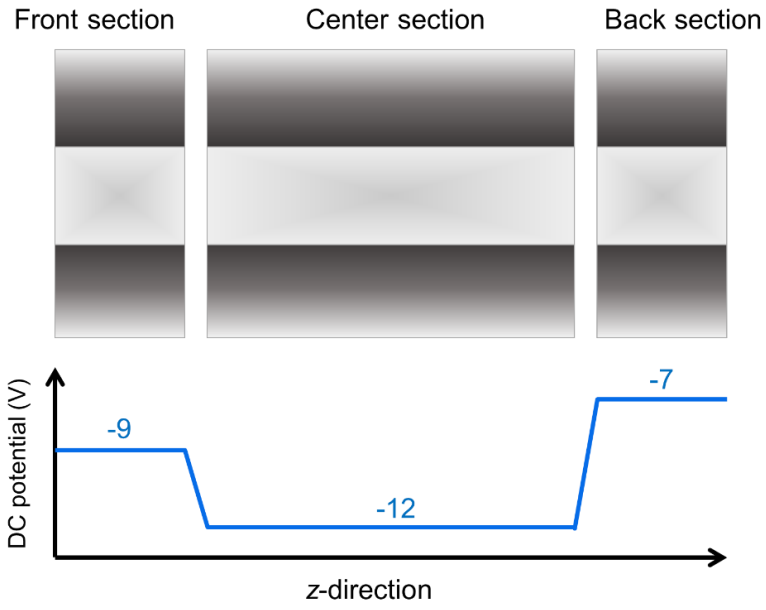

Figure 2.11. Schematic of the three sections of the ion trap with typical DC potential (blue) applied to each section. As DC voltages applied to the front and back sections are greater than the voltage applied to the center section, ions are trapped in the center section.

As an ion moves from the front section (high DC voltage applied) into the center section (low DC voltage applied), its electric potential energy converts into kinetic energy. The kinetic energy prevents the ion to be localized in the center section because an ion with high kinetic energy can move back and forth between the front and back sections. In order to confine the ions within the center section, helium is used as a buffer gas to reduce the kinetic energies of the ions.[57,62]As a result, the ions are trapped in the center section.

2.4.2 Ion ejection for detection

To eject ions from the ion trap in a controlled manner, two scan methods are often utilized: ion axial instability scan and ion resonance ejection.[49,62-65] In both methods, the DC voltage (U) is set to zero, which causes the a_u to be zero. Therefore, both methods eject ions only by adjusting the value of q_u, which is determined by the RF voltage amplitude (V).

In axial instability scan, the RF voltage amplitude is increased until the q_u of each ion reaches 0.908.[49,63] As shown in Figure 2.10, ions with q_u values larger than 0.908 have unstable trajectories and are ejected from the ion trap. According to Equation 2.15, smaller ions have greater q_u values than larger ions, and thus will be ejected prior to larger ions (Figure 2.10). This enables ejection of all ions from the trap in a mass-selective manner. The main disadvantage of the axial instability scan is its low sensitivity because some of the ions at q_u = 0.908 may collide with the electrodes due to their unstable trajectories and thus cannot be detected.[63]

In order to improve the sensitivity of ion detection, resonance ejection can be applied.[62,64,65] In this ejection mode, a supplementary RF voltage with a fixed frequency is applied to the x-electrodes. At the same time, the main RF voltage amplitude is increased to bring q_u of the ion to be ejected to 0.880. As the main RF voltage rises, the secular frequency of the ions in the ion trap also increases, as their secular frequency ω_u is proportional to q_u (when a_u = 0) according to Equations 2.16 and 2.17. At q_u = 0.880, the supplementary RF voltage is in resonance with the secular motion of the ions that are being ejected. The supplementary RF voltage accelerates these ions and hence increases the amplitude of the ion oscillation in the x-direction, which causes ejection of these ions through the slit on the x-electrode. According to Equations 2.15, 2.16 and 2.17, the secular frequency of the ions is inversely proportional to their m/z. Therefore, smaller ions will be ejected prior to larger ions.

The main RF voltage amplitude can be utilized to eject ions of different *m/z* ratios based on Equation 2.15. These ions are then transmitted into the two detectors on both sides of the ion trap and their relative abundances are determined as discussed in Section 2.3.3. Mass spectra are produced by combining the ion relative abundances and their *m/z* ratios.

2.4.3 Tandem mass spectrometry

The LQIT mass spectrometer is especially powerful for structural elucidation of unknown compounds,[24,66] because tandem mass spectrometry (MS^n) experiments can be conducted on mass-selected ions by using this instrument.[67] In MS^n experiments, multiple ion isolation and ion activation events are performed in a stepwise manner in the ion trap. The simplest tandem mass spectrometry experiment (MS^2) is conducted by isolating the ions of interest and subjecting them to reactions, such as collision-activated dissociation (CAD), in order to obtain structural information. The so-generated product ions can be isolated and subjected to additional reactions in MS^3 experiments. This isolation-reaction process can be repeated for several times (MS^n) if the signal permits. The principles of ion isolation and dissociation as well as bimolecular gas-phase ion-molecule reactions are discussed below.

2.4.3.1 Ion isolation

As discussed above, isolation of ions with a specific *m/z* ratio is the first step required for MS^n experiments. The ion isolation is accomplished by ejecting all other, unwanted ions from the ion trap.

The ejection of unwanted ions consists of two steps: 1) Ramping up the main RF amplitude until the q_u value of the ions to be isolated has increased to 0.803.[47] At this point, most of the ions with lower *m/z* ratios than the ions of interest no longer possess a stable trajectory as their q_u values are greater than 0.908 (Figure 2.12). As a result, these ions are ejected from the ion trap. 2) Applying a broad-band RF excitation waveform to the x-electrode.[47] The waveform is composed of a wide distribution of frequencies ranging from 5 kHz to 500 kHz, some of which are in resonance with the secular frequencies of the ions in the ion trap except for the ions of interest. The broad-band RF excitation waveform increases the amplitude of the oscillation of all the

unwanted ions in the x-direction. Hence, these unwanted ions are ejected from the ion trap, resulting in the isolation of the desired ions (Figure 2.12).

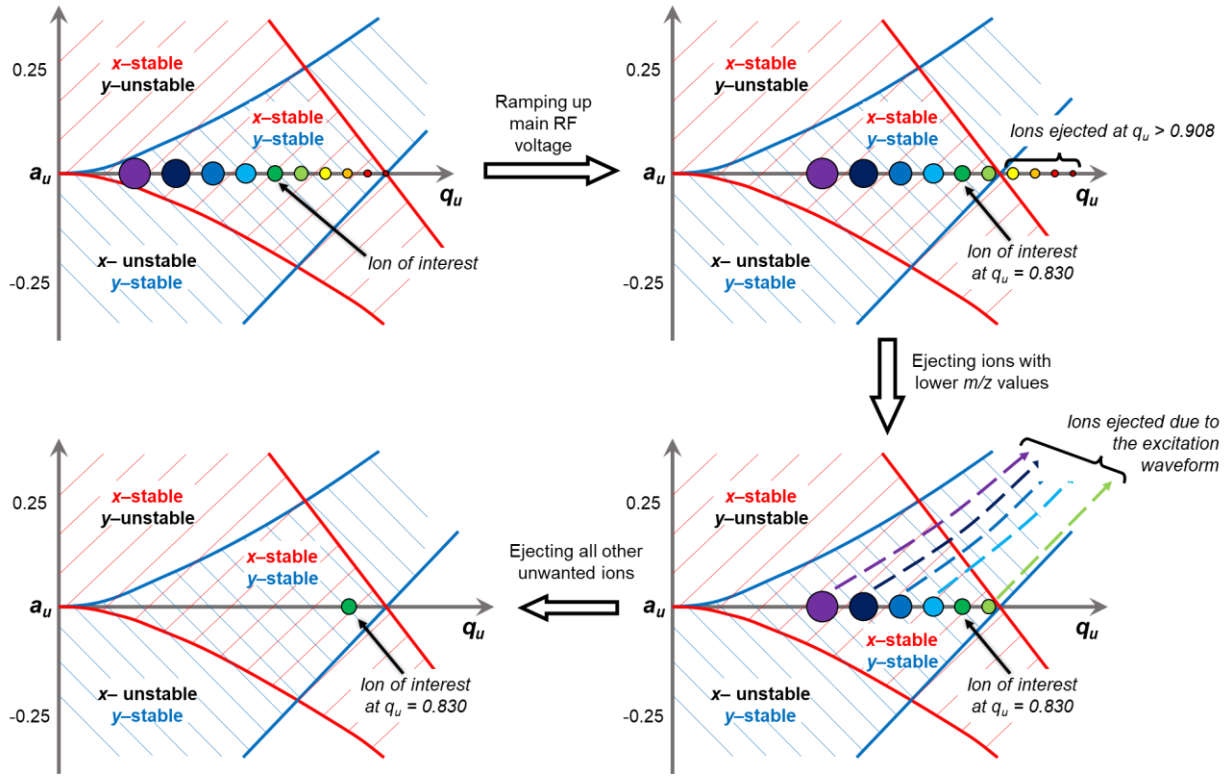

Figure 2.12. Demonstration of the ion isolation process in the ion trap. All the ions are trapped initially, followed by ramping up the main RF voltage until the q_u value of the ion of interest (shown in dark green color) reaches 0.830. At this point, some ions with lower *m/z* ratios (shown in red, orange, yellow and light green colors) have $q_u > 0.908$ and therefore are ejected from the ion trap. A broad-band RF excitation waveform with a wide distribution of frequencies (except the secular frequency of the ions of interest) is then applied on the x-electrode in order to eject all other unwanted ions (shown in purple, black, light and dark blue colors). This leads to isolation of the ion of interest.

2.4.3.2 Collision-activated dissociation (CAD)

After the isolation of an ion with a specific *m/z* value, the ion can be subjected to collision-activated dissociation (CAD) to obtain structural information. CAD process consists of two steps described below.

1) The main RF amplitude is decreased from what it was during ion isolation until the q_u value of the isolated ion reaches approximately 0.25.[47] The goal of reducing the RF amplitude is

to stabilize the trajectories of the fragment ions, whose *m/z* ratios are smaller than that of the fragmenting ion. As discussed above, ions with smaller *m/z* possess greater q_u values at a given RF amplitude. As the main RF amplitude drops, the q_u values of the fragment ions decrease, which allows trapping of many of the fragment ions.

2) A supplementary RF voltage with a small amplitude is applied to the x-electrodes.[47] The frequency of the supplementary RF voltage is same as the secular frequency of the isolated ion, which results in acceleration of the isolated ion. The accelerated ion undergoes collisions with the helium buffer gas in the ion trap. During each collision, part of the ion kinetic energy is converted into its internal energy. The internal energy accumulates via several collisions with helium gas until it overcomes the dissociation threshold of the fragmenting ion. Based on the discussion above, CAD can also be considered as a slow heating process, which is achieved by multiple collisions of the isolated ion with the helium buffer gas.[20,21]

Adjusting q_u value of the fragmenting ion is of importance because it determines the fragmentation efficiency as well as the low mass cut-off. As mentioned above, q_u is set to be approximately 0.25 in order to stabilize the trajectories of the fragment ions that are going to be generated. If the q_u value is decreased, more fragment ions with lower *m/z* ratios can be trapped and detected (Figure 2.13a). However, the secular frequency of the fragmenting ion drops as q_u decreases, which requires a supplementary RF voltage with lower frequency that is same as the secular frequency of the fragmenting ion. Consequently, the fragmenting ion gains less kinetic energy upon acceleration, resulting in a poor fragmentation efficiency. On the other hand, increasing q_u of the fragmenting ion allows the ion to fragment in a more efficient manner but some fragment ions with low *m/z* ratios may not be detectable (Figure 2.13b). Therefore, in CAD experiments, q_u value of the fragmenting ion must be optimizedaccording to obtain optimal fragmentation behavior.[20]

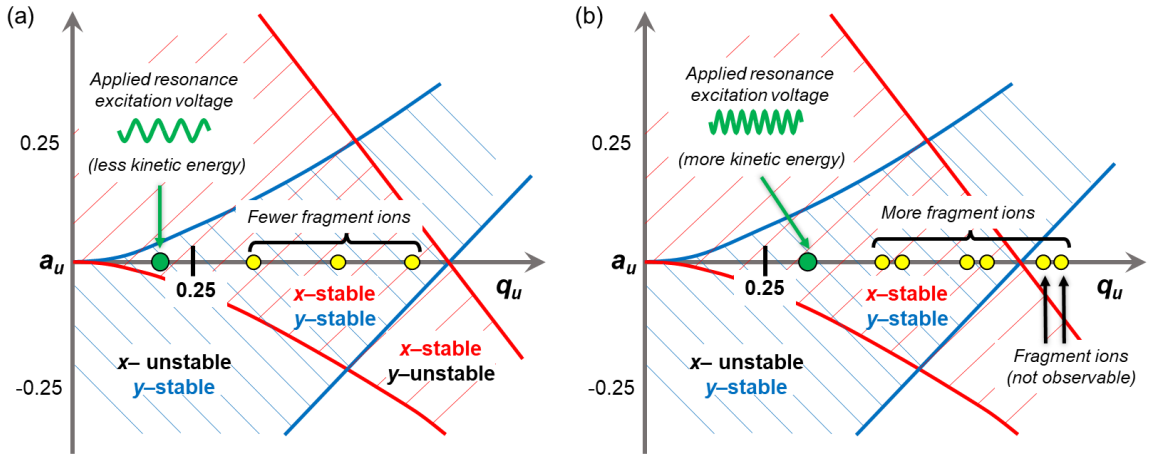

Figure 2.13. Demonstration of the effect of the q_u value on the fragmentation efficiency of an isolated ion and on the low mass cut-off. (a) At a lower q_u value, the fragmenting ion gains less kinetic energy from the resonance excitation voltage and fragments to fewer fragment ions but fragment ions with lower *m/z* ratios can be detected. (b) At a greater q_u value, the fragmenting ion gains more kinetic energy from the resonance excitation voltage and fragments to more fragment ions but fragment ions with lower *m/z* ratios are not detectable.

2.5 Gas-phase ion-molecule reactions

Although tandem mass spectrometry coupled with CAD is a powerful tool for structural elucidation of gas-phase ions, identification of unknown compounds by using this method is still challenging for three reasons: (1) Identification of ions by using MS^n coupled with CAD requires access to authentic model compounds, which are sometimes unavailable.[68,69] (2) CAD occasionally generates identical fragmentation patterns for isomeric fragmenting ions.[70,71] (3) Sometimes ions undergo only nondiagnostic fragmentation reactions, such as elimination of water or CO. To address these limitations, diagnostic gas-phase ion-molecule reactions have been developed for the identification of specific functional groups in ions in a predictable and reliable manner.[24] Additionally, gas-phase ion-molecule reactions have been extensively utilized to study the reactivities and kinetics of highly reactive species (e.g., polyradicals, carbenes and carbyne anions) in order to avoid the impact of solvent on their reactions.[72-74]

In gas-phase ion-molecule reaction experiments, ions are isolated in a LQIT as described above for CAD experiments and then are allowed to react with reagent molecules in the ion trap without acceleration. In this research, the reagent molecules were introduced via an external reagent mixing manifold[75,76] into the ion trap. The product ions can be isolated and subjected to

CAD in order to explore their structures. In this section, the instrument modifications and the mechanisms and the kinetics of gas-phase ion-molecule reactions are discussed in detail.

2.5.1 Instrument modifications

The Thermo^{TM} LTQ XL linear quadrupole ion trap mass spectrometer was modified by attaching an external reagent mixing manifold for the introduction of the reagents into the ion trap.[75,76] This sort of a manifold has been successfully utilized for a long time for continuous reagent introduction into ion traps.[51,77-79] The setup of the manifold used in this research is illustrated in Figure 2.14(a). The reagent is injected into the manifold via a syringe pump at a flow rate of 5 – 10 μL h^{-1} and vaporized and diluted with helium. Part of the diluted gaseous reagent is introduced into the ion trap via the control of a Granville-Phillips variable leak valve. The pressure in the ion trap is adjusted by the leak valve until the ion gauge reading is $0.7 – 1.2 \times 10^{-5}$ Torr. The rest of the gaseous reagent flows into the exhaust.

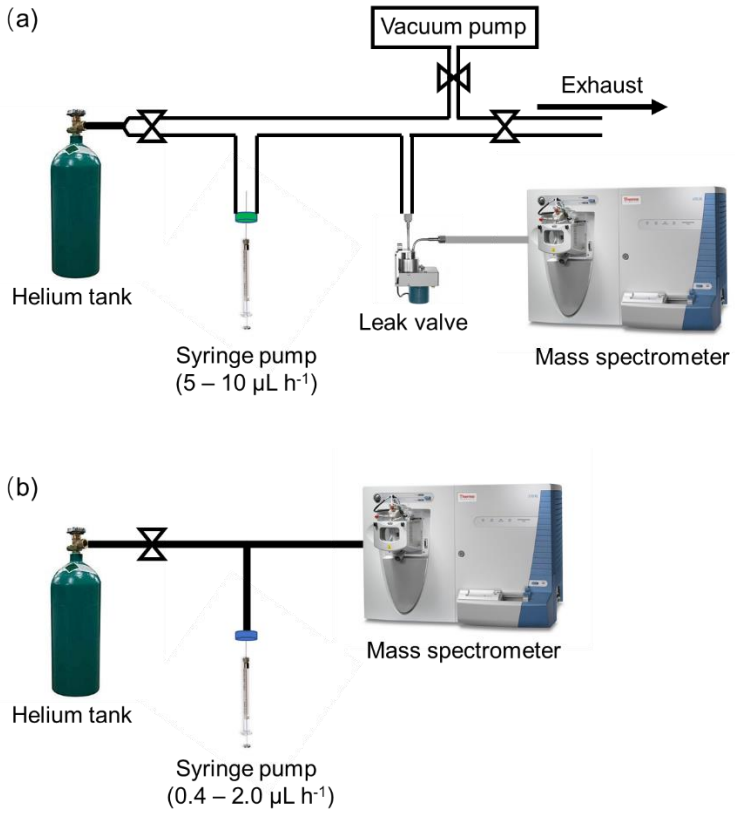

Figure 2.14. Schematic of (a) the external reagent mixing manifold for ion-molecule reactions and (b) a simplified, air-free manifold utilized for ion-molecule reactions of highly reactive species.

Although the external reagent mixing manifold shown in Figure 2.14(a) efficiently introduces reagents into the ion trap, it also mixes molecules from the air (*e.g.*, H_2O, O_2 and CO_2) into the gaseous reagent due to its large inner space and numerous junctions. In some experiments performed on highly reactive ions, the air molecules cause unwanted reactions, which hinders the examination of the reactivity of the ions of interest towards the reagent of interest. For example, the hydroxyphenylcarbyne anion shown in Figure 2.15(a) rapidly adds to water and CO_2 molecules, which hinders the exploration of its reactions with acetonitrile. To address the limitations of the traditional manifold, a simpler, air-free reagent mixing manifold was invented as shown in Figure 2.14(b). Compared with the traditional manifold, the simplified manifold does not include the exhaust line or the leak valve. The reagent is injected into the simplified manifold at a lower flow rate of 0.4-2.0 μL h^{-1} than into the traditional manifold. The reagent is then vaporized, diluted with helium, and transferred into the ion trap. As shown in Figure 2.15(b), the simplified manifold

diminished the formation of the water adduct and completely eliminated the formation of the CO_2 adduct.

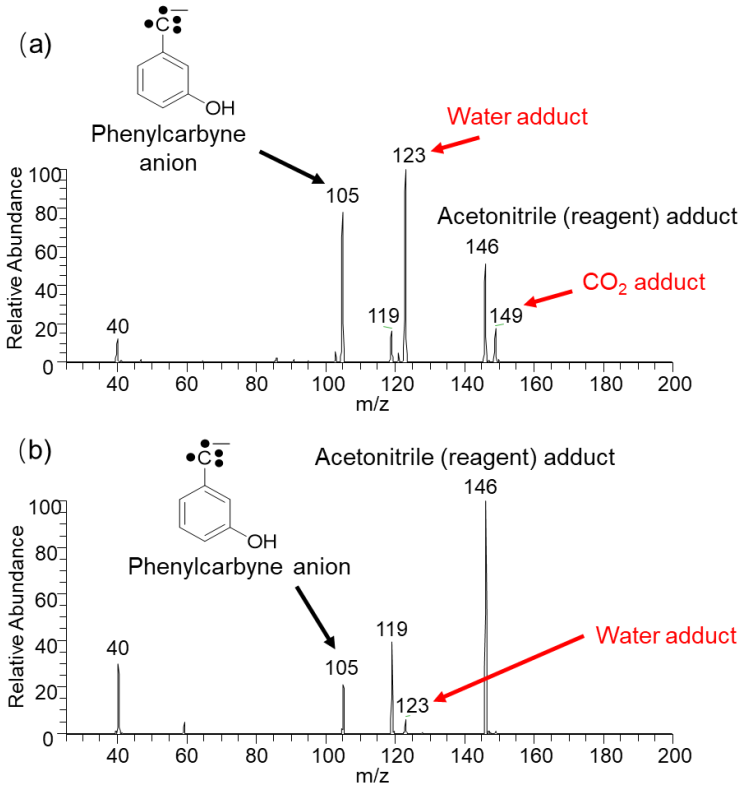

Figure 2.15. Mass spectrum measured after 1000 ms reactions of 4-hydroxy-phenylcarbyne anion with acetonitrile introduced into the ion trap by using (a) the traditional reagent mixing manifold and (b) simplified manifold. Due to the presence of water and CO_2 (from air) in the manifold, water and CO_2 adducts (labelled in red color) were observed when using the traditional manifold. However, less water and CO_2 adducts were generated when using the simplified manifolds.

2.5.2 Brauman's double-well potential energy surface

In 1977, a model called double-well potential energy surface[80,81] was proposed by Brauman to describe ion-molecule reactions in the gas phase (Figure 2.16). According to this model, the ion and the molecule approach each other due to long-distance ion-dipole (for polar molecules) or ion-induced dipole (for non-polar molecules) attraction. A reactant complex is formed when the reactant ion and the reactant molecule are close enough. The formation of the complex releases energy that is stored as internal energy of the reactant complex and is referred to as solvation energy (Figure 2.16). Solvation energy can be utilized by the reactant complex to overcome energy

barriers to generate the product complex. The product complex dissociates to form the separated product ion and product molecule.

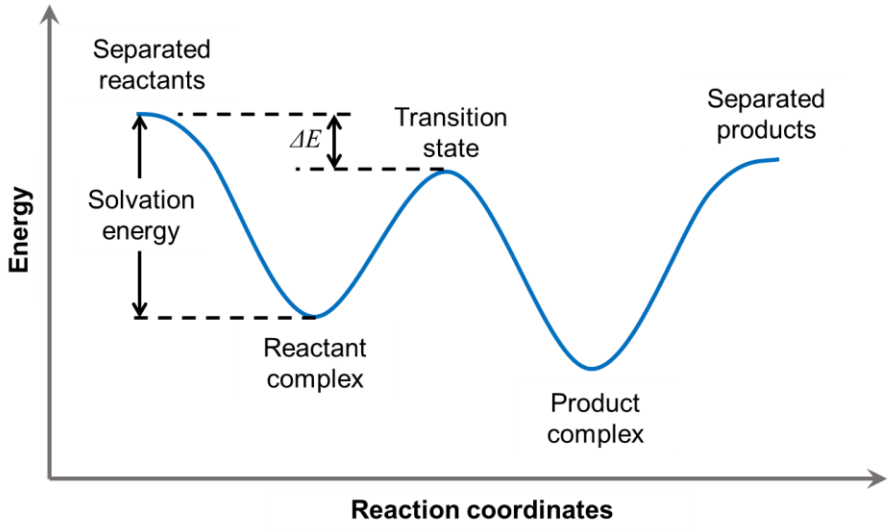

Figure 2.16. Brauman's double-well potential energy surface model

For the reaction to be thermoneutral or exothermic (and hence fast), the total energy of the separated reactants has to be equal or greater than that of the separated products. Otherwise, the reaction cannot take place unless extra energy is provided (*e.g.*, via collisional activation). Generally, the energy difference between the separated reactants and the transition state (ΔE, Figure 2.16) determines the rate of an exothermic gas-phase ion-molecule reaction. The greater the energy difference, the faster the reaction.

Many gas-phase ion-molecules that are exothermic occur very fast. However, sometimes, exothermic reactions proceed slowly or do not proceed at all even when ΔE is great. That is because the transition state is more rigid than the separated reactants. Therefore, the separated reactants have greater entropy and hence their reformation is more favorable than overcoming the transition state.

2.5.3 Kinetics of gas-phase ion-molecule reactions

Gas-phase ion-molecule reactions generally follow the kinetics of second-order reactions, which can be expressed as:

$$v = k_{exp} \times [R] \times [I] \qquad \text{Equation 2.18}$$

where v is the reaction rate, k_{exp} is the rate constant, and [R] and [I] are the concentrations of the reagent molecules and isolated ions, respectively. In all gas-phase ion-molecule reactions studied using mass spectrometry, the number of reagent molecules greatly exceeds the number of ions. Therefore, [R] can be considered to be a constant, and [I] is the only variable in Equation 2.18. Hence, the ion-molecule reaction can be considered as a pseudo first-order reaction described as shown below:

$$v = k_{obs} \times [I] \qquad \text{Equation 2.19}$$

where k_{obs} is the experimental rate constant of the pseudo first-order reaction and can be expressed as:

$$k_{obs} = k_{exp} \times [R] \qquad \text{Equation 2.20}$$

According to Equation 2.19, k_{obs} can be measured by plotting $ln\frac{[I]_{reactant}}{\Sigma[I]}$ as a function of time, where $[I]_{reactant}$ refers to the concentration of reactant ions and Σ[I] refers to the sum of the concentrations of reactant ions and product ions. k_{obs} is the negative slope of this semi-logarithmic plot. Occasionally, the semi-logarithmic plot is not linear because a mixture of isomeric ions with different reactivities were isolated. Isomeric ions cannot be isolated from each other by using the current mass spectrometry methods.

In order to obtain the second-order rate constant k_{exp}, the concentration of the reagent molecule, [R], must be determined (Equation 2.20). [R] can be estimated by converting the pressure in the ion trap (p_{trap}) with a conversion factor 1 Torr = 3.239×10^{16} molecules cm^{-3} as follows:

$$[R] = p_{trap} \times 3.239 \times 10^{16} \ \frac{molecules}{cm^3 \times Torr} \qquad \text{Equation 2.21}$$

However, as discussed in Section 2.3.3, the pressure in the ion trap cannot be measured directly. The ion gauge is utilized to monitor the pressure in the ion trap, but it does not accurately reflect the ion trap pressure due to the pressure gradient between the ion trap and the ion gauge and the varying ionization energies of the compounds to be measured. Therefore, an ion gauge correction factor (*IGCF*) was utilized to correct the difference between the pressure measured by the ion gauge (p_{gauge}) and the real pressure in the ion trap (p_{trap}). For the experiments using acetone or dimethyl disulfide as the reagent, *IGCF* was determined by measuring the rate of electron abstraction by the CS_2 radical cation from the reagent. On the other hand, for the experiments using

acetic acid or acetonitrile as the reagent, the rates of proton abstraction by the reagents from protonated methanol and protonated formaldehyde, respectively, were utilized for the determination of *IGCF*. All these proton transfer and electron transfer reactions are assumed to occur at the collision rate as they are highly exothermic and not sterically hindered.

Additionally, ion gauges have different sensitivities toward reagents with different polarizabilities, as an ion gauge measures the pressure by ionizing the gaseous molecules. Therefore, a correction factor – Baratron Factor (*B/I*) – was utilized to convert the measured pressure p_{gauge} to the real pressure, which can be expressed as:[58]

$$B/I = \frac{1}{0.36\alpha + 0.3} \qquad \text{Equation 2.22}$$

where α is the polarizability of the reagent molecule.

Based on the discussion above, Equation 2.21 can be converted to:

$$[R] = B/I \times IGCF \times p_{gauge} \times 3.239 \times 10^{16} \qquad \text{Equation 2.23}$$

Combining Equations 2.20 and 2.23, the rate constant of an ion-molecule reaction can be described as shown below:

$$k_{exp} = \frac{k_{obs}}{B/I \times IGCF \times p_{gauge} \times 3.239 \times 10^{16}} \qquad \text{Equation 2.24}$$

The efficiency of an ion-molecule reaction can be determined by dividing k_{exp} with a theoretical collision rate constant (k_{coll}) calculated using an empirical formula of a parameterized trajectory theory shown below:[82]

$$k_{coll} = \begin{cases} 0.4767x + 0.6200; & x \geq 2 \\ \dfrac{(x + 0.5090)^2}{10.526} + 0.9754; & x \leq 2 \end{cases} \qquad \text{Equation 2.25}$$

where x can be expressed as $\frac{\mu_D}{\sqrt{2\alpha k_B T}}$. μ_D is the dipole moment of the reagent, k_B is Boltzmann constant, and T is the temperature in the ion trap. The efficiency of the ion-molecule reaction is defined as the percentage of the collisions that lead to a reaction. Therefore, the efficiency is expressed as:

$$Efficiency = \frac{k_{exp}}{k_{coll}} \times 100\% \qquad \text{Equation 2.26}$$

Besides reaction efficiencies, the branching ratios of different primary product ions were also determined. The branching ratio of each product ion corresponds to the ratio of the abundance

of this product ion and the sum of the abundances of all the primary product ions. In order to distinguish secondary product ions (product ions generated upon reactions of primary product ions with the reagent) from the primary ones, the branching ratios were measured at short reaction times at which no secondary reactions occurred.

2.6 High-performance liquid chromatography coupled with tandem mass spectrometry

Although tandem mass spectrometry (MS^n) based on gas-phase ion-molecule reactions is a powerful tool in the identification of different functionalities in organic ions, a separation method is required prior to the identification process in order to analyze compounds in complex mixtures. High-performance liquid chromatography (HPLC) has been proven to be an effective separation method and compatible with tandem mass spectrometry for the analysis of mixtures.[83,84] Therefore, HPLC/MS^n experiments were sometimes conducted in this research to demonstrate the practicality of using MS^n methods based on diagnostic ion-molecule reactions in characterization of compounds in mixtures.

In this dissertation, HPLC/MS^n experiments were performed using a Thermo Surveyor HPLC coupled to a Thermo Scientific LQIT. The HPLC was equipped with an autosampler, a quaternary pump and a photodiode array detector. In HPLC experiments, separation of different compounds is based on the hydrophobicity of the analytes and interactions with the adsorbent material in the stationary phase. Therefore, the selection of the stationary and mobile phases greatly impacts the efficiency of the separation. They are discussed below. On the other hand, in order to determine the sensitivity of the HPLC/MS^n methods that have been developed, the limit of detection must be determined, which isl also discussed below.

2.6.1 Selection of stationary and mobile phases

In the process of HPLC method development, the stationary phase, *i.e.*, the material used to pack the column, must be initially selected. The stationary phase can be selected based on two characteristics:[85] (1) The bonded phase. Analyte molecules can interact with the stationary phase in four ways: van der Waals interactions, dipole-dipole interactions, hydrogen bonding and π-π interactions. By figuring out the structural differences between the analytes of interest, one or more of these four interactions can be utilized to separate the analytes. According to the interaction(s)

that is(are) selected, a proper stationary phase can be chosen for the separation. In order to separate the compounds by their van der Waals interactions, C18 or C8 column is often selected. For π-π interactions, phenyl column can be used. For dipole-dipole interactions, cyano column can be utilized. For hydrogen-bonding, amino column is often the best choice. (2) The physical characteristics of the particles. Particle size, column length, column inner diameter, surface area, pore size, bonding type and particle shape are the physical parameters of a stationary phase. These parameters can affect the efficiency, capacity, resolution, stability, sensitivity and time of the separation. The physical parameters of an average analytical column that is applicable in most cases are as follows: 150 mm × 4.6 mm, 5-μm inner diameter, 100-Å pore size, 200-m^2 g^{-1} surface area, 10% carbon load, monomeric bonding and spherical particles.[85]

After picking up a suitable stationary phase, the mobile phase also needs to be selected. The solubility of the analytes in the mobile phase, as well as the volatility, the viscosity and the inertness of the mobile phase must be considered.[86] Methanol-water and acetonitrile-water systems are the two mobile phases that are commonly used. Methanol-water system is cheap and less toxic, but it has a high viscosity and does only poorly dissolve nonpolar organic compounds.[87] On the other hand, acetonitrile has a lower viscosity and hence provides a better peak shape but is more toxic and is more expensive.

The analytes dissolved in the mobile phase must be neutral to be separated. Therefore, the pH value of the mobile phase must be controlled to prevent ionization of the separated compounds.[88] In this dissertation, formic acid was utilized as the pH modifier at a concentration of 0.1% (v/v) in HPLC experiments to prevent the deprotonation of compounds during separation.

2.6.2 Limit of detection measurement

The limit of detection is often defined as the lowest concentration of an analyte at which the signal-to-noise ratio of the analyte signal is at least three in a HPLC chromatograph or a mass spectrum.[89] For HPLC/MS^n methods based on ion-molecule reactions, the signal-to-noise ratios of the mass spectrometer peaks are always greater than for HPLC peaks at low concentrations, because as the analyte concentration decreases, the signal-to-noise ratio of the HPLC peaks decreases greater than that of the mass spectrometer peaks.[89] Therefore, the limits of detection in this dissertation were determined from the HPLC chromatographs. In this dissertation, the HPLC

signals of the product ions generated in the ion-molecule reactions were utilized to determine the limit of detection of the analytical method.

2.7 References

1. Petrović, M., Hernando, M.D., Díaz-Cruz, M.S. and Barceló, D., Liquid chromatography–tandem mass spectrometry for the analysis of pharmaceutical residues in environmental samples: a review. *J. Chromatogr. A* **2005**, *1067*, 1-14.

2. Bantscheff, M., Schirle, M., Sweetman, G., Rick, J. and Kuster, B., Quantitative mass spectrometry in proteomics: a critical review. *Anal. Bioanal. Chem.* **2007**, *389*, 1017-1031.

3. Bantscheff, M., Lemeer, S., Savitski, M.M. and Kuster, B., Quantitative mass spectrometry in proteomics: critical review update from 2007 to the present. *Anal. Bioanal. Chem.* **2012**, *404*, 939-965.

4. Crotty, S., Gerişlioğlu, S., Endres, K.J., Wesdemiotis, C. and Schubert, U.S., Polymer architectures via mass spectrometry and hyphenated techniques: a review. *Anal. Chim. Acta* **2016**, *932*, 1-21.

5. Benson, S., Lennard, C., Maynard, P. and Roux, C., Forensic applications of isotope ratio mass spectrometry—a review. *Forensic Sci. Int.* **2006**, *157*, 1-22.

6. Richardson, S.D., Environmental mass spectrometry: emerging contaminants and current issues. *Anal. Chem.* **2012**, *84*, 747-778.

7. Shushan, B., A review of clinical diagnostic applications of liquid chromatography – tandem mass spectrometry. *Mass Spectrom. Rev.* **2010**, *29*, 930-944.

8. Dempster, A.J., A new method of positive ray analysis. *Phys. Rev.* **1918**, *11*, 316-325.

9. Whitehouse, C.M., Dreyer, R.N., Yamashita, M. and Fenn, J.B., Electrospray interface for liquid chromatographs and mass spectrometers. *Anal. Chem.* **1985**, *57*, 675-679.

10. Yamashita, M. and Fenn, J.B., Electrospray ion source. another variation on the free-jet theme. *J. Phys. Chem.* **1984**, *88*, 4451-4459.

11. Carroll, D.I., Dzidic, I., Stillwell, R.N., Haegele, K.D. and Horning, E.C., Atmospheric pressure ionization mass spectrometry. corona discharge ion source for use in a liquid chromatograph-mass spectrometer-computer analytical system. *Anal. Chem.* **1975**, *47*, 2369-2373.

12. Carroll, D.I., Dzidic, I., Stillwell, R.N., Horning, M.G. and Horning, E.C., Subpicogram detection system for gas phase analysis based upon atmospheric pressure ionization (API) mass spectrometry. *Anal. Chem.* **1974**, *46*, 706-710.

13. Karas, M., Bahr, U. and Gießmann, U., Matrix-assisted laser desorption ionization mass spectrometry. *Mass Spectrom. Rev.* **1991**, *10*, 335-357.

14. Takats, Z., Wiseman, J.M., Gologan, B. and Cooks, R.G., Mass spectrometry sampling under ambient conditions with desorption electrospray ionization. *Science* **2004**, *306*, 471-473.

15. Taya, S., An experimental study on the stigmatic focusing condition of a magnetic sector mass analyzer. *Nucl. Instrum. Methods* **1978**, *152*, 399-405.

16. Grix, R., Kutscher, R., Li, G., Grüner, U., Wollnik, H. and Matsuda, H., A time-of-flight mass analyzer with high resolving power. *Rapid Commun. Mass Spectrom.* **1988**, *2*, 83-85.

17. Hu, Q., Noll, R.J., Li, H., Makarov, A., Hardman, M. and Graham Cooks, R., The orbitrap: a new mass spectrometer. *J. Mass Spectrom.* **2005**, *40*, 430-443.

18. Blaum, K., High-accuracy mass spectrometry with stored ions. *Phys. Rep.* **2006**, *425*, 1-78.

19. Douglas, D.J., Frank, A.J. and Mao, D., Linear ion traps in mass spectrometry. *Mass Spectrom. Rev.* **2005**, *24*, 1-29.

20. McLuckey, S.A., Principles of collisional activation in analytical mass spectrometry. *J. Am. Soc. Mass Spectrom.* **1992**, *3*, 599-614.

21. Mayer, P.M. and Poon, C., The mechanisms of collisional activation of ions in mass spectrometry. *Mass Spectrom. Rev.* **2009**, *28*, 608-639.

22. Brodbelt, J.S., Analytical applications of ion-molecule reactions. *Mass Spectrom. Rev.* **1997**, *16*, 91-110.

23. Stirk, K.M., Kiminkinen, L.M. and Kenttämaa, H.I., Ion-molecule reactions of distonic radical cations. *Chem. Rev.* **1992**, *92*, 1649-1665.

24. Liu, J.K.Y., Niyonsaba, E., Alzarieni, K.Z., Boulos, V.M., Yerabolu, R. and Kenttämaa, H.I., Determination of the compound class and functional groups in protonated analytes via diagnostic gas-phase ion-molecule reactions. *Mass Spectrom. Rev.* **2021**, mas.21727

25. Kebarle, P. and Verkerk, U.H., Electrospray: from ions in solution to ions in the gas phase, what we know now. *Mass Spectrom. Rev.* **2009**, *28*, 898-917.

26. Cech, N.B. and Enke, C.G., Practical implications of some recent studies in electrospray ionization fundamentals. *Mass Spectrom. Rev.* **2001**, *20*, 362-387.

27. Smith, R.D., Loo, J.A., Edmonds, C.G., Barinaga, C.J. and Udseth, H.R., New developments in biochemical mass spectrometry: electrospray ionization. *Anal. Chem.* **1990**, *62*, 882-899.

28. Veenstra, T.D., Electrospray ionization mass spectrometry in the study of biomolecular non-covalent interactions. *Biophys. Chem.* **1999**, *79*, 63-79.

29. Wu, X., Oleschuk, R.D. and Cann, N.M., Characterization of microstructured fibre emitters: in pursuit of improved nano electrospray ionization performance. *Analyst* **2012**, *137*, 4150-4161.

30. Konermann, L., Ahadi, E., Rodriguez, A.D. and Vahidi, S., Unraveling the mechanism of electrospray ionization. *Anal. Chem.* **2013**, *85*, 2-9.

31. Taylor, G.I., Disintegration of water drops in an electric field. *Proc. R. Soc. Lond., A Math. Phys. Sci.* **1964**, *280*, 383-397.

32. Wilm, M.S. and Mann, M., Electrospray and Taylor-Cone theory, Dole's beam of macromolecules at last?. *Int. J. Mass Spectrom. Ion Processes* **1994**, *136*, 167-180.

33. Rayleigh, L., On the equilibrium of liquid conducting masses charged with electricity. *London, Edinburgh Dublin Philos. Mag. J. Sci.* **1882**, *14*, 184-186.

34. Duft, D., Achtzehn, T., Müller, R., Huber, B.A. and Leisner, T., Rayleigh jets from levitated microdroplets. *Nature* **2003**, *421*, 128.

35. Iribarne, J.V. and Thomson, B.A., On the evaporation of small ions from charged droplets. *J. Chem. Phys.* **1976**, *64*, 2287-2294.

36. Thomson, B.A. and Iribarne, J.V., Field induced ion evaporation from liquid surfaces at atmospheric pressure. *J. Chem. Phys.* **1979**, *71*, 4451-4463.

37. Iavarone, A.T. and Williams, E.R., Mechanism of charging and supercharging molecules in electrospray ionization. *J. Am. Chem. Soc.* **2003**, *125*, 2319-2327.

38. Konermann, L., Rodriguez, A.D. and Liu, J., On the formation of highly charged gaseous ions from unfolded proteins by electrospray ionization. *Anal. Chem.* **2012**, *84*, 6798-6804.

39. Weston, D.J., Ambient ionization mass spectrometry: current understanding of mechanistic theory; analytical performance and application areas. *Analyst* **2010**, *135*, 661-668.

40. Liang, X., Xia, Y. and McLuckey, S.A., Alternately pulsed nanoelectrospray ionization/atmospheric pressure chemical ionization for ion/ion reactions in an electrodynamic ion trap. *Anal. Chem.* **2006**, *78*, 3208-3212.

41. Kolakowski, B.M., Grossert, J.S. and Ramaley, L., Studies on the positive-ion mass spectra from atmospheric pressure chemical ionization of gases and solvents used in liquid chromatography and direct liquid injection. *J. Am. Soc. Mass Spectrom.* **2004**, *15*, 311-324.

42. Jin, C., Viidanoja, J., Li, M., Zhang, Y., Ikonen, E., Root, A., Romanczyk, M., Manheim, J., Dziekonski, E. and Kenttämaa, H.I., Comparison of atmospheric pressure chemical ionization and field ionization mass spectrometry for the analysis of large saturated hydrocarbons. *Anal. Chem.* **2016**, *88*, 10592-10598.

43. Chang, J.S., Lawless, P.A. and Yamamoto, T., Corona discharge processes. *IEEE Trans. Plasma Sci.* **1991**, *19*, 1152-1166.

44. Shahin, M.M., Mass-spectrometric studies of corona discharges in air at atmospheric pressures. *J. Chem. Phys.* **1966**, *45*, 2600-2605.

45. Owen, B.C., Gao, J., Borton, D.J., Amundson, L.M., Archibold, E.F., Tan, X., Azyat, K., Tykwinski, R., Gray, M. and Kenttämaa, H.I., Carbon disulfide reagent allows the characterization of nonpolar analytes by atmospheric pressure chemical ionization mass spectrometry. *Rapid Commun. Mass Spectrom.* **2011**, *25*, 1924-1928.

46. Horning, E.C., Horning, M.G., Carroll, D.I., Dzidic, I. and Stillwell, R.N., New picogram detection system based on a mass spectrometer with an external ionization source at atmospheric pressure. *Anal. Chem.* **1973**, *45*, 936-943.

47. Schwartz, J.C., Senko, M.W. and Syka, J.E., A two-dimensional quadrupole ion trap mass spectrometer. *J. Am. Soc. Mass Spectrom.* **2002**, *13*, 659-669.

48. March, R.E. and Todd, J.F. *Quadrupole Ion Trap Mass Spectrometry*; John Wiley & Sons, Inc.: Hoboken, NJ, 2005.

49. March, R.E., An introduction to quadrupole ion trap mass spectrometry. *J. Mass Spectrom.* **1997**, *32*, 351-369.

50. Nanduri, A., Kulkarni, S.S. and Mills, P.L., Experimental techniques to gain mechanistic insight into fast pyrolysis of lignocellulosic biomass: a state-of-the-art review. *Renew. Sust. Energ. Rev.* **2021**, *148*, 111262-111279.

51. Gronert, S., Quadrupole ion trap studies of fundamental organic reactions. *Mass Spectrom. Rev.* **2005**, *24*, 100-120.

52. Macek, B., Waanders, L.F., Olsen, J.V. and Mann, M., Top-down protein sequencing and MS^3 on a hybrid linear quadrupole ion trap-orbitrap mass spectrometer. *Mol. Cell. Proteomics* **2006**, *5*, 949-958.

53. Bondarenko, P.V., Second, T.P., Zabrouskov, V., Makarov, A.A. and Zhang, Z., Mass measurement and top-down HPLC/MS analysis of intact monoclonal antibodies on a hybrid linear quadrupole ion trap-orbitrap mass spectrometer. *J. Am. Soc. Mass Spectrom.* **2009**, *20*, 1415-1424.

54. Bessette, E.E., Goodenough, A.K., Langouët, S., Yasa, I., Kozekov, I.D., Spivack, S.D. and Turesky, R.J., Screening for DNA adducts by data-dependent constant neutral loss-triple stage mass spectrometry with a linear quadrupole ion trap mass spectrometer. *Anal. Chem.* **2009**, *81*, 809-819.

55. Bessette, E.E., Spivack, S.D., Goodenough, A.K., Wang, T., Pinto, S., Kadlubar, F.F. and Turesky, R.J., Identification of carcinogen DNA adducts in human saliva by linear quadrupole ion trap/multistage tandem mass spectrometry. *Chem. Res. Toxicol.* **2010**, *23*, 1234-1244.

56. Reuben, A.J., Smith, G.B., Moses, P., Vagov, A.V., Woods, M.D., Gordon, D.B. and Munn, R.W., Ion trajectories in exactly determined quadrupole fields. *Int. J. Mass Spectrom. Ion Processes* **1996**, *154*, 43-59.

57. Stafford Jr., G.C., Kelley, P.E., Syka, J.E.P., Reynolds, W.E. and Todd, J.F.J., Recent improvements in and analytical applications of advanced ion trap technology. *Int. J. Mass Spectrom. Ion Processes* **1984**, *60*, 85-98.

58. Bartmess, J.E. and Georgiadis, R.M., Empirical methods for determination of ionization gauge relative sensitivities for different gases. *Vacuum* **1983**, *33*, 149-153.

59. Stanton, H.E., Chupka, W.A. and Inghram, M.G., Electron multipliers in mass spectrometry; effect of molecular structure. *Rev. Sci. Instrum.* **1956**, *27*, 109-109.

60. Douglas, D.J., Linear quadrupoles in mass spectrometry. *Mass Spectrom. Rev.* **2009**, *28*, 937-960.

61. Ruby, L., Applications of the Mathieu equation. *Am. J. Phys.* **1996**, *64*, 39-44.

62. Xu, W., Song, Q., Smith, S.A., Chappell, W.J. and Ouyang, Z., Ion trap mass analysis at high pressure: a theoretical view. *J. Am. Soc. Mass Spectrom.* **2009**, *20*, 2144-2153.

63. Kaiser Jr., R.E., Cooks, R.G., Stafford Jr., G.C., Syka, J.E. and Hemberger, P.H., Operation of a quadrupole ion trap mass spectrometer to achieve high mass/charge ratios. *Int. J. Mass Spectrom. Ion Processes* **1991**, *106*, 79-115.

64. Schwartz, J.C., Syka, J.E. and Jardine, I., High resolution on a quadrupole ion trap mass spectrometer. *J. Am. Soc. Mass Spectrom.* **1991**, *2*, 198-204.

65. Snyder, D.T., Peng, W.P. and Cooks, R.G., Resonance methods in quadrupole ion traps. *Chem. Phys. Lett.* **2017**, *668*, 69-89.

66. Banoub, J., Delmas Jr., G.H., Joly, N., Mackenzie, G., Cachet, N., Benjelloun-Mlayah, B. and Delmas, M., A critique on the structural analysis of lignins and application of novel tandem mass spectrometric strategies to determine lignin sequencing. *J. Mass Spectrom.* **2015**, *50*, 5-48.

67. De Hoffmann, E., Tandem mass spectrometry: a primer. *J. Mass Spectrom.* **1996**, *31*, 129-137.

68. Grebe, S.K. and Singh, R.J., LC-MS/MS in the clinical laboratory–where to from here?. *The Clin. Biochem. Rev.* **2011**, *32*, 5-31.

69. Xiao, J.F., Zhou, B. and Ressom, H.W., Metabolite identification and quantitation in LC-MS/MS-based metabolomics. *Trends Analyt. Chem.* **2012**, *32*, 1-14.

70. Kong, J.Y., Yu, Z., Easton, M.W., Niyonsaba, E., Ma, X., Yerabolu, R., Sheng, H., Jarrell, T.M., Zhang, Z., Ghosh, A.K. and Kenttämaa, H.I., Differentiating isomeric deprotonated glucuronide drug metabolites via ion/molecule reactions in tandem mass spectrometry. *Anal. Chem.* **2018**, *90*, 9426-9433.

71. Zhu, H., Ma, X., Kong, J.Y., Zhang, M. and Kenttämaa, H.I., Identification of carboxylate, phosphate, and phenoxide functionalities in deprotonated molecules related to drug metabolites via ion–molecule reactions with water and diethylhydroxyborane. *J. Am. Soc. Mass Spectrom.* **2017**, *28*, 2189-2200.

72. Williams, P.E., Jankiewicz, B.J., Yang, L. and Kenttämaa, H.I., Properties and reactivity of gaseous distonic radical ions with aryl radical sites. *Chem. Rev.* **2013**, *113*, 6949-6985.

73. Hu, J., Hill, B.T. and Squires, R.R., New approach to carbene chemistry via distonic carbene ions. a case of spin-forbidden proton transfer and carbene− biradical tautomerism. *J. Am. Chem. Soc.* **1997**, *119*, 11699-11700.

74. Seburg, R.A., Hill, B.T., Jesinger, R.A. and Squires, R.R., The phenylcarbyne anion. *J. Am. Chem. Soc.* **1999**, *121*, 6310-6311.

75. Gronert, S., Estimation of effective ion temperatures in a quadrupole ion trap. *J. Am. Soc. Mass Spectrom.* **1998**, *9*, 845-848.

76. Gronert, S., Mass spectrometric studies of organic ion/molecule reactions. *Chem. Rev.* **2001**, *101*, 329-360.

77. Derkits, D., Wiseman, A., Snead, R.F., Dows, M., Harge, J., Lamp, J.A. and Gronert, S., Development and evaluation of a variable-temperature quadrupole ion trap mass spectrometer. *J. Am. Soc. Mass Spectrom.* **2015**, *27*, 339-343.

78. Feng, E., Ma, X. and Kenttämaa, H.I., Characterization of protonated substituted ureas by using diagnostic gas-phase ion-molecule reactions followed by collision-activated dissociation in tandem mass spectrometry experiments. *Anal. Chem.* **2021**, *93*, 7851-7859.

79. Ma, X., Feng, E., Jiang, H., Boulos, V.M., Gao, J., Nash, J.J. and Kenttämaa, H.I., Protonated ground-state singlet *meta*-pyridynes react from an excited triplet state. *J. Org. Chem.* **2021**, *86*, 3249-3260.

80. Olmstead, W.N. and Brauman, J.I., Gas-phase nucleophilic displacement reactions. *J. Am. Chem. Soc.* **1977**, *99*, 4219-4228.

81. Pellerite, M.J. and Brauman, J.I., Intrinsic barriers in nucleophilic displacements. *J. Am. Chem. Soc.* **1980**, *102*, 5993-5999.

82. Su, T. and Chesnavich, W.J., Parametrization of the ion–polar molecule collision rate constant by trajectory calculations. *J. Chem. Phys.* **1982**, *76*, 5183-5185.

83. Polati, S., Bottaro, M., Frascarolo, P., Gosetti, F., Gianotti, V. and Gennaro, M.C., HPLC-UV and HPLC-MS^n multiresidue determination of amidosulfuron, azimsulfuron, nicosulfuron, rimsulfuron, thifensulfuron methyl, tribenuron methyl and azoxystrobin in surface waters. *Anal. Chim. Acta* **2006**, *579*, 146-151.

84. Harry-O'kuru, R.E., Payne-Wahl, K.L. and Busman, M., Medicinal components recoverable from Sicklepod (Senna obtusifolia) seed: analysis of components by HPLC-MS^n. *J Chromatogr. Sep. Tech.* **2012**, *S1*, 1-6.

85. Young, C.S. and Weigand, R.J., An efficient approach to column selection in HPLC method development. *LC GC N. Am.* **2002**, *20*, 464-473.

86. Barwick, V.J., Strategies for solvent selection—a literature review. *Trends Analyt. Chem.* **1997**, *16*, 293-309.

87. Subirats, X., Roses, M. and Bosch, E., On the effect of organic solvent Composition on the pH of buffered HPLC mobile phases and the pK_a of analytes—a review. *Sep. Purif. Rev.* **2007**, *36*, 231-255.

88. Sadek, P.C. and Sadek, P.C. *The HPLC solvent guide*; John Wiley & Sons, Inc.: New York, NY, 1996.

89. Easterling, L.F., Yerabolu, R., Kumar, R., Alzarieni, K.Z. and Kenttämaa, H.I., Factors affecting the limit of detection for HPLC/tandem mass spectrometry experiments based on gas-phase ion–molecule reactions. *Anal. Chem.* **2020**, *92*, 7471-7477.

CHAPTER 3. QUANTUM CHEMICAL CALCULATIONS AND DENSITY FUNCTIONAL THEORY

3.1 Overview

Quantum chemical calculations provide a powerful tool that have been utilized to elucidate the structures of compounds,[1-3] predict the physical properties of molecules,[1,4,5] and determine reasonable mechanisms for reactions in solution[1-3,6] and in the gas phase.[7,8] Among the applications listed above, calculations are especially appropriate for the determination of gas-phase reaction mechanisms because the calculations usually correspond to gas-phase conditions.[7,8] In this thesis, quantum chemical calculations were utilized for the exploration of the reaction mechanisms of gas-phase ion-molecule reactions. For the parts regarding the identification of different functionalities in protonated compounds by using tandem mass spectrometry based on diagnostic gas-phase ion-molecule reactions (Chapters 4 and 5), calculations were utilized to rationalize the formation of the diagnostic product ions and fragment ions to prove the reliability and the predictability of the analytical methods based on these reactions. For the parts regarding the examination of the reactivity of the reaction intermediates (phenylcarbyne anions and phenylcarbene anions, Chapter 6), calculations were utilized to rationalize the observed reactions and to provide mechanistical understanding of their reactivities.

As discussed in Section 2.5.2, Brauman's double-well potential energy surface model is utilized to mechanistically explain the processes of gas-phase ion-molecule reactions.[9,10] Quantum chemical calculations can provide the approximate energy values for reaction intermediates and transition states in the Brauman's double-well potential energy surface model.[11,12] Enthalpy changes were usually calculated to describe the energy values for the reaction intermediates and transition states, because the enthalpy changes directly reflect the difference of the bond energies between the reactants, products and transition states.[13]

In this dissertation, all the calculations were conducted based on the density functional theory (DFT). Its derivation and formalism within the Born-Oppenheimer approximation will be discussed below.

3.2 Born-Oppenheimer approximation

The computational methods that are utilized in this dissertation aim to calculate the energy of a system, *E*, by solving the time-independent Schrödinger Equation:[14-16]

$$\hat{H}|\Psi\rangle = E|\Psi\rangle \qquad \text{Equation 3.1}$$

where $|\Psi\rangle$ refers to a multi-electron wave function that can be described by a linear combination of Slater determinants, in which each Slater determinant can be expressed as follows:[17]

$$|\Psi\rangle = |\chi_1, \chi_2, \cdots, \chi_n\rangle = \frac{1}{\sqrt{N!}}\begin{vmatrix} \chi_1(x_1) & \chi_2(x_1) & \cdots & \chi_n(x_1) \\ \chi_1(x_2) & \chi_2(x_2) & \cdots & \chi_n(x_2) \\ \vdots & \vdots & \ddots & \vdots \\ \chi_1(x_n) & \chi_2(x_n) & \cdots & \chi_n(x_n) \end{vmatrix}$$

Equation 3.2

$\hat{H}$ is called the Hamiltonian operator. The wavefunctions are the eigenvalues of the Hamiltonian. Thus, solving the eigenvalue problem gives us access to the energy of a system by solving the Schrödinger Equation.[14,15] The Hamiltonian is composed of the kinetic and potential energies, which can be expressed as:[14]

$$\hat{H} = -\sum_{i=1}^{electrons} \frac{1}{2}\nabla_i^2 - \sum_{k=1}^{nuclei} \frac{1}{2M_k}\nabla_k^2 - \sum_{i=1}^{electrons}\sum_{k=1}^{nuclei} \frac{Z_k}{r_{ik}} + \sum_{\substack{i<j \\ i=1}}^{electrons} \frac{1}{r_{ij}} + \sum_{\substack{k<l \\ k=1}}^{nuclei} \frac{Z_k Z_l}{r_{kl}}$$

Equation 3.3

In the equation above, *i* and *j* describe the counting of the electrons and *k* and *l* describe the counting of the nuclei. ∇^2 is the Laplacian operator, *Z* is the number of protons in the nucleus, and *r* is the distance between different particles (nuclei or electrons). Among the terms in Equation 3.3, the first and second terms represent the kinetic energy of the electrons and nuclei, respectively.[14] The third, fourth and fifth terms represent the electron-nucleus interaction, the electron-electron interaction and the nucleus-nucleus interaction, respectively.[14]

Due to the great computational complexity of the Hamiltonian operator shown in Equation 3.3, the Born-Oppenheimer approximation is often applied in order to simplify the Hamiltonian operator.[14,18] The Born-Oppenheimer approximation assumes the nuclei to be stationary, because the nuclei are much heavier than the electrons, and hence move much slower than the electrons.[18] According to the Born-Oppenheimer approximation, the Schrödinger equation can be simplified as:[18]

$$\hat{H}|\Psi\rangle = \left(-\sum_{i=1}^{n} \frac{1}{2}\nabla_i^2 - \sum_{i=1}^{n}\sum_{k=1}^{N} \frac{Z_k}{r_{ik}} + \sum_{\substack{i<j \\ i=1}}^{n} \frac{1}{r_{ij}} + C \right) |\Psi\rangle \qquad \text{Equation 3.4}$$

which only includes the operators for the kinetic energy of the electrons (the first term), the external potential energy due to electron-nucleus interaction (the second term) and the potential energy due to electron-electron repulsion (the third term). Other terms in Equation 3.3 can be considered as constants and are expressed as *C* in Equation 3.4.

3.3 Density functional theory

Although Schrödinger equation provides a way of calculating the total energy of a chemical system, solving the Schrödinger equation can become unmanageable for systems containing more than a few electrons given the expansion of the wavefunction in Slater determinants (Equation 3.2).[14] The most complicated part for a multi-electron Schrödinger equation is the electron-electron repulsion term in Hamiltonian (the third term in Equation 3.4), because r_{ij} relies on two variables – position of electron *i* and *j* – and they cannot be separated to solve the Schrödinger equation.[14]

Density functional theory (DFT), on the other hand, provides an alternative to calculate the energy without solving the Schrödinger equation.[19] DFT calculates the energy of a system by using the electron density, which can be defined as follows:[19]

$$\rho(r) = N \iint \cdots \int |\Psi(r, r_2, \cdots, r_n)|^2 \, dr_2 \cdots dr_N \qquad \text{Equation 3.5}$$

where *N* is the number of electrons, and r_2, … r_N are the spatial coordinates of the electrons. The electron density indicates the probability of finding any electrons in volume *dr*.

The total energy is a function of electron density because electron density is uniquely determined by the potential of the nuclei of the system. The previous statement has been proved by Hohenberg and Kohn.[20] Since the electron density is also a function of *r*, the total energy is called ‘density functional’.

Kohn and Hohenberg also deduced that the electron kinetic energy, the external potential energy and the electron-electron repulsion potential energy are also functionals of electron density.[20] The external potential energy can be expressed as:[19]

$$V_{ext}[\rho(r)] = \sum_{k}^{N} \int \frac{Z_k}{|r - r_k|} \rho(r) dr \qquad \text{Equation 3.6}$$

where r_k is the nucleus position and Z_k is the nucleus charge.

Therefore, the total energy can be expressed as:[19]

$$E[\rho(r)] = T[\rho(r)] + V_{ee}[\rho(r)] + \sum_{k}^{N} \int \frac{Z_k}{|r - r_k|} \rho(r) dr \qquad \text{Equation 3.7}$$

where $T[\rho(r)]$ and $V_{ee}[\rho(r)]$ are density functionals of kinetic energy and electron-electron repulsion potential energy, respectively.

Unfortunately, the exact expressions of $T[\rho(r)]$ and $V_{ee}[\rho(r)]$ in terms of electron density remain unknown. Hence, approximations of the two energies is required. For $V_{ee}[\rho(r)]$, a reasonable approximation is to simplify the interaction between individual electrons as the interaction between the electron density with itself. Consequently, $V_{ee}[\rho(r)]$ can be approximated as:[19]

$$V_{ee}[\rho(r)] \approx E_H[\rho(r)] = \frac{1}{2} \iint \frac{\rho(r_1)\rho(r_2)}{|r_1 - r_2|} dr_1 dr_2 \qquad \text{Equation 3.8}$$

Determination of the $T[\rho(r)]$ is more complicated, as there is no known formula that expresses the relationship between the kinetic energy of the electrons and the electron density of a system.[19] In order to achieve the density functional of the kinetic energy, many models have been proposed, such as Thomas-Fermi model,[21,22] Thomas-Fermi-Dirac model[23] and Thomas-Fermi-Dirac-Weizsacker model.[24] However, these models failed to depict the density functional of the kinetic energy accurately, and hence cannot meet the requirements for total energy calculations.[19]

In order to address the above problem, Kohn and Sham introduced a system of non-interactive electrons, that have the same electronic density as the full interactive system.[25] In this fictitious system, one can calculate the kinetic energy in terms of the orbitals of these electrons as below.[25]

$$T[\rho(r)] \approx T_{KS}[\rho(r)] = -\frac{1}{2} \sum_{i=1}^{n} \int \langle \varphi_i(r) | \nabla_i^2 | \varphi_i(r) \rangle \, dr \qquad \text{Equation 3.9}$$

where $T_{KS}[\rho(r)]$ is called Kohn-Sham kinetic energy (non-interacting kinetic energy), and $\varphi_i(r)$ refers to the single-electron orbitals. Although $\rho(r)$ does not appear in Equation 3.9, $T_s[\rho(r)]$ is still a density functional as the electron density $\rho(r)$ is related with $\varphi_i(r)$, which is shown below.[25]

$$\rho(r) = \sum_{i=1}^{n} \langle \varphi_i(r) | \varphi_i(r) \rangle \qquad \text{Equation 3.10}$$

By adding the external potential energy (Equation 3.6), the Coulomb repulsion potential energy (Equation 3.8) and Kohn-Sham kinetic energy (Equation 3.9), the approximate total energy can be expressed as:[25]

$$E_{approx}[\rho(r)] = T_{KS}[\rho(r)] + E_H[\rho(r)] + V_{ext}[\rho(r)] \qquad \text{Equation 3.11}$$

Nevertheless, replacing the electron kinetic energy and electron-electron repulsion potential energy with $T_{KS}[\rho(r)]$ and $E_H[\rho(r)]$ inevitably introduces error from the exact $T[\rho(r)]$ and $V_{ee}[\rho(r)]$. Electron exchange and correlation are the two contributors to the error.[25] The exchange effect exists because the Pauli exclusion principle prevents electrons of the same spin to occupy the same orbital.[19] On the other hand, correlation effect is derived from the electrostatic potential itself, as two electrons are more likely to reside at the position with lower potential, hence get separated from each other.[19] Therefore, the exchange-correlation term, $E_{XC}[\rho(r)]$, can be expressed as:[25]

$$E_{XC}[\rho(r)] = T[\rho(r)] - T_{KS}[\rho(r)] + V_{ee}[\rho(r)] - E_H[\rho(r)] \qquad \text{Equation 3.12}$$

and the total energy can be calculated exactly as:[25]

$$E[\rho(r)] = T_{KS}[\rho(r)] + E_H[\rho(r)] + V_{ext}[\rho(r)] + E_{XC}[\rho(r)] \qquad \text{Equation 3.13}$$

Nevertheless, the exchange-correlation term, $E_{XC}[\rho(r)]$, is not known as an explicit functional of the density.[25] Therefore, approximations for this term are required to obtain the correlation and exchange energy. A series of density functional approximations, such as local density approximation[26] (LDA), local spin-density approximation[26] (LSDA) and generalized gradient approximation[27] (GGA), has been developed to estimate the exchange-correlation energy. Further, including a fraction of exchange from HF theory can help achieve more accurate results.[28-31] The exchange-correlation terms in above approximations hence are hybridized with the HF energy to achieve more accurate results.[28,29] In this dissertation, B3LYP[30] and M06-2X[31] are two hybridization methods that were utilized for calculations of proton affinities and reaction mechanisms, respectively. B3LYP is an accurate and economic method that has been utilized for calculations of proton affinities in many previous studies.[32-35] M06-2X, on the other hand, is efficient for the simulation of main-group thermochemistry and kinetics.[31] Hence, M06-2X was utilized to calculate the potential energy surfaces for the ion-molecule reactions and fragmentation

reactions in this dissertation, as all the reactants and products of interest were composed with main-group elements.[11,12]

3.4 References

1. Tantillo, D.J., Walking in the woods with quantum chemistry–applications of quantum chemical calculations in natural products research. *Nat. Prod. Rep.* **2013**, *30*, 1079-1086.

2. Odoh, S.O., Cramer, C.J., Truhlar, D.G. and Gagliardi, L., Quantum-chemical characterization of the properties and reactivities of metal–organic frameworks. *Chem. Rev.* **2015**, *115*, 6051-6111.

3. Cavalli, A., Carloni, P. and Recanatini, M., Target-related applications of first principles quantum chemical methods in drug design. *Chem. Rev.* **2006**, *106*, 3497-3519.

4. Lodewyk, M.W., Siebert, M.R. and Tantillo, D.J., Computational prediction of ^{1}H and ^{13}C chemical shifts: a useful tool for natural product, mechanistic, and synthetic organic chemistry. *Chem. Rev.* **2012**, *112*, 1839-1862.

5. Rusakov, Y.Y. and Krivdin, L.B., Modern quantum chemical methods for calculating spin–spin coupling constants: theoretical basis and structural applications in chemistry. *Russ. Chem. Rev.* **2013**, *82*, 99-130.

6. Ruiperez, F., Application of quantum chemical methods in polymer chemistry. *Int. Rev. Phys. Chem.* **2019**, *38*, 343-403.

7. Leonardi, A., Ricker, H.M., Gale, A.G., Ball, B.T., Odbadrakh, T.T., Shields, G.C. and Navea, J.G., Particle formation and surface processes on atmospheric aerosols: A review of applied quantum chemical calculations. *Int. J. Quantum Chem.* **2020**, *120*, 26350-26367.

8. Khrapkovskii, G.M., Shamov, A.G., Nikolaeva, E.V.E. and Chachkov, D.V., Mechanisms of gas phase decomposition of C-nitro compounds from quantum chemical data. *Russ. Chem. Rev.* **2009**, *78*, 903-943.

9. Olmstead, W.N. and Brauman, J.I., Gas-phase nucleophilic displacement reactions. *J. Am. Chem. Soc.* **1977**, *99*, 4219-4228.

10. Pellerite, M.J. and Brauman, J.I., Intrinsic barriers in nucleophilic displacements. *J. Am. Chem. Soc.* **1980**, *102*, 5993-5999.

11. Feng, E., Ma, X. and Kenttämaa, H.I., Characterization of protonated substituted ureas by using diagnostic gas-phase ion-molecule reactions followed by collision-activated dissociation in tandem mass spectrometry experiments. *Anal. Chem.* **2021**, *93*, 7851-7859.

12. Zhang, J., Feng, E., Li, W., Sheng, H., Milton, J.R., Easterling, L.F., Nash, J.J. and Kenttämaa, H.I., Studies of the fragmentation mechanisms of deprotonated lignin model compounds in tandem mass spectrometry. *Anal. Chem.* **2020**, *92*, 11895-11903.

13. Klopper, W. and Noga, J., Accurate quantum-chemical prediction of enthalpies of formation of small molecules in the gas phase. *ChemPhysChem* **2003**, *4*, 32-48.

14. Szabo, A.; Ostlund, N. S. Modern quantum chemistry: introduction to advanced electronic structure theory; Dover Publications: Mineola, N.Y, 1996.

15. Schrödinger, E., Quantisierung als eigenwertproblem. *Ann. Phys.* **1926**, *385*, 437-490.

16. Schrödinger, E., An undulatory theory of the mechanics of atoms and molecules. *Phys. Rev.* **1926**, *28*, 1049-1070.

17. Slater, J.C., The theory of complex spectra. *Phys. Rev.* **1929**, *34*, 1293-1322.

18. Born, M.; Oppenheimer, R. Zur quantentheorie der molekeln. *Ann. Phys.* **1927**, *389*, 457–484.

19. Jones, R.O. and Gunnarsson, O., The density functional formalism, its applications and prospects. *Rev. Mod. Phys.* **1989**, *61*, 689-746.

20. Hohenberg, P. and Kohn, W., Inhomogeneous electron gas. *Phys. Rev.* **1964**, *136*, B864-B871.

21. Thomas, L. H. The calculation of atomic fields. *Math. Proc. Camb. Phil. Soc.* **1927**, *23*, 542–548.

22. Fermi, E. Un metodo statistico per la determinazione di alcune prioprietà dell'atomo. *Rend. Accad. Naz. Lincei* **1927**, *6*, 602–607.

23. Dirac, P.A., Note on exchange phenomena in the Thomas atom. *Math. Proc. Camb. Phil. Soc.* **1930**, *26*, 376-385.

24. von Weizsäcker, C.F., Zur Theorie der Kernmassen. *Z. phys*. **1935**, *96*, 431-458.

25. Kohn, W.; Sham, L. J. Self-consistent equations including exchange and correlation effects. *Phys. Rev.* **1965**, *140*, A1133–A1138.

26. Parr, R.G.; Yang, W. Density-functional theory of atoms and molecules; Oxford: Oxford University Press, N.Y. 1989

27. Hammer, B.H.L.B., Hansen, L.B. and Nørskov, J.K., Improved adsorption energetics within density-functional theory using revised Perdew-Burke-Ernzerhof functionals. *Phys. Rev.* **1999**, *59*, 7413-7421.

28. Ivády, V., Armiento, R., Szász, K., Janzén, E., Gali, A. and Abrikosov, I.A., Theoretical unification of hybrid-DFT and DFT+ U methods for the treatment of localized orbitals. *Phys. Rev. B* **2014**, *90*, 1-13.

29. Franchini, C., Podloucky, R., Paier, J., Marsman, M. and Kresse, G., Ground-state properties of multivalent manganese oxides: Density functional and hybrid density functional calculations. *Phys. Rev. B* **2007**, *75*, 1-11.

30. Stephens, P. J.; Devlin, F. J.; Chabalowski, C. F.; Frisch, M. J. Ab initio calculation of vibrational absorption and circular dichroism spectra using density functional force fields. *J. Phys. Chem.* **1994**, *98*, 11623-11627.

31. Zhao, Y.; Truhlar, D. G. The M06 suite of density functionals for main group thermochemistry, thermochemical kinetics, noncovalent interactions, excited states, and transition elements: Two new functionals and systematic testing of four M06-class functionals and 12 other functionals. *Theor. Chem. Acc.* **2008**, *120*, 215-241.

32. Duan, P.; Fu, M.; Gillespie, T. A.; Winger, B. E.; Kenttämaa, H. I., Identification of aliphatic and aromatic tertiary N-oxide functionalities in protonated analytes via ion/molecule and dissociation reactions in an FT-ICR mass spectrometer. *J. Org. Chem.* **2009,** *74*, 1114–1123.

33. Feng, E.; Ma, X.; Kenttämaa, H. I., Characterization of protonated substituted ureas by using diagnostic gas-phase ion-molecule reactions followed by collision-activated dissociation in tandem mass spectrometry experiments. *Anal. Chem.* **2021,** *93*, 7851–7859.

34. Sheng, H.; Williams, P. E.; Tang, W.; Riedeman, J. S.; Zhang, M.; Kenttämaa, H. I., Identification of the sulfone functionality in protonated analytes via ion/molecule reactions in a linear quadrupole ion trap mass spectrometer. *J. Org. Chem.* **2014,** *79*, 2883–2889.

35. Watkins, M. A.; Price, J. M.; Winger, B. E.; Kenttämaa, H. I., Ion−molecule reactions for mass spectrometric identification of functional groups in protonated oxygen-containing monofunctional compounds. *Anal. Chem.* **2004,** *76*, 964–976.

CHAPTER 4. CHARACTERIZATION OF PROTONATED SUBSTITUTED UREAS BY USING DIAGNOSTIC GAS-PHASE ION-MOLECULE REACTIONS FOLLOWED BY COLLISION-ACTIVATED DISSOCIATION IN TANDEM MASS SPECTROMETRY EXPERIMENTS

4.1 Introduction

Phenylurea[1] and sulfonyl urea herbicides[2] have been utilized as pre- and post-emergence treatment in weed control. Their residues in soil may persist for over six months[3] and contaminate surface water and groundwater as they are toxic to mammals, including human beings.[4,5] Therefore, unambiguous detection of substituted ureas in soil and water is essential for the evaluation of soil and water quality.

Many analytical methods, such as high-performance liquid chromatography (HPLC),[6,7] have been utilized to analyze complex mixtures of organic compounds. An especially powerful method for the identification of previously unknown compounds in complex mixtures is HPLC coupled with tandem mass spectrometry (MS^2) based on collision-activated dissociation (CAD).[8,9] However, this experimental approach requires access to authentic model compounds. Even then, CAD often generates similar fragmentation patterns for isomeric ions.[10,11] In order to address this issue, MS^2 methods based on diagnostic and predictable gas-phase ion-molecule reactions have been developed[12,13] for the identification of specific functional groups, such as sulfone,[14] amido,[15] *N*-oxide and sulfoxide,[16] in previously unknown protonated compounds in complex mixtures.

Many approaches based on diagnostic gas-phase ion-molecule reactions have used organoboron reagents.[17-19] These reactions are usually initiated by proton transfer from the protonated analyte to the organoboron reagent (Scheme 4.1). After this, a nucleophilic site in the neutral analyte adds to the boron atom of the protonated reagent. Depending on its exact structure, the addition product fragments to generate product ions that are diagnostic for specific functionalities. Nevertheless, protonated compounds with different functionalities sometimes yield the same product ion. In these cases, subjecting the product ion to CAD may yield diagnostic fragment ions.[20] For example, reactions of protonated analytes with tris(dimethylamino)borane (TDMAB) reagent followed by CAD of the product ions $[M + H + TDMAB - HN(CH_3)_2]^+$ can be used to differentiate amido functionalities from *N*-oxo and sulfoxo functionalities and from

pyridines based on the observation of the diagnostic fragment ions $((CH_3)_2N)_2B^+$ and [M + H + TDMAB – 2 $HN(CH_3)_2$]$^+$ (M = analyte), of which the first one is only formed for amides.[16,21]

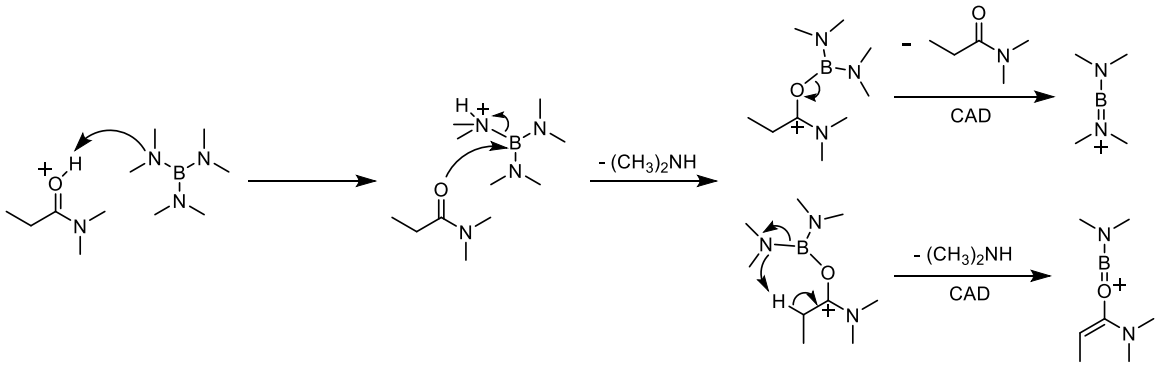

Scheme 4.1 Previously proposed mechanisms[21] for the reactions between a protonated amide and TDMAB to yield an adduct that has eliminated $(CH_3)_2NH$. CAD on this product ion leads to the elimination of *N*,*N*-dimethylpropionamide (top) and $(CH_3)_2NH$ (bottom).

This study focuses on the development of diagnostic gas-phase ion-molecule reactions followed by CAD to differentiate differently substituted ureas from each other and from other similar compounds. The known proton affinities (PAs) of ureas[22] are large, ranging from 209 up to 222 kcal mol^{-1} (urea: PA = 208.8 kcal mol^{-1}, *N,N'*-dimethylurea: 215.9 kcal mol^{-1}; tetramethylurea: 222.4 kcal mol^{-1}). Therefore, TDMAB was chosen as the reagent for this study as the proton affinity[21] of TDMAB (230 kcal mol^{-1}) is close to the proton affinities of substituted ureas. Another advantage associated with using TDMAB is that its reactions with many different protonated compounds have been studied previously in Fourier-transform ion cyclotron resonance and linear quadrupole ion traps.[16,21,23] Most compounds have a far lower proton affinity than TDMAB. Therefore, these protonated compounds just transfer a proton to TDMAB.[16,21,23,24] However, many protonated basic compounds, including protonated amides, *N*-oxides, sulfoxides and pyridines, transfer a proton to TDMAB followed by addition to the boron atom and elimination of dimethylamine (Scheme 4.1). [16,21,23] When this product ion is subjected to CAD, the following reactions have been observed: elimination of dimethylamine as well as formation of $((CH_3)_2N)_2B^+$ for amides (Scheme 4.1),[16,21] elimination of dimethylamine and $HOB(N(CH_3)_2)_2$ for N-oxides,[16,21,23] elimination of $(CH_3)_2NBO$, dimethylamine and $HOB(N(CH_3)_2)_2$ for sulfoxides,[16] and elimination of $[B(N(CH_3)_2)_2]^+$ for pyridines.[21]

4.2 Experimental section

4.2.1 Chemicals

TDMAB (99% purity) was purchased from Sigma-Aldrich. Fifteen substituted ureas, seven amides and three carbamates as shown in Scheme 4.2 were used as model compounds. The commercially available model compounds (and their sources and purities) are as follows: urea (Aablock, 95%), 1,3-dimethylurea (Aablock, 95%), 1,3-diphenylurea (Aablock, 98%), 1-methyl-3-phenylurea (Aablock, 98%), tetramethylurea (AKScientific, 98%), 1,3-dimethyltetrahydropyrimidin-2(1H)-one (Aablock, 95%), benzamide (Sigma-Aldrich, 99%), acetanilide (Sigma-Aldrich, 97%), benzanilide (Alfa Aesar, 98%), *N*-methylacetamide (Sigma-Aldrich, 99%), *N*-methylacectanilide (Aablocks, 98%), *N*,*N*-diethylacetamide (Aablocks, 95%), *N*,*N*-diphenylacetamide (Aablock, 98%), phenyl carbamate (Sigma-Aldrich, 97%), benzyl carbamate (Sigma-Aldrich, 99%), *tert*-butyl-*N*-(2-furyl)carbamate (Combi-blocks Inc., 97%), linuron (Sigma-Aldrich, analytical standard), monolinuron (Sigma-Aldrich, analytical standard), chlortoluron (Sigma-Aldrich, analytical standard), tebuthiuron (Sigma-Aldrich, analytical standard), triclocarban (Sigma-Aldrich, analytical standard), tolbutamide (Sigma-Aldrich, analytical standard), zileuton (Sigma-Aldrich, analytical standard). Water (LC/MS grade, ≥99.9%) and methanol (LC/MS grade, ≥99.9%) were purchased from Fisher Scientific. All purchased chemicals were used as received.

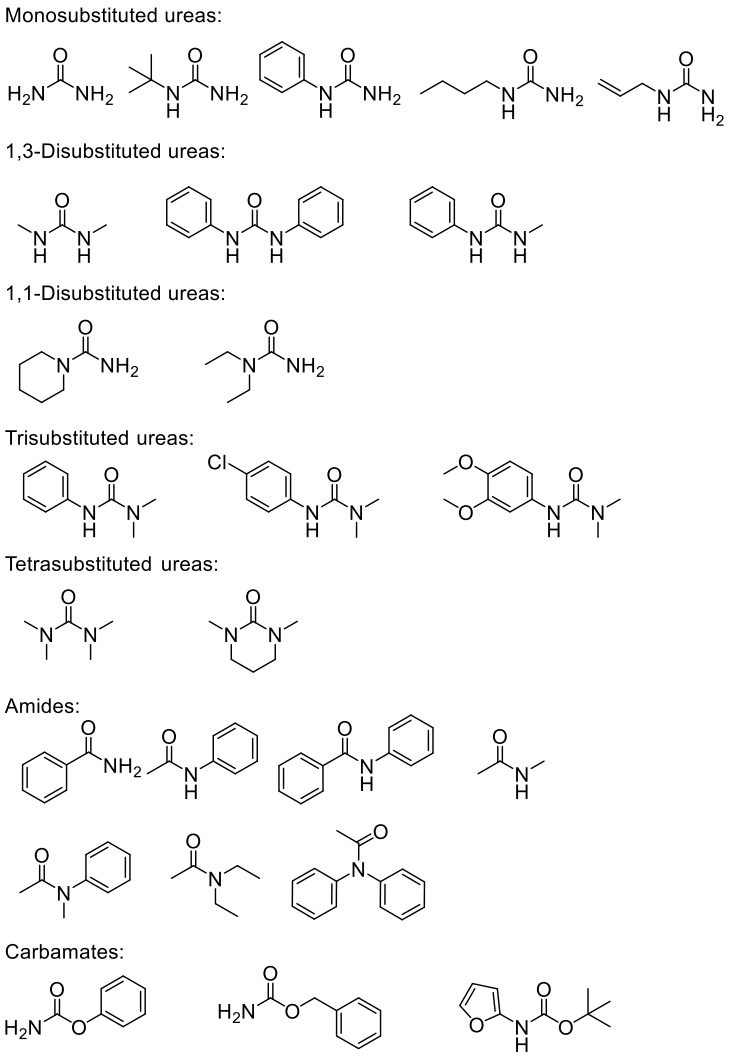

Scheme 4.2. Structures of urea, amide and carbamate model compounds used to demonstrate the applicability of the new method

The known compounds *tert*-butylurea, *n*-butylurea, allylurea, 1,1-diethylurea and 1-piperidinecarboxamide were synthesized using previously published procedures.[25] 1,1-Dimethyl-3-phenylurea, 1,1-dimethyl-3-(4-chlorophenyl)urea, and 1,1-dimethyl-3-(3,4-dimethoxylphenyl)urea were also synthesized using previously published procedures.[26] The reagents utilized for synthesis (and their sources and purities) are as follows: *tert*-butylamine (Sigma-Aldrich, 98%), *n*-butylamine (Sigma-Aldrich, 99.5%), allylamine (Sigma-Aldrich, 99%), piperidine (Alfa Aesar, 99%), diethylamine (Sigma-Aldrich, 99.5%), potassium cyanate (Alfa Aesar, 97%), hydrochloric acid (Fisher Scientific, 36.5%-38%), aniline (Sigma-Aldrich, 99.5%), 4-chloroaniline (Sigma-Aldrich, 98%), 3,4-dimethoxyaniline (Sigma-Aldrich, 98%),

dimethylcarbamyl chloride (Sigma-Aldrich, 98%), pyridine (Alfa Aesar, 99%), 4-dimethylaminopyridine (Sigma-Aldrich, 99%), and methylene chloride (Fisher Scientific, 99.5%).

Stock solutions of all analytes were prepared at a concentration of 10 mM in methanol.

4.2.2 Instrumentation

All experiments were conducted using a LQIT mass spectrometer equipped with an APCI source. The analyte solutions were injected into the APCI source at a flow rate of 15 μL min^{-1} by using a 500 μL Hamilton syringe. All analytes were protonated in the APCI source. Typical APCI source conditions were as follows: 4.2 μA discharge current, 20 (arbitrary units) sheath gas (N_2) flow rate, 10 (arbitrary units) auxiliary gas (N_2) flow rate, 300 ˚C vaporizer temperature, 275 ˚C capillary temperature, 10 V capillary voltage, and 70 V tube lens voltage.

After protonation of the analytes, the ions were transferred into the ion trap, isolated, and allowed to react with TDMAB (MS^2 experiments). TDMAB was introduced into the traditional external reagent mixing manifold (discussed in Section 2.5.1) via a syringe pump at a flow rate of 10 μL h^{-1}. TDMAB was then diluted with helium before entering the ion trap through a variable leak valve. The pressure in the ion trap was adjusted using the leak valve until the ion gauge reading was 0.7-0.8 $\times 10^{-5}$ torr. Reaction time was 300 ms for all experiments except for those where no products were detected after this time. In those cases, a reaction time of 1000 ms was also used. The reproducibility of the relative abundances of the product ions was ± 30%.

Product ions $[M + H + TDMAB - HN(CH_3)_2]^+$ formed upon reactions of the analyte ions with TDMAB were subjected to two steps of collision-activated dissociation (CAD) (MS^3 and MS^4 experiments). In the CAD experiments, the advanced scan features of the LTQ Tune Plus interface were used to isolate the ions by using a *m/z* window of 2 units. At a *q* value of 0.25, the ions were subjected to CAD (collision energy 30 arbitrary units) for 30 ms by using helium as the collision gas. The reproducibility of the relative abundances of the fragment ions was ± 20%.

The detection mass range was from m/z 50 up to 500. All mass spectra acquired were an average of at least 20 individual mass spectra. Xcalibur 2.0 software was used for processing of all the data.

4.2.3 HPLC/MS^4 conditions

HPLC/MS^4 experiments were performed using a Thermo Surveyor HPLC coupled to a LQIT. The samples were injected via an autosampler with full-loop injection (25 μL). The mobile phases used were water (A) and acetonitrile (B), both containing 0.1% formic acid. The column used was an Agilent ZORBAX SB-C18 (5 μm, 4.6 × 250 mm). The flow rate was 0.5mL min^{-1} and the percentage of B in the mobile phase was increased linearly from 60% to 75% within 20 min. The analytes eluting from the HPLC were introduced into the APCI source where they were protonated, transferred into the ion trap, isolated by ejecting all other ions from the ion trap, and allowed to react with TDMAB for 30 ms. The product ions $[M + H + TDMAB – HN(CH_3)_2]^+$ were subjected to two steps of CAD (MS^3 and MS^4 experiments).

4.2.4 Computational methods

All calculations were performed using the Gaussian 16 program.[27] The optimized molecular structures and their energies needed for the potential energy surfaces were calculated at the M06-2X/6-311++G(d,p) level of theory. All geometries were verified to be local minima by computation of analytic vibrational frequencies. These (unscaled) frequencies were used to compute zero-point vibrational energies (ZPVE) and 298 K thermal contributions ($H_{298} - E_0$). All transition state structures were determined to contain exactly one negative frequency. Intrinsic reaction coordinate (IRC) calculations were performed for all transition states to ensure that the optimized structure connected the correct reactants and products.

4.3 Results and discussion

The results obtained for the gas-phase reactions of protonated substituted ureas, amides and carbamates with TDMAB will be discussed first, followed by the results obtained using quantum chemical calculations performed to explore the ion-molecule reaction mechanisms. After this, CAD of selected product ions generated in the ion-molecule reactions is discussed, followed by examination of their fragmentation mechanisms by quantum chemical calculations. A description of the results obtained for seven protonated drugs and herbicides containing the urea moiety follows. Finally, HPLC/MS^4 experiments are discussed.

4.3.1 Reactions of protonated ureas, amides and carbamates with TDMAB

All model compounds were protonated via APCI, transferred into the linear quadrupole ion trap, isolated, and allowed to react with TDMAB for 300 ms. All ions (except protonated *tert*-butyl-N-(2-furyl)carbamate) reacted with TDMAB to form an addition product that had lost a dimethylamine molecule, $[M + H + TDMAB – HN(CH_3)_2]^+$ (M = analyte), although for some ions, this was a minor product (Figure 4.1a). This type of product ions has been previously reported for reactions of TDMAB with protonated amides, pyridines, *N*-oxides, sulfoxides, and some amines in Fourier-transform ion cyclotron resonance and linear quadrupole ion trap mass spectrometers.[16,21,23] The results for five differently substituted ureas, one amide and two carbamates are shown in Table 4.1 as examples.

Table 4.1. Product ions, with their relative abundances,[a] detected after 300 ms reactions of eight selected protonated analytes with TDMAB. The product ions $[M + H + TDMAB – HN(CH_3)_2]^+$, which were subjected to CAD experiments, are shown in red.

Analyte Category	Analyte (*m/z* of $[M + H]^+$)	Ion-molecule Reaction Product Ions (*m/z*)	Relative Abundance
Urea	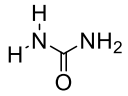 (61)	$[M + H + TDMAB – HN(CH_3)_2]^+$ (159) $[TDMAB + H]^+$ (144)	4% 100%
Monosubstituted urea	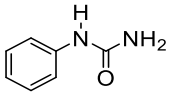 (137)	$[M + H + TDMAB – HN(CH_3)_2]^+$ (235) $[M + H + HN(CH_3)_2]^+$ (182) $[TDMAB + H]^+$ (144)	94% 13% 100%
1,3-Disubstituted urea	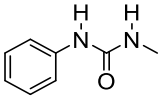 (151)	$[M + H + TDMAB – HN(CH_3)_2]^+$ (249) $[M + H + HN(CH_3)_2]^+$ (196) $[TDMAB + H]^+$ (144)	100% 78% 22%
1,1-Disubstituted urea	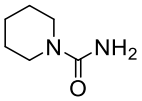 (129)	$[M + H + TDMAB – HN(CH_3)_2]^+$ (227) $[M + H + HN(CH_3)_2]^+$ (174) $[TDMAB + H]^+$ (144)	100% 62% 28%
Trisubstituted urea	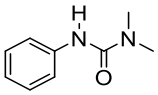 (165)	$[M + H + TDMAB – HN(CH_3)_2]^+$ (263) $[M + H + HN(CH_3)_2]^+$ (210) $[TDMAB + H]^+$ (144)	46% 100% 8%
Tetrasubstituted urea	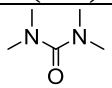 (117)	$[M + H + TDMAB – HN(CH_3)_2]^+$ (215) $[M + H + HN(CH_3)_2]^+$ (162) $[TDMAB + H]^+$ (144)	34% 55% 100%

Table 4.1 continued

Amide	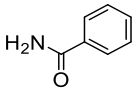 (122)	[M + H + TDMAB – $HN(CH_3)_2$]$^+$ (220) [TDMAB + H]$^+$ (144)	6% 100%
Carbamate	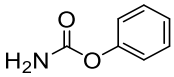 (138)	[M + H + TDMAB – $HN(CH_3)_2$]$^+$ (236) [TDMAB+H]$^+$ (144)	1% 100%
Carbamate	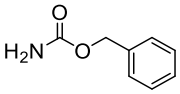 (152)	[M+H+TDMAB – $HN(CH_3)_2$]$^+$ (250) [TDMAB+H]$^+$ (144)	9% 100%

[a]*Reproducibility ± 30%.*

In order to explore the mechanism(s) leading to the generation of the product ions [M + H + TDMAB – $HN(CH_3)_2$]$^+$ upon reactions of protonated substituted ureas with TDMAB, a potential energy surface was calculated (M06-2X/6-311++G(d,p) level of theory) for the reactions of protonated 1-phenylurea with TDMAB (Figure 4.1b). Formation of a doubly hydrogen-bound dimer between the ion and TDMAB is highly exothermic. This dimer can undergo elimination of dimethylamine, which is calculated to be exothermic by as much as 24.5 kcal mol^{-1} (Figure 4.1b) A similar mechanism is suggested for the reactions of protonated amides.

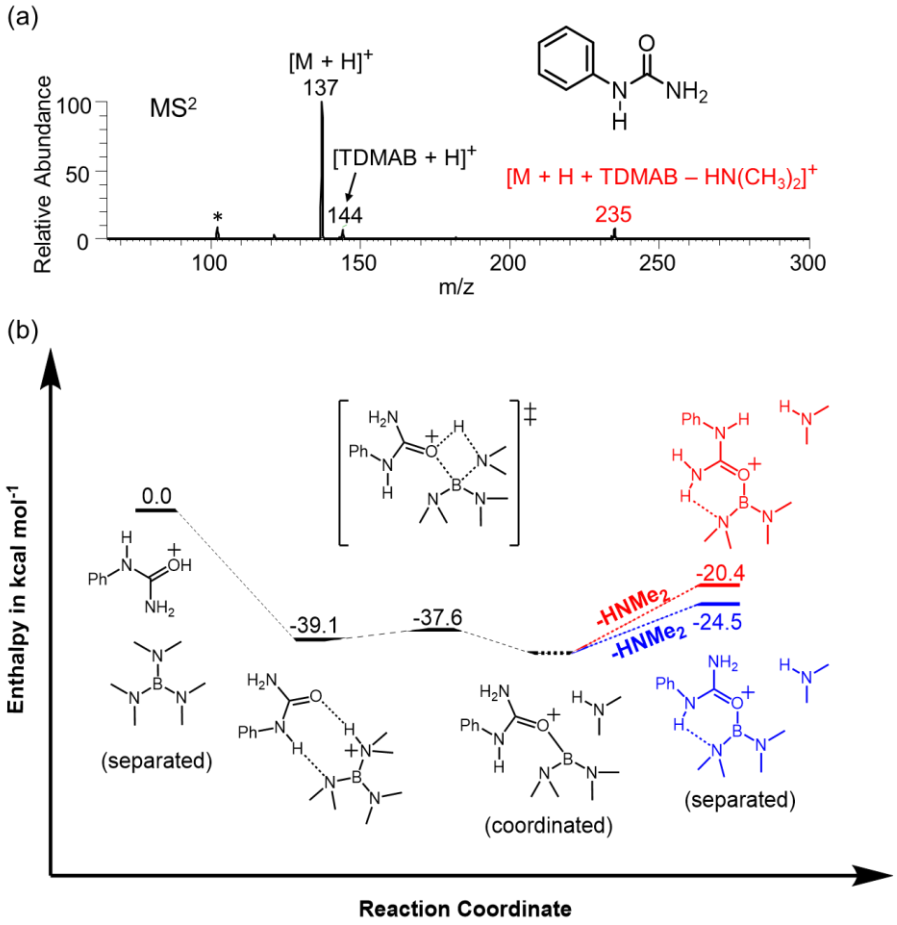

Figure 4.1. (a) MS^2 spectrum measured after 300 ms reactions of protonated 1-phenylurea (*m/z* 137; $[M + H]^+$) with TDMAB, showing the $[M + H + TDMAB – HN(CH_3)_2]^+$ product ion (*m/z* 235; M = analyte). (b) Potential energy surface calculated at the M06-2X/6-311++G(d,p) level of theory for the formation of the ion-molecule reaction product ions $[M + H + TDMAB – HN(CH_3)_2]^+$ upon reactions of protonated 1-phenylurea (M) with TDMAB. Formation of two possible products containing a hydrogen bond involving different nitrogen atoms are indicated in red and blue color.

4.3.2 CAD of the product ion $[M + H + TDMAB – HN(CH_3)_2]^+$

Because the same product ion $[M + H + TDMAB – HN(CH_3)_2]^+$ (M = analyte) was generated in the reactions of all types of protonated substituted ureas as well as protonated amides and carbamates (with one exception) with TDMAB, this product ion was subjected to CAD (in MS^3 experiments) to explore the possibility of differentiating the different analytes (Table 4.2). All the product ions (with the exception of those generated from tetrasubstituted ureas to be discussed later) fragmented via the loss of another $HN(CH_3)_2$ molecule to generate $[M + H + TDMAB – 2\ HN(CH_3)_2]^+$ fragment ions. Five differently substituted ureas, one amide and two carbamates were

selected as examples (Table 4.2) to illustrate this behavior (the third carbamate did not yield the M + H + TDMAB – $HN(CH_3)_2]^+$ ion-molecule reaction product; to be discussed later).

Table 4.2. Fragmentations/fragment ions observed upon CAD[a] of the ion-molecule reaction product ions $[M + H + TDMAB – HN(CH_3)_2]^+$ (MS^3 experiments) for selected protonated substituted ureas, amides and carbamates. The neutral fragments $HN(CH_3)_2$, whose corresponding ionic fragments $[M + H + TDMAB – 2\ HN(CH_3)_2]^+$ were subjected to subsequent CAD experiments, are shown in red.

Analyte Category	Analyte (*m/z* of $[M + H]^+$)	Neutral fragments (m/z value of the ionic fragment) or fragment ions (m/z) formed upon CAD of $[M + H + TDMAB – HN(CH_3)_2]^+$ (MS^3)[b]
Monosubstituted urea	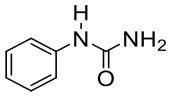 (137)	– $HN(CH_3)_2$ (190)
1,3-Disubstituted urea	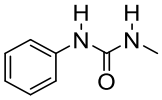 (151)	– $HN(CH_3)_2$ (204)
1,1-Disubstituted urea	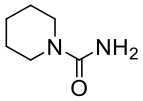 (129)	– $HN(CH_3)_2$ (182)
Trisubstituted urea	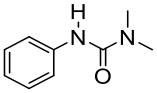 (165)	– $HN(CH_3)_2$ (218)
Tetrasubstituted urea	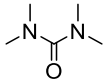 (117)	$[TDMAB + H]^+$ (144) $[M + H]^+$ (117) $[TDMAB + H – HN(CH_3)_2]^+$ (99)
Amide	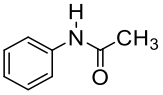 (136)	– $HN(CH_3)_2$ (189)
Carbamate	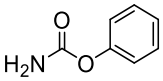 (138)	– HN=C=O (193)
Carbamate	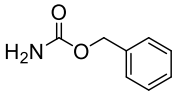 (152)	– $HN(CH_3)_2$ (205) $[TDMAB + H]^+$ (144) $PhCH_2^+ + HN(CH_3)_2$ (136)

[a] *All collision energies were 30 arbitrary units.* [b] *The water/dimethylamine/TDMAB adducts of* $[M + H + TDMAB – HN(CH_3)_2]^+$ *were sometimes detected in the* MS^3 *spectra but are not listed here as they are not fragment ions.*

To differentiate protonated mono-, di- and trisubstituted ureas from each other and from amides and most carbamates, another CAD experiment was employed on the fragment ions [M + H + TDMAB – 2 $HN(CH_3)_2$]$^+$ to examine their fragmentation (MS^4 experiments; Figures 4.2). These experiments revealed the elimination of isocyanic acid (H-N=C=O; MW 43 Da) or R-N=C=O (R = substituent at N) for those ureas with at least one primary or secondary amino group, respectively (Table 4.3). These elimination reactions were not observed for carbamates or amides. On the other hand, ions [M + H + TDMAB – 2 $HN(CH_3)_2$ – $(CH_3)_2N$-B=O]$^+$ generated via elimination of a boron moiety were observed as minor fragment ions for ureas with one tertiary amino group and for amides (usually the only fragment ion) but not for carbamates (Figure 4.2 b and c). Therefore, mono-, di- and trisubstituted ureas can be differentiated from amides and carbamates as well as from each other with this method.

Table 4.3. Fragmentations/fragment ions observed upon CAD[a] of the fragment ions [M + H + TDMAB – 2 $HN(CH_3)_2$]$^+$ (MS^4 experiments) for selected protonated substituted ureas, amides and carbamates, with their relative abundances.[b] The fragment ions [M + H + TDMAB – 2 $HN(CH_3)_2$ – R-N=C=O]$^+$ (R = H or substituent) are diagnostic for ureas (except for the tetrasubstituted ones) and are indicated in red color. The fragment ions [M + H + TDMAB – 2 $HN(CH_3)_2$ – $(CH_3)_2$N-B=O]$^+$, formed via elimination of a boron moiety, are diagnostic for ureas with one tertiary amino group and amides, and they are indicated in blue color.

Analyte Category	Analyte (*m/z* of [M + H]$^+$)	Neutral fragments (m/z value of the ionic fragment) or fragment ions (m/z) and their relative abundances formed upon CAD of [M + H + TDMAB – 2 $HN(CH_3)_2$]$^+$ (MS^4)[c]
Monosubstituted urea	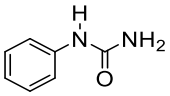 (137)	– H-N=C=O (147) 5% – H-N=C=O + H_2O (165) 100% – Ph-N=C=O (71) 22% – Ph-N=C=O + H_2O (89) 26% – Ph-N=C=O + TDMAB – $HN(CH_3)_2$ (169) 13% [TDMAB + H]$^+$ (144) 54% [TDMAB + H – $HN(CH_3)_2$]$^+$ (99) 22% [TDMAB + H – $HN(CH_3)_2$ + H_2O]$^+$ (117) 5%
1,3-Disubstituted urea	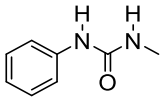 (151)	– CH_3-N=C=O (147) 1% – CH_3-N=C=O + H_2O (165) 27% – CH_3-N=C=O + 2 H_2O (183) 26% – CH_3-N=C=O + $HN(CH_3)_2$ (192) 7% – Ph-N=C=O (85) 50% – Ph-N=C=O + $HN(CH_3)_2$ (130) 71% – Ph-N=C=O + H_2O (103) 100% [TDMAB + H]$^+$ (144) 23% [TDMAB + H – $HN(CH_3)_2$]$^+$ (99) 10% [TDMAB + H – $HN(CH_3)_2$ + H_2O]$^+$ (117) 15%
1,1-Disubstituted urea	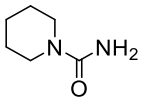 (129)	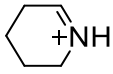 (84) 9% – H-N=C=O (139) 100% – H-N=C=O + H_2O (157) 37% – H-N=C=O + $HN(CH_3)_2$ (192) 58% – $(CH_3)_2$N-B=O (111) 3%
Trisubstituted urea	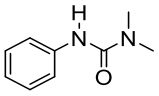 (165)	– $(CH_3)_2$N-B=O (147) 5% – Ph-N=C=O (99) 100% – Ph-N=C=O + H_2O (117) 64% [TDMAB + H]$^+$ (144) 56%
Amide	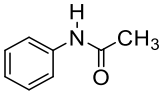 (136)	– $(CH_3)_2$N-B=O (118) 100%

(Table 4.3 Continued)

Carbamate	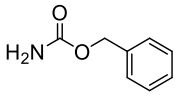 (152)	– •CH_2Ph (114) $PhCH_2^+$ + $HN(CH_3)_2$ (136) $PhCH_2^+$ (91)	22% 28% 100%

[a] All collision energies were 30 arbitrary units. [b] Reproducibility ± 20%. [c] The water/dimethylamine/TDMAB adducts of $[M + H + TDMAB – 2\ HN(CH_3)_2]^+$ were sometimes observed in the MS^4 spectra but are not listed here as they are not fragment ions.

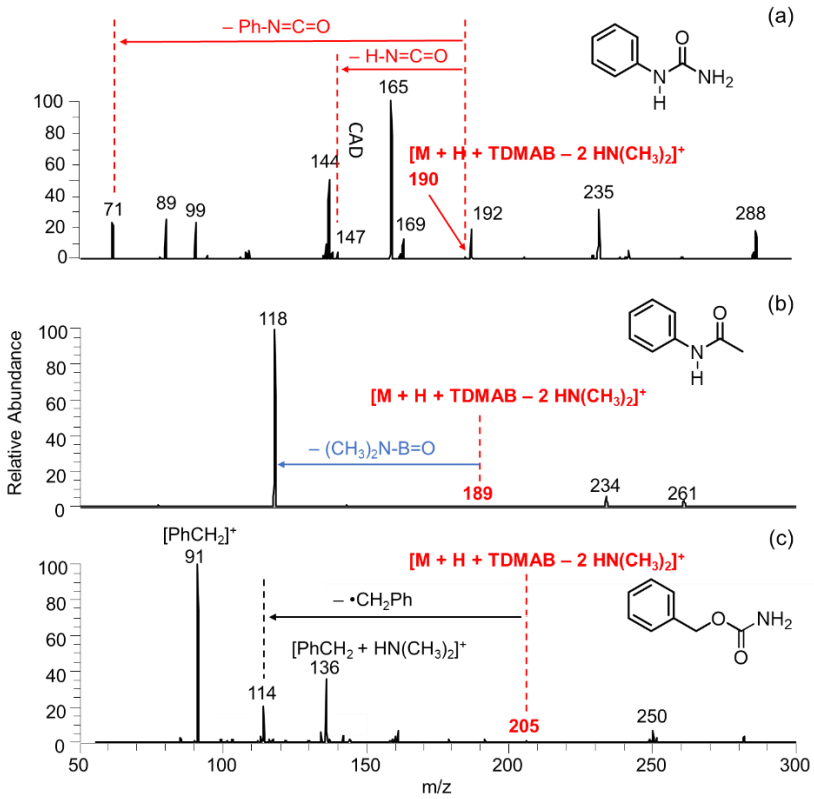

Figure 4.2. (a) MS^4 spectrum for 1-phenylurea (M) measured after CAD (collision energy 30 arbitrary units) of the fragment ions $[M + TDMAB – 2\ HN(CH_3)_2]^+$ (*m/z* 190) formed in the MS^3 CAD experiment. Diagnostic fragment ions of m/z 147 and 71 formed via elimination of Ph-N=C=O and H-N=C=O are visible. The ions of *m/z* 144 and *m/z* 99 correspond to protonated TDMAB and $[TDMAB + H – HN(CH_3)_2]^+$. The fragment ions of *m/z* 89, *m/z* 165 and *m/z* 117 correspond to water adducts of the fragment ions of *m/z* 71, *m/z* 147 and *m/z* 99, respectively. The fragment ions of *m/z* 288 and *m/z* 169 correspond to TDMAB adducts of the ions of *m/z* 190 and 71, respectively. (b) MS^4 CAD spectrum for *N*-phenylacetamide (M) measured after CAD (collision energy 30 arbitrary units) of the fragment ions $[M + TDMAB – 2\ HN(CH_3)_2]^+$ (*m/z* 189) formed in the MS^3 CAD experiment. Diagnostic fragment ions of m/z 118 formed via elimination of $(CH_3)_2N$-B=O are visible. (c) MS^4 CAD spectrum for benzyl carbamate (M) measured after CAD (collision energy 30 arbitrary units) of the fragment ions $[M + TDMAB – 2\ HN(CH_3)_2]^+$ (*m/z* 205). Formation of benzyl cations (m/z 91) and elimination of benzyl radicals were observed.

The potential energy surfaces calculated for the elimination of the second $HN(CH_3)_2$ and R-N=C=O (R = H or substitutent) from the ion-molecule reaction product ions $[M + H + TDMAB – HN(CH_3)_2]^+$ of protonated 1-phenylurea (M) upon two consecutive CAD experiments are shown in Figure 4.3. Based on these calculations, two different proton transfer reactions can trigger different fragmentation pathways that are colored in red and blue in Figure 4.3a. After the initial intramolecular proton transfer, a new boron-nitrogen bond is generated that results in the formation of a four-membered ring (Figure 4.3a). The following elimination of a $HN(CH_3)_2$ molecule was calculated to be endothermic by at least 60.7 kcal mol^{-1} (red pathway). The so-generated ion with a four-membered ring will undergo an exothermic ring-opening reaction (Figure 4.3b and 4.3c) and then eliminate an R-N=C=O (R = H or substituent) molecule with a barrier of 19.1 kcal mol^{-1} or 18.7 kcal mol^{-1} (Figures 4.3b and 4.3c, respectively). Elimination of $(CH_3)_2N$-B=O upon CAD of the $[M + H + TDMAB – 2\ HN(CH_3)_2]^+$ fragment ion in the second CAD step was calculated to start from the structure with the four-membered ring, and has a barrier of 29.0 kcal mol^{-1} or 40.8 kcal mol^{-1} (Figures 4.3b and 4.3c, respectively). After the ion with the four-membered ring has undergone exothermic ring opening, $(CH_3)_2N$-B=O elimination is unlikely to occur. This explains why only R-N=C=O (R = H or substituent) elimination was observed for substituted *ureas containing no tertiary amino groups* (Figures 4.2 and Table 4.3).

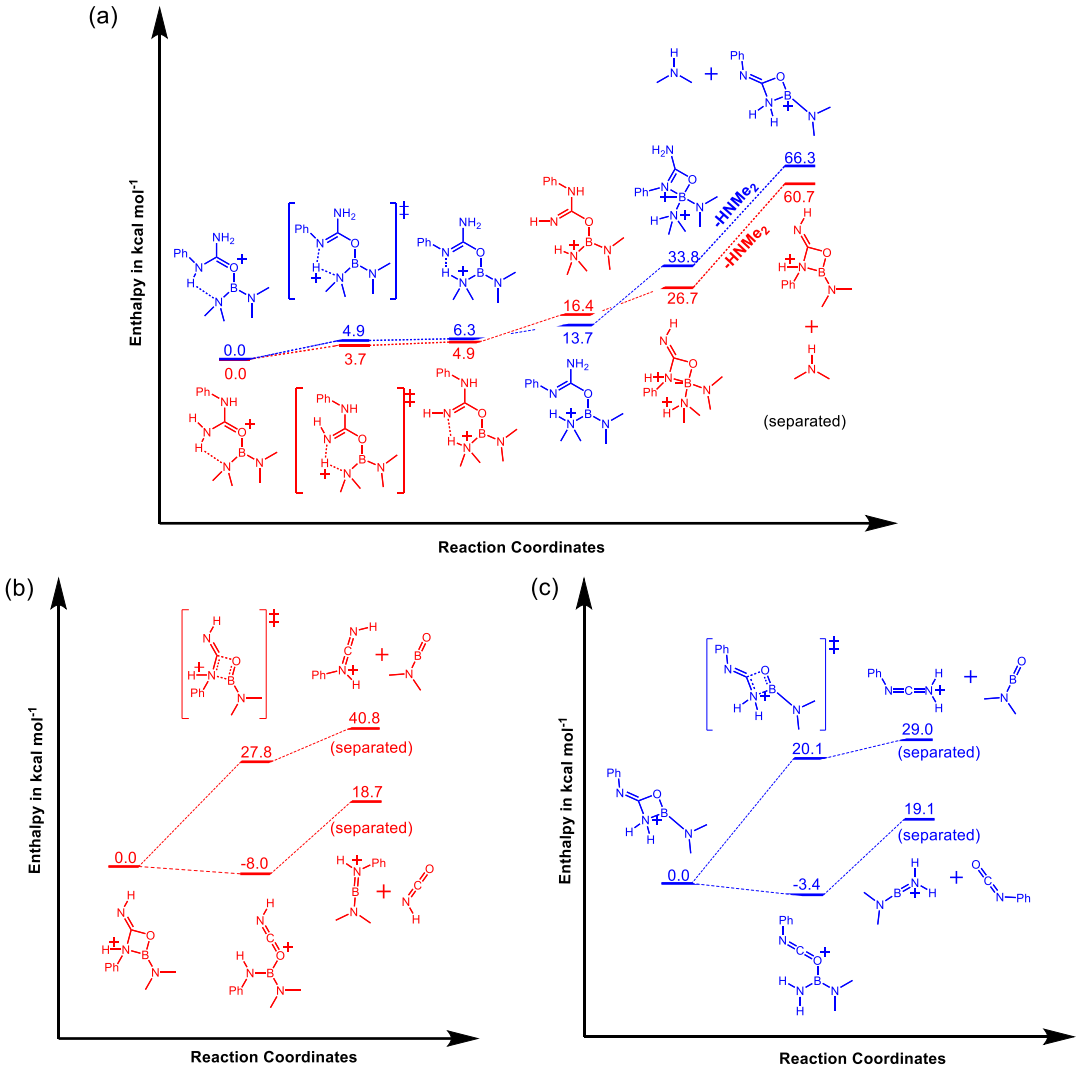

Figure 4.3. (a) Potential energy surfaces calculated at the M06-2X/6-311++G(d,p) level of theory for the CAD of the product ions $[M + H + TDMAB – HN(CH_3)_2]^+$ generated upon reactions of protonated 1-phenylurea (M) with TDMAB. Two possible pathways triggered by proton transfer from different nitrogen atoms are shown in red and blue color, generating two isomeric ions $[M + H + TDMAB – 2\ HN(CH_3)_2]^+$. All enthalpy values are given relative to that of the ion-molecule reaction products. Note that all intermediates shown in red color lie 4.1 kcal mol^{-1} higher in energy than all intermediates shown in blue color (also see the final product structures in Figure 4.1). (b) Potential energy surfaces calculated at the M06-2X/6-311++G(d,p) level of theory for the CAD fragmentation of the fragment ion $[M + H + TDMAB – 2\ HN(CH_3)_2]^+$ in red color. Enthalpy values are given relative to that of the ion $[M + H + TDMAB – 2\ HN(CH_3)_2]^+$ shown in red color. (c) Potential energy surfaces calculated at the M06-2X/6-311++G(d,p) level of theory for the CAD fragmentation of the fragment ion $[M + H + TDMAB – 2\ HN(CH_3)_2]^+$ shown in blue color. Enthalpy values are given relative to that of $[M + H + TDMAB – 2\ HN(CH_3)_2]^+$ shown in blue color. Note that the product ion shown in blue color lies 1.5 kcal mol^{-1} higher in energy than the product ion shown in red color (also see the final product structures in Figures 4.1 and 4.3a).

For *ureas containing one tertiary amino group*, only minor $[M + H + TDMAB - 2\ HN(CH_3)_2 - (CH_3)_2N\text{-}B{=}O]^+$ fragment ions were observed in the MS^4 experiments, in addition to the major R-N=C=O elimination (R = H or substituent; Table 4.3). These reactions were examined using calculations. The potential energy surfaces calculated for the fragmentation of the ion-molecule reaction product ions $[M + H + TDMAB - HN(CH_3)_2]^+$ of 1-piperidinecarboxamide via elimination of $HN(CH_3)_2$ (Figure 4.4a) followed by elimination of $(CH_3)_2N$-B=O or H-N=C=O (Figures 4.4b and 4.4c, respectively) suggest that proton transfer occurs from the amino group of the substituted urea to a dimethylamino group of the boron moiety, followed by N-B bond formation to generate one of two possible four-membered cyclic intermediates. After the elimination of the second $HN(CH_3)_2$, an H-N=C=O molecule can be eliminated (red pathway), which was the major reaction observed (Figure 4.4b and Table 4.3), via a reaction calculated to be endothermic by 23.5 kcal mol^{-1}. Along the second (blue) pathway, a $(CH_3)_2N$-B=O molecule is eliminated to form a final product with a higher enthalpy (62.3 kcal mol^{-1}) than that formed via H-N=C=O loss (Figure 4.4c). In spite of the much greater enthalpy of the latter product, also this product was generated albeit with a very low abundance (Table 4.3).

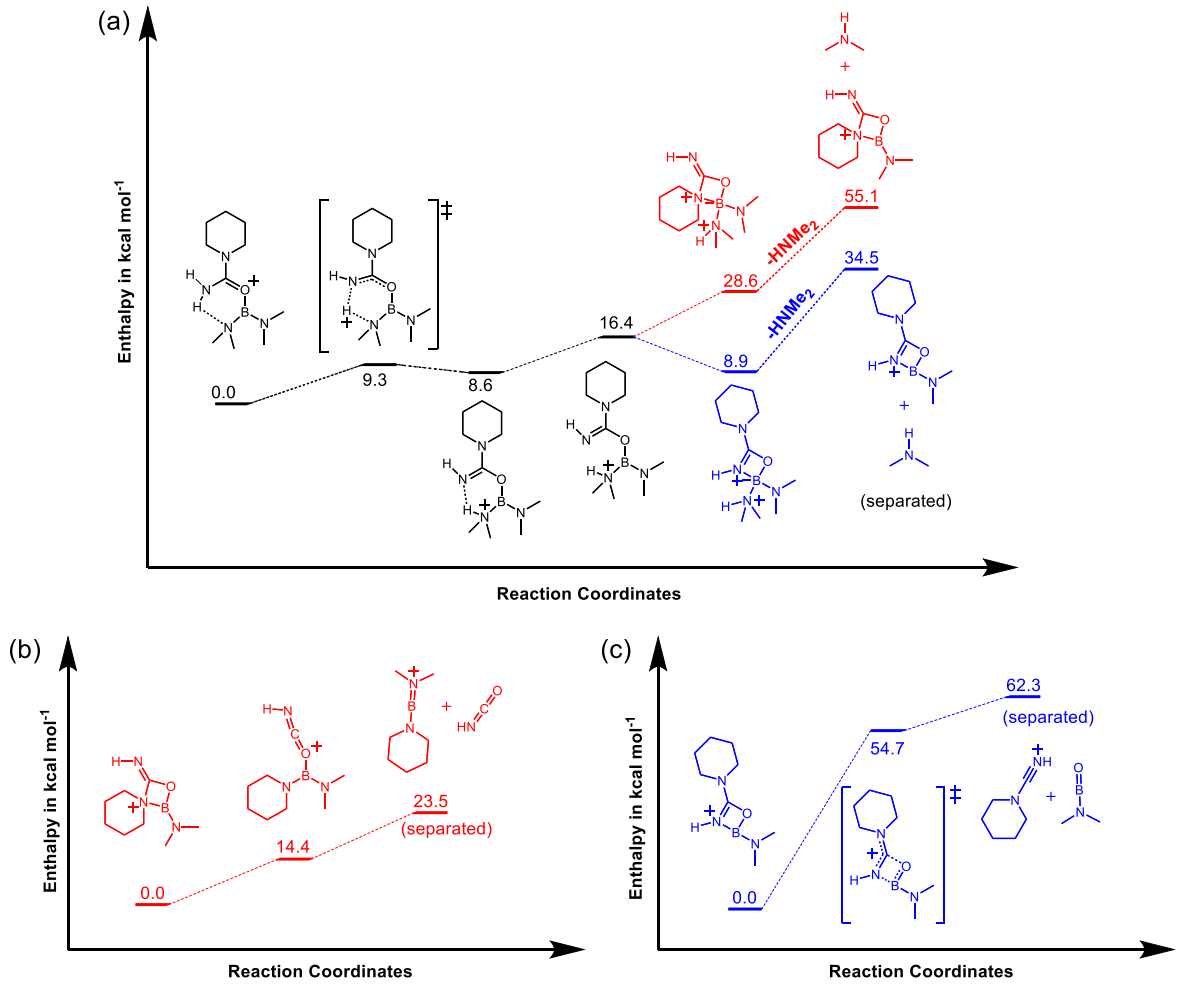

Figure 4.4.(a) Potential energy surface calculated at the M06-2X/6-311++G(d,p) level of theory for the CAD fragmentations of the ion-molecule reaction product ions $[M + H + TDMAB – HN(CH_3)_2]^+$ generated upon reactions of protonated 1-piperidinecarboxamide (M) with TDMAB. Two possible pathways triggered by proton transfer from different nitrogen atoms are colored in red and blue, generating two isomeric fragment ions $[M + H + TDMAB – HN(CH_3)_2]^+$. (b) Potential energy surface calculated at the M06-2X/6-311++G(d,p) level of theory for the CAD fragmentations of the fragment ions $[M + H + TDMAB – 2\ HN(CH_3)_2]^+$ in red color. (c) Potential energy surface calculated at the M06-2X/6-311++G(d,p) level of theory for the CAD fragmentations of the fragment ions $[M + H + TDMAB – 2\ HN(CH_3)_2]^+$ in blue color. Note that the product ion shown in red color lies 20.6 kcal mol^{-1} higher in energy than the product ion shown in blue color (Figure 4.4a).

The reason for the minor elimination of $(CH_3)_2N$-B=O observed in the MS^4 spectra of ureas containing one tertiary amino group is that the two intermediates with the four-membered ring (pathways in red and blue color; enthalpies 28.6 and 8.9 kcal mol^{-1}, respectively; Figure 4.4a) can both be generated in the ion trap upon the first CAD experiment (on [M + H + TDMAB –

$HN(CH_3)_2]^+$) and they fragment via elimination of a $HN(CH_3)_2$ molecule. The two isomeric fragment ions $[M + H + TDMAB – 2\ HN(CH_3)_2]^+$ decompose differently: one can only eliminate H-N=C=O (Figure 4.4b) while the other can only eliminate $(CH_3)_2$N-B=O (Figure 4.4c). The latter elimination requires more energy, which explains why it only yields a minor product.

For *tetrasubstituted ureas*, the ion-molecule reaction product ions of did not eliminate $HN(CH_3)_2$ upon CAD of $[M + H + TDMAB – HN(CH_3)_2]^+$, as the initial intramolecular proton transfer (Figures 4.3 and 4.4) from an amino group in the urea moiety to the dimethylamino group in the boron moiety cannot occur since neither of the two nitrogen atoms contain a H atom. Instead, the $[M + H + TDMAB – HN(CH_3)_2]^+$ product ions fragment via elimination of the neutral analyte molecule (M) by breaking the B-O bond to generate the fragment ions $[TDMAB + H – 2\ HN(CH_3)_2]^+$ (Table 4.2). Therefore, tetrasubstituted ureas can be distinguished from the other analytes based on this observation.

The behavior observed for protonated *amides* was quite different. $(CH_3)_2$N-B=O loss occurred in the second CAD experiment of the fragment ions $[M + H + TDMAB – 2\ HN(CH_3)_2]^+$ of amides, but no R-N=C=O loss was detected (Table 4.3). Indeed, R-N=C=O loss cannot occur for amides because they only contain only one amino group. Amides can therefore be differentiated from substituted ureas based on the MS^4 experiments of their reactions with TDMAB. A mechanism has been previously proposed for the elimination of $(CH_3)_2$N-B=O for protonated amides in the same MS^4 experiments as conducted here.[21]

The ion-molecule reaction product of one of the *carbamates*, phenyl carbamate, did not lose $HN(CH_3)_2$ but instead H-N=C=O upon CAD of $[M + H + TDMAB – HN(CH_3)_2]^+$ (Table 4.2). This is rationalized by the greater amount of energy (43.5 kcal mol^{-1}) required to eliminate a dimethylamine molecule (Figure 4.5, in blue color) compared to the energy required for H-N=C=O loss (28.9 kcal mol^{-1}; Figure 4.5, in red color) for this product ion. As dimethylamine elimination is not a diagnostic reactivity for all protonated carbamates upon MS^3, the behavior of the carbamates is not as predictable as that of the other analytes discussed here.

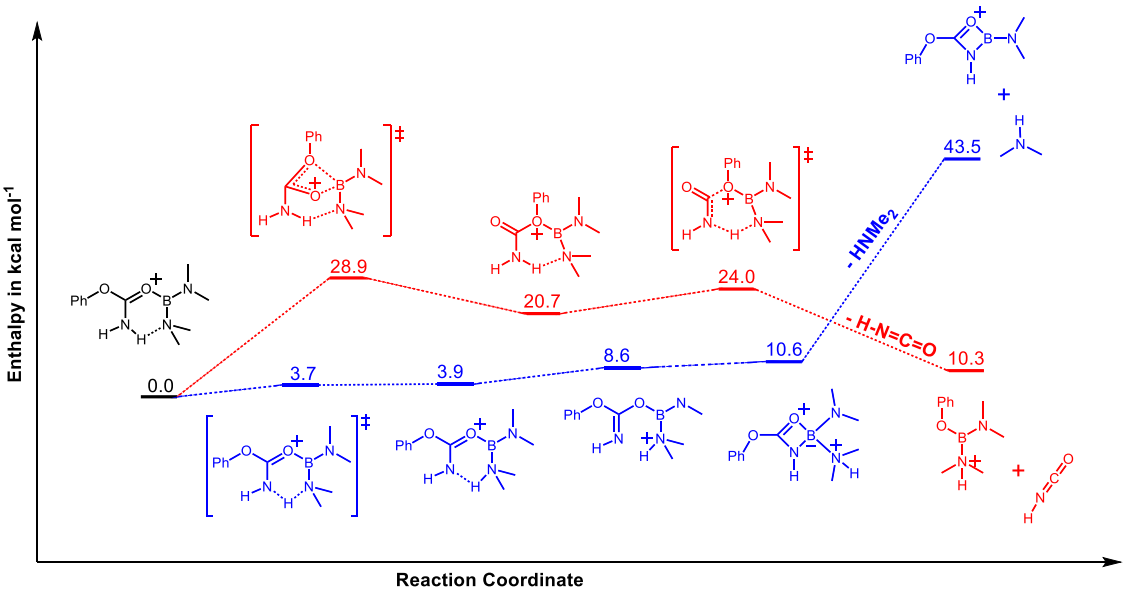

Figure 4.5. Potential energy surface calculated at the M06-2X/6-311++G(d,p) level of theory for the elimination of H-N=C=O (observed experimentally; in red color) and $HN(CH_3)_2$ (not observed; in blue color) upon CAD of the ion-molecule reaction product [M + H + TDMAB – $HN(CH_3)_2$]$^+$ of protonated phenyl carbamate.

The reactivities of protonated *N-oxides* and *sulfoxides* toward TDMAB have been explored previously by using Fourier-transform ion cyclotron resonance and linear quadrupole ion trap mass spectrometers.[16,21] These ions react with TDMAB to form the same product ions [M + H + TDMAB – $HN(CH_3)_2$]$^+$ as protonated ureas and amides. Upon CAD, these product ions fragment via elimination of $HN(CH_3)_2$ and $HO\text{-}B(N(CH_3)_2)_2$ (MS^3 experiments).[16,21] However, for sulfoxides, an additional fragment ion, [TDMAB + H – $HN(CH_3)_2$ – $(CH_3)_2N\text{-}B{=}O$]$^+$, was also formed (MS^3 experiments),[16] which enables the differentiation of sulfoxides from N-oxides. For *pyridines*, these CAD experiments yielded only $[B(N(CH_3)_2)_2]^+$.[21] As the MS^3 experiments of *N*-oxides, sulfoxides and pyridines generated different fragment ions than the MS^3 experiments of substituted ureas and amides, all these analytes can be differentiated based on these experiments (Figure 4.6).

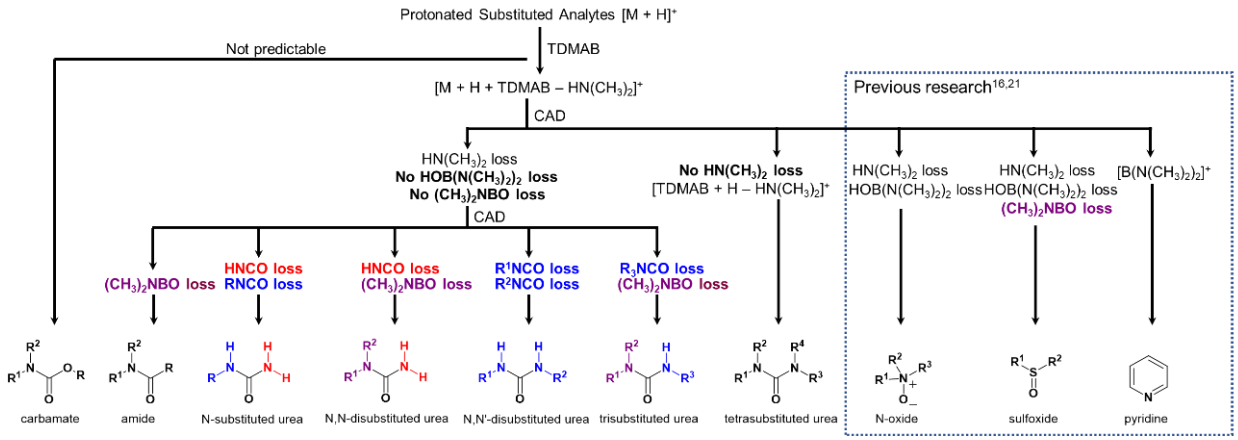

Figure 4.6. Distinction of differently substituted ureas from each other and from amides, N-oxides, sulfoxides[16] and pyridines[21] via diagnostic fragment ions generated upon one or two CAD experiments on the ion-molecule reaction product ions $[M + H + TDMAB – HN(CH_3)_2]^+$ formed upon reactions of the protonated analytes (M) with TDMAB.

4.3.3 Reactions of protonated drugs and herbicides with TDMAB

As the urea moiety is a common functional group in drugs and herbicides, reactivities of seven protonated drugs and herbicides containing the urea moiety were tested (Table 4.4). The structures of these urea compounds are more complicated than the model compound discussed above. Some of them have additional functionalities, such as a methoxy (linuron and monolinuron), sulfonyl (tolbutamide) or hydroxy group (zileuton). Many of them also contain a chlorine atom. Upon reactions with TDMAB for 300 ms or 1000 ms, all of the protonated drug/herbicide compounds formed $[M + H + TDMAB – HN(CH_3)_2]^+$ product ions (MS^2), as expected. Upon CAD, these product ions generated fragment ions $[M + H + TDMAB – 2\ HN(CH_3)_2]^+$ (MS^3), again as expected. When these fragment ions were subjected to CAD, elimination of R-N=C=O (R = substituent) was observed for all analytes as expected, with the exception of zileuton (MS^4; Table 4.4).

Table 4.4. Fragmentations/fragment ions observed upon CAD[a] of the fragment ions [M + H + TDMAB – 2 $HN(CH_3)_2$]$^+$ (MS^4) for urea herbicides (M) and urea drugs (M). The fragment ions [M + H + TDMAB – 2 $HN(CH_3)_2$ – R-N=C=O]$^+$ (R = H or substituent) are indicated in red color. The fragment ions [M + H + TDMAB – 2 $HN(CH_3)_2$ – $(CH_3)_2$N-B=O]$^+$ are indicated in blue color.

Analyte (*m/z* of [M + H]$^+$)	Ions (*m/z*) formed upon CAD of [M + H + TDMAB – 2$HN(CH_3)_2$]$^+$ and their relative abundances[b] (MS^4)	
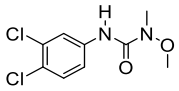 Linuron (249)	– •CH_3 (287)	100%
	– •Cl (267)	35%
	– CH_3-N=CH_2 (259)	44%
	– $HN(CH_3)_2$ (257)	71%
	– H_3C-N=C=O (245)	42%
	[$Cl_2C_6H_3$-NH=B-OCH_3]$^+$ (202)	56%
	[$Cl_2C_6H_3$-NH=B-OCH_3 + H_2O]$^+$ (220)	64%
	[$Cl_2C_6H_3$-NH=B-OCH_3 + $HN(CH_3)_2$]$^+$ (247)	30%
	[$Cl_2C_6H_3$-NH_3]$^+$ (162)	85%
	[TDMAB + H]$^+$ (144)	59%
	[TDMAB + H + 2 MeOH]$^+$ (209)	56%
	– $Cl_2C_6H_3$-N=C=O (115)	47%
	– $Cl_2C_6H_3$-N=C=O + H_2O (143)[a]	51%
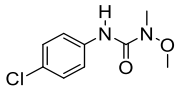 Monolinuron (215)	– •CH_3 (253)	28%
	– CH_3OH (236)	20%
	– $HN(CH_3)_2$ (223)	100%
	– H_3C-N=C=O (211)	12%
	[ClC_6H_4-NH=B-OCH_3]$^+$ (168)	3%
	[ClC_6H_4-NH=B-OCH_3 + H_2O]$^+$ (186)	16%
	[ClC_6H_4-NH=B-OCH_3 + $HN(CH_3)_2$]$^+$ (213)	12%
	[TDMAB + H]$^+$ (144)	22%
	[ClC_6H_4-NH_3]$^+$ (128)	12%
	– ClC_6H_4-N=C=O (115)	16%
	– ClC_6H_4-N=C=O + H_2O (143)	17%
	– ClC_6H_4-N=C=O + MeOH + H_2O (175)	21%
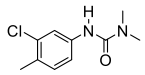 Chlortoluron (213)	– $(CH_3)_2$N-B=O (195)	21%
	[TDMAB + H]$^+$ (144)	57%
	[2 TDMAB + H – $HN(CH_3)_2$]$^+$ (242)	8%
	–ClC_7H_6-N=C=O (99)	100%
	–ClC_7H_6-N=C=O + H_2O (117)	45%
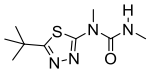 Tebuthiuron (229)	– CH_3-N=C=O (225)	100%
	– CH_3-N=C=O + $HN(CH_3)_2$ (270)	76%
	– (*t*-Bu-(C_2N_2S))-NH=CH_2 (170)	25%
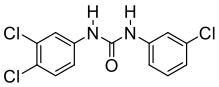 Triclocarban (315)	– ClC_6H_4-N=C=O (215)	7%
	– ClC_6H_4-N=C=O + $HN(CH_3)_2$ (260)	24%
	– ClC_6H_4-N=C=O + H_2O (233)	100%
	– ClC_6H_4-N=C=O – HCl (179)	18%
	– $Cl_2C_6H_3$-N=C=O (181)	12%
	– $Cl_2C_6H_3$-N=C=O + $HN(CH_3)_2$ (226)	21%
	– $Cl_2C_6H_3$-N=C=O + H_2O (199)	90%
	[TDMAB + H]$^+$ (144)	42%

(Table 4.4 continued)

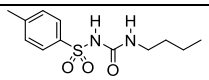 Tolbutamide (271)	– *n*-Bu-N=C=O (225)	100%
	– *n*-Bu-N=C=O + $HN(CH_3)_2$ (270)	71%
	– *n*-Bu-N=C=O + TDMAB – $HN(CH_3)_2$ (323)	54%
	– *n*-Bu-N=C=O + TDMAB – $HN(CH_3)_2$ – $N(CH_3)=CH_2$ (280)	42%
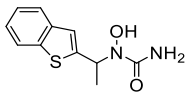 Zileuton (237)	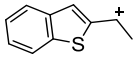 (161)	100%
	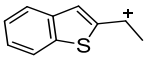 + $HN(CH_3)_2$ (206)	15%
	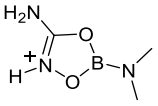 (130)	49%
	[TDMAB + H]$^+$ (144)	10%

[a] *All collision energies were 30 arbitrary units.* [b] *Reproducibility ± 20%.*

Different from the simple trisubstituted ureas discussed above (Table 4.3), elimination of $(CH_3)_2$N-B=O was not observed upon CAD of $[M + H + TDMAB – 2\ HN(CH_3)_2]^+$ (MS^4) for linuron, monolinuron or tebuthiuron but it was observed for chlortoluron, even though all above compounds are trisubstituted ureas. Formation of a much more favorable five- or six-membered ring (Scheme 4.3) rather than a four-membered ring (Figures 4.3 and 4.4) probably explains the lack of elimination of a boron moiety for linuron, monolinuron and tebuthiuron due to the presence of other heteroatoms that can add to the boron atom via a more favorable transition state. As shown in Scheme 4.3, after the formation of the product ion $[M + H + TDMAB – HN(CH_3)_2]^+$ and the intramolecular proton transfer, the boron is more likely to form a bond with the nitrogen atom in the aromatic ring instead of the nitrogen atom of the secondary amino group due to the formation of a more favorable six-membered rather than a four-membered ring. Therefore, elimination of CH_3-N=C=O dominates. On the other hand, elimination of $(CH_3)_2$N-B=O was observed for chlortoluron because this analyte does not contain additional oxygen or nitrogen atoms. Therefore, observation of a fragment ion $[M + H + TDMAB – 2\ HN(CH_3)_2 – (CH_3)_2N\text{-}B=O]^+$ cannot be used to identify *N,N*-disubstituted or trisubstituted ureas with a heteroatom close to the nitrogen atom of the urea moiety.

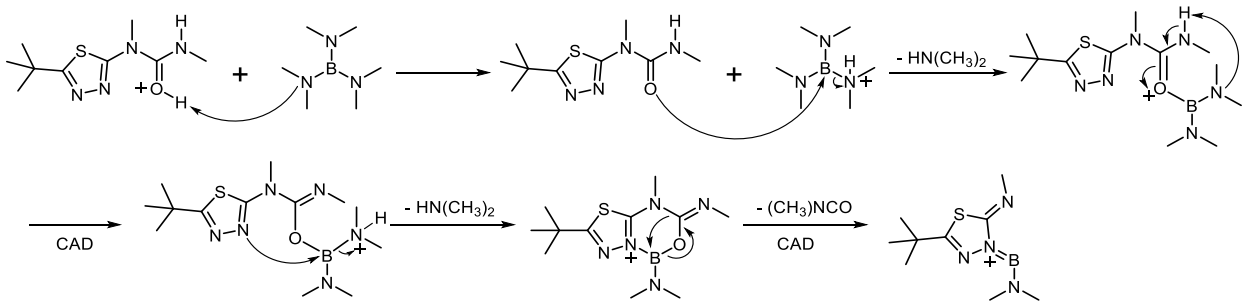

Scheme 4.3. A proposed fragmentation mechanism leading to the [M + H + TDMAB – 2 $HN(CH_3)_2$]$^+$ fragment ions for some of the polyfunctional trisubstituted ureas tested. tebuthiuron is used as an example.

In the MS^4 experiment of zileuton (a *N*,*N*-disubstituted urea), the expected fragment ions [M + H + TDMAB – 2 $HN(CH_3)_2$ – H-N=C=O]$^+$ were not generated (Table 4.4), which is probably due to other, more favorable fragmentation reactions. Based on calculations shown in Figure 4.7, after the formation of the product ion [M + H + TDMAB – $HN(CH_3)_2$]$^+$, the boron will form a bond with the oxygen of the hydroxyl group (pathway in blue color) instead of the nitrogen of the amino group (pathway in black color) because formation of a five-membered ring is more favorable than formation of a four-membered ring (Figure 4.7). The intermediate with a five-membered ring (in blue color) fragments by breaking the C-N bond to generate one of the two fragment ions (Table 4.4) (another fragment ion is likely generated by a subsequent proton transfer from the first fragment ion to the neutral molecule that was eliminated).

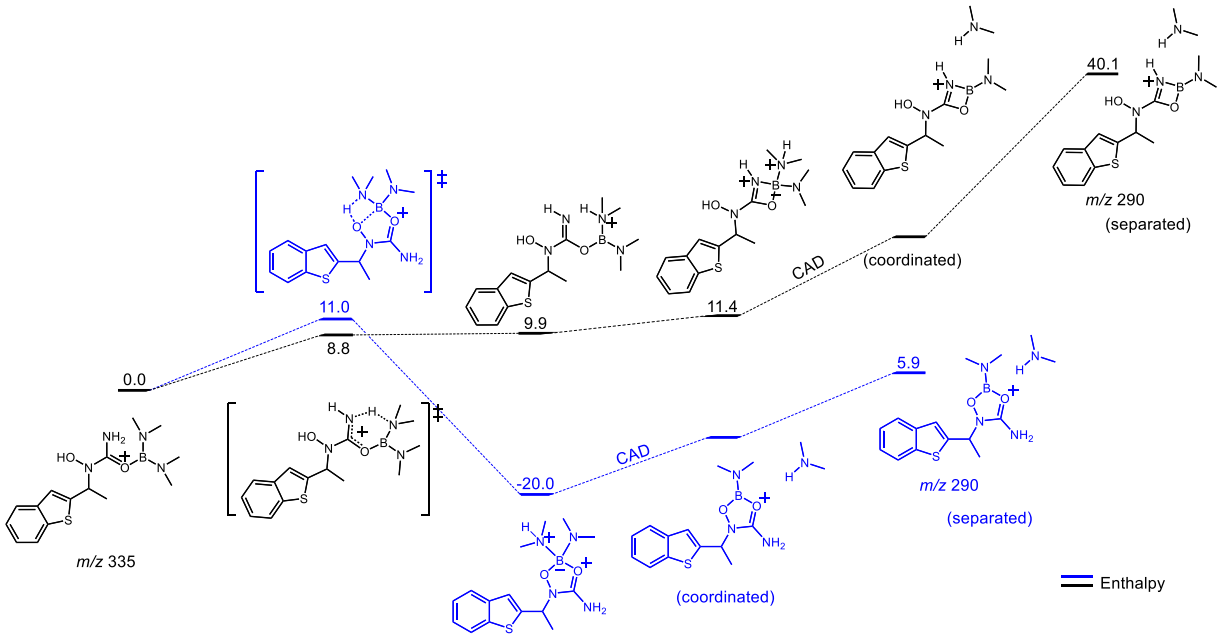

Figure 4.7. Potential energy surface calculated at the M06-2X/6-311++G(d,p) level of theory for CAD of the product ions $[M + H + TDMAB – DMA]^+$ generated upon reactions of protonated zileuton with TDMAB. Two possible pathways triggered by proton transfer from a nitrogen atom or an oxygen atom are indicated in black and blue color, respectively. This surface supports the assumption that five-membered rings are formed more easily from these compounds than four-membered rings.

4.3.4 HPLC/MS^4 experiments

HPLC/MS^4 experiments were carried out to test the practicality of the proposed analytical method when coupled to a separation method. A mixture of four trisubsituted urea herbicides were separated by reversed-phase HPLC chromatography (Figure 4.8a). The eluted compounds were protonated by (+)APCI and transferred into the ion trap. The protonated analytes were monitored to obtain the chromatogram shown in Figure 4.8a. The major peaks shown in Figure 4.8a correspond to the four analytes.

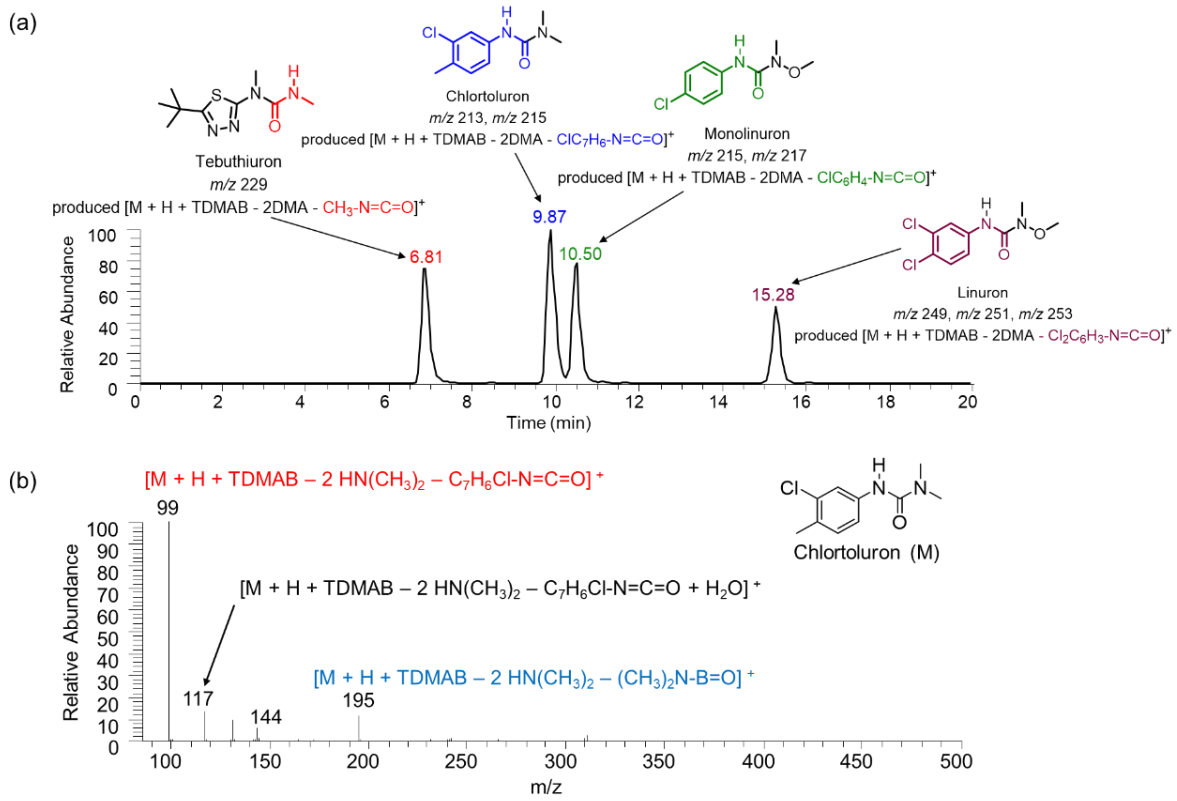

Figure 4.8. (a) HPLC/(+)APCI MS chromatogram measured for a mixture of four urea herbicides. The protonated analytes were monitored to obtain the chromatogram. (b) MS^4 spectrum for chlortoluron (M) measured upon CAD of the fragment ion $[M + H + TDMAB – 2 HN(CH_3)_2]^+$. The fragment ion $[M + H + TDMAB – 2 HN(CH_3)_2]^+$ was generated upon CAD of the the product ion $[M + H + TDMAB – HN(CH_3)_2]^+$ that was formed upon reactions of protonated chlortoluron with TDMAB. chlortoluron eluted at 9.6-10.2 min.

After being transferred into the ion trap, the protonated analytes were isolated and allowed to react with TDMAB for 30 ms. The product ions $[M + H + TDMAB – HN(CH_3)_2]^+$ were isolated and subjected to CAD (MS^3, collision energy 30 arbitrary units). The fragment ions $[M + H + TDMAB – 2 HN(CH_3)_2]^+$ were isolated and subjected to CAD (MS^4, collision energy 30 arbitrary units). The MS^4 CAD spectrum of chlortoluron was shown in Figure 4.8b as an example. Based on the observation of fragment ions $[M + H + TDMAB – 2 HN(CH_3)_2 – R\text{-}N=C=O]^+$ (R = substituent) in the MS^4 spectra (Figure 4.8b), the compounds were unambiguously identified as trisubstituted ureas.

This HPLC/MS^4 method based on ion-molecule reactions has an approximate limit of detection from 100 nM up to 20 μM. The data measured to determine the limit of detection are shown in Figure 4.9 (using chlortoluron as an example), where the extracted ion HPLC

chromatogram for the diagnostic ion-molecule reaction product ion [M + H + TDMAB – $HN(CH_3)_2$]$^+$ was monitored. At the concentration of 100 nM, the signal-to-noise ratio of the product ion is three (Figure 4.9a), and the diagnostic fragment ions [M + H + TDMAB – 2 $HN(CH_3)_2$ – R-N=C=O]$^+$ and [M + H + TDMAB – 2 $HN(CH_3)_2$ – $(CH_3)_2$N-B=O]$^+$ can still be observed in the MS^4 spectrum (Figure 4.9b). Therefore, the limit of detection for chlortoluron is 100 nM. Further, the limits of detection for the HPLC/MS^2 experiments of the other three urea herbicides, linuron, monolinuron and tebuthiuron, were determined to be 20 µM, 3 µM and 300 nM, respectively.

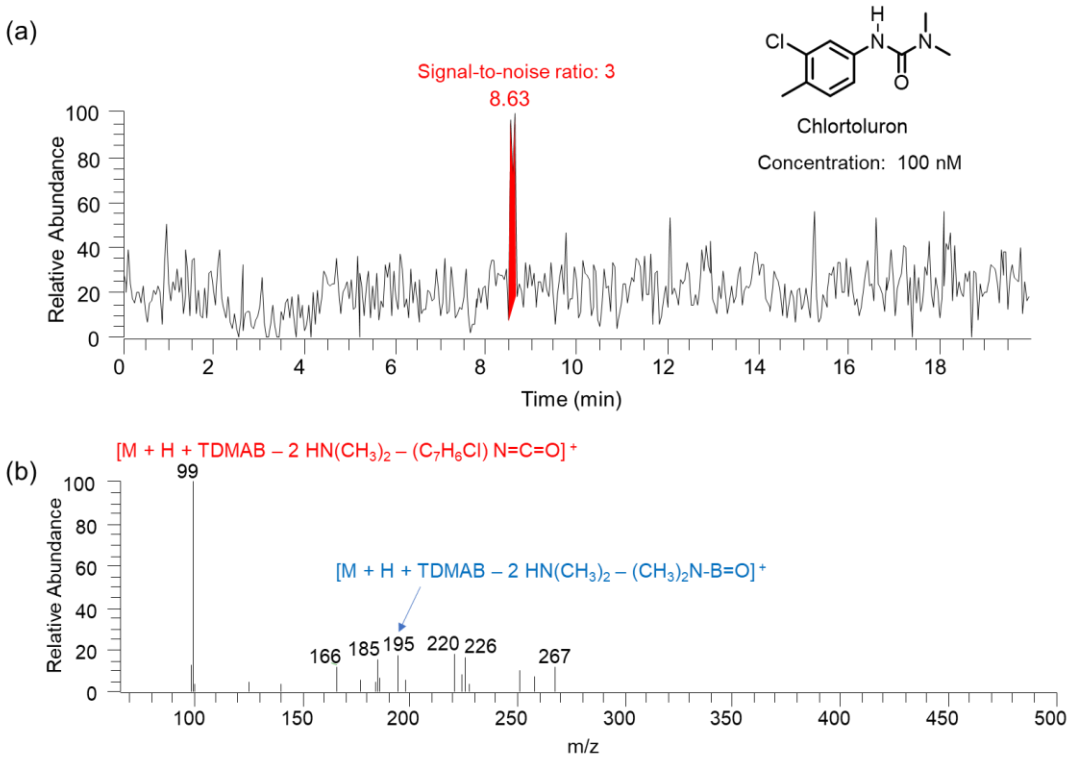

Figure 4.9. (a) Extracted ion HPLC chromatogram for the diagnostic ion-molecule reaction product ion of *m/z* 311 (generated in an MS/MS experiment) measured for chlortoluron at the limit of detection concentration (100 nM). The chromatogram shows the analyte peak at 8.63 min. (b) MS^4 spectrum measured for chlortoluron at 100 nM concentration. The MS^4 spectrum shows the diagnostic fragment ions (*m/z* 99 and *m/z* 195) also shown in Figure 4.8. The limit of detection measurement was performed three times.

4.4 Conclusions

Most protonated analytes react with TDMAB in Fourier-transform ion cyclotron resonance and linear quadrupole ion trap mass spectrometers by proton transfer. However, protonated ureas, amides, and carbamates as well as previously studied protonated N-oxides,[16,21,23] sulfoxides[16] and pyridines[21] react with TDMAB to generate the product ion $[M + H + TDMAB – HN(CH_3)_2]^+$ (MS^2), with the exception of one carbamate. To distinguish differently substituted ureas from other analytes and from each other, the product ions $[M + H + TDMAB – HN(CH_3)_2]^+$ were subjected to CAD (MS^3) in a linear quadrupole ion trap mass spectrometer. For substituted ureas (with the exception of tetrasubstituted ureas) and amides, fragment ions were generated via elimination of another $HN(CH_3)_2$ molecule. On the other hand, another $HN(CH_3)_2$ loss was not observed for tetrasubstituted ureas, *N*-oxides, sulfoxides or pyridines, which enables distinction of these compounds from other substituted ureas and amides. Instead, fragment ions $[TDMAB + H – HN(CH_3)_2]^+$ were observed for tetrasubstituted ureas, which can be differentiated from the other analytes based on this observation. Both $HO\text{-}B(N(CH_3)_2)_2$ and $HN(CH_3)_2$ losses occurred for *N*-oxides and sulfoxides in the MS^3 experiments. However, sulfoxides also eliminated $(CH_3)_2N\text{-}B{=}O$ in the MS^3 experiments, which enables differentiation of *N*-oxides from sulfoxides.[16,21,23] For pyridines, $[B(N(CH_3)_2)_2]^+$ was generated in the MS^3 experiments,[21] which was not observed for any other analytes explored. This enables the identification of the pyridine functionality.

Fragment ions diagnostic for differently substituted ureas were obtained by subjecting the fragment ions $[M + H + TDMAB – 2\ HN(CH_3)_2]^+$ to another CAD event. Loss of one or two R-N=C=O molecules (R = H or a substituent) was observed for monosubstituted, disubstituted and trisubstituted ureas. On the other hand, also $(CH_3)_2N\text{-}B{=}O$ elimination was observed for ureas with a tertiary amino group, which can be used to differentiate these compounds from ureas with no tertiary amino groups. $(CH_3)_2N\text{-}B{=}O$ loss also occurred for all amides. However, H-N=C=O/R-N=C=O loss was not observed in the reactions of the seven amides studied (with one exception, benzamide), which enables the differentiation of the amides from the ureas.

Successful coupling of this ion-molecule reaction/CAD MS^4 experiment with HPLC demonstrated the practicality of this approach in the analysis of complex mixtures containing substituted ureas and related compounds. The limits of detection for the diagnostic ion-molecule reaction product ion in HPLC/MS^2 experiments were determined to be 20 μM, 3 μM, 300 nM, and 100 nM for linuron, monolinuron, chlortouron and tebuthiuron, respectively.

The analytical method discussed above can be utilized in three ways: 1. It can be used to differentiate the five categories of ureas based on diagnostic fragment ions ([M + H + TDMAB – 2 $HN(CH_3)_2$ – R-N=C=O]$^+$ (R = substituent) and [M + H + TDMAB – 2 $HN(CH_3)_2$ – $(CH_3)_2$N-B=O]$^+$). 2. It can be used to differentiate ureas from amides, carbamates, pyridines, sulfoxides and N-oxides as only ureas generate the diagnostic fragment ions [M + H + TDMAB – 2 $HN(CH_3)_2$ – R-N=C=O]$^+$ (R = H or substituent). 3. It can be used to differentiate mono- and 1,1-disubstituted ureas based on diagnostic fragment ions ([M + H + TDMAB – 2 $HN(CH_3)_2$ – H-N=C=O]$^+$). Finally, several mechanistic pathways that likely underlie the formation of the diagnostic fragment ions were identified by quantum chemical calculations.

4.5 References

1. Bending, G. D., Lincoln, S. D., Sørensen, S. R., Morgan, J. A. W., Aamand, J., Walker, A., In-field spatial variability in the degradation of the phenylurea herbicide isoproturon is the result of interactions between degradative *sphingomonas* spp. and soil pH. *Appl. Environ. Microb.* **2003**, *69*, 827-834.

2. Howard, A. L., Taylor, L. T., Quantitative supercritical fluid extraction of sulfonyl urea herbicides from aqueous matrices via solid phase extraction disks. *J. Chromatogr. Sci.* **1992**, *30*, 374-382.

3. Miller, J., Keeley, P., Thullen, R., Carter, C., Persistence and movement of ten herbicides in soil. *Weed Sci.* **1978**, *26*, 20-27.

4. Murray, D., Rieck, W., Lynd, J., Microbial degradation of five substituted urea herbicides. *Weed Sci.* **1969**, *17*, 52-55.

5. Gatidou, J., Stasinakis, A. S., Iatrou, E. I., Assessing single and joint toxicity of three phenylurea herbicides using *Lemna minor* and *Vibrio fischeri* bioassays. *Chemosphere* **2014**, *119*, S69-S74.

6. Zhai, X. and Lu, Y., Development and validation of a simple LC method for the determination of phenacetin, coumarin, tolbutamide, chlorzoxazone, testosterone and their metabolites as markers of cytochromes 1A2, 2A6, 2C11, 2E1 and 3A2 in rat microsomal medium. *Pharmazie* **2013**, *68*, 19-26.

7. Yang, R.-S.; Beard, A.; Sheng, H.; Zhang, L.-K.; Helmy, R. Applications of TiCl3 as a diagnostic reagent for the detection of Nitro- and N-Oxide-containing compounds as potentially mutagenic impurities using ultrahigh-performance liquid chromatography coupled with high-resolution mass spectrometry. *Org. Process Res. Dev.* **2015**, *20*, 59-64.

8. Brockman, A.H., Hiller, D.L. and Cole, R.O., High-speed HPLC/MS/MS analysis of biological fluids: a practical review. *Curr. Opin. Drug Disc.*, **2000.** *3*, 432-438.

9. Grebe, S.K. and Singh, R.J., LC-MS/MS in the clinical laboratory–where to from here? *Clin. Biochem. Rev*. **2011**, *32*, 5-31.

10. Yamagaki, T. and Sato, A., Peak width-mass correlation in CID MS/MS of isomeric oligosaccharides using traveling-wave ion mobility mass spectrometry. *J. Mass Spectrom.* **2009**, *44*, 1509-1517.

11. Kong, J. Y.; Yu, Z.; Easton, M. W.; Niyonsaba, E.; Ma, X.; Yerabolu, R.; Sheng, H.; Jarrell, T. M.; Zhang, Z.; Ghosh, A. K.; Kenttämaa, H. I., Differentiating isomeric deprotonated glucuronide drug metabolites via ion/molecule reactions in tandem mass spectrometry. *Anal. Chem.* **2018**, *90*, 9426–9433.

12. Osburn, S.; Ryzhov, V., Ion–molecule reactions: analytical and structural tool. *Anal. Chem.* **2013**, *85*, 769–778.

13. Eberlin, M.N., Structurally diagnostic ion/molecule reactions: class and functional-group identification by mass spectrometry. *J. Mass Spectrom.* **2006**, *41*, 141-156.

14. Tang, W.; Sheng, H.; Kong, J. Y.; Yerabolu, R.; Zhu, H.; Max, J.; Zhang, M.; Kenttämaa, H. I., Gas-phase ion-molecule reactions for the identification of the sulfone functionality in protonated analytes in a linear quadrupole ion trap mass spectrometer. *Rapid Commun. Mass Spectrom.* **2016**, *30*, 1435−1441.

15. Campbell, K. M.; Watkins, M. A.; Li, S.; Fiddler, M. N.; Winger, B.; Kenttämaa, H. I., Functional group selective ion/molecule reactions: mass spectrometric identification of the amido functionality in protonated monofunctional compounds. *J. Org. Chem.* **2007**, *72*, 3159−3165.

16. Sheng, H.; Tang, W.; Yerabolu, R.; Max, J.; Kotha, R. R.; Riedeman, J. S.; Nash, J. J.; Zhang, M.; Kenttämaa, H. I., Identification of N-oxide and sulfoxide functionalities in protonated drug metabolites by using ion–molecule reactions followed by collisionally activated dissociation in a linear quadrupole ion trap mass spectrometer. *J. Org. Chem.* **2016**, *81*, 575−586.

17. Watkins, M.A., Price, J.M., Winger, B.E. and Kenttämaa, H.I., Ion-molecule reactions for mass spectrometric identification of functional groups in protonated oxygen-containing monofunctional compounds. *Anal. Chem.* **2004**, *76*, 964-976.

18. Watkins, M.A., Winger, B.E., Shea, R.C. and Kenttämaa, H.I., Ion−molecule reactions for the characterization of polyols and polyol mixtures by ESI/FT-ICR mass spectrometry. *Anal. Chem.* **2005**, *77*, 1385-1392.

19. Somuramasami, J., Duan, P., Watkins, M.A., Winger, B.E. and Kenttämaa, H.I., Ion–molecule reactions of trimethylborate allow the mass spectrometric identification and counting of functional groups in protonated bifunctional oxygen-containing compounds and polyols. *Int. J. Mass Spectrom.* **2007**, *265*, 359-371.

20. Falvo, F., Fiebig, L., Dreiocker, F., Wang, R., Armentrout, P.B. and Schäfer, M., Fragmentation reactions of thiourea-and urea-compounds examined by tandem MS, energy-resolved CID experiments, and theory. *Int. J. Mass Spectrom.* **2012**, *330*, 124-133.

21. Duan, P., Fu, M., Gillespie, T.A., Winger, B.E. and Kenttämaa, H.I., Identification of aliphatic and aromatic tertiary N-oxide functionalities in protonated analytes via ion/molecule and dissociation reactions in an FT-ICR mass spectrometer. *J Org. Chem.* **2009**, *74*, 1114-1123.

22. Hunter, E. P.; Lias, S. G., Proton Affinity Evaluation. In *NIST Chemistry WebBook, NIST Standard Reference Database*; Linstrom, P. J., Mallard, W. G., Eds.; National Institute of Standards and Technology: Gaithersburg, MD, 2005 (http://webbook.nist.gov)

23. Habicht, S.C., Duan, P., Vinueza, N.R., Fu, M. and Kenttämaa, H.I., Liquid chromatography/tandem mass spectrometry utilizing ion-molecule reactions and collision-activated dissociation for the identification of N-oxide drug metabolites. *J. Pharm. Biomed.* **2010**, *51*, 805-811.

24. Kong, J.Y., Hilger, R.T., Jin, C., Yerabolu, R., Zimmerman, J.R., Replogle, R.W., Jarrell, T.M., Easterling, L., Kumar, R. and Kenttämaa, H.I., Integration of a Multichannel Pulsed-Valve Inlet System to a Linear Quadrupole Ion Trap Mass Spectrometer for the Rapid Consecutive Introduction of Nine Reagents for Diagnostic Ion/Molecule Reactions. *Anal. Chem.* **2019**. *91*, 15652-15660.

25. Christian, A.H., Jia, S., Cao, W., Zhang, P., Meza, A.T., Sigman, M.S., Chang, C.J. and Toste, F.D., A physical organic approach to tuning reagents for selective and stable methionine bioconjugation. *J. Am. Chem. Soc.* **2019**. 141(32), 12657-12662.

26. Nishikata, T., Abela, A.R., Huang, S. and Lipshutz, B.H., Cationic Pd (II)-catalyzed C–H activation/cross-coupling reactions at room temperature: synthetic and mechanistic studies. *Beilstein J. Org. Chem.* **2016**. 12(1), 1040-1064.

27. Frisch, M. J.; Trucks, G. W.; Schlegel, H. B.; Scuseria, G. E.; Robb, M. A.; Cheeseman, J. R.; Scalmani, G.; Barone, V.; Petersson, G. A.; Nakatsuji, H.; Li, X.; Caricato, M.; Marenich, A. V.; Bloino, J.; Janesko, B. G.; Gomperts, R.; Mennucci, B.; Hratchian, H. P.; Ortiz, J. V.; Izmaylov, A. F.; Sonnenberg, J. L.; Williams-Young, D.; Ding, F.; Lipparini, F.; Egidi, F.; Goings, J.; Peng, B.; Petrone, A.; Henderson, T.; Ranasinghe, D.; Zakrzewski, V. G.; Gao, J.; Rega, N.; Zheng, G.; Liang, W.; Hada, M.; Ehara, M.; Toyota, K.; Fukuda, R.; Hasegawa, J.; Ishida, M.; Nakajima, T.; Honda, Y.; Kitao, O.; Nakai, H.; Vreven, T.; Throssell, K.; Montgomery, J. A., Jr.; Peralta, J. E.; Ogliaro, F.; Bearpark, M. J.; Heyd, J. J.; Brothers, E. N.; Kudin, K. N.; Staroverov, V. N.; Keith, T. A.; Kobayashi, R.; Normand, J.; Raghavachari, K.; Rendell, A. P.; Burant, J. C.; Iyengar, S. S.; Tomasi, J.; Cossi, M.; Millam, J. M.; Klene, M.; Adamo, C.; Cammi, R.; Ochterski, J. W.; Martin, R. L.; Morokuma, K.; Farkas, O.; Foresman, J. B.; Fox, D. J., *Gaussian 16, Revision B.01*. Gaussian, Inc., Wallingford CT, 2016.

CHAPTER 5. DIFFERENTIATION OF SULFONATE ESTERS FROM ISOMERIC SULFITE ESTERS AND SULFONES BY USING DIAGNOSTIC GAS-PHASE ION-MOLECULE REACTIONS FOLLOWED BY COLLISION-ACTIVATED DISSOCIATION IN TANDEM MASS SPECTROMETRY EXPERIMENTS

5.1 Introduction

In the process of drug synthesis, sulfonate esters, especially alkyl sulfonates, are among the major alkylating agents used and often remain in the final drug products.[1,2] Further, sulfonate esters tend to be generated as impurities from the sulfonic salts of active pharmaceutical ingredients.[3] For instance, sulfonate esters can be produced upon esterification of the sulfonic acids by alcohol solvents that are used to facilitate the recrystallization of the sulfonic salts.[4] Unfortunately, acyclic sulfonate esters[5,6] and cyclic sulfonate esters[7,8] (known as sultones) have been conclusively reported to be a genotoxic impurities (GTI). Indeed, ethyl methanesulfonate, as a GTI, has been discovered as a contaminant in Viracept (nelfinavir mesilate) tablets, which has led to the withdrawal of the drug from the market.[5,6] European Medicines Agency declared the maximum intake of ethyl methane sulfonate for human is 2 μg/g/day.[5,6] Furthermore, in order to control the concentration levels of sulfonate esters as a category of compounds, threshold of toxicological concern has also been set by European Medicines Agency as 1.5 μg/g/day in drug products.[1,9-11] Therefore, it is of critical importance to be able to identify sulfonate esters at relatively low concentrations and to differentiate them from other similar compounds potentially present in drug products.

A limited number of analytical methods have been published for the detection and identification of sulfonate esters.[12-14] Additionally, no methods have been reported for the differentiation of sulfonate esters from isomeric compounds, such as sulfite esters[15] and sulfones.[16] Most of these compounds are inactive drug ingredients with limited safety concerns.[17-20] Therefore, the ability to differentiate mutagenic sulfonate esters from their safe isomers, sulfite esters and sulfones, is important.

Tandem mass spectrometry experiments based on functional-group selective ion-molecule reactions have been successfully employed for the identification of different functionalities in many protonated or deprotonated compounds.[21-30] Here, gas-phase ion-molecule reactions coupled

with diagnostic collision-activated dissociation (CAD) of a specific ion-molecule reaction product ion in a linear quadrupole ion trap mass spectrometer is introduced for the identification of protonated sulfonate esters, and for the differentiation of these compounds from isomeric protonated compounds, such as protonated sulfones and sulfite esters. Organoboron reagents have been utilized to react with many oxygen-containing functionalities in gas phase in order to identify these funtionalities.[21-25] These reactions are usually initiated by proton transfer from the protonated analyte to the organoboron reagent.[21-24] Therefore, the proton affinity (PA) of reagent must be slightly higher than that of the analyte. Otherwise, no reaction will occur (if the reagent has a too low PA) or only proton transfer will be observed (if the reagent has a too high PA). Proton affinities of the sulfonate esters, sulfite esters and sulfones were calculated to be ranging from 187 – 205 kcal mol^{-1} (Figure 5.1, calculated at B3LYP/6-311++G(d,p) level of theory). However, existing reagents have either too high proton affinity (TDMAB,[21,22] PA = 230 kcal mol^{-1}) or too low proton affinity (TMB,[23] PA = 195 kcal mol^{-1}; DEMB,[24] PA = 191 kcal mol^{-1}. Therefore, a new reagent, diisopropoxymethylborane (DIMB), is introduced here, whose proton affinity is 208.5 kcal mol^{-1} (calculated at B3LYP/6-311++G(d,p) level of theory). In this study, DIMB is utilized to react with the analytes to generate ion-molecule reaction product ions, whose fragmentation will produce diagnostic fragment ions. Quantum chemical calculations were employed to explore the mechanisms of the formation of the product ions of interest as well as the diagnostic fragmentations. High-performance liquid chromatography (HPLC) was successfully coupled with the mass spectrometry method for the characterization of compounds in mixtures at relatively low concentrations (3-50 μM).

Figure 5.1. Structures of sulfite ester, sulfonate ester and sulfone model compounds used to demonstrate the applicability of this method and their names, purchase sources, purities and calculated proton affinities (calculated at B3LYP/6-311++G(d,p) level of theory).

Sulfite esters

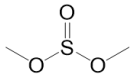

Dimethyl sulfite
Purchased from Aablocks
Purity > 99%
PA = 198.0 kcal mol^{-1}

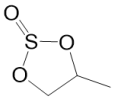

1,2-Propyleneglycol sulfite
Purchased from Sigma-Aldrich
Purity ≥ 98%
PA = 192.4 kcal mol^{-1}

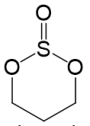

1,3-Propyleneglycol sulfite
Purchased from 1Click Chemistry
Purity 98%
PA = 196.3 kcal mol^{-1}

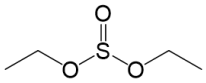

Diethyl sulfite
Purchased from Aablocks
Purity > 98%
PA = 203.2 kcal mol^{-1}

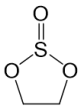

Ethylene sulfite
Purchased from Sigma-Aldrich
Purity 98%
PA = 188.7 kcal mol^{-1}

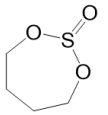

1,4-Butyleneglycol sulfite
Synthesized
PA = 201.2 kcal mol^{-1}

Sulfonate esters

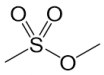

Methyl methanesulfonate
Purchased from Sigma-Aldrich
Purity 99%
PA = 187.7 kcal mol^{-1}

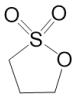

1,3-Propanesultone
Purchased from Sigma-Aldrich
Purity ≥ 99%
PA = 190.8 kcal mol^{-1}

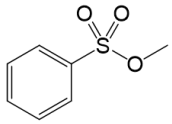

Methyl benzenesulfonate
Purchased from TCI America
Purity ≥ 98%
PA = 197.4 kcal mol^{-1}

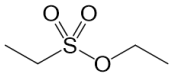

Ethyl ethanesulfonate
Purchased from Sigma-Aldrich
Purity TraceCERT® grade
PA = 196.6 kcal mol^{-1}

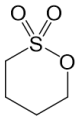

1,4-Butanesultone
Purchased from Sigma-Aldrich
Purity ≥ 99%
PA = 193.3 kcal mol^{-1}

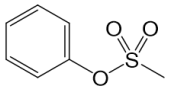

Phenyl methanesulfonate
Purchased from Aablocks
Purity 99%
PA = 192.2 kcal mol^{-1}

Sulfones

Dimethyl sulfone
Purchased from Sigma-Aldrich
Purity 98%
PA = 195.2 kcal mol^{-1}

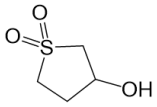

Tetrahydrothiophene-3-ol 1,1-dioxide
Purchased from 1Click Chemistry
Purity 95%
PA = 199.8 kcal mol^{-1}

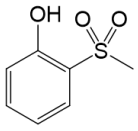

2-(Methylsulfonyl)phenol
Purchased from Aablocks
Purity 98%
PA = 194.6 kcal mol^{-1}

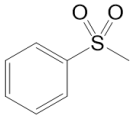

Methyl phenyl sulfone
Purchased from Aablocks
Purity 98%
PA = 204.2 kcal mol^{-1}

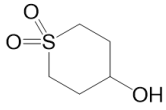

4-Hydroxytetrahydro-2H-thiopyran
1,1-dioxide
Purchased from 1Click Chemistry
Purity 98%
PA = 202.7 kcal mol^{-1}

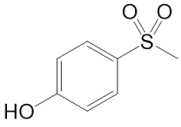

4-(Methylsulfonyl)phenol
Purchased from Alfa Aesar
Purity 97%
PA = 204.9 kcal mol^{-1}

5.2 Experimental section

5.2.1 Chemicals

Diisopropoxymethylborane (DIMB, 97% purity) was purchased from Sigma-Aldrich and used without purification. Six sulfonate esters, six sulfite esters and six sulfones as shown in Figure 5.1 were used as model compounds. All of the model compounds were obtained commercially and used as received (with the exception of 1,4-butylene sulfite). Their structures, names, purities and commercial sources are listed in the Figure 5.1. 1,4-Butylene sulfite, on the other hand, was synthesized using previously published procedures.[31] This is a reported compound, and its NMR spectrum matched the published one. Water (LC/MS grade, ≥99.9%) and methanol (LC/MS grade, ≥99.9%) were purchased from Fisher Scientific.

Stock solutions of all model compounds were prepared at a concentration of 10 mM in methanol.

5.2.2 Instrumentation

Gas-phase ion-molecule reactions were studied using a Thermo LTQ linear quadrupole ion trap mass spectrometer coupled with the traditional reagent mixing manifold that is discussed in Section 2.5.1. The analytes in these solutions were ionized via atmospheric pressure chemical ionization (APCI) operated in positive ion mode. The ionization conditions were as follows: 4.2 μA discharge current, 20 (arbitrary units) sheath gas (N_2) flow rate, 10 (arbitrary units) auxiliary gas (N_2) flow rate, 300 ˚C vaporizer temperature, 275 ˚C capillary temperature, 10 V capillary voltage, and 70 V tube lens voltage. After protonation of the analytes, the ions were transferred into the ion trap.

At the same time, DIMB was injected into the manifold via a syringe pump at a flow rate of 5 μL h^{-1}, vaporized, diluted with helium, and introduced into the ion trap. The pressure in the ion trap was adjusted by the leak valve until the ion gauge reading was 0.7 - 0.8 × 10^{-5} torr. The protonated analytes were allowed to react with DIMB in the ion trap for 30 ms. The reproducibility of the relative abundances of the ion-molecule reaction product ions was ± 30%.

The product ions $[M + H + TDMAB – CH_3CH(OH)CH_3]^+$ formed upon reactions of the analyte ions with DIMB were isolated and subjected to CAD to obtain structural information. In the CAD experiments, the advanced scan features of the LTQ Tune Plus interface were used to

isolate the ions by using a *m/z* window of 2 units. At a *q* value of 0.25, the ions were subjected to CAD (collision energy 30 arbitrary units) for 30 ms by using helium as the collision gas. The reproducibility of the relative abundances of the fragment ions was ± 20%.

The detection mass range was from m/z 50 up to 500. All mass spectra acquired were an average of at least 20 individual mass spectra. Xcalibur 2.0 software was used for processing of all the data.

5.2.3 HPLC/MS^3 conditions

The samples were injected via an autosampler with full-loop injection (25 μL). HPLC separation was performed using an Agilent Zorbax SB-C18 column (4.6 × 250 mm, 5 μm particle size) in a Thermo Scientific Surveyor HPLC system. The flow rate was 0.5 mL min^{-1}. Gradient elution involved mobile phase A containing 0.1% formic acid in water and mobile phase B containing 0.1% formic acid in methanol. The percentage of B in the mobile phase was increased linearly from 15% to 85% within 15 min. The HPLC system was coupled to the Thermo LTQ Linear Quadrupole ion trap (LQIT) mass spectrometer described above.

5.2.4 Computational methods

All calculations were performed using the Gaussian 16 program.[32] The molecular structures were optimized and their energies were calculated at the M06-2X/6-311++G(d,p) level of theory. The geometries were verified to be local minima by computation of analytic vibrational frequencies. These (unscaled) frequencies were used to compute zero-point vibrational energies (ZPVE) and 298 K thermal contributions ($H_{298} - E_0$). All transition state structures were determined to contain exactly one negative frequency. Intrinsic reaction coordinate (IRC) calculations were performed for all transition states to ensure that the optimized transition state structure connected the correct reactants and products.

5.3 Results and discussion

The results obtained upon examination of the gas-phase ion-molecule reactions of protonated sulfite esters, sulfonate esters and sulfones with DIMB are discussed first, followed by the computational results obtained to explore the ion-molecule reaction mechanisms. After this,

CAD of selected product ions generated in the ion-molecule reactions is discussed, followed by the examination of their fragmentation mechanisms by quantum chemical calculations. Further, results obtained in studies of additional protonated analytes with other functionalities are described. Finally, HPLC/MS^4 experiments and detection limits are addressed.

5.3.1 Reactions of protonated sulfite esters, sulfonate esters and sulfones with DIMB

Six sulfite esters, six sulfonate esters and six sulfones (Figure 5.1) were protonated via APCI, transferred into the linear quadrupole ion trap, isolated, and allowed to react with DIMB for 30 ms. All ions reacted with DIMB to form an adduct ion that had lost an isopropanol molecule, $[M + H + DIMB - CH_3CH(OH)CH_3]^+$ (M = analyte) (Tables 5.1-5.3). Mass spectra measured for the reactions of protonated dimethyl sulfite, methyl methanesulfonate and dimethyl sulfone are shown in Figure 5.2 as examples of the data measured for protonated sulfite esters, sulfonate esters and sulfones.

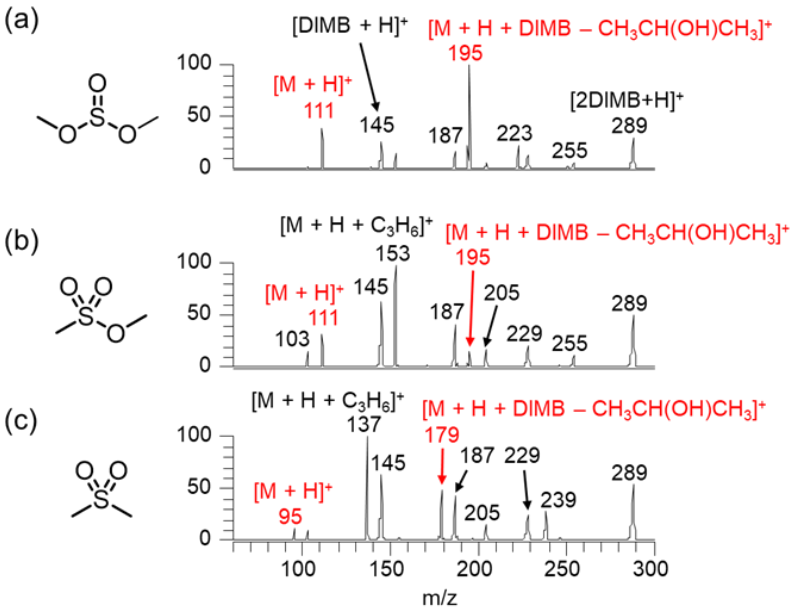

Figure 5.2. (a) MS^2 spectrum measured after 30 ms reactions of protonated dimethylsulfite ($[M + H]^+$; *m/z* 111) with DIMB, showing the $[M + H + DIMB – CH_3CH(OH)CH_3]^+$ product ions (*m/z* 195). (b) MS^2 spectrum measured after 30 ms reactions of protonated methyl methanesulfonate ($[M + H]^+$; m/z 111) with DIMB, showing the $[M + H + DIMB – CH_3CH(OH)CH_3]^+$ product ions (*m/z* 195). (c) MS^2 spectrum measured after 30 ms reactions of protonated dimethylsulfone ($[M + H]^+$; *m/z* 95) with DIMB, showing the $[M + H + DIMB – CH_3CH(OH)CH_3]^+$ product ions (*m/z* 179). The ions of *m/z* 145 correspond to protonated DIMB. The ions of *m/z* 103 correspond to $[DIMB + H – CH_2{=}CHCH_3]^+$. The ions of *m/z* 187 and *m/z* 205 correspond to $CH_2{=}CHCH_3$ adducts and $CH_3CH(OH)CH_3$ adducts of the ions of *m/z* 145, respectively. The ions of *m/z* 229 correspond to $[2\ DIMB + H – CH_3CH(OH)CH_3]^+$. In (a) and (b), ions of *m/z* 223 and *m/z* 255 correspond to $[2\ M + H]^+$ and $[M + H + DIMB]^+$, respectively. In (c), ions of *m/z* 239 correspond to $[M + H + DIMB]^+$.

Table 5.1. Product ions, with their relative abundances,[a] detected after 30 ms reactions of six protonated sulfite esters (M) with DIMB. The product ions **[M + H + DIMB – $CH_3CH(OH)CH_3$]$^+$**, which were subjected to CAD experiments, are shown in red.

Analyte (m/z of $[M + H]^+$)	Ion-molecule Reaction Product Ions (m/z)	Relative Abundance
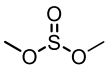 (111)	$[DIMB + H - CH_3\text{-}CH{=}CH_2]^+$ (103)	4%
	$[DIMB + H]^+$ (145)	42%
	$[M + H + CH_3\text{-}CH{=}CH_2]^+$ (153)	29%
	$[DIMB + H + CH_3\text{-}CH{=}CH_2]^+$ (187)	27%
	$[M + H + DIMB - CH_3CH(OH)CH_3]^+$ (195)	**100%**
	$[DIMB + H + CH_3CH(OH)CH_3]^+$ (205)	10%
	$[2\ M + H]^+$ (223)	36%
	$[2\ DIMB + H - CH_3CH(OH)CH_3]^+$ (229)	15%
	$[M + H + DIMB]^+$ (255)	10%
	$[2\ DIMB + H]^+$ (289)	30%
 (109)	$[DIMB + H - CH_3\text{-}CH{=}CH_2]^+$ (103)	16%
	$[DIMB + H]^+$ (145)	47%
	$[M + H + CH_3\text{-}CH{=}CH_2]^+$ (151)	100%
	$[DIMB + H + CH_3\text{-}CH{=}CH_2]^+$ (187)	28%
	$[M + H + DIMB - CH_3CH(OH)CH_3]^+$ (193)	**12%**
	$[DIMB + H + CH_3CH(OH)CH_3]^+$ (205)	12%
	$[2\ DIMB + H - CH_3CH(OH)CH_3]^+$ (229)	16%
	$[M + H + DIMB]^+$ (253)	6%
	$[2\ DIMB + H]^+$ (289)	31%
 (123)	$[DIMB + H]^+$ (145)	49%
	$[M + H + CH_3\text{-}CH{=}CH_2]^+$ (165)	55%
	$[DIMB + H + CH_3\text{-}CH{=}CH_2]^+$ (187)	15%
	$[M + H + DIMB - CH_3CH(OH)CH_3]^+$ (207)	**100%**
	$[2\ DIMB + H - CH_3CH(OH)CH_3]^+$ (229)	13%
	$[M + H + DIMB]^+$ (267)	12%
	$[2\ DIMB + H]^+$ (289)	22%
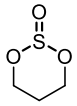 (123)	$[DIMB + H]^+$ (145)	16%
	$[M + H + CH_3\text{-}CH{=}CH_2]^+$ (165)	27%
	$[DIMB + H + CH_3\text{-}CH{=}CH_2]^+$ (187)	9%
	$[M + H + DIMB - CH_3CH(OH)CH_3]^+$ (207)	**100%**
	$[2\ DIMB + H - CH_3CH(OH)CH_3]^+$ (229)	5%
	$[M + H + DIMB]^+$ (267)	6%
	$[2\ DIMB + H]^+$ (289)	11%
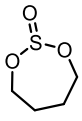 (137)	$[M + H + CH_3\text{-}CH{=}CH_2]^+$ (179)	13%
	$[M + H + DIMB - CH_3CH(OH)CH_3]^+$ (221)	**100%**
	$[M + H + DIMB]^+$ (281)	9%
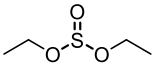 (139)	$[M + H + DIMB - CH_3CH(OH)CH_3 - CH_3B{=}O]^+$ (181)	12%
	$[M + H + DIMB - CH_3CH(OH)CH_3]^+$ (223)	**100%**

[a] *Reproducibility ± 30%.*

Table 5.2. Product ions, with their relative abundances,[a] detected after 30 ms reactions of six protonated sulfonate esters (M) with DIMB. The product ions **[M + H + DIMB – $CH_3CH(OH)CH_3$]$^+$**, which were subjected to CAD experiments, are shown in red.

Analyte (m/z of $[M + H]^+$)	Ion-molecule Reaction Product Ions (m/z)	Relative Abundance
 (111)	$[DIMB + H - CH_3\text{-}CH{=}CH_2]^+$ (103)	12%
	$[DIMB + H]^+$ (145)	58%
	$[M + H + CH_3\text{-}CH{=}CH_2]^+$ (153)	100%
	$[DIMB + H + CH_3\text{-}CH{=}CH_2]^+$ (187)	34%
	$[M + H + DIMB - CH_3CH(OH)CH_3]^+$ (195)	**7%**
	$[DIMB + H + CH_3CH(OH)CH_3]^+$ (205)	17%
	$[2\ DIMB + H - CH_3CH(OH)CH_3]^+$ (229)	21%
	$[M + H + DIMB]^+$ (255)	11%
	$[2\ DIMB + H]^+$ (289)	44%
 (123)	$[DIMB + H - CH_3\text{-}CH{=}CH_2]^+$ (103)	19%
	$[DIMB + H]^+$ (145)	58%
	$[M + H + CH_3\text{-}CH{=}CH_2]^+$ (165)	100%
	$[DIMB + H + CH_3\text{-}CH{=}CH_2]^+$ (187)	15%
	$[M + H + DIMB - CH_3CH(OH)CH_3]^+$ (207)	**4%**
	$[2\ DIMB + H - CH_3CH(OH)CH_3]^+$ (229)	8%
	$[M + H + DIMB]^+$ (267)	15%
	$[2\ DIMB + H]^+$ (289)	16%
 (137)	$[DIMB + H]^+$ (145)	26%
	$[M + H + CH_3\text{-}CH{=}CH_2]^+$ (179)	100%
	$[DIMB + H + CH_3\text{-}CH{=}CH_2]^+$ (187)	20%
	$[M + H + DIMB - CH_3CH(OH)CH_3]^+$ (221)	**14%**
	$[2\ DIMB + H]^+$ (289)	31%
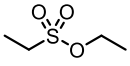 (139)	**$[M + H + DIMB - CH_3CH(OH)CH_3]^+$ (223)**	**82%**
	$[M + H + DIMB - CH_3\text{-}CH{=}CH_2]^+$ (241)	53%
	$[M + H + DIMB]^+$ (283)	100%
	$[DIMB + H]^+$ (145)	29%
	$[DIMB + H + CH_3\text{-}CH{=}CH_2]^+$ (187)	12%
	$[DIMB + H + CH_3CH(OH)CH_3]^+$ (205)	7%
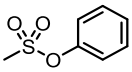 (173)	$[M + H + CH_3\text{-}CH{=}CH_2]^+$ (215)	100%
	$[2\ DIMB + H - CH_3CH(OH)CH_3]^+$ (229)	7%
	$[M + H + DIMB - CH_3CH(OH)CH_3]^+$ (257)	**32%**
	$[2\ DIMB + H]^+$ (289)	16%
	$[M + H + DIMB]^+$ (317)	17%
	$[DIMB + H]^+$ (145)	30%
	$[DIMB + H + CH_3\text{-}CH{=}CH_2]^+$ (187)	20%
	$[M + H + CH_3\text{-}CH{=}CH_2]^+$ (215)	100%
	$[M + H + CH_3CH(OH)CH_3]^+$ (233)	2%
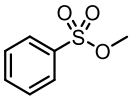 (173)	**$[M + H + DIMB - CH_3CH(OH)CH_3]^+$ (257)**	**37%**
	$[M + H + CH_3CH(OH)CH_3 + CH_3\text{-}CH{=}CH_2]^+$ (275)	4%
	$[2\ DIMB + H]^+$ (289)	31%
	$[M + H + DIMB]^+$ (317)	24%

[a]*Reproducibility ± 30%.*

Table 5.3. Product ions, with their relative abundances,[a] detected after 30 ms reactions of six protonated sulfones (M) with DIMB. The product ions **[M + H + DIMB – $CH_3CH(OH)CH_3$]$^+$**, which were subjected to CAD experiments, are shown in red.

Analyte (m/z of $[M + H]^+$)	Ion-molecule Reaction Product Ions (m/z)	Relative Abundance
 (95)	$[DIMB + H - CH_3\text{-}CH{=}CH_2]^+$ (103)	13%
	$[M + H + CH_3\text{-}CH{=}CH_2]^+$ (137)	100%
	$[DIMB + H]^+$ (145)	61%
	$[M + H + DIMB - CH_3CH(OH)CH_3]^+$ (179)	**40%**
	$[DIMB + H + CH_3\text{-}CH{=}CH_2]^+$ (187)	27%
	$[DIMB + H + CH_3CH(OH)CH_3]^+$ (205)	12%
	$[2\ DIMB + H - CH_3CH(OH)CH_3]^+$ (229)	15%
	$[M + H + DIMB]^+$ (239)	24%
	$[2\ DIMB + H]^+$ (289)	32%
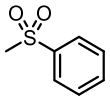 (157)	$[DIMB + H]^+$ (145)	5%
	$[DIMB + H + CH_3\text{-}CH{=}CH_2]^+$ (187)	5%
	$[M + H + CH_3\text{-}CH{=}CH_2]^+$ (199)	29%
	$[M + H + DIMB - CH_3CH(OH)CH_3]^+$ (241)	**100%**
	$[2\ DIMB + H]^+$ (289)	3%
	$[M + H + DIMB]^+$ (301)	28%
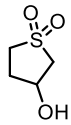 (137)	$[DIMB + H]^+$ (145)	31%
	$[M + H + DIMB - 2\ CH_3CH(OH)CH_3]^+$ (161)	45%
	$[M + H + CH_3\text{-}CH{=}CH_2]^+$ (179)	67%
	$[DIMB + H + CH_3\text{-}CH{=}CH_2]^+$ (187)	14%
	$[M + H + DIMB - CH_3CH(OH)CH_3]^+$ (221)	**100%**
	$[2\ DIMB + H - CH_3CH(OH)CH_3]^+$ (229)	11%
	$[M + H + DIMB - CH_3CH(OH)CH_3 + CH_3\text{-}CH{=}CH_2]^+$ (263)	10%
	$[M + H + DIMB]^+$ (281)	45%
	$[2\ DIMB + H]^+$ (289)	21%
	$[M + H + 2\ DIMB - 2\ CH_3CH(OH)CH_3]^+$ (305)	41%
	$[M + H + 2\ DIMB - CH_3CH(OH)CH_3]^+$ (365)	8%
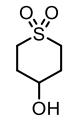 (151)	$[M + H + DIMB - 2\ CH_3CH(OH)CH_3]^+$ (175)	7%
	$[M + H + CH_3\text{-}CH{=}CH_2]^+$ (193)	22%
	$[M + H + DIMB - CH_3CH(OH)CH_3]^+$ (235)	**100%**
	$[M + H + DIMB]^+$ (295)	23%
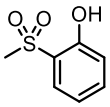 (173)	$[DIMB + H]^+$ (145)	32%
	$[DIMB + H + CH_3\text{-}CH{=}CH_2]^+$ (187)	9%
	$[M + H + DIMB - 2\ CH_3CH(OH)CH_3]^+$ (197)	100%
	$[M + H + CH_3\text{-}CH{=}CH_2]^+$ (215)	23%
	$[2\ DIMB + H - CH_3CH(OH)CH_3]^+$ (229)	10%
	$[M + H + DIMB - CH_3CH(OH)CH_3]^+$ (257)	**48%**
	$[2\ DIMB + H]^+$ (289)	20%
	$[M + H + DIMB]^+$ (317)	16%
	$[M + H + 2\ DIMB - 2\ CH_3CH(OH)CH_3]^+$ (341)	9%
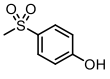 (173)	$[M + H + CH_3\text{-}CH{=}CH_2]^+$ (215)	14%
	$[M + H + DIMB - CH_3CH(OH)CH_3]^+$ (257)	**100%**
	$[M + H + DIMB]^+$ (317)	22%

[a]*Reproducibility ± 30%.*

In order to explore the mechanism(s) leading to the formation of the product ion [M + H + DIMB – $CH_3CH(OH)CH_3$]$^+$, the potential energy surfaces were calculated (M06-2X/6-311++G(d,p) level of theory) for the reactions of protonated methyl methanesulfonate, dimethyl sulfite and dimethyl sulfone with DIMB (Figure 5.3). As shown in Figure 5.3a (protonated methyl methanesulfonate as an example), the reaction is initiated by proton transfer from the protonated sulfonate ester to DIMB, followed by addition of an oxygen atom of neutral methanesulfonate to the boron atom of protonated DIMB. The adduct ion undergoes elimination of $CH_3CH(OH)CH_3$ in a reaction that is overall exothermic (-17.8 kcal mol^{-1}). The potential energy surfaces calculated for protonated dimethyl sulfite and protonated dimethyl sulfone are similar and also these reactions are exothermic (-11.7 kcal mol^{-1} for dimethyl sulfite, Figure 5.3b; -16.2 kcal mol^{-1} for dimethyl sulfone, Figure 5.3c).

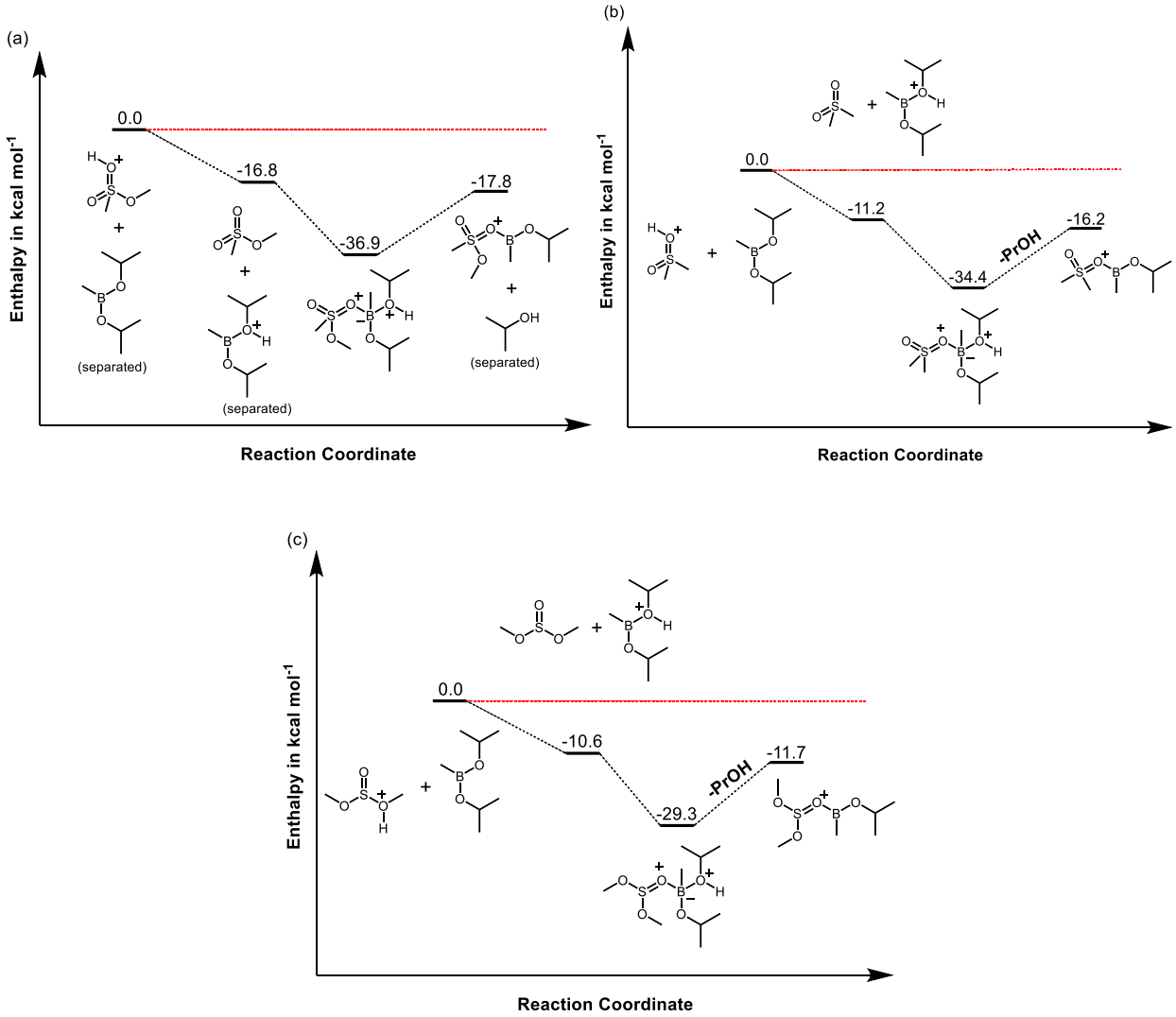

Figure 5.3. Potential energy surface calculated at the M06-2X/6-311++G(d,p) level of theory for the formation of the ion-molecule reaction product ions $[M + H + DIMB - CH_3CH(OH)CH_3]^+$ upon reactions with DIMB of (a) protonated methyl methanesulfonate, (b) protonated dimethyl sulfite, and (c) protonated dimethyl sulfone.

5.3.2 CAD of the product ions $[M + H + DIMB - CH_3CH(OH)CH_3]^+$

Since the product ions $[M + H + DIMB - CH_3CH(OH)CH_3]^+$ (M = analyte) were generated in the reactions of protonated sulfite esters, sulfonate esters and sulfones, these product ions were subjected to CAD to explore the possibly of diagnostic fragmentation patterns (Tables 5.4-5.6).

Table 5.4. All ions observed upon CAD of the ion-molecule reaction product ions [M + H + DIMB – $CH_3CH(OH)CH_3$]$^+$ for all six tested protonated sulfite esters, with their relative abundances.[a] The neutral fragments **SO_2** are diagnostic for sulfite esters and are indicated in red color. The neutral fragments **$CH_3B{=}O + (CH_3)_2C{=}O$** are diagnostic for sulfonate esters and are indicated in blue color.

Analyte (m/z of [M + H]$^+$)	Neutral fragments (m/z ratio of the ionic fragment) or ions observed (m/z) upon CAD of [M + H + DIMB – $CH_3CH(OH)CH_3$]$^+$	Relative Abundance
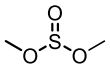 (111)	**– SO_2 (131)**	**12%**
	– SO_2 – CH_3-CH=CH_2 (89)	34%
	– SO_2 – MeOH – CH_3-CH=CH_2 + $CH_3CH(OH)CH_3$ (117)	16%
	– SO_2 – MeOH + $CH_3CH(OH)CH_3$ (159)	9%
	– $CH_3B{=}O$ (153)	14%
	[DIMB + H – CH_3-CH=CH_2]$^+$ (103)	12%
	[DIMB + H]$^+$ (145)	100%
	[DIMB + H + CH_3-CH=CH_2]$^+$ (187)	32%
	[DIMB + H + $CH_3CH(OH)CH_3$]$^+$ (205)	13%
	[2 DIMB + H – $CH_3CH(OH)CH_3$]$^+$ (229)	21%
	[2 DIMB + H]$^+$ (289)	40%
	+ CH_3-CH=CH_2 (237)	59%
	– SO_2 (129)	**100%**
	– SO_2 – CH_3-CH=CH_2 (87)	37%
	– $CH_3B{=}O$ (151)	27%
	– $CH_3B{=}O$ – $(CH_3)_2C{=}O$ (93)	**24%**
 (109)	– $CH_3B{=}O$ – CH_3-CH=CH_2 + SO_2 (173)	13%
	– $CH_3B{=}O$ + SO_2 (215)	13%
	[DIMB + H]$^+$ (145)	57%
	[DIMB + H + CH_3-CH=CH_2]$^+$ (187)	39%
	[DIMB + H – CH_3-CH=CH_2]$^+$ (103)	17%
	[DIMB + H + $CH_3CH(OH)CH_3$]$^+$ (205)	9%
	[2 DIMB + H – $CH_3CH(OH)CH_3$]$^+$ (229)	14%
	[2 DIMB + H]$^+$ (289)	21%
	– SO_2 (143)	**100%**
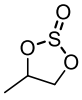 (123)	– SO_2 – CH_3-CH=CH_2 (101)	33%
	– $CH_3B{=}O$ (165)	13%
	[DIMB + H]$^+$ (145)	49%
	[DIMB + H + CH_3-CH=CH_2]$^+$ (187)	56%
	[2 DIMB + H – $CH_3CH(OH)CH_3$]$^+$ (229)	22%
	[2 DIMB + H]$^+$ (289)	20%

(Table 5.4 continued)

	– SO_2 (143)	**100%**
	– SO_2 – CH_3-CH=CH_2 (101)	24%
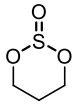	– SO_2 – CH_2=CH_2 (115)	23%
	[DIMB + H]$^+$ (145)	46%
	[DIMB + H – CH_3-CH=CH_2]$^+$ (103)	13%
(123)	[DIMB + H + CH_3-CH=CH_2]$^+$ (187)	44%
	[2 DIMB + H – $CH_3CH(OH)CH_3$]$^+$ (229)	14%
	[2 DIMB + H]$^+$ (289)	16%
	– SO_2 (157)	**100%**
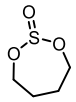	– SO_2 – CH_3-CH=CH_2 (115)	4%
	[DIMB + H]$^+$ (145)	6%
(137)	[DIMB + H + CH_3-CH=CH_2]$^+$ (187)	7%
	– CH_3B=O (181)	11%
	– CH_3B=O – $(CH_3)_2C$=O (123)	**32%**
	– CH_3B=O – CH_3-CH=CH_2 (139)	12%
	– SO_2 (159)	**100%**
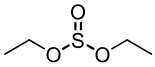	– SO_2 – EtOH + $CH_3CH(OH)CH_3$ (173)	8%
	– SO_2 – CH_3-CH=CH_2 (117)	20%
(139)	+ CH_3-CH=CH_2 (265)	21%
	[DIMB + H]$^+$ (145)	46%
	[DIMB + H + CH_3-CH=CH_2]$^+$ (187)	13%
	[2 DIMB + H –$CH_3CH(OH)CH_3$]$^+$ (229)	8%
	[2 DIMB + H]$^+$ (289)	16%

[a]*Reproducibility ± 20%.*

Table 5.5. All ions observed upon CAD of the ion-molecule reaction product ions [M + H + DIMB – $CH_3CH(OH)CH_3$]$^+$ (MS^3 experiments) for all tested protonated sulfite esters, with their relative abundances.[a] The neutral fragments **CH_3B=O + $(CH_3)_2C$=O** are diagnostic for sulfonate esters and are indicated in blue color.

Analyte (*m/z* of [M + H]$^+$)	Neutral fragments (m/z value of the ionic fragment) or ions observed (m/z) upon CAD of [M + H + DIMB – $CH_3CH(OH)CH_3$]$^+$	Relative Abundance
	– CH_3B=O (153)	100%
	– CH_3B=O – $(CH_3)_2C$=O (95)	**46%**
	– CH_3B=O – CH_3-CH=CH_2 (111)	26%
	+ CH_3-CH=CH_2 (237)	5%
(111)	[DIMB + H]$^+$ (145)	10%
	[DIMB + H + CH_3-CH=CH_2]$^+$ (187)	7%
	– CH_3B=O (165)	100%
	**– CH_3B=O – $(CH_3)_2C$=O (107)**	**24%**
	– CH_3B=O – CH_3-CH=CH_2 (123)	9%
(123)	[DIMB + H + CH_3-CH=CH_2]$^+$ (187)	10%
	[2 DIMB + H]$^+$ (289)	5%

(Table 5.5 continued)

 (137)	– CH_3B=O (179)	100%
	– CH_3B=O – $(CH_3)_2C$=O (121)	**24%**
	– CH_3B=O – CH_3-CH=CH_2 (137)	23%
	– $(CH_3)_2C$=O (163)	2%
	+ CH_3-CH=CH_2 (263)	3%
	[DIMB + H + CH_3-CH=CH_2]$^+$ (187)	6%
	[2 DIMB + H]$^+$ (289)	5%
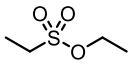 (139)	– CH_3B=O (181)	52%
	– CH_3B=O – $(CH_3)_2C$=O (123)	**66%**
	– CH_3B=O – CH_3-CH=CH_2 (139)	100%
	– $(CH_3)_2C$=O (165)	14%
	– 2 $(CH_3)_2C$=O (107)	6%
	– CH_3B=O (215)	97%
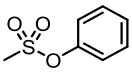 (173)	**– CH_3B=O – $(CH_3)_2C$=O (157)**	**7%**
	– CH_3B=O – CH_3-CH=CH_2 (173)	100%
	– CH_3B=O – CH_3-CH=CH_2 + $CH_3CH(OH)CH_3$ (233)	12%
	+ $CH_3CH(OH)CH_3$ (317)	25%
	[DIMB + H]$^+$ (145)	8%
	[DIMB + H + CH_3-CH=CH_2]$^+$ (187)	5%
	– CH_3B=O (215)	100%
	– CH_3B=O – $(CH_3)_2C$=O (157)	**6%**
	– CH_3B=O – CH_3-CH=CH_2 (173)	37%
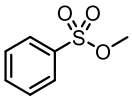 (173)	– CH_3B=O – CH_3-CH=CH_2 + $CH_3CH(OH)CH_3$ (233)	9%
	– CH_3B=O + $CH_3CH(OH)CH_3$ (275)	5%
	+ $CH_3CH(OH)CH_3$ (317)	20%
	+ $CH_3CH(OH)CH_3$ – CH_3OH (285)	7%
	– 2 $(CH_3)_2C$=O (141)	4%
	[DIMB + H]$^+$ (145)	10%
	[DIMB + H + CH_3-CH=CH_2]$^+$ (187)	7%

[a]*Reproducibility ± 20%.*

Table 5.6. All ions observed upon CAD of the ion-molecule reaction product ions [M + H + DIMB – $CH_3CH(OH)CH_3$]$^+$ (MS^3 experiments) for all tested protonated sulfones, with their relative abundances.[a] The neutral fragments **$CH_3CH(OH)CH_3$** are diagnostic for sulfones with a hydroxyl group and are indicated in green color.

Analyte (*m/z* of [M + H]$^+$)	Neutral fragments (m/z value of the ionic fragment) or ions observed (m/z) upon CAD of [M + H + DIMB – $CH_3CH(OH)CH_3$]$^+$	Relative Abundance
 (95)	– CH_3B=O (137)	100%
	+ $CH_3CH(OH)CH_3$ (239)	4%
	[DIMB + H]$^+$ (145)	10%
	[DIMB + H + CH_3-CH=CH_2]$^+$ (187)	10%
	[2 DIMB + H]$^+$ (289)	4%

(Table 5.6 continued)

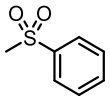 (157)	**– $CH_3CH(OH)CH_3$ (161)**	**100%**
	+ DIMB – $CH_3CH(OH)CH_3$ (305)	12%
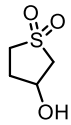 (137)	**– $CH_3CH(OH)CH_3$ (175)**	**100%**
	+ DIMB – $CH_3CH(OH)CH_3$ (319)	6%
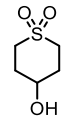 (151)	– $CH_3B{=}O$ (199)	100%
	– $CH_3B{=}O$ – CH_3-$CH{=}CH_2$ (157)	62%
	– $CH_3B{=}O$ – CH_3-$CH{=}CH_2$ + $CH_3CH(OH)CH_3$ (217)	6%
	+ $CH_3CH(OH)CH_3$] (301)	20%
	$[DIMB + H]^+$ (145)	9%
	$[DIMB + H + CH_3\text{-}CH{=}CH_2]^+$ (187)	9%
	$[2\ DIMB + H]^+$ (289)	3%
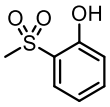 (173)	– $CH_3B{=}O$ (215)	76%
	– $CH_3B{=}O$ – CH_3-$CH{=}CH_2$ (173)	62%
	– $CH_3CH(OH)CH_3$ (197)	**100%**
	+ $CH_3CH(OH)CH_3$ (317)	31%
	$[DIMB + H]^+$ (145)	6%
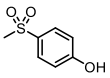 (173)	– $CH_3B{=}O$ (215)	73%
	– $CH_3B{=}O$ – CH_3-$CH{=}CH_2$ (173)	100%
	– $CH_3B{=}O$ – CH_3-$CH{=}CH_2$ + $CH_3CH(OH)CH_3$ (233)	9%
	+ $CH_3CH(OH)CH_3$ (317)	16%
	$[DIMB + H]^+$ (145)	4%
	$[DIMB + H + CH_3\text{-}CH{=}CH_2]^+$ (187)	2%

[a]*Reproducibility ± 20%.*

The ion-molecule reaction product ions $[M + H + DIMB – CH_3CH(OH)CH_3]^+$ of *sulfite esters* underwent a diagnostic elimination of a SO_2 molecule upon CAD (Table 5.4, see the CAD mass spectrum measured for dimethyl sulfite in Figure 5.4a as an example). Quantum chemical calculations (M06-2X/6-311++G(d,p) level of theory) indicate that the isopropoxymethylboryl group is transferred from the sulfinyl oxygen to the ester oxygen of the sulfite (Figure 5.4b). The intermediate will undergo SO_2 elimination via a methyl cation transfer in a transition state whose enthalpy is 53.8 kcal mol^{-1} greater than the enthalpy of the fragmenting ion $[M + H + DIMB – CH_3CH(OH)CH_3]^+$ (Figure 5.4b).

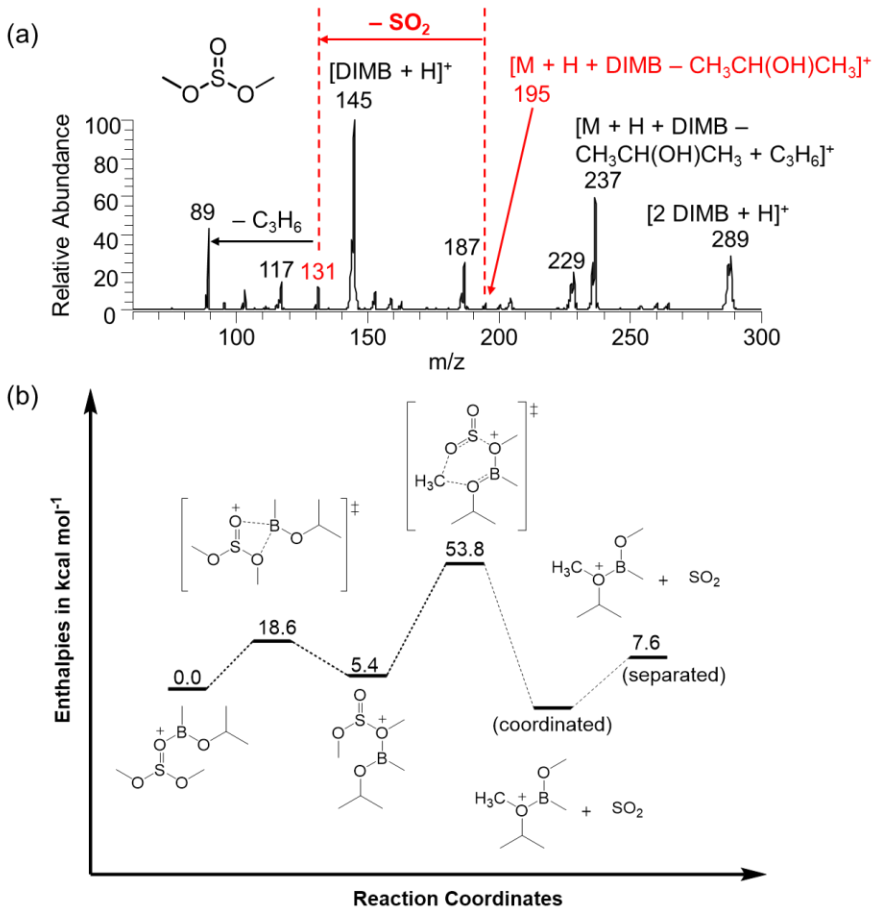

Figure 5.4. (a) CAD MS^3 spectrum measured for the ion-molecule reaction product ions $[M + H + DIMB – CH_3CH(OH)CH_3]^+$ (*m/z* 195) of dimethyl sulfite (M) (collision energy 25 arbitrary units). Two CAD fragment ions were observed. The fragment ions $[M + H + DIMB – CH_3CH(OH)CH_3 – SO_2]^+$ (*m/z* 131) diagnostic for sulfites were observed. These fragment ions fragment further to generate ions of *m/z* 117 ($[M + H + DIMB – SO_2 – MeOH – CH_3\text{-}CH{=}CH_2]^+$). The remaining ions are formed from DIMB: ions of *m/z* 187 correspond to $[DIMB + H + CH_3\text{-}CH{=}CH_2]^+$ and ions of *m/z* 229 correspond to $[2 DIMB + H – CH_3CH(OH)CH_3]^+$. (b) Potential energy surface calculated at the M06-2X/6-311++G(d,p) level of theory for the elimination of SO_2 upon CAD of the ion-molecule reaction product ion $[M + H + DIMB – CH_3CH(OH)CH_3]^+$ of protonated dimethyl sulfite.

Upon CAD of the ion-molecule reaction product ions $[M + H + DIMB – CH_3CH(OH)CH_3]^+$ of *sulfonate esters*, diagnostic elimination of neutral molecules whose added MWs correspond to 100 Da was observed (Table 5.5, see the CAD mass spectrum measured for methyl methanesulfonate in Figure 5.5a as an example). The elimination of neutral molecules whose added MWs correspond to 100 Da loss could correspond to the initial elimination of $CH_3B{=}O$ (MW 42) followed by elimination of $(CH_3)_2C{=}O$ (MW 58) since the fragment ions [M + H +

DIMB – $CH_3CH(OH)CH_3$ – $CH_3B{=}O]^+$ were also observed in the MS^3 spectra for sulfonate esters. On the other hand, the ions [M + H + DIMB – $CH_3CH(OH)CH_3$ – $SO_2]^+$ (*m/z* 131) were not generated (Figure 5.5a). Hence, the sulfite esters could be differentiated from the sulfonate esters based on these observations.

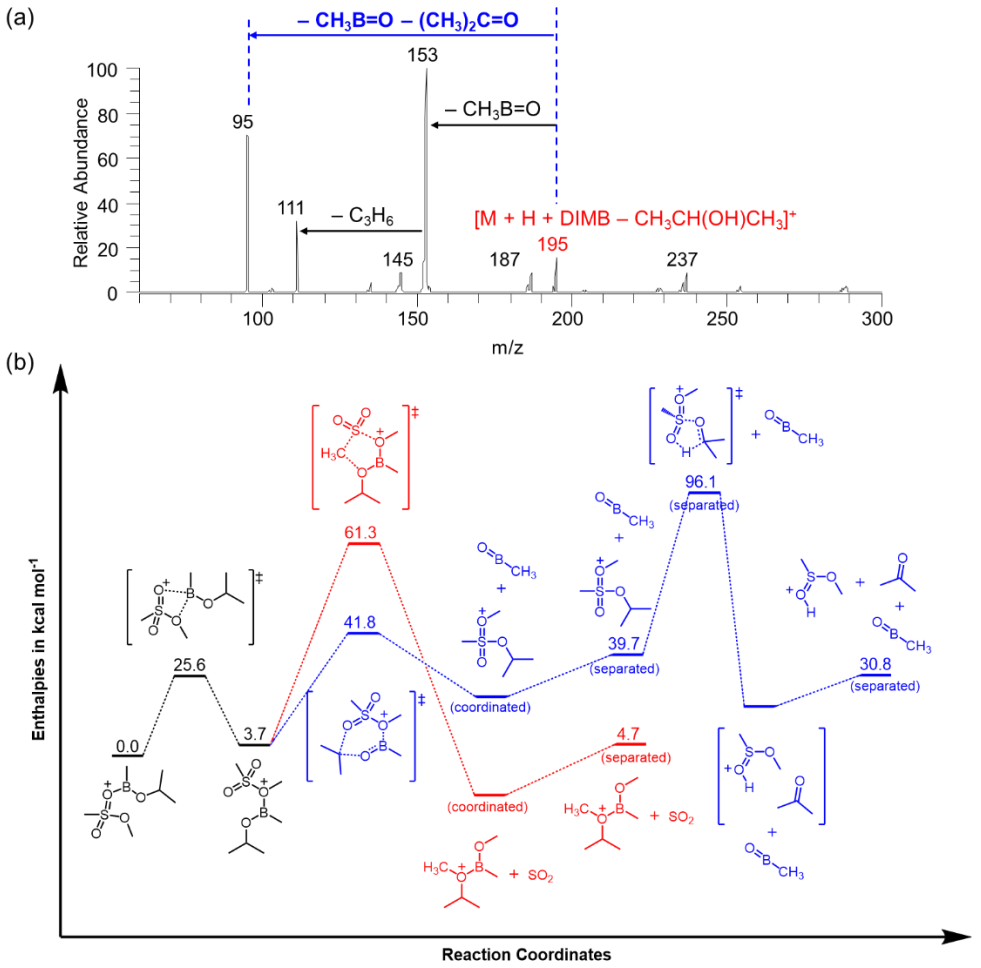

Figure 5.5. (a) The CAD MS^3 spectrum measured for the ion-molecule reaction product ions [M + H + DIMB – $CH_3CH(OH)CH_3]^+$ (*m/z* 195) of methyl methanesulfonate (M) (collision energy 25 arbitrary units). The fragment ions [M + H + DIMB – $CH_3CH(OH)CH_3$ – $CH_3B{=}O$ – $(CH_3)_2C{=}O]^+$ (*m/z* 95) were observed. The ions of *m/z* 145 correspond to protonated DIMB. The ions of *m/z* 187 and *m/z* 237 correspond to $CH_2{=}CHCH_3$ adducts of the ions of *m/z* 145 and *m/z* 195, respectively. (b) Potential energy surfaces calculated at the M06-2X/6-311++G(d,p) level of theory for the elimination of $CH_3B{=}O$ followed by $(CH_3)_2C{=}O$ loss (observed experimentally, in red color) and elimination of SO_2 (not observed, in blue color) upon CAD of the ion-molecule reaction product ion [M + H + DIMB – $CH_3CH(OH)CH_3]^+$ of protonated methyl methanesulfonate.

The calculated potential energy surfaces (Figure 5.5b; blue pathway) rationalize the elimination of $CH_3B=O$ followed by $(CH_3)_2C=O$ loss from the ion-molecule reaction product ions $[M + H + DIMB – CH_3CH(OH)CH_3]^+$ of protonated methyl methanesulfonate (M). Based on these calculations, the elimination of $CH_3B=O$ is triggered by the transfer of the isopropoxymethylboryl group from the sulfonyl oxygen to the alkoxide oxygen in methyl methanesulfonate. This reaction is the first step for the pathways leading to $CH_3B=O$ loss (observed; Figure 5.5b) as well as SO_2 loss (not observed; Figure 5.4b). After the isopropoxymethylboryl group transfer, the isopropyl group is transferred from the boron-oxygen to the sulfur-oxygen, and the $CH_3B=O$ molecule is eliminated simultaneously. The elimination of $CH_3B=O$ requires a transition state whose enthalpy is 41.8 kcal mol^{-1} above the energy of the ion-molecule reaction product ion $[M + H + DIMB – CH_3CH(OH)CH_3]^+$. After the elimination of $CH_3B=O$, a proton is transferred from the isopropyl group to the sulfur-oxygen and $(CH_3)_2C=O$ is eliminated at the same time. The enthalpy of the transition state is 96.1 kcal mol^{-1} above the energy of the ion-molecule reaction product ion $[M + H + DIMB – CH_3CH(OH)CH_3]^+$. The greater energy barrier for $(CH_3)_2C=O$ elimination than for $CH_3B=O$ elimination rationalizes the greater abundance of the fragment ions $[M + H + DIMB – CH_3CH(OH)CH_3 – CH_3B=O]^+$ than the fragment ions $[M + H + DIMB – CH_3CH(OH)CH_3 – CH_3B=O – (CH_3)_2C=O]^+$ in the CAD MS^3 spectra.

The fact that the fragment ions $[M + H + DIMB – CH_3CH(OH)CH_3 – SO_2]^+$ (diagnostic for sulfite esters, Figure 5.4) were not generated for sulfonate esters can be rationalized by the energy barriers of SO_2 elimination and $CH_3B=O$ elimination. SO_2 elimination can also occur theoretically for sulfonate esters (Figure 5.5b, red pathway) via a similar pathway to the SO_2 elimination for sulfite esters (Figure 5.4b). However, for sulfonate esters, the energy barrier for SO_2 elimination is 61.3 kcal mol^{-1} (Figure 5.5b, red pathway), which is greater than the energy barrier for $CH_3B=O$ elimination (41.8 kcal mol^{-1}, Figure 5.5b, blue pathway). Therefore, SO_2 elimination does not occur for sulfonate esters, but instead, $CH_3B=O$ elimination takes place, followed by the elimination of $(CH_3)_2C=O$.

Since the fragment ions $[M + H + DIMB – CH_3CH(OH)CH_3 – CH_3B=O – (CH_3)_2C=O]^+$ can be observed in the MS^3 CAD spectra of all sulfonate esters, these fragment ions are diagnostic for sulfonate esters. However, these same fragment ions can be observed in the MS^3 CAD spectra of some sulfite esters (Table 5.4). Therefore, identification of a sulfonate ester requires elimination of a $CH_3B=O$ molecule followed by a $(CH_3)_2C=O$ molecule from the ion-molecule reaction

product ion $[M + H + DIMB - CH_3CH(OH)CH_3]^+$ ***as well as*** the lack of elimination of a SO_2 molecule upon CAD.

Unfortunately, for *sulfones*, neither the $CH_3B=O$ elimination followed by $(CH_3)_2C=O$ loss nor the SO_2 elimination was observed upon CAD of the ion-molecule reaction product ions $[M + H + DIMB - CH_3CH(OH)CH_3]^+$ (Table 5.6, Figure 5.6a). This different fragmentation behavior is due to the lack of an sp^3 oxygen in sulfones, which prevents the sulfones from accepting the isopropoxymethylboryl group transfer before the SO_2 or $CH_3B=O$ elimination occurs (Figures 5.4b and 5.5b).

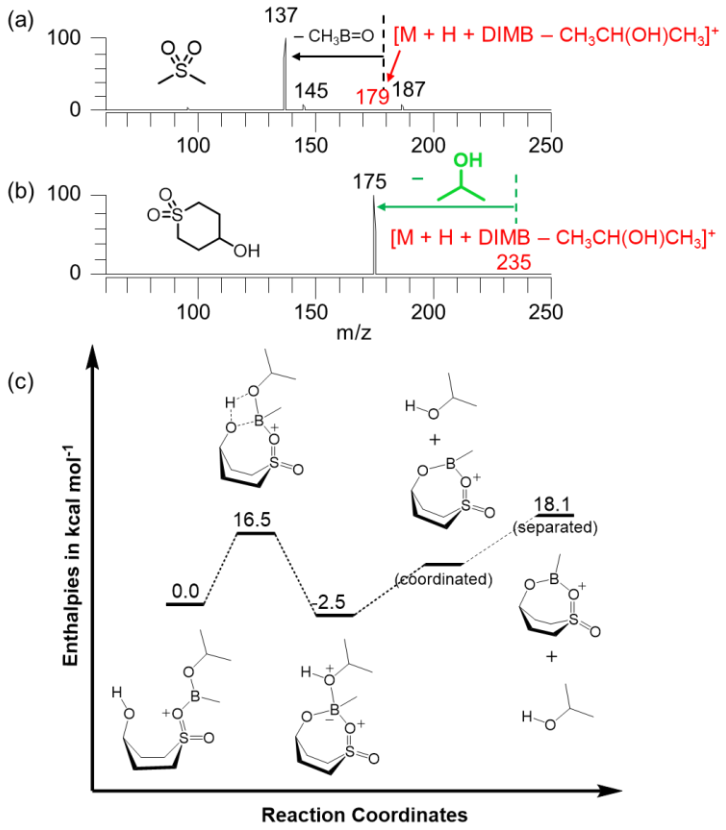

Figure 5.6. (a) The CAD MS^3 spectrum (collision nergy 25 arbitrary units) measured for the ion-molecule reaction product ions $[M + H + DIMB – CH_3CH(OH)CH_3]^+$ (*m/z* 179) of dimethyl sulfone. The ions of *m/z* 145 correspond to protonated DIMB. The ions of *m/z* 187 correspond to CH_2=$CHCH_3$ adducts of the ions of *m/z* 145. (b) The CAD MS^3 spectrum (collision energy 25 arbitrary units) measured for the ion-molecule reaction product ions $[M + H + DIMB – CH_3CH(OH)CH_3]^+$ (*m/z* 235) of tetrahydro-2H-thiopyran-4-ol. Elimination of $CH_3CH(OH)CH_3$ was observed. (c) Potential energy surface calculated at the M06-2X/6-311++G(d,p) level of theory for the elimination of $CH_3CH(OH)CH_3$ upon CAD of the ion-molecule reaction product ion $[M + H + DIMB – CH_3CH(OH)CH_3]^+$ of protonated tetrahydro-2H-thiopyran-4-ol-1,1-dioxide.

Nevertheless, a fragment ion $[M + H + DIMB – 2\ CH_3CH(OH)CH_3]^+$ diagnostic for sulfones with a hydroxyl group was observed upon CAD of the ion-molecule reaction product ion $[M + H + DIMB – CH_3CH(OH)CH_3]^+$ of these compounds (Table 5.6, with the exception of 4-hydroxyphenyl methyl sulfone; see Figure 5.6b for an example). Calculations performed at the M06-2X/6-311++G(d,p) level of theory indicate that a proton on the hydroxyl group can be transferred to the oxygen in the isopropoxyl group while a new boron-oxygen bond forms (Figure 5.6c). This is followed by elimination of a $CH_3CH(OH)CH_3$ molecule. The reaction as a whole was calculated to be endothermic by 18.1 kcal mol^{-1}.

Although 4-hydroxyphenyl methyl sulfone has a hydroxyl group, no $CH_3CH(OH)CH_3$ elimination was observed upon fragmentation of the ion-molecule reaction product ions $[M + H + DIMB - CH_3CH(OH)CH_3]^+$ (*m/z* 195) (Figure 5.7a). This is rationalized by the large distance between the hydroxyl group and the isopropoxyl group (Figure 5.7b).

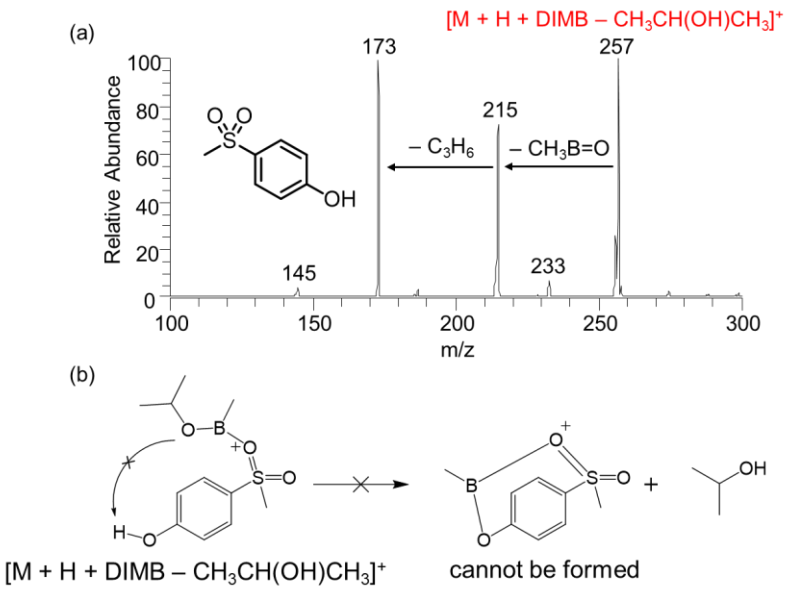

Figure 5.7. (a) The CAD MS^3 spectrum (collision energy 25 arbitrary units) of the ion-molecule reaction product ions $[M + H + DIMB - CH_3CH(OH)CH_3]^+$ (*m/z* 257) of 4-hydroxyphenyl methyl sulfone (M). (b) Proton transfer from the hydroxyl group to the isopropoxyl group in the ion-molecule reaction product ions $[M + H + DIMB - CH_3CH(OH)CH_3]^+$ shown in Figure 5.7a is prevented by the large separation of these two groups.

5.3.3 Reactions of other protonated analytes with DIMB

In order to test whether the ion-molecule reaction product ions and fragment ions discussed above can only be generated for sulfonate esters, sulfite esters and sulfones with a hydroxyl group, many protonated analytes with other functionalities were allowed to react with DIMB. The product ions generated upon their reactions with DIMB are listed in Table 5.7. As the product ions $[M + H + DIMB - CH_3CH(OH)CH_3]^+$ were observed for some of the analytes, those product ions were subjected to CAD (Table 5.7).

As shown in Table 5.7, protonated alcohols, aldehydes, amines, anilines, *N*-oxides, sulfonamides and thioamides do not react with DIMB. On the other hand, only proton transfer to DIMB was observed for protonated phenols, thiophenols and tetrahydrothiophenes. However,

protonated ethers, ketones, carboxylic acids, esters, amides and sulfoxides react with DIMB to generate the important product ion $[M + H + DIMB - CH_3CH(OH)CH_3]^+$ also observed for the sulfonate esters, sulfite esters and sulfones. Fortunately, the behavior of these ions upon CAD were distinctly different from those generated from sulfonate and sulfite esters and sulfones as none of them fragmented via elimination of a SO_2 molecule (diagnostic for sulfite esters), elimination of $CH_3B{=}O$ followed by elimination of $(CH_3)_2C{=}O$ (diagnostic for sulfonate esters) or $CH_3CH(OH)CH_3$ (diagnostic for sulfones with a hydroxyl group). Therefore, DIMB can be used not only for the differentiation of sulfite esters, sulfonate esters and sulfones with a hydroxyl group from each other, but also for their differentiation from other compounds with different functionalities.

Table 5.7. Ion-molecule reaction product ions (with their relative abundances) observed upon reactions of different types of protonated analytes ($[M + H]^+$) with DIMB (MS^2 experiments) and the fragmentations/fragment ions[a] (with their m/z-values and relative abundances) observed upon CAD of the product ions $[M + H + DIMB – CH_3CH(OH)CH_3]^+$ (MS^3 experiments). The important ion-molecule reaction product ions $[M + H + DIMB – i\text{-}PrOH]^+$ are indicated in red color.

Analyte Category	Analyte Name (*m/z* of $[M + H]^+$)	Ion-molecule Reaction Product Ions (*m/z*) and Their Relative Abundances[b] (MS^2)	Neutral Fragments and Ionic Fragments (m/z) Formed upon CAD of $[M + H + DIMB – CH_3CH(OH)CH_3]^+$ (MS^3) and the Relative Abundances[c] of the Fragment Ions
Alcohol	1-Hexanol (103)	No Reactions	Not Applicable
Ether	Tetrahydrofuran (73)	$[M + H + DIMB – CH_3CH(OH)CH_3]^+$ (157) 100% $[M + H + DIMB – CH_3CH(OH)CH_3 – CH_3B=O]^+$ (115) 39%	– $CH_3B=O$ (115) 100% – $CH_3B=O$ – $CH_2=CHCH_3$ (73) 37% – C_4H_6 (103) 33%
Aldehyde	Butyraldehyde (73)	No Reaction	Not Applicable
Ketone	Acetone (59)	$[DIMB + H]^+$ (145) 100% $[DIMB + H – CH_3B=O]^+$ (103) 75% $[M + H + DIMB – CH_3CH(OH)CH_3]^+$ (143) 45% $[M + H + DIMB – CH_3CH(OH)CH_3 – CH_3B=O]^+$ (101) 93%	– $CH_3B=O$ (101) 100%
Carboxylic acid	*n*-Hexanoic acid (117)	$[M + H + DIMB – CH_3CH(OH)CH_3]^+$ (201) 61% $[M + H + DIMB – CH_3CH(OH)CH_3 – CH_3B=O]^+$ (159) 100% $[DIMB + H]^+$ (145) 19% $[M + H + DIMB – CH_3CH(OH)CH_3 – CH_3B=O]^+$ (261) 14%	– $CH_3B=O$ (159) 100%
Ester	Methyl propanoate (89)	$[M + H + DIMB – CH_3CH(OH)CH_3]^+$ (173) 100% $[M + H + DIMB – CH_3CH(OH)CH_3 – CH_3B=O]^+$ (131) 75% $[DIMB + H]^+$ (145) 86%	– $CH_3B=O$ (131) 100%
Phenol	Phenol (95)	$[DIMB + H]^+$ (145) 100%	Not Applicable
Amide	Dimethylacetamide (88)	$[M + H + DIMB – CH_3CH(OH)CH_3]^+$ (172) 100% $[M + H + DIMB – CH_3CH(OH)CH_3 – CH_3B=O]^+$ (130) 29%	– $CH_3B=O$ (130) 100% – $CH_3B=O$ – $CH_2=CHCH_3$ (88) 81%
Amine	Triethylamine (102)	No Reaction	Not Applicable

(Table 5.7 continued)

Aniline	4-Chloroaniline (128)	No Reaction	Not Applicable
N-oxide	Trimethylamine *N*-oxide (76)	No Reaction	Not Applicable
Sulfoxide	Dimethyl sulfoxide (79)	$[M + H + DIMB - CH_3CH(OH)CH_3]^+$ (163) 100%	$- CH_3B{=}O$ (130) 51% $- CH_3B{=}O - CH_2{=}CHCH_3$ (88) 100%
Sulfonamide	Tetraethyl sulfonamide (209)	No Reaction	Not Applicable
Other sulfur containing compounds	Tetrahydrothiophene (89)	$[DIMB + H]^+$ (145) 100%	Not Applicable
	Thiophenol (111)	$[DIMB + H]^+$ (145) 100%	Not Applicable
	Thiobenzamide (138)	No Reaction	Not Applicable

[a] All collision energies were 25 arbitrary units. [b] For the relative abundances of the ion-molecule reaction product ions, reproducibility was ± 30%. [c] For the relative abundances of the fragment ions, reproducibility was ± 20%.

5.3.4 HPLC/MS^3 experiments

HPLC/MS^3 experiments were carried out to test the practicality of coupling the analytical method developed here for the identification of sulfonate esters, sulfite esters and sulfones with a separation method. A mixture of three isomeric analytes (all at a concentration of 0.05 mM) – 1,4-butylene sulfite (sulfite ester), 1,4-butane sultone (sulfonate ester) and tetrahydrothiophene-3-ol-1,1-dioxide (sulfone) – were separated by reversed-phase HPLC chromatography (Figure 5.8). The eluted compounds were protonated by (+)APCI in the linear quadrupole ion trap mass spectrometer and transferred into the ion trap. The protonated analytes (*m/z* 137) were allowed to react with DIMB for 30 ms to generate the product ions $[M + H + DIMB - CH_3CH(OH)CH_3]^+$ (M = analyte). The product ions (*m/z* 221) were monitored to obtain the chromatogram shown in Figure 5.8a. The major peaks shown in the HPLC chromatogram correspond to the three analytes (Figure 5.8a).

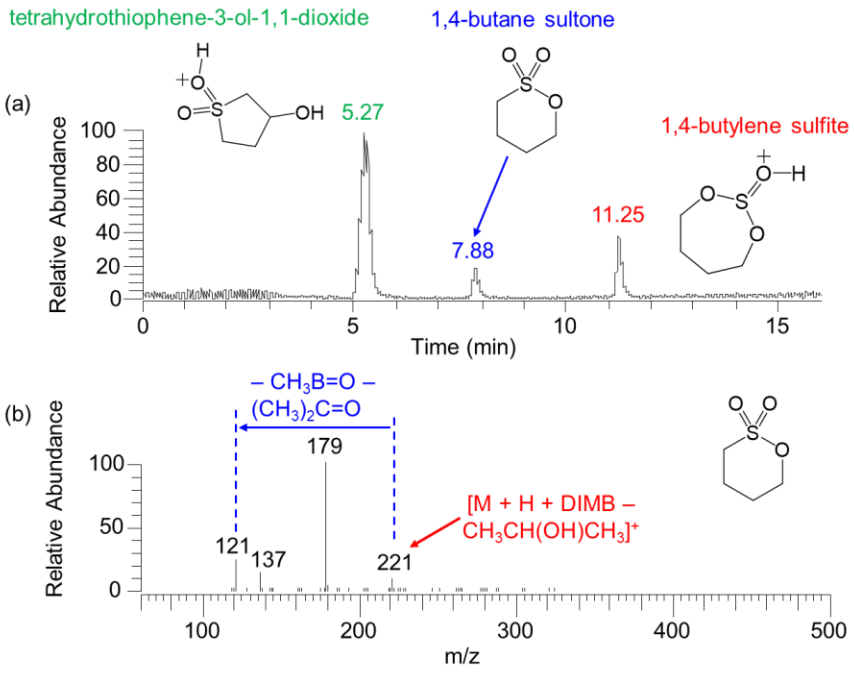

Figure 5.8. (a) HPLC/(+)APCI MS^2 chromatogram measured for a mixture of a sulfite ester, a sulfonate ester and a sulfone (all at a concentration of 0.05 mM). The ion-molecule reaction product ions $[M + H + DIMB - CH_3CH(OH)CH_3]^+$ (M = analyte) were monitored to obtain the chromatogram. (b) CAD MS^3 spectrum measured for the product ions $[M + H + DIMB - CH_3CH(OH)CH_3]^+$ formed upon reactions of protonated 1,4-butane sultone with DIMB. 1,4-Butane sultone eluted at 7.5-8.0 min.

The product ions $[M + H + DIMB – CH_3CH(OH)CH_3]^+$ were isolated and subjected to CAD (MS^3). Based on the observation of the diagnostic fragment ions $[M + H + DIMB – CH_3CH(OH)CH_3 – CH_3B=O – (CH_3)_2C=O]^+$ in the CAD MS^3 spectra for 1,4-butane sultone (Figure 5.8b), the compound can be unambiguously identified as a sulfonate ester. For the other two isomeric compounds, diagnostic fragment ions $[M + H + DIMB – CH_3CH(OH)CH_3 – SO_2]^+$ and $[M + H + DIMB – 2\ CH_3CH(OH)CH_3]^+$ were also observed, which enables the unambiguous identification of them as a sulfite ester and sulfone.

In order to determine lowest analyte concentration that can be identified by using the HPLC/MS^3 analytical method above, limit of detection (LoD) for the three analytes in the mixture are examined. The limit of detection measurement is shown in Figure 5.9 (using 1,4-butane sultone as an example), where the extracted ion HPLC chromatogram for the diagnostic ion-molecule reaction product ion $[M + H + DIMB – CH_3CH(OH)CH_3]^+$ was monitored. At the concentration of 50 μM, the signal-to-noise ratio of the product ion is 3 (Figure 5.9a), and the diagnostic fragment ions $[M + H + DIMB – CH_3CH(OH)CH_3 – CH_3B=O – (CH_3)_2C=O]^+$ can still be observed in the CAD spectrum (Figure 5.9b). Therefore, the limit of detection for chlortoluron is 50 μM. Further, the LoD for 1,4-butylene sulfite and tetrahydrothiophene-3-ol-1,1-dioxide are determined to be 5 μM and 3 μM, respectively. These values are not as low as those published earlier when using the same method but a different reagent and analytes (50 - 250 nM),[33] but is below the daily threshold of toxicological concern for sulfonate esters (1.5 μg/g).[1,9-11]

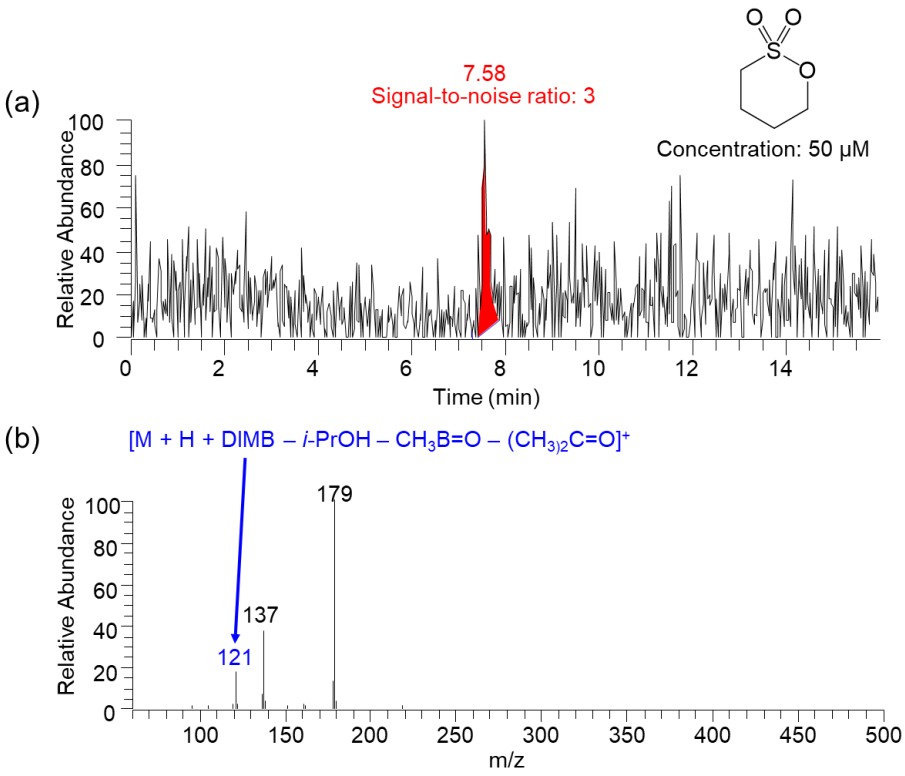

Figure 5.9. (a) Extracted ion HPLC chromatogram for the diagnostic ion-molecule reaction product ion of *m/z* 221 (generated in an MS/MS experiment) measured for 1,4-butene sultone at the limit of detection concentration (50 µM). The chromatogram shows the analyte peak at 7.58 min. (b) MS^3 CAD spectrum measured for 1,4-butene sultone at 50 µM concentration. The MS^3 spectrum shows the diagnostic fragment ion (*m/z* 121) that was also shown in Figure 5.8b. The limit of detection measurement was performed three times.

5.4 Conclusions

In order to differentiate sulfonate esters from their isomeric analogs – sulfite esters and sulfones – with diagnostic ion-molecule reaction, organoboron reagents can be a good choice, because many organoboron reagents have been utilized to react with oxygen containing functionalities and identify them successfully.[21-24] These ion-molecule reactions are usually initiated by proton transfer from the protonated analyte to the organoboron reagent. Therefore, the proton affinity of the organoboron reagent must be slightly higher than that of analytes. However, none of the reported organoboron reagent (TMB,[23] PA = 195 kcal mol^{-1}; DEMB,[24] PA = 191 kcal mol^{-1} and TDMAB,[21,22] PA = 230 kcal mol^{-1}) has a suitable proton affinity for the identification of sulfonate esters, sulfite esters and sulfones, whose proton affinities are ranging from 187 – 205 kcal mol^{-1} (Figure 5.1, calculated at B3LYP/6-311++G(d,p) level of theory). Therefore, a new

reagent – DIMB – was utilized to identify these analytes of interest, as the proton affinity of DIMB (208.5 kcal mol^{-1}, calculated at B3LYP/6-311++G(d,p) level of theory) is slightly higher than the proton affinities of these analytes.

All protonated sulfonate esters, sulfite esters and sulfones reacted with DIMB to generate the same product ions $[M + H + DIMB – CH_3CH(OH)CH_3]^+$. Therefore, examination of the dissociation behavior of these products was necessary to differentiate these analytes of interest. The product ions $[M + H + DIMB – CH_3CH(OH)CH_3]^+$ were subjected to CAD and different diagnostic fragment ions were generated for corresponding analyte categories. For sulfite esters, fragment ions were generated via elimination of a SO_2 molecule. On the other hand, SO_2 elimination does not occur for sulfonate esters; instead the elimination of a $CH_3B{=}O$ molecule followed by elimination of an $(CH_3)_2C{=}O$ molecule takes place, which enables the distinction of sulfonate esters from sulfite esters. For sulfones, no diagnostic fragment ions were observed upon CAD of the product ions $[M + H + DIMB – CH_3CH(OH)CH_3]^+$; however, diagnostic fragment ions $[M + H + DIMB – 2\ CH_3CH(OH)CH_3]^+$ were generated for sulfones with a hydroxyl group. Therefore, the sulfones with a hydroxyl group can be differentiated from sulfonate esters and sulfite esters. While the ion-molecule reaction product ions $[M + H + DIMB – CH_3CH(OH)CH_3]^+$ were not observed for most other protonated analytes, protonated ethers, ketones, carboxylic acids, esters, amides and sulfoxides did produce these ions. However, none of the diagnostic fragment ions mentioned above were generated upon CAD of these product ions (Table 5.7). Therefore, sulfite esters, sulfonate esters and sulfones with a hydroxyl group can be unambiguously differentiated from other categories of small molecules (Figure 5.10).

Successful coupling of the above ion-molecule reaction/CAD MS^3 experiment with HPLC demonstrated the practicality of this approach for the analysis of complex mixtures containing isomeric sulfonate esters, sulfite esters and sulfones. The limits of detection for the ion-molecule reaction product ions in HPLC/MS^2 experiments were determined to be 5 μM, 50 μM, 3μM for 1,4-butylene sulfite, 1,4-butane sultone and tetrahydrothiophene-3-ol-1,1-dioxide, respectively.

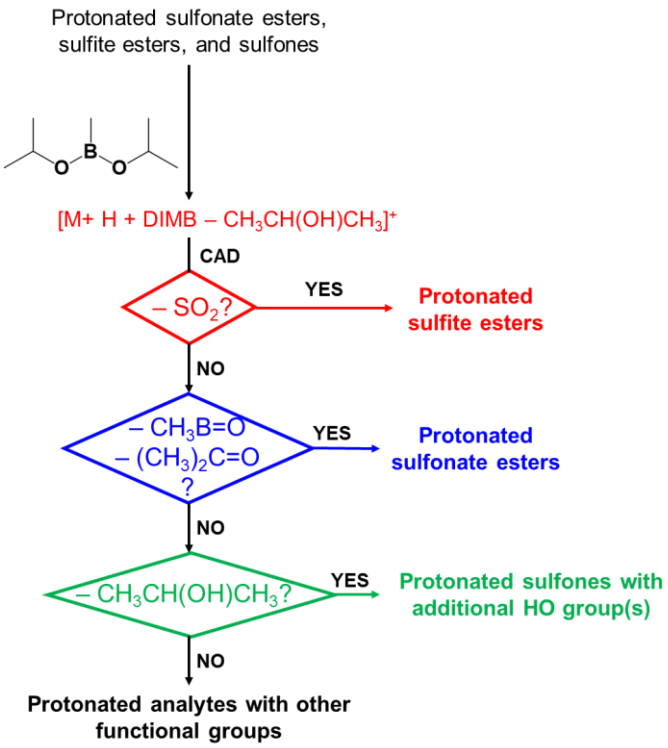

Figure 5.10. Distinction of sulfite esters, sulfonate esters and sulfones with additional hydroxyl groups (M) from each other as well as from other analytes via protonation and generation of product ions $[M + H + DIMB – CH_3CH(OH)CH_3]^+$ upon ion-molecule reactions with DIMB, followed by generation of diagnostic fragment ions upon CAD on the ion-molecule reaction product ions.

5.5 References

1. Galloway, S. M.; Vijayaraj Reddy, M.; McGettigan, K.; Gealy, R.; Bercu, J., potentially mutagenic impurities: analysis of structural classes and carcinogenic potencies of chemical intermediates in pharmaceutical syntheses supports alternative methods to the default TTC for calculating safe levels of impurities. *Regul. Toxicol. Pharmacol.* **2013,** *66*, 326–335.

2. Raphael, M. J.; Donaldson, R. M., A "significant" stenosis: Thirty years on. *Lancet* **1989,** *333*, 207–209.

3. Teasdale, A.; Delaney, E. J.; Eyley, S. C.; Jacq, K.; Taylor-Worth, K.; Lipczynski, A.; Hoffmann, W.; Reif, V.; Elder, D. P.; Facchine, K. L.; Golec, S.; Schulte Oestrich, R.; Sandra, P.; David, F., A detailed study of sulfonate ester formation and solvolysis reaction rates and application toward establishing sulfonate ester control in pharmaceutical manufacturing processes. *Org. Process Res. Dev.* **2010,** *14*, 999–1007.

4. Elder, D.; Facchine, K. L.; Levy, J. N.; Parsons, R.; Ridge, D.; Semo, L.; Teasdale, A., An approach to control strategies for sulfonate ester formation in pharmaceutical manufacturing based on recent scientific understanding. *Org. Process Res. Dev.* **2012,** *16*, 1707–1710.

5. Müller, L.; Gocke, E.; Lavé, T.; Pfister, T., Ethyl methanesulfonate toxicity in Viracept—A comprehensive human risk assessment based on threshold data for genotoxicity. *Toxicol. Lett.* **2009,** *190*, 317–329.

6. Müller, L.; Gocke, E., Considerations regarding a permitted daily exposure calculation for ethyl methanesulfonate. *Toxicol. Lett.* **2009,** *190*, 330–332.

7. Kim, J.-Y.; Lee, A. R.; Choi, Y. J.; Back, S.-M.; Kim, O.-H.; Moon, K.-S.; Kim, S. K., In vitro and in vivo assessment of the genotoxic effects of ceric ammonium nitrate and 1,3-propane sultone. *Toxicol. Lett.* **2020,** *332*, 202–212.

8. Robbiano, L.; Brambilla, M., DNA damage in the central nervous system of rats after in vivo exposure to chemical carcinogens: correlation with the induction of brain tumors. *Teratog. Carcinog. and Mutagen.* **1987,** *7*, 175–181.

9. Raman, N. V. V. S. S.; Prasad, A. V. S. S.; Ratnakar Reddy, K., Strategies for the identification, control and determination of genotoxic impurities in drug substances: A pharmaceutical industry perspective. *J. Pharm. Biomed. Anal.* **2011,** *55*, 662–667.

10. Müller, L.; Mauthe, R. J.; Riley, C. M.; Andino, M. M.; Antonis, D. D.; Beels, C.; DeGeorge, J.; De Knaep, A. G. M.; Ellison, D.; Fagerland, J. A.; Frank, R.; Fritschel, B.; Galloway, S.; Harpur, E.; Humfrey, C. D. N.; Jacks, A. S.; Jagota, N.; Mackinnon, J.; Mohan, G.; Ness, D. K.; O'Donovan, M. R.; Smith, M. D.; Vudathala, G.; Yotti, L., A rationale for determining, testing, and controlling specific impurities in pharmaceuticals that possess potential for genotoxicity. *Regul. Toxicol. and Pharmacol.* **2006,** *44*, 198–211.

11. Kroes, R.; Renwick, A. G.; Cheeseman, M.; Kleiner, J.; Mangelsdorf, I.; Piersma, A.; Schilter, B.; Schlatter, J.; van Schothorst, F.; Vos, J. G.; Würtzen, G., Structure-based thresholds of toxicological concern (TTC): Guidance for application to substances present at low levels in the diet. *Food Chem. Toxicol.* **2004**, *42*, 65–83.

12. Devenport, N. A.; Sealey, L. C.; Alruways, F. H.; Weston, D. J.; Reynolds, J. C.; Creaser, C. S., Direct detection of a sulfonate ester genotoxic impurity by atmospheric-pressure thermal desorption–extractive electrospray–mass spectrometry. *Anal. Chem.* **2013,** *85*, 6224–6227.

13. Guo, T.; Shi, Y.; Zheng, L.; Feng, F.; Zheng, F.; Liu, W., Rapid and simultaneous determination of sulfonate ester genotoxic impurities in drug substance by liquid chromatography coupled to tandem mass spectrometry: comparison of different ionization modes. *J. Chromatogr. A* **2014,** *1355*, 73–79.

14. Zhang, C.; Huang, L.; Wu, Z.; Chang, C.; Yang, Z., Determination of sulfonate ester genotoxic impurities in imatinib mesylate by gas chromatography with mass spectrometry. *J. Sep. Sci.* **2016,** *39*, 3558–3563.

15. Green, J. L.; Reed, G. A., Characterization of (±)-7,8,10-trihydroxy-7,8,9,10-tetrahydrobenzo-[α]pyrene-9-sulfonate. *Chem. Res. Toxicol.* **1992,** *5*, 823–827.

16. Ward, R. S.; Diaper, R. L.; Roberts, D. W., Kinetics and thermodynamics of sulfuric acid-mediated cleavage of substituted diaryl sulfones. *J. Surfactants Deterg.* **2001,** *4*, 185–190.

17. Committee on D., "Inactive" ingredients in pharmaceutical products: Update (subject review). *Pediatrics* **1997,** *99*, 268.

18. Lester, M. R., Sulfite sensitivity: significance in human health. *J. Am. Coll. Nutr.* **1995,** *14*, 229–232.

19. Thompson, H. J. J., C.; Lu, J.; Mehta, R. G.; Piazza, G. A.; Paranka, N.S.; Pamukcu, R.; Ahnen, D. J., Sulfone metabolite of sulindac inhibits mammary carcinogenesis. *Cancer Res.* **1997,** *57*, 267–271.

20. Piazza, G. A. R., A. L. K.; Krutzsch, M.; Speri, G.; Paranka, N. S.; Gross, P. H.; Brendel, K.; Burt, R. W.; Alberts, D. S.; Pamukcu, R.; Ahnen, D. J., Antineoplastic drugs sulindac sulfide and sulfone inhibit cell growth by inducing apoptosis. *Cancer Res.* **1995,** *55*, 3110–3116.

21. Duan, P.; Fu, M.; Gillespie, T. A.; Winger, B. E.; Kenttämaa, H. I., Identification of aliphatic and aromatic tertiary N-oxide functionalities in protonated analytes via ion/molecule and dissociation reactions in an FT-ICR mass spectrometer. *J. Org. Chem.* **2009,** *74*, 1114–1123.

22. Feng, E.; Ma, X.; Kenttämaa, H. I., Characterization of protonated substituted ureas by using diagnostic gas-phase ion-molecule reactions followed by collision-activated dissociation in tandem mass spectrometry experiments. *Anal. Chem.* **2021,** *93*, 7851–7859.

23. Sheng, H.; Williams, P. E.; Tang, W.; Riedeman, J. S.; Zhang, M.; Kenttämaa, H. I., Identification of the sulfone functionality in protonated analytes via ion/molecule reactions in a linear quadrupole ion trap mass spectrometer. *J. Org. Chem.* **2014,** *79*, 2883–2889.

24. Watkins, M. A.; Price, J. M.; Winger, B. E.; Kenttämaa, H. I., Ion−molecule reactions for mass spectrometric identification of functional groups in protonated oxygen-containing monofunctional compounds. *Anal. Chem.* **2004,** *76*, 964–976.

25. Zhu, H.; Max, J. P.; Marcum, C. L.; Luo, H.; Abu-Omar, M. M.; Kenttämaa, H. I., identification of the phenol functionality in deprotonated monomeric and dimeric lignin degradation products via tandem mass spectrometry based on ion–molecule reactions with diethylmethoxyborane. *J. Am. Soc. Mass Spectrom.* **2016,** *27*, 1813–1823.

26. Niyonsaba, E.; Easton, M. W.; Liu, J. K. Y.; Yu, Z.; Sheng, H.; Kong, J. Y.; Zhang, Z.; Easterling, L. F.; Milton, J.; Kenttämaa, H. I., Identification of protonated primary carbamates by using gas-phase ion–molecule reactions followed by collision-activated dissociation in tandem mass spectrometry experiments. *Org. Process Res. Dev.* **2019,** *23*, 1159–1166.

27. Kong, J. Y.; Yu, Z.; Easton, M. W.; Niyonsaba, E.; Ma, X.; Yerabolu, R.; Sheng, H.; Jarrell, T. M.; Zhang, Z.; Ghosh, A. K.; Kenttämaa, H. I., Differentiating isomeric deprotonated glucuronide drug metabolites via ion/molecule reactions in tandem mass spectrometry. *Anal. Chem.* **2018,** *90*, 9426–9433.

28. Niyonsaba, E.; Easton, M. W.; Feng, E.; Yu, Z.; Zhang, Z.; Sheng, H.; Kong, J.; Easterling, L. F.; Milton, J.; Chobanian, H. R.; Deprez, N. R.; Cancilla, M. T.; Kilaz, G.; Kenttämaa, H. I., Differentiation of deprotonated acyl-, N-, and O-glucuronide drug metabolites by using tandem mass spectrometry based on gas-phase ion–molecule reactions followed by collision-activated dissociation. *Anal. Chem.* **2019,** *91*, 11388–11396.

29. Gronert, S.; Huang, R.; Li, K. H., Gas phase derivatization in peptide analysis I: the utility of trimethyl borate in identifying phosphorylation sites. *Int. J. Mass Spectrom.* **2004,** *231*, 179–187.

30. Hancock, S. E.; Maccarone, A. T.; Poad, B. L. J.; Trevitt, A. J.; Mitchell, T. W.; Blanksby, S. J., Reaction of ionised steryl esters with ozone in the gas phase. *Chem. Phys. Lipids* **2019,** *221*, 198–206.

31. Bonnaventure, I.; Charette, A. B., Probing the importance of the hemilabile site of bis(phosphine) monoxide ligands in the copper-catalyzed addition of diethylzinc to N-phosphinoylimines: discovery of new effective chiral ligands. *J. Org. Chem.* **2008,** *73*, 6330–6340.

32. Frisch, M. J. T., G. W.; Schlegel, H. B.; Scuseria, G. E.; Robb, M. A.; Cheeseman, J. R.; Scalmani, G.; Barone, V.; Petersson, G. A.; Nakatsuji, H.; Li, X.; Caricato, M.; Marenich, A. V.; Bloino, J.; Janesko, B. G.; Gomperts, R.; Mennucci, B.; Hratchian, H. P.; Ortiz, J. V.; Izmaylov, A. F.; Sonnenberg, J. L.; Williams-Young, D.; Ding, F.; Lipparini, F.; Egidi, F.; Goings, J.; Peng, B.; Petrone, A.; Henderson, T.; Ranasinghe, D.; Zakrzewski, V. G.; Gao, J.; Rega, N.; Zheng, G.; Liang, W.; Hada, M.; Ehara, M.; Toyota, K.; Fukuda, R.; Hasegawa, J.; Ishida, M.; Nakajima, T.; Honda, Y.; Kitao, O.; Nakai, H.; Vreven, T.; Throssell, K.; Montgomery, J. A. Jr.; Peralta, J. E.; Ogliaro, F.; Bearpark, M. J.; Heyd, J. J.; Brothers, E. N.; Kudin, K. N.; Staroverov, V. N.; Keith, T. A.; Kobayashi, R.; Normand, J.; Raghavachari, K.; Rendell, A. P.; Burant, J. C.; Iyengar, S. S.; Tomasi, J.; Cossi, M.; Millam, J. M.; Klene, M.; Adamo, C.; Cammi, R.; Ochterski, J. W.; Martin, R. L.; Morokuma, K.; Farkas, O.; Foresman, J. B.; Fox, D. J. *Gaussian 16*, Gaussian 16, Revision C.01; Gaussian, Inc.: Wallingford CT, 2016.

33. Easterling, L. F.; Yerabolu, R.; Kumar, R.; Alzarieni, K. Z.; Kenttämaa, H. I., Factors affecting the limit of detection for HPLC/tandem mass spectrometry experiments based on gas-phase ion–molecule reactions. *Anal. Chem.* **2020,** *92*, 7471–7477.

CHAPTER 6. GAS-PHASE REACTIVITY OF PHENYLCARBYNE ANIONS

6.1 Introduction

The possible existence of carbynes was first proposed in 1960s.[1-4] These compounds are of interest because of their unusual structure containing a monovalent carbon atom (Figure 6.1a). However, only a few experimental studies have been published on carbynes[5-11] as they only have a short lifetime in solution.[7-9] Carbynes have an open valence shell with a doublet ground-electronic state. Methylidyne, the simplest carbyne, has been experimentally measured to possess a doublet-quartet energy splitting (ΔE_{D-Q}) of -17.1 kcal mol^{-1} (Figure 6.1b).[12-14] Halocarbynes are predicted to have much greater ΔE_{D-Q} (-37.0 – -78.4 kcal mol^{-1}) than methylidyne.[15-18] In sharp contrast to carbynes, their nearest analogs – carbenes (Figure 6.1a) – have been explored extensively.[19-21] The simplest carbene, methylene, possesses a singlet ground state with a singlet-triplet energy splitting (ΔE_{S-T}) of -9.05 kcal mol^{-1} (Figure 6.1b).[22] When the hydrogen atom is replaced with an alkyl group, ΔE_{S-T} decreases.[23,24]

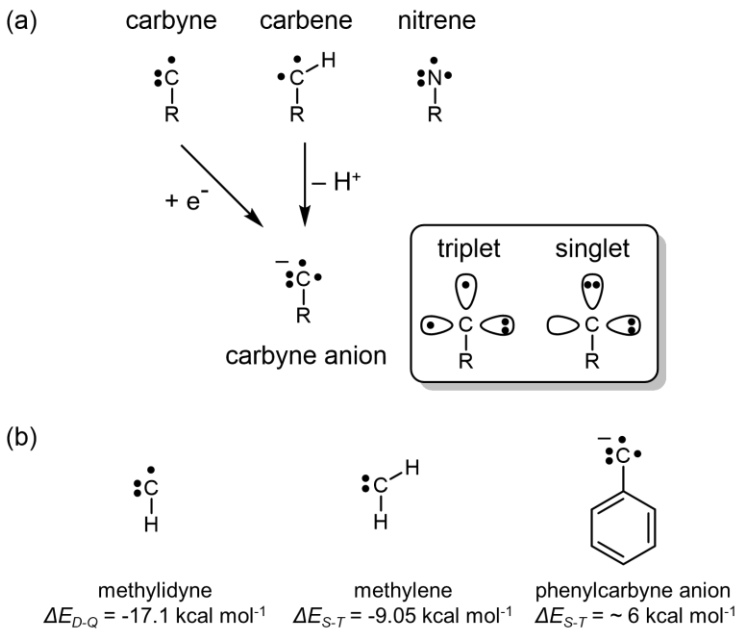

Figure 6.1. (a) Generic structures for a doublet carbyne, a triplet carbene, a triplet nitrene and a triplet carbyne anion, and the electronic structures of triplet and singlet carbyne anions. (b) The structures of the simplest doublet carbyne, singlet carbene and triplet phenylcarbyne anion and the relevant doublet-quartet and singlet-triplet splittings.[12,14,22]

If a triplet carbene is deprotonated, a triplet carbanion – carbyne anion – is produced as shown in Figure 6.1a. Carbyne anions are isoelectronic with the corresponding nitrenes (Figure 6.1a). Many phenylnitrenes have been reported to have a triplet ground state although substituents on the phenyl ring can greatly impact their ground state multiplicity.[25] Moreover, the reactivities of phenylnitrenes are sensitive to their electronic structures (e.g., triplet phenylnitrenes are more reactive than singlet ones[26]). Since altering the substitution of phenylnitrenes can influence their reactivity, the same may be expected to be true for phenylcarbyne anions. The phenylcarbyne anion (with a triplet ground state ($\Delta E_{S\text{-}T}$ ~ +6 kcal mol^{-1}); Figure 6.1b) is the only carbyne anion that has been detected experimentally (in the gas phase).[14] This study demonstrated that the phenylcarbyne anion undergoes unusual reactions that other carbanions do not, such as S atom abstraction from CS_2 and two O atom abstractions from SO_2.[14] These unprecedented reactions are driven by the large amount of energy released upon quenching the phenylcarbyne anion. Nevertheless, mechanistic details of these reactions have not been explored.

In order to explore the reactivity of phenylcarbyne anions in a more comprehensive manner and also to investigate the influence of substituents, a gas-phase reactivity study was carried out

on the phenylcarbyne anion (**1**) and its four derivatives (**2 - 5**) (Figure 6.2a). Reactions of the phenylcarbyne anions **1 - 5** were examined with four reagents (Figure 6.2b; for selection of the reagents, see discussion in Section 6.3.2).

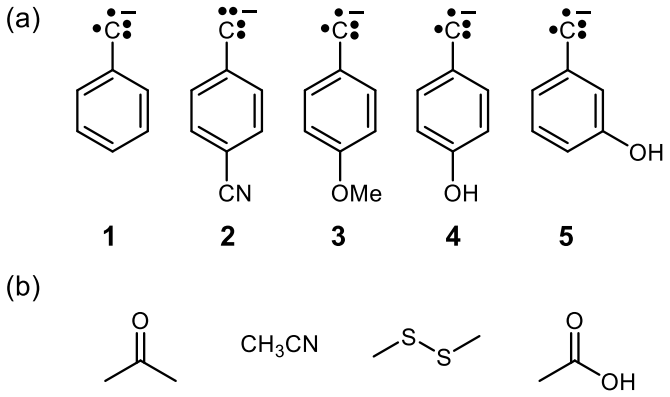

Figure 6.2. (a) Structures of the phenylcarbyne anions **1 - 5**. (b) Reagents used in this study.

6.2 Experimental section

6.2.1 Chemicals

5-Phenyl-1H-tetrazole (**P1**; purity 99%) was purchased from AK Scientific Inc. 4-(1H-Tetrazol-5-yl)phenol (**P4**; purity 97%) and 3-(1H-tetrazol-5-yl)phenol (**P5**; purity 97%) were purchased from Alfa Aesar. 5-(4-Cyanophenyl)-1H-tetrazole (**P2**) and 5-(4-methoxyphenyl)-1H-tetrazole (**P3**) are known compounds but not commercially available. They were synthesized via procedures described in the literature.[27] The starting materials for the synthesis were as follows: sodium azide (Sigma-Aldrich; purity ≥ 99.5%), copper(II) sulfate pentahydrate (Sigma-Aldrich; purity≥98%), 1,4-dicyanobenzene (Sigma-Aldrich; purity 98%) and 4-methoxybenzonitrile (Sigma-Aldrich; purity 99%). These chemicals were used as received. Acetone (purity ≥ 99.9%), acetonitrile (purity 99.8%) and dimethyl disulfide (purity≥ 99%) were obtained from Sigma Aldrich. Acetic acid (purity ≥ 99.7%) was purchased from Macron. All chemicals were used within one year after being received. Precursors **P4** and **P5** were utilized to generate deuterated phenylcarbyne anions **d-4** and **d-5** by exposing them to D_2O (Sigma-Aldrich; purity 99.9 % D atom).

Stock solutions of precursors **P1 - P5** (Figure 6.3) were prepared at a concentration of 10 mM in methanol. Stock solutions of precursors **d-P4** and **d-P5** (Figure 6.3) were prepared by dissolving precursors **P4** and **P5** at a concentration of 50 mM in D_2O and stirring the solution for 48 h.

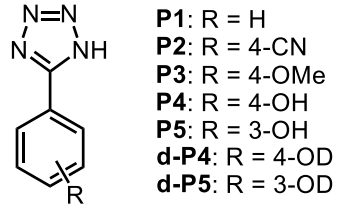

Figure 6.3. Structures of precursors **P1 - P5**, **d-P4** and **d-P5**.

6.2.2 Mass spectrometry experiments

All mass spectrometry experiments were performed using a linear quadrupole ion trap mass spectrometer (LTQ XL^{TM} Linear Ion Trap Mass Spectrometer, Thermo Scientific^{TM}) equipped with an electrospray ion (ESI) source (Thermo Scientific^{TM}, ESI Heated Probe and Ion Max M2 Housing). Stock solutions of the precursors **P1 - P5**, **d-P4** and **d-P5** were injected at a flow rate of 15 μL min^{-1} into the ESI source operated in the negative ion mode. In the ESI source, the precursor molecules were deprotonated and evaporated. All precursor anions were transferred into the linear quadrupole ion trap and isolated. At the same time, the reagents were introduced into the ion trap via the simplified, portable manifold as discussed in Section 2.5.1. The flow rates for acetone, acetonitrile, and dimethyl disulfide were 2.0 μL h^{-1} while the flow rate for acetic acid was 0.3 μL h^{-1}. The reagents were mixed with helium buffer gas before introduction into the ion trap.

The isolated phenylcarbyne anions were allowed to react with acetone, acetonitrile, dimethyl disulfide and acetic acid for various periods of time (0.03 – 5000 ms). Based on the measured reactant and product ion *m/z*-ratios and relative abundances, pseudo-first order reaction rate plots were generated to differentiate between the primary and secondary product ions and to determine the reaction efficiencies as discussed in Section 2.5.3.

The reaction efficiency (precision ± 10%; accuracy ± 50%) is the percentage of the ion-molecule collisions that leads to a reaction and was expressed as $k_{exp}/k_{coll}\times100\%$, where k_{exp} is the experimental second-order reaction rate constant and k_{coll} is the collision rate constant that can be calculated using Equation 2.25. k_{exp} was obtained by dividing the nominal rate constant k_{obs} with

the concentration of the reagent (Equation 2.24), where k_{obs} was the negative slope of a semilogarithmic plot of the relative abundance of the phenylcarbyne anion over time. The concentration of the reagent can be obtained by using Equation 2.23. In Equation 2.23, IGCF must be measured correct for the location of the ion gauge far away from the ion trap and its sensitivity toward the reagents. For the experiments using acetone and dimethyl disulfide as the reagent, IGCF was determined by measuring the rate of electron abstraction by the CS_2 radical cation from the reagent. For the experiments using acetic acid and acetonitrile as the reagent, the rates of proton abstraction by the reagents from protonated methanol and protonated formaldehyde, respectively, were utilized for the determination of IGCF. All these proton transfer and electron transfer reactions are assumed to occur at the collision rate as they are highly exothermic.

Branching ratios (precision ± 10%; accuracy ± 30%) for the primary products were determined by taking the ratio of the abundance of each primary product ion and the abundances of all product ions at early reaction times where secondary reactions had not yet taken place.

6.2.3 Computational methods

Molecular geometries for neutral **P4** and **P5** and the same compounds deprotonated at the nitrogen site or the oxygen site (Scheme 6.2) and all compounds shown in Figures 6.4 - 6.8, 6.10 and 6.11 were optimized at M06-2X/6-311++G(d,p) level of theory. The geometries for all optimized molecular structures were verified to correspond to local minima by computation of analytic vibrational frequencies. These (unscaled) frequencies were used to compute zero-point vibrational energies (ZPVE) and 298 K thermal contributions ($H_{298} - E_0$). All transition state structures were determined to have exactly one negative vibrational frequency. Intrinsic reaction coordinate (IRC) calculations were performed for all transition states to ensure that the optimized transition state structure connected the correct reactants and products.

To improve the accuracy of the molecular orbital calculations, dynamic electron correlation was accounted for with multireference second-order perturbation theory[28,29] (CASPT2) for multiconfigurational self-consistent field (MCSCF) reference wave functions. The electronic energies given are of the CASPT2/CASSCF(m,n)/cc-pVTZ//CASSCF(m,n)/cc-pVTZ variety for phenylcarbyne anions **1**-**5** and phenylcarbene anions **4'** and **5'** (where m is the number of active electrons and n is the number of active orbitals). Estimates of the thermodynamic quantities, E_0

and H_{298}, were derived by adding to these electronic energies zero-point vibrational energies (ZPVE), and the sum of ZPVE and ($H_{298} - E_0$), respectively, by using the (unscaled) CASSCF(m,n)/cc-pVTZ frequencies.

Proton affinities (PA) of phenylcarbyne anions **1-5** and phenylcarbene anions **4'** and **5'** were calculated "directly" (i.e., by using the calculated enthalpy change for proton transfer from the phenylcarbyne and phenylcarbene anions to produce the neutral phenylcarbenes. As noted above, these calculations were carried out at the CASPT2/CASSCF(m,n)/cc-pVTZ//CASSCF(m,n)/cc-pVTZ level of theory. In all cases, the calculated PAs were corrected for zero-point vibrational energy differences at 298 K by using the (unscaled) CASSCF(m,n)/cc-pVTZ frequencies.

In this chapter, all DFT calculations were carried out with Gaussian 16[30] electronic structure program suites. All of the CASPT2 and CASSCF calculations were carried out by Dr. John J. Nash (Department of Chemistry, Purdue University) by using the MOLCAS 8.0[31] electronic structure program suites.

6.3 Results and discussion

The results and discussion section is divided into three parts. The formation and structural elucidation of the phenylcarbyne anions are discussed first. After this, the observed gas-phase reactions and their efficiencies are compared and rationalized. Finally, the isomerization of the hydroxy-substituted phenylcarbyne anions to the corresponding phenylcarbene anions is discussed.

6.3.1 Generation and structural characterization of the phenylcarbyne anions

As deprotonated phenyl tetrazole has been reported to eliminate two nitrogen molecules upon CAD in a linear quadrupole ion trap (the structure of the product ion was not examined),[32] tetrazole precursors **P1 - P5**, **d-P4** and **d-P5** were selected as the precursors for the phenylcarbyne anions **1 - 5**, **d-4** and **d-5** as shown in Scheme 6.1.

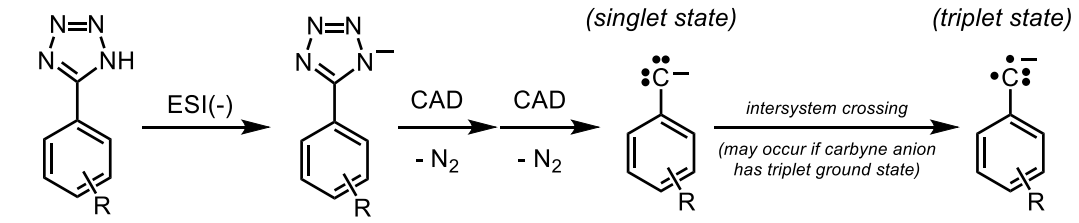

P1: R = H
P2: R = 4-CN
P3: R = 4-OMe
P4: R = 4-OH
P5: R = 3-OH
d-P4: R = 4-OD
d-P5: R = 3-OD

Scheme 6.1 Generation of the phenylcarbyne anions **1 - 5**, **d-4** and **d-5** from the precursors **P1 - P5**, **d-P4** and **d-P5**, respectively.

Tetrazole precursors **P1 - P5**, **d-P4** and **d-P5** were deprotonated via electrospray ionization operated in the negative ion mode. Upon two consecutive collision-activated dissociation (CAD) events, each of which resulted in the elimination of a nitrogen molecule, deprotonated **P1 - P3** generated ions with the *m/z*-ratios of the corresponding phenylcarbyne anions **1** – **3**. As opposed to precursors **P1 - P3**, precursors **P4** and **P5** can be deprotonated at two different sites, the oxygen atom and the nitrogen atom (Scheme 6.2). Therefore, two isomeric anions – the phenylcarbyne anions **4/5** and the distonic phenylcarbene anions **4'/5'** – may be generated upon deprotonation of **P4/P5** and two steps of CAD (Scheme 6.2). However, based on quantum chemical calculations, the formation of both isomeric anions is not equally likely.

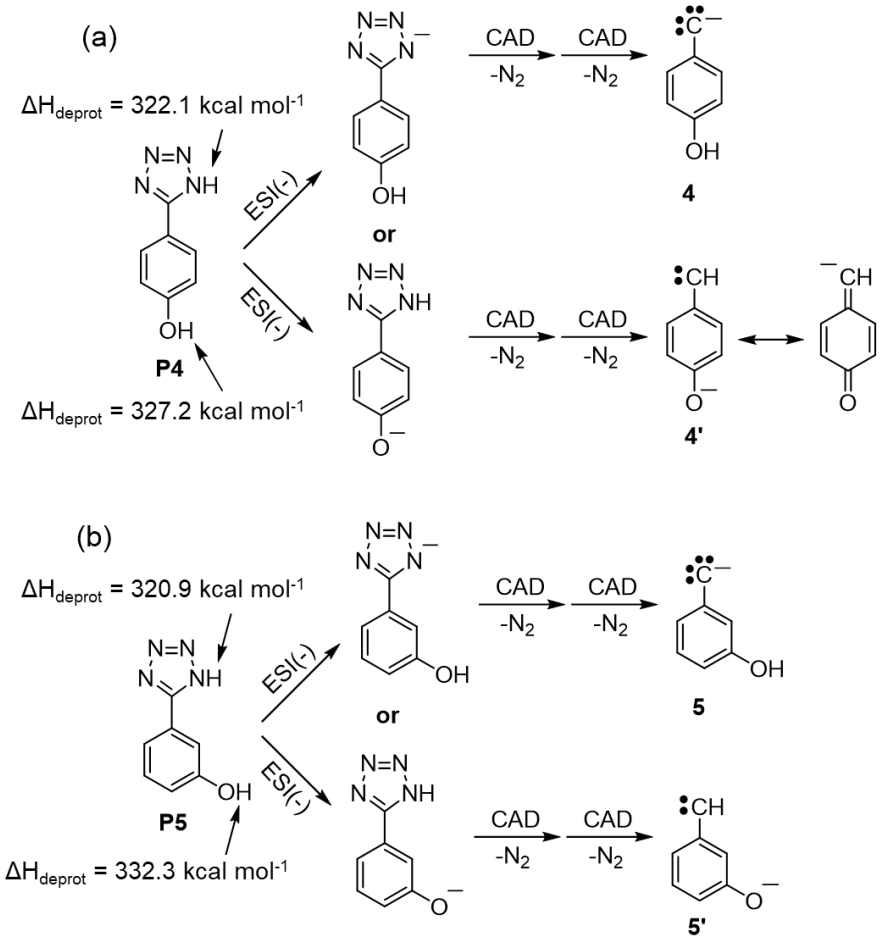

Scheme 6.2 Calculated enthalpy changes for the deprotonation (ΔH_{deprot}) of (a) **P4** and (b) **P5** at the nitrogen site and the oxygen site. The *N*-deprotonated precursors **P4** and **P5** may generate singlet phenylcarbyne anions **4** and **5**, respectively, upon two consecutive CAD events, whereas the *O*-deprotonated precursors **P4** and **P5** may generate distonic singlet phenylcarbene anions **4'** and **5'**, respectively. Enthalpies were calculated at the M06-2X/6-311++(d,p) level of theory.

The calculated enthalpy changes for deprotonation (ΔH_{deprot}) of **P4** and **P5** shown in Scheme 6.2 reveal that the deprotonation at the nitrogen atom of **P4** and **P5** requires less energy (by 5.1 and 11.4 kcal mol^{-1}, respectively) than deprotonation at the oxygen atom. Moreover, the potential energy surfaces calculated for the following CAD pathways (Figure 6.4) suggest that the generation of **4** and **5** (Figures 6.4b and 6.4d; highest barriers 51.8 and 48.8 kcal mol^{-1}, respectively) consumes less energy than the generation of **4'** and **5'** (Figures 6.4c and 6.4e; highest barriers 56.8 and 55.7 kcal mol^{-1}, respectively). Therefore, singlet phenylcarbyne anions **4** and **5** are the most likely initially formed product anions.

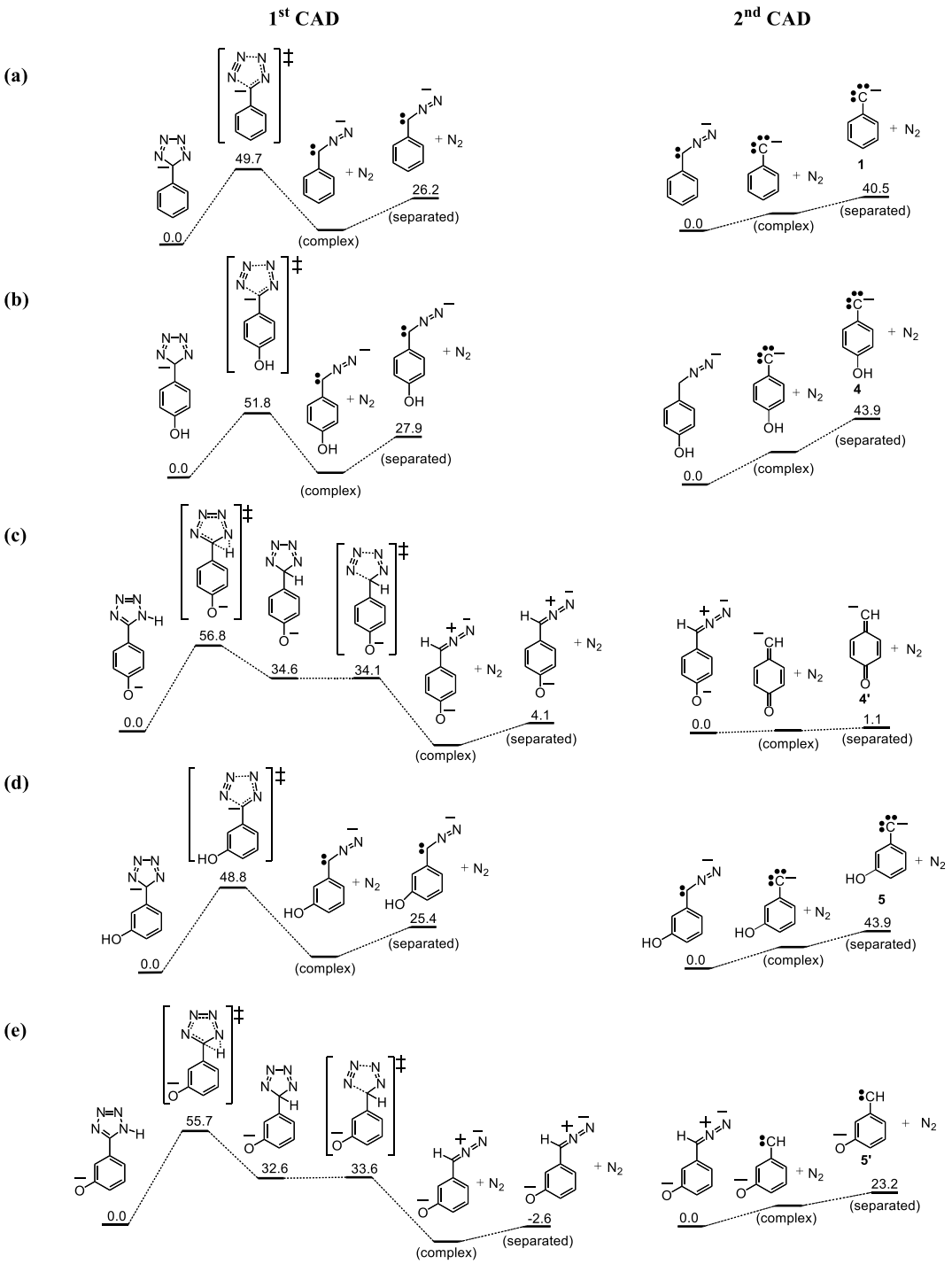

Figure 6.4. Potential energy surfaces calculated for the generation of (a) singlet phenylcarbyne anion **1** from deprotonated **P1**, (b) singlet phenylcarbyne anion **4** from **P4** deprotonated at carbon, (c) distonic singlet phenylcarbene anion **4'** from P**4** deprotonated at oxygen; this fragmentation pathway is not likely to occur, (d) singlet phenylcarbyne anion **5** from **P5** deprotonated at carbon, and (e) distonic singlet phenylcarbene anion **5'** from **P5** deprotonated at oxygen; this fragmentation pathway is not likely to occur. Enthalpies (in kcal mol^{-1}) were calculated at the M06-2X/6-311++(d,p) level of theory.

MCSCF calculations (Table 6.1) indicate that the phenylcarbyne anions **1** and **3 – 5** have triplet ground states ($E_{S\text{-}T}$ = 5.9, 7.4, 9.0, and 4.4 kcal mol^{-1}, respectively) whereas the phenylcarbyne anion **2** has a singlet ground state ($E_{S\text{-}T}$ = –1.9 kcal mol^{-1}). Therefore, the phenylcarbyne anions **1** and **3 – 5** that were initially generated in an excited singlet state upon fragmentation of their precursor ions are likely to undergo intersystem crossing to form the substantially lower energy ground-state triplet phenylcarbyne anions while being trapped. This expectation is supported by the experimental conditions used here as the anions have long lifetimes (several ms) and they undergo many collisions with the helium buffer gas. Indeed, facile intersystem crossing has been reported previously for a similar system, the distonic phenylcarbene anion.[33]

Table 6.1. Relative enthalpies[a] calculated CASPT2/CASSCF(m,n)/cc-pVTZ//CASSCF(m,n)/cc-pVTZ level of theory for the phenylcarbyne anions **1 - 5** and the distonic phenylcarbene anions **4'** and **5'** with a closed-shell singlet (CSS state (^{1}A')), open-shell singlet (OSS state (^{1}A")) and triplet state (T state (^{3}A")).

	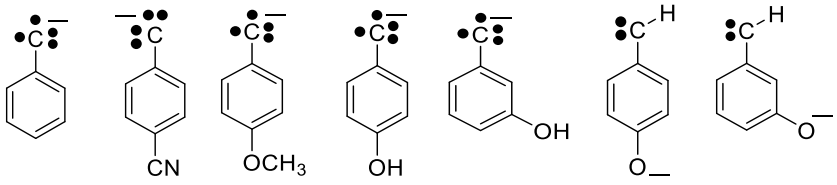						
	1	**2**	**3**	**4**	**5**	**4'**	**5'**
H_{rel} (CSS state (^{1}A')), kcal mol^{-1}	5.9	**0.0**	7.4	9.0	4.4	**0.0**	**0.0**
H_{rel} (T state (^{3}A")), kcal mol^{-1}	**0.0**	1.9	**0.0**	**0.0**	**0.0**	16.2	3.3
H_{rel} (OSS state (^{1}A")), kcal mol^{-1}	11.6	12.1	11.1	12.4	11.6	29.8	27.8

6.3.2 Reactivity of the phenylcarbyne anions

Four reagents were selected for this study. Acetic acid was chosen to study the basic nature[14] of the phenylcarbyne anions. Dimethyl disulfide was selected to explore the possibility of radical-type reactions since many organic radicals abstract •SCH_3 or •$SSCH_3$ from dimethyl disulfide.[34-36] Acetone was chosen to test whether oxygen atom abstraction reactions by the phenylcarbyne anions take place since this type of a reaction has been reported for the distonic singlet phenylcarbene anion in the gas phase.[33] Acetonitrile was selected to test whether the phenylcarbyne anions can add to acetonitrile to form an ylide or insert into a C-H single bond of acetonitrile since

these types of reactions have been reported for triplet and singlet carbenes, respectively (Scheme 6.3).[37] The results obtained upon examination of the reactions of **1 - 5** (as well as of two deuterated analogs, **d-4** and **d-5**, to be discussed later) with acetic acid, acetone, acetonitrile and dimethyl disulfide are shown in Table 6.2.

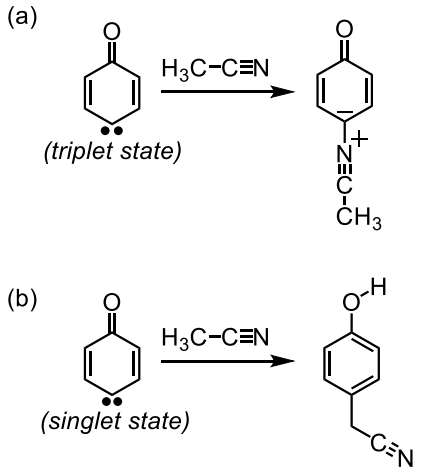

Scheme 6.3 (a) Reaction of triplet 4-oxocyclohexa-2,5-dienylidene with acetonitrile that generates an ylide.[37] (b) Reaction of singlet 4-oxocyclohexa-2,5-dienylidene with acetonitrile that generates 4-hydroxybenzylcyanide.[37]

Reactions of the phenylcarbyne anions with *acetic acid* are dominated by proton abstraction (Table 6.2) due to the high acidity of acetic acid. The conjugate base of acetic acid has a lower proton affinity[38] (PA = 348.5 kcal mol^{-1}) than most of the phenylcarbyne anions (Table 6.2); and even though **2** has a slightly lower PA (346.1 kcal mol^{-1}) than acetic acid, this anion also rapidly abstracted a proton from acetic acid.

Table 6.2. Reactions, their efficiencies,[a] and primary product branching ratios[b] for reactions of the phenylcarbyne anions **1 - 5**, **d-4** and **d-5** with acetone, acetonitrile, dimethyl disulfide and acetic acid, and the S-T gaps ($\Delta E_{S\text{-}T}$) calculated[c] for **1 - 5** as well as the proton affinities[c] (PA) calculated for **1 - 5** and the conjugate bases of the reagents.

	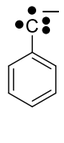 **1**	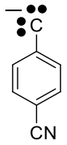 **2**	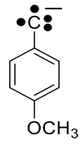 **3**	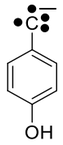 **4**	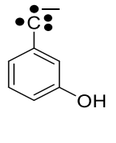 **5**	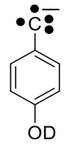 **d-4**	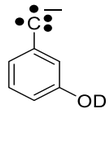 **d-5**
$\Delta E_{S\text{-}T}$, kcal mol^{-1}	5.9	-1.9	7.4	9.0	4.4		
PA, kcal mol^{-1}	376.6	346.1	379.7	379.7	375.0		
Acetone (PA[d] = 370.0 kcal mol^{-1})	H^+ abs.[e] 30% O abs. 3% Addition 67%	Addition 100%	H^+ abs. 5% O abs 2% Addition 73% Addition – $\bullet CH_3$ 20%	H^+ abs. 25% O abs. 24% Addition 20% Addition – $\bullet CH_3$ 31%	H^+ abs 7% O abs. 85% Addition 7% Addition – $\bullet CH_3$ 1%	H^+ abs. 12% O abs. 15% Addition 15% Addition – $\bullet CH_3$ 16% Rearrangement to **4'** 34% O abs. (by **4'**) 7% Addition (by **4'**) 2%	H^+ abs. 4% O abs. 27% Addition 5% Rearrangement to **5'**,[g] 27% O abs. (by **5'**) 37%
	Efficiency = 10%	**Efficiency = 0.1%**	**Efficiency = 9%**	**Efficiency = 4%** LRI[f] 19%	**Efficiency = 3%** LRI[f] 9%	**Efficiency = 6%**	**Efficiency = 5%**
Acetonitrile (PA[d] = 373.5 kcal mol^{-1})	H^+ abs. 100%	No Reaction	H^+ abs. 100%	H^+ abs. 68% CH_2 abs. 19% Addition 13%	H^+ abs. 63% CH_2 abs. 15% Addition 22%	H^+ abs. 13% Rearrangement to **4'**,[g] 83% CH_2 abs. (by **4'**) 3% Addition (of **4'**) 1%	H^+ abs. 8% Rearrangement to **5'**,[g] 89% CH_2 abs. (by **5'**) 1% Addition (of **5'**) 1%
	Efficiency = 21%		**Efficiency = 8%**	**Efficiency = 3%**	**Efficiency = 0.6%**	**Efficiency = 13%**	**Efficiency = 8%**
Dimethyl disulfide (PA[d] = 364.1 kcal mol^{-1})	Formation of CH_3S^- 60% $\bullet SSCH_3$ abs. 38% $\bullet SS\bullet$ abs. 2%	$\bullet SSCH_3$ abs. 94% $\bullet SS\bullet$ abs. 4% CH_2S abs. 4%	Formation of CH_3S^- 52% $\bullet SSCH_3$ abs. 43% $\bullet SS\bullet$ abs. 5%	Formation of CH_3S^- 7% $\bullet SSCH_3$ abs. 7% CH_2S abs. 45% CH_2S abs. – H_2S 19% CH_2S abs. – C_2H_2O 22%	Formation of CH_3S^- 4% $\bullet SSCH_3$ abs. 3% CH_2S abs. 69% CH_2S abs. – H_2S 12% CH_2S abs. – C_2H_2O 12%	Formation of CH_3S^- 9% $\bullet SSCH_3$ abs. 7% CH_2S abs.[h] 46% CH_2S abs.[h] – H_2S 14% CH_2S abs.[h] – C_2H_2O 20% Rearrangement to **4'**,[g] 5%	Formation of CH_3S^- 4% $\bullet SSCH_3$ abs. 2% CH_2S abs.[h] 69% CH_2S abs.[h] – H_2S 12% CH_2S abs.[h] – C_2H_2O 11% Rearrangement to **5'** 2%
	Efficiency = 41%	**Efficiency = 12%**	**Efficiency = 14%**	**Efficiency = 30%**	**Efficiency = 28%**	**Efficiency = 25%**	**Efficiency = 27%**
Acetic acid (PA[d] = 348.5 kcal mol^{-1})	H^+ abs. 100% (2°) Addition	H^+ abs. 58% (2°) Addition H_2O abs. 36% $H_2C{=}C{=}O$ abs. 5% Addition 1%	H^+ abs. 99% Addition 1%	H^+ abs. 98% (2°) Addition Addition 2%	H^+ abs. 94% (2°) Addition Addition 6%	H^+ abs. 71% (2°) Addition Rearrangement to **4'**,[g] 29%	H^+ abs. 70% (2°) Addition Rearrangement to **5'**,[g] 30%
	Efficiency = 57%	**Efficiency = 29%**	**Efficiency = 23%**	**Efficiency = 57%**	**Efficiency = 45%**	**Efficiency = 44%**	**Efficiency = 37%**

*[a] Reaction efficiency = k(reaction) / k(collision) × 100%; precision ±10%; accuracy ±30%. [b] Secondary products are listed below the primary product that produced them and indicated by (2°). [c] S-T gaps and PAs of the phenylcarbyne anions were calculated at the CASSCF(m,n)/cc-pVTZ level of theory. [d] PA of the conjugated bases of dimethyl disulfide are given below the reagents and they were calculated at the B3LYP/6-311++G(d,p) level of theory. [e] abs. = abstraction. [f] LRI = less reactive isomer. [g] The rearrangement to distonic phenylcarbene anions can only be detected for the deuterated phenylcarbyne anions **d-4** and **d-5** because their m/z values (m/z 106) are different from those of the distonic phenylcarbene anions **4'** and **5'** (m/z 105). These rearranged ions cannot be detected for **4** and **5** (m/z 105). [h] The CH_2S abstraction product ions of deuterated phenylcarbyne anion **d-4** and **d-5** do not contain deuterium atoms. The mechanism of this reaction is shown in Figure 6.10.*

Besides proton abstraction, only phenylcarbyne anion **2** (with the singlet ground state) abstracted a H_2O molecule (slower than proton abstraction but faster than abstraction of $H_2C{=}C{=}O$) or a $H_2C{=}C{=}O$ molecule from acetic acid. The mechanisms proposed for these reactions based on quantum chemical calculations (Figure 6.5) are initiated by nucleophilic addition of the singlet phenylcarbyne anion **2** to the carbonyl group of acetic acid followed by the formation of a cyclopropane ring (Figure 6.5), in agreement with the singlet ground state of **2**. The intermediate with a cyclopropane ring then undergoes ring opening due to ring strain, and either a $H_2C{=}C{=}O$ molecule or a H_2O molecule is eliminated via transition states at -36.7 and -15.6 kcal mol^{-1}, respectively (Figure 6.5). The lower barrier for the elimination of $H_2C{=}C{=}O$ rationalizes the greater abundance of H_2O abstraction product ions than the $H_2C{=}C{=}O$ abstraction product ions. The H_2O and $H_2C{=}C{=}O$ abstractions are both calculated to be exothermic (Figure 6.5; by -38.4 and -20.3 kcal mol^{-1}, respectively). The other phenylcarbyne anions abstract neither H_2O nor $H_2C{=}C{=}O$, likely due to their triplet ground states.

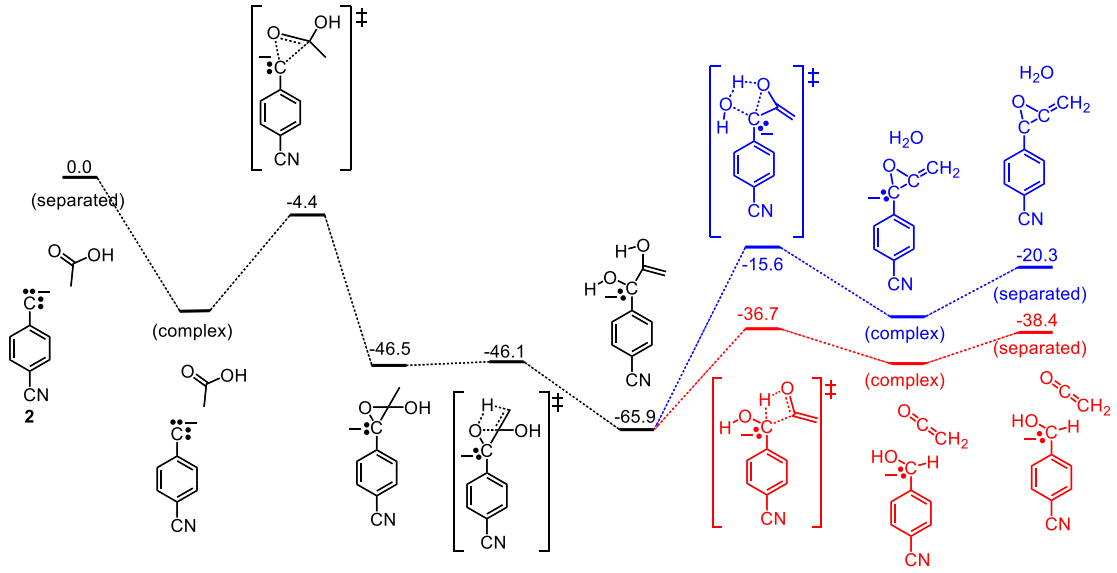

Figure 6.5. Potential energy surface (enthalpies in kcal mol^{-1}) calculated for H_2O (labeled in blue) and $H_2C{=}C{=}O$ abstraction (labeled in red) reactions by the phenylcarbene anion **2** (with singlet ground state) from acetic acid. Enthalpies were calculated at the M06-2X/6-311++G(d,p) level of theory.

Proton abstraction was found to dominate the reactions of the phenylcarbyne anions **1** and **3 - 5** with *acetonitrile* (Table 6.2). This finding can be rationalized based on the calculated PAs of

these phenylcarbyne anions (375 – 380 kcal mol^{-1}) as they are greater than that of deprotonated acetonitrile (372.1 kcal mol^{-1}).[38] On the other hand, deprotonated acetonitrile has a PA that is greater than that of the phenylcarbyne anion **2** (PA = 346.1 kcal mol^{-1}); therefore, this anion (with a singlet electronic ground state) is unreactive toward acetonitrile.

Formation of a stable adduct occurs upon interactions of all phenylcarbyne anions with *acetone* (possibly as shown in the first three steps of the reactions shown in Figure 6.6; exothermic by at least 50 kcal mol^{-1} for **4** and **5**). Phenylcarbyne anions **1** and **3 – 5** also abstract a proton from acetone as the PA of its conjugate base[38] (370.0 kcal mol^{-1}) is lower than that of the phenylcarbyne anions. In addition, the phenylcarbyne anions (with a triplet ground state) abstract an oxygen atom from acetone. For **4** and **5**, this is the major reaction pathway while for **1** and **3**, formation of a stable adduct dominates. Based on quantum chemical calculations, the oxygen atom abstraction involves a radical addition of the triplet carbyne anions to the C=O double bond of acetone to generate a biradical intermediate (Figure 6.6). This biradical intermediate undergoes intersystem crossing and a bond is formed spontaneously to generate an adduct ion with a cyclopropane ring. This formation of the adduct ion was calculated to be highly exothermic (Figure 6.6; -51.5 kcal mol^{-1} for **4** and -51.2 kcal mol^{-1} for **5**). After the addition, a propene molecule is eliminated to generate the oxygen atom abstraction product, which is highly exothermic (Figure 6.6; -43.7 kcal mol^{-1} for **4** and -39.8 kcal mol^{-1} for **5**). The phenylcarbyne anion **2** does not abstract an oxygen atom from acetone, possibly due to its singlet ground state (although the singlet-triplet splitting is only -1.9 kcal mol^{-1}).

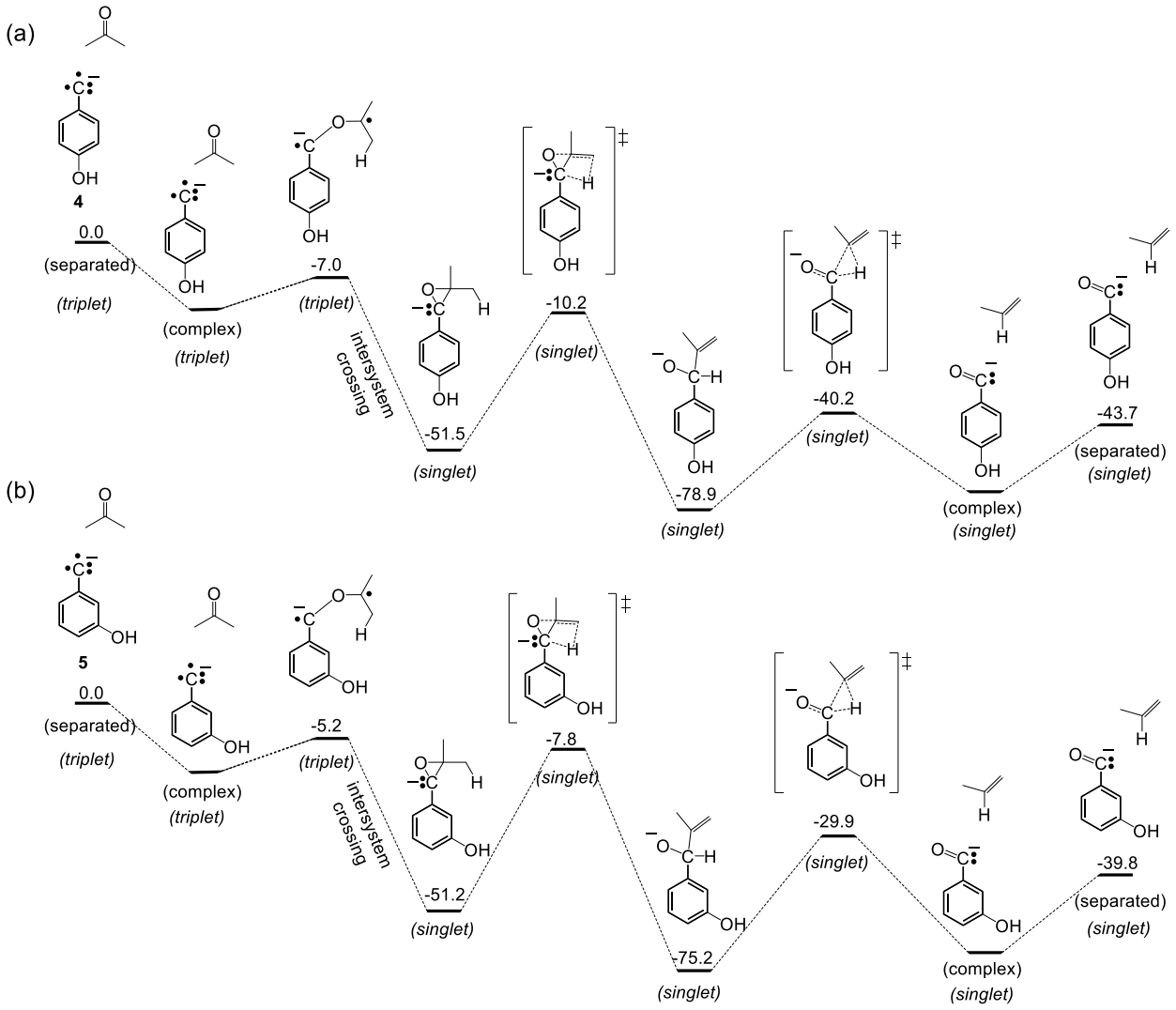

Figure 6.6. Potential energy surfaces (enthalpies in kcal mol^{-1}) calculated at the M06-2X/6-311++G(d,p) level of theory for oxygen atom abstraction by the phenylcarbyne anions (a) **4** and (b) **5** from acetone.

No deprotonated *dimethyl disulfide* was observed upon reactions of the phenylcarbyne anions **1** – **5** with dimethyl disulfide (Table 6.2) even though the PAs of all phenylcarbyne anions with triplet ground states are greater than that of deprotonated dimethyl disulfide (369.8 kcal mol^{-1}, calculated at the B3LYP/6-311++G(d,p) level of theory). A likely reason for this finding is the spontaneous elimination of thioformaldehyde upon deprotonation of dimethyl disulfide to form the methanethiolate anion (CH_3S^-) that was the dominant product ion for reactions of **1** and **3** with dimethyl disulfide (Figure 6.7a; Table 6.2). This reaction was calculated to be exothermic by 88.1

kcal mol^{-1} (for **1**, see Figure 6.7b). The formation of CH_3S^- is also dominant for **4** and **5** but in these cases, it reacts with the biradical product, which will be discussed later.

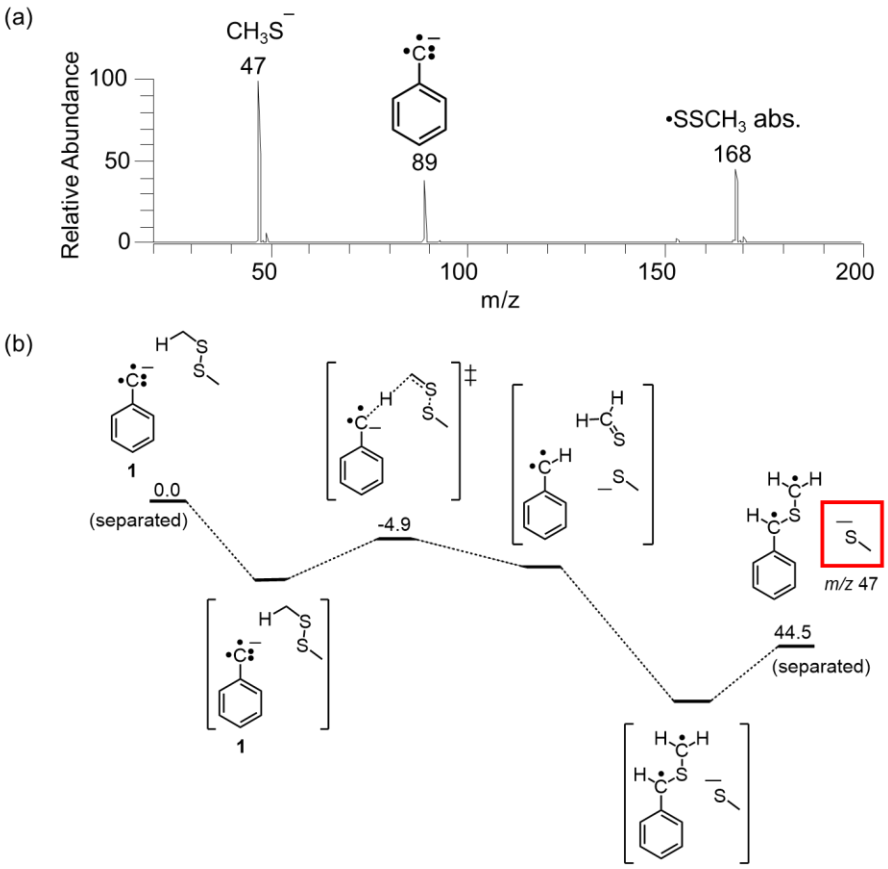

Figure 6.7. (a) Mass spectrum measured after 100 ms reaction of the isolated phenylcarbyne anion **1** with dimethyl disulfide. (b) Potential energy surface (enthalpies in kcal mol^{-1}) calculated at the M06-2X/6-311++G(d,p) level of theory for the generation of the methanethiolate anion (*m/z* 47) upon reactions of **1** with dimethyl disulfide via proton abstraction followed by radical addition to $H_2C{=}S$ leading to formation of CH_3S^-.

In addition to the reactions discussed above, all phenylcarbyne anions abstract •$SSCH_3$ from dimethyl disulfide (Table 6.2). This reaction has been reported to be common for phenyl mono- and biradicals.[34,36,39] Therefore, this radical reaction is in agreement with the triplet ground states of the phenylcarbyne anions **1** and **3 - 5**. Although **2** has a singlet ground state, the small S-T splitting (-1.9 kcal mol^{-1}) still allows **2** to abstract •$SSCH_3$ from dimethyl disulfide. The •$SSCH_3$ abstraction probably involves abstraction of two •CH_3S radicals by the phenylcarbyne anions and then dissociation of the adduct via a homolytic C-S bond cleavage and elimination of a methyl

radical (see Scheme 6.4 using phenylcarbyne anion **1** as an example), as •CH_3S abstraction from dimethyl disulfide has been reported to occur for many triplet biradicals[34,36,39] and the homolytic C-S bond dissociation energy is low.[40,41]

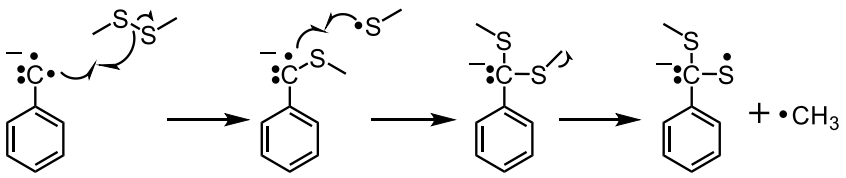

Scheme 6.4. Proposed mechanisms for •$SSCH_3$ abstraction by the triplet phenylcarbyne anion **1** from dimethyl disulfide.

CH_2S abstraction has been observed in the reactions of aromatic singlet biradicals with dimethyl disulfide.[36,39,42] Therefore, the observation of this reaction for the phenylcarbyne anion **2** (with a singlet ground state) is not surprising. However, the phenylcarbyne anions **4** and **5** also generated an abundant CH_2S-abstraction product, despite their triplet ground states. This reactivity will be discussed in more detail in Section 6.3.4.

The unsubstituted phenylcarbyne anion **1** has a substantially higher reactivity towards all the four reagents than its derivatives (**2 - 5**, **d-4** and **d-5**). The lower efficiency for substituted phenylcarbyne anions can be rationalized by the extra delocalization of the negative charge provided by the π-orbitals of the substituents. On the other hand, the phenylcarbyne anion **2** demonstrates lower reactivity than its derivatives, likely due to its singlet electronic ground state (S-T splitting = -1.9 kcal mol^{-1}, Table 6.2), which suggests that most reactions observed for the derivatized phenylcarbyne anions are radical reactions and occur from their triplet ground states. The lower proton affinity of **2** (346.1 kcal mol^{-1}) than that of the other phenylcarbyne anions partially explains its low reactivity.

6.3.3 Isomerization of the hydroxy-substituted phenylcarbyne anions 4 and 5

Although most of the observations have been rationalized above, some results obtained for the hydroxy-substituted phenylcarbyne anions remain a puzzle. For example, the hydroxy-substituted phenylcarbyne anions **4** and **5** abstract a proton from acetonitrile far more slowly than **1** and somewhat less slowly than **3** (Table 6.2). However, the proton affinities of **4** and **5** (379.7

and 375.0 kcal mol^{-1}, respectively) are similar to those of **1** and **3** (376.6 and 379.7 kcal mol^{-1}, respectively). Therefore, some unidentified competing reaction that reduces the rate of proton abstraction from acetonitrile must exist. The above observation was not made for the reactions of **4** and **5** with acetic acid because the proton affinities of **4** and **5** are far greater than that of the acetate anion, which makes proton abstraction fast. Moreover, phenylcarbyne anions **4** and **5** abstract CH_2 from acetonitrile and dimethyl disulfide, which was not observed for phenylcarbyne anions **1 – 3**. These unexpected observations require a more in-depth look into the chemistry of **4** and **5**.

Since **4** and **5** both contain a hydroxyl group, they may be able to isomerize to the substantially lower-energy distonic phenylcarbene anions with the aid of a neutral molecule (Scheme 6.5). Neutral compounds have been reported to facilitate isomerization of gas-phase ions. For instance, gaseous *N*-protonated 4-aminobenzoic acid has been demonstrated to isomerize to *O*-protonated 4-aminobenzoic acid via the assistance of methanol molecules.[43] The energy of *O*-protonated 4-aminobenzoic acid is 5.6 kcal mol^{-1} lower than *N*-protonated 4-aminobenzoic acid, which is a driving force for the isomerization.[43] This isomerization was proposed to be initiated by proton transfer from the *N*-protonated 4-aminobenzoic acid to the methanol molecule, which is followed by proton transfer from the protonated methanol to the carbonyl oxygen of the neutral 4-aminobenzoic acid (Scheme 6.5a). Isomerization of the triplet phenylcarbyne anions **4** and **5** to the distonic triplet phenylcarbene anions **4'(T)** and **5'(T)** may also take place with the assistance of reagent molecules in the ion trap. These isomerizations are calculated to be exothermic by -54.3 kcal mol^{-1} and -36.4 kcal mol^{-1}, respectively (Scheme 6.5b).

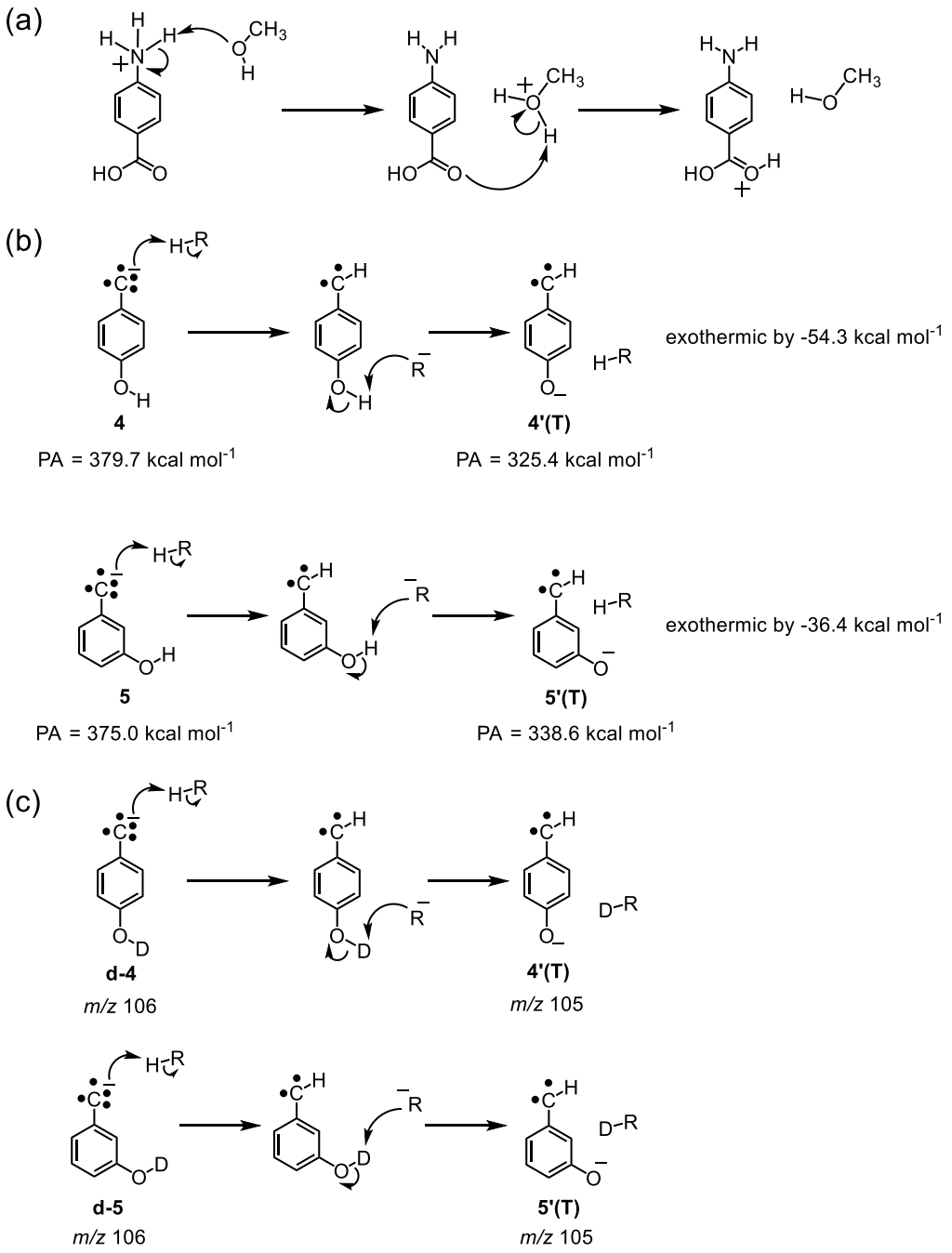

Scheme 6.5. (a) A mechanism reported[43] for the isomerization of *N*-protonated 4-aminobenzoic acid to *O*-protonated 4-aminobenzoic acid with the assistance of a methanol molecule in the gas phase. (b) Possible mechanisms of isomerization for the triplet phenylcarbyne anions **4** and **5** to the distonic triplet phenylcarbene anions **4'(T)** and **5'(T)** with the assistance of a reagent molecule (R-H = Reagent). (c) The deuterated triplet phenylcarbyne anions **d-4** and **d-5** (*m/z* 106) can rearrange to undeuterated distonic triplet phenylcarbene anions **4'(T)** and **5'(T)** (*m/z* 105) with the assistance of a reagent molecule (R-H).

Although **4'(T)** and **5'(T)** were likely initially generated in their triplet states as shown in Scheme 6.5b, they are likely to undergo intersystem crossing and then react from their singlet ground states (Table 6.1, S/T splitting -16.2 kcal mol^{-1} for **4'** and -3.3 kcal mol^{-1} for **5'**). This is likely as the time scale of intersystem crossing is on the order of 10^{-12} – 10^{-3} s,[44-46] whereas the time scale of the ion-molecule reactions studied here is on the order of 10^{-3} – 10 s.

In order to be able to assist in the isomerization, the conjugate base of the reagent molecule must have a PA that is between the PAs (Figure 6.5b) of the phenylcarbyne anions (**4** and **5**) and the distonic phenylcarbene anions (**4'** and **5'**).[47-49] Therefore, acetone (PA of its conjugated base[38] = 370.0 kcal mol^{-1}), acetonitrile (PA of its conjugated base[38] = 373.5 kcal mol^{-1}), dimethyl disulfide (calculated PA of its conjugated base = 364.1 kcal mol^{-1}) and acetic acid (PA of its conjugated base[38] = 348.5 kcal mol^{-1}) are all able to assist in the isomerization. However, water cannot assist in the isomerization because the PA of the hydroxide anion[50] (390.8 kcal mol^{-1}) is even greater than that of **4** and **5**.

Although the isomerization discussed above are likely to occur as they are highly exothermic and barrierless (proton transfer reactions are usually barrierless unless they are sterically hindered), they cannot be experimentally observed as the rearranged distonic phenylcarbene anions **4'** and **5'** have the same *m/z*-ratios as the phenylcarbyne anions **4** and **5**. Therefore, to explore the possibility of isomerization of **4** and **5**, precursors **d-P4** and **d-P5** (Scheme 6.5c) were utilized to generate deuterated phenylcarbyne anions **d-4** and **d-5**. If these anions undergo rearrangement facilitated by a reagent molecule, the proton on the reagent molecule will be abstracted by **d-4** or **d-5**, followed by deuterium transfer from protonated **d-4**/**d-5** to the deprotonated reagent molecule (Scheme 6.6c). This process generates undeuterated distonic triplet phenylcarbene anions **4'(T)** and **5'(T)** from the deuterated phenylcarbyne anions. Therefore, the rearrangement products – distonic phenylcarbene anions **4'** and **5'** (*m/z* 105) – can be differentiated from the deuterated phenylcarbyne anions **d-4** and **d-5** based on their different *m/z*-ratios (*m/z* 106).

The observation of the generation of ions of *m/z* 105 upon the reactions of deuterated phenylcarbyne anions **d-4** and **d-5** with acetic acid (Table 6.2) demonstrates that acetic acid can cause the rearrangement of deuterated phenylcarbyne anions **d-4** and **d-5** to the undeuterated distonic phenylcarbene anions **4'** and **5'**. Nevertheless, proton abstraction from acetic acid still dominates for both **d-4** and **d-5**. Therefore, the reaction efficiencies were barely affected by the rearrangement. The singlet distonic phenylcarbene anions **4'** and **5'** are not expected to abstract

proton from acetic acid because their PAs (338.6 and 325.4 kcal mol^{-1}, Scheme 6.5b) are even smaller than that of deprotonated acetic acid (348.5 kcal mol^{-1}).

Another reagent that can cause the above rearrangement is acetonitrile. The ions thought to be the triplet phenylcarbyne anions **4** and **5** were observed to abstract CH_2 from acetonitrile (Figure 6.8a using the phenylcarbyne anion **4** as an example). However, the CH_2 abstraction product ions (*m/z* 119) observed in the reactions of **d-4** and **d-5** (Figure 6.8b using **d-4** as an example) have the same *m/z* value as the corresponding product ions of reactions of **4** and **5**. These results indicate that the CH_2 abstraction product ions of **d-4** and **d-5** do not contain deuterium. Therefore, it can be concluded that CH_2 was abstracted by the undeuterated distonic phenylcarbene anions **4'** and **5'** instead of the phenylcarbyne anions **d-4** and **d-5**. The methylene abstraction by the distonic phenylcarbene anions may be initiated by C-H insertion, which is common for singlet carbenes.[51,52] As indicated in Figures 6.8c and 6.8d, the distonic singlet phenylcarbene anion **4'** can insert into a C-H bond of acetonitrile in a concerted manner. The adduct ion eliminates a hydrogen cyanide molecule to generate the CH_2 abstraction product ion (Figures 6.8c and 6.8d). The isomerization, intersystem crossing and CH_2 abstraction by **4'** and **5'** were calculated to be exothermic by -86.3 and -78.5 kcal mol^{-1}, respectively (Figures 6.8c and 6.8d).

As shown in Table 6.2, **d-4** and **d-5** have much greater total reaction efficiencies toward acetonitrile (13% and 8%) than **4** and **5** (3% and 0.6%). The reason for this is that acetonitrile causes the most efficient isomerization (83% and 89% branching ratios, Table 6.2; see Section 6.2.2 for the method of obtaining the branching ratios) among all the reagents. Since the isomerized ions cannot be detected in the mass spectra of **4** and **5** as they have the same *m/z*-ratios as **4** and **5** the isomerization must be ignored when determining the reaction efficiencies for **4** and **5**. On the other hand, the isomerized ions can be detected in the reactions of deuterated phenylcarbyne anions **d-4** and **d-5**. Therefore, the experiments performed for **d-4** and **d-5** revealed the real reaction efficiencies for the reactions of the phenylcarbyne anions **4** and **5**.

Figure 6.8. (a) Mass spectra measured after 300 ms reactions of a mixture of the isolated phenylcarbyne anion **4** and the distonic phenyl carbene anion **4'**. (b) Mass spectra measured after 300 ms reactions of a mixture of the isolated phenylcarbyne anion **d-4** and the distoinic phenylcarbene anion **4'** with acetonitrile. (c) Potential energy surfaces (enthalpies in kcal mol^{-1}) calculated at the M06-2X/6-311++G(d,p) level of theory for the isomerization of the phenylcarbyne anion **4** to the distonic triplet phenylcarbene anion **4'(T)** upon interactions with acetonitrile, followed by intersystem crossing to distonic singlet phenylcarbene anion **4'**, which abstract a CH_2 from acetonitrile. (d) Potential energy surfaces (enthalpies in kcal mol^{-1}) calculated at the M06-2X/6-311++G(d,p) level of theory for the phenylcarbyne anion **5** that undergoes the same process shown in Figure 6.8c.

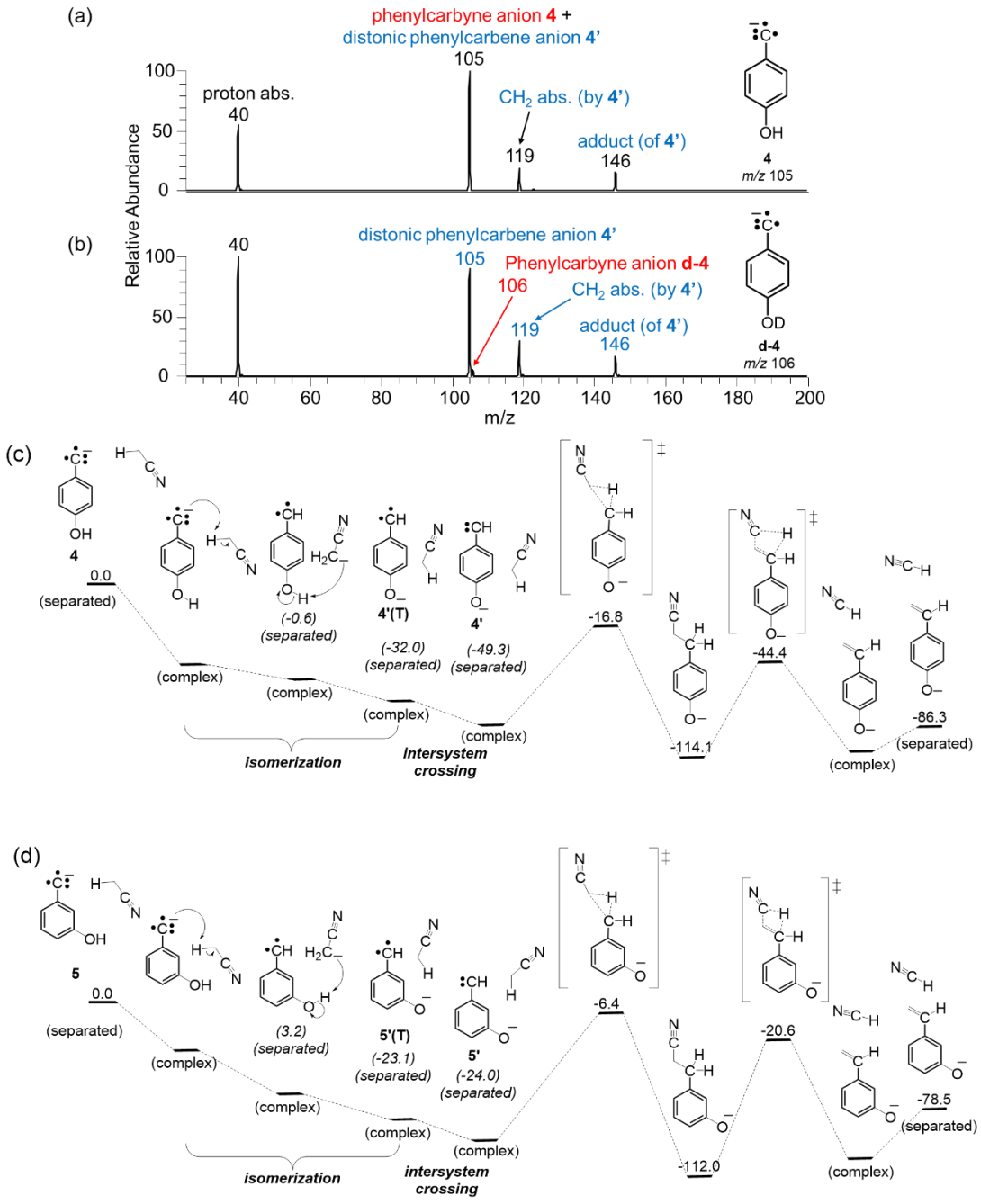
(a)
phenylcarbyne anion 4 +
distonic phenylcarbene anion 4'
105
proton abs.
40
CH2 abs. (by 4')
119
adduct (of 4')
146
4
m/z 105
(b)
distonic phenylcarbene anion 4'
40
105
Phenylcarbyne anion d-4
106
CH2 abs. (by 4')
119
adduct (of 4')
146
d-4
m/z 106
Relative Abundance
m/z
(c)
4
0.0
(separated)
(-0.6)
(separated)
4'(T)
(-32.0)
(separated)
4'
(-49.3)
(separated)
(complex)
(complex)
(complex)
(complex)
isomerization
intersystem crossing
-16.8
-114.1
-44.4
(complex)
-86.3
(separated)
(d)
5
0.0
(separated)
(3.2)
(separated)
5'(T)
(-23.1)
(separated)
5'
(-24.0)
(separated)
(complex)
(complex)
(complex)
(complex)
isomerization
intersystem crossing
-6.4
-112.0
-20.6
(complex)
-78.5
(separated)

As discussed above, all tested phenylcarbyne anions with a triplet ground state were observed to abstract an oxygen atom from acetone (Table 6.2), likely via a radical mechanism (Figure 6.6). Examination of the reactivities of the mixtures of **d-4/d-5** and **4'**/**5'** (Table 6.2) indicates that both the triplet phenylcarbyne anions (**d-4** and **d-5**) and the distonic singlet phenylcarbene anions (**4'** and **5'**) can abstract an oxygen atom from acetone, as ions of *m/z* 122 (oxygen atom abstraction product of **d-4/d-5**) and *m/z* 121 (oxygen atom abstraction product of **4'/5'**) were both observed (Figures 6.9a and 6.9b). This finding suggests that the distonic singlet phenylcarbene anions generated upon isomerization of the triplet phenylcarbyne anions catalyzed by acetone rapidly reacted within the same collision complex with the same acetone molecule to abstract an oxygen atom. This finding is in agreement with the similar reaction efficiencies measured for **4/5** and **d-4/d-5**, as opposed to the very different reaction efficiencies measured for these ion pairs upon interactions with acetonitrile. The oxygen atom abstraction by **4'** and **5'** from acetone is consistent with the reported reactions of singlet methylene[53] ($^1CH_2$) and distonic singlet phenylcarbene anion **5'**,[33] which abstract an oxygen atom from CO_2 and NO_2, respectively. The oxygen abstraction from CO_2 by methylene was proposed to involve nucleophilic addition to the C=O group followed by the elimination of a CO molecule.[49] Therefore, the oxygen atom abstraction from acetone by **4'** and **5'** may be initiated by nucleophilic addition followed by the elimination of a propene molecule (Figure 6.9c, **4'** as an example).

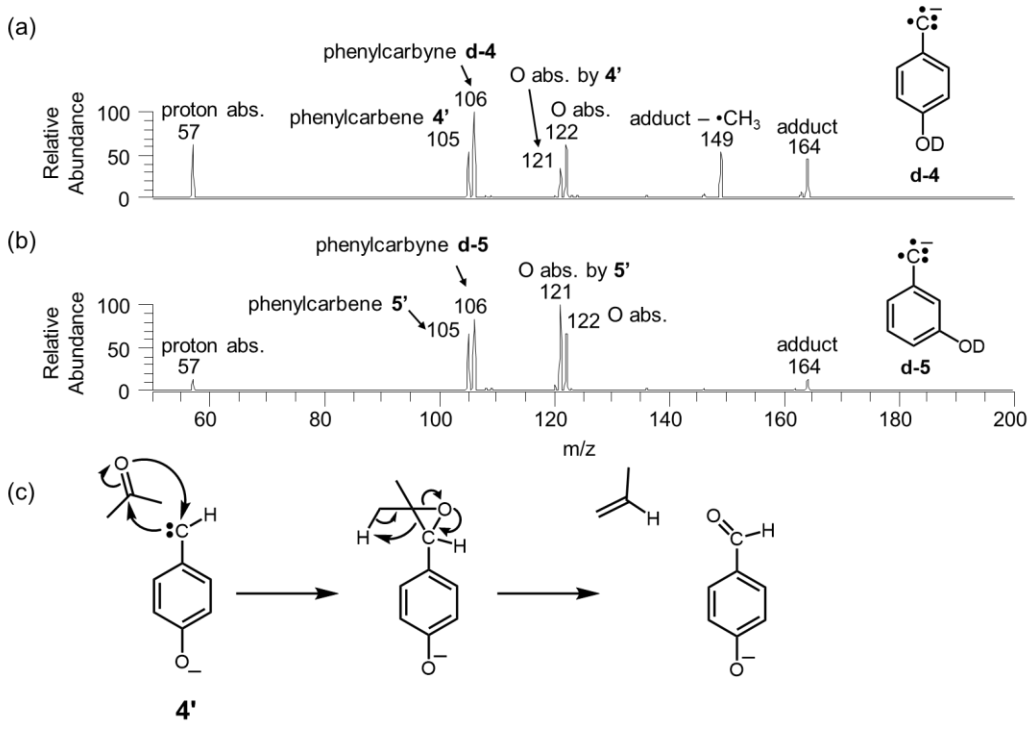

Figure 6.9. (a) Mass spectra measured after 300 ms reactions of a mixture of the isolated phenylcarbyne anion **d-4** and the distoinic phenylcarbene anion **4'** with acetone. (b) Mass spectra measured after 300 ms reactions of a mixture of the isolated phenylcarbyne anion **d-5** and the distoinic phenylcarbene anion **5'** with acetone. (c) Proposed mechanisms for oxygen atom abstraction by the singlet distonic phenylcarbene anion **4'** from acetone.

6.3.4 Abstraction of CH_2S from dimethyl disulfide by 4 and 5

The isomerization discussed above barely occur upon interactions of **4** and **5** with dimethyl disulfide as few distonic phenylcarbene anions (*m/z* 105) were observed to be generated upon reactions of **d-4** and **d-5** upon interactions with dimethyl disulfide (Table 6.2, Figure 6.10b). Isomerization is not favorable because the S-S bond in deprotonated dimethyl disulfide readily breaks when the phenylcarbyne anions **4** and **5** abstract a proton from dimethyl disulfide (Figure 6.10d using **4** as an example). The products are the neutral triplet phenylcarbene, the methanethiolate anion (CH_3S^-) and thioformaldehyde (CH_2S). The neutral triplet phenylcarbene can add to CH_2S to generate a triplet biradical and the methanethiolate anion (CH_3S^-). This reaction was calculated to be exothermic by -46.1 kcal mol^{-1} (Figure 6.10d). If intersystem crossing occurred and the triplet biradical underwent cyclization, the reaction would be exothermic by -90.3 kcal mol-1 (Figure 6.10d).

Figure 6.10. (a) Mass spectrum measured after 100 ms reaction of isolated phenylcarbyne anion **4** with dimethyl disulfide. (b) Mass spectrum measured after 100 ms reaction of isolated phenylcarbyne anion **d-4** with dimethyl disulfide. (c) A CAD mass spectrum of the final product ions of *m/z* 151 isolated after reactions of **4** with dimethyl disulfide (Figure 6.10a). The calculated potential energy surfaces for these fragmentation reactions are shown in Figure 6.11. (d) Potential energy surface (enthalpies in kcal mol^{-1}) calculated at the M06-2X/6-311++G(d,p) level of theory for the generation of CH_3S^- for **4** (as shown in Figure 6.7 for **1**) followed by abstraction of a proton by CH_3S^- to yield the final CH_2S abstraction product (ions of *m/z* 151).

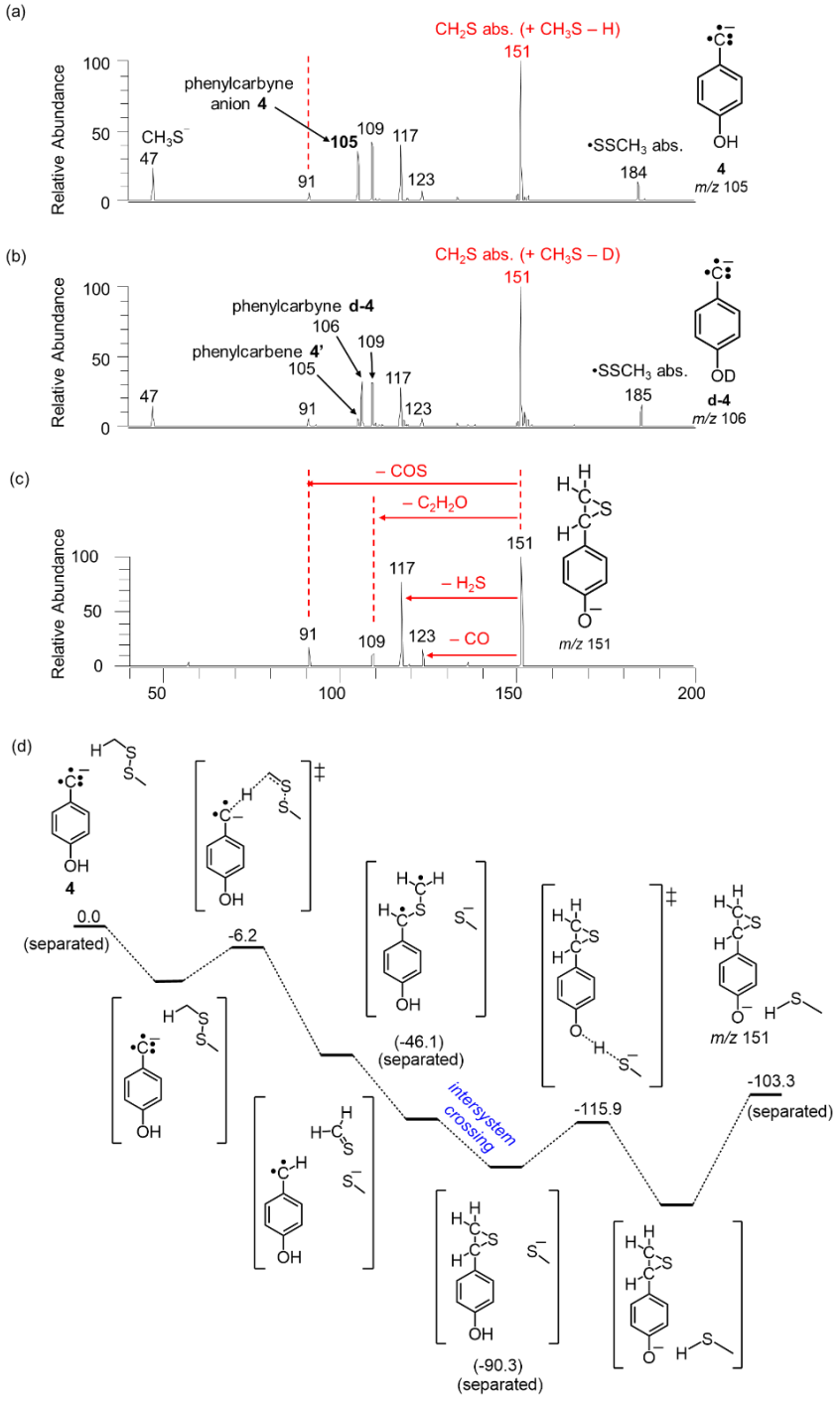
(a)
CH2S abs. (+ CH3S – H)
151
phenylcarbyne anion 4
105
109
117
CH3S
47
91
123
•SSCH3 abs.
184
4
m/z 105
Relative Abundance
100
50
0
(b)
CH2S abs. (+ CH3S – D)
151
phenylcarbyne d-4
106
109
phenylcarbene 4'
105
117
47
91
123
•SSCH3 abs.
185
OD
d-4
m/z 106
(c)
– COS
– C2H2O
151
117
– H2S
91
109
123
– CO
m/z 151
50
100
150
200
(d)
4
0.0
(separated)
-6.2
(-46.1)
(separated)
intersystem crossing
-115.9
-103.3
(separated)
m/z 151
(-90.3)
(separated)

As discussed above, CH_2S abstraction from dimethyl disulfide was observed for **2**, **4** and **5** (Table 6.2) and it was the fastest reaction for **4** and **5** (Figure 6.10a using **4** as an example). As this reaction has been reported for some singlet biradicals whose radical sites are close to each other,[36] CH_2S abstraction by **2** was expected. However, this was not expected for the reactions of triplet phenylcarbyne anions **4** and **5**. Therefore, there must be a different mechanism for CH_2S abstraction by the hydroxyl substituted phenylcarbyne anions **4** and **5**.

Reactions of the deuterated phenylcarbyne anions **d-4** and **d-5** with dimethyl disulfide provide some evidence for the mechanism of CH_2S abstraction. Upon reactions of **d-4** and **d-5** with dimethyl disulfide, the product ions of *m/z* 151 were generated (Figure 6.10b), whose *m/z*-ratio is the same as that of the product ions of the undeuterated phenylcarbyne anions **4** and **5** (*m/z* 151, Figure 6.10a). This finding indicates that the deuterated phenylcarbyne anions **d-4** and **d-5** produce undeuterated CH_2S abstraction product ions upon reactions with dimethyl disulfide. A feasible mechanism was proposed to rationalize the generation of the undeuterated CH_2S abstraction product ions (Figure 6.10d). As discussed above, the CH_3S^- anion is likely to be generated upon reactions of **d-4** and **d-5** with dimethyl disulfide. The CH_3S^- anion may then abstract a deuterium cation from the neutral distonic phenylcarbene to form undeuterated CH_2S abstraction product ions (Figure 6.10d). The formation of the CH_2S abstraction product ions was calculated to be exothermic by -103.3 kcal mol^{-1}. The structure of the CH_2S abstraction product ion for **4** and **d-4** is proposed to be that shown in Figure 6.10c. The CH_2S abstraction product ion (*m/z* 151) formed for **4** and **d-4** was subjected to CAD to probe its structure (Figure 6.10c). Ions of *m/z* 91, 109, 117 and 123 were generated upon elimination of S=C=O, H_2C=C=O, H_2S or CO, respectively. These ions were also observed in the reaction mass spectra of **4** and **d-4** as shown in Figures 6.10a and 6.10b. Calculated mechanisms for the fragmentations are illustrated in Figure 6.11, which supports the proposed structure of the product ion *m/z* 151.

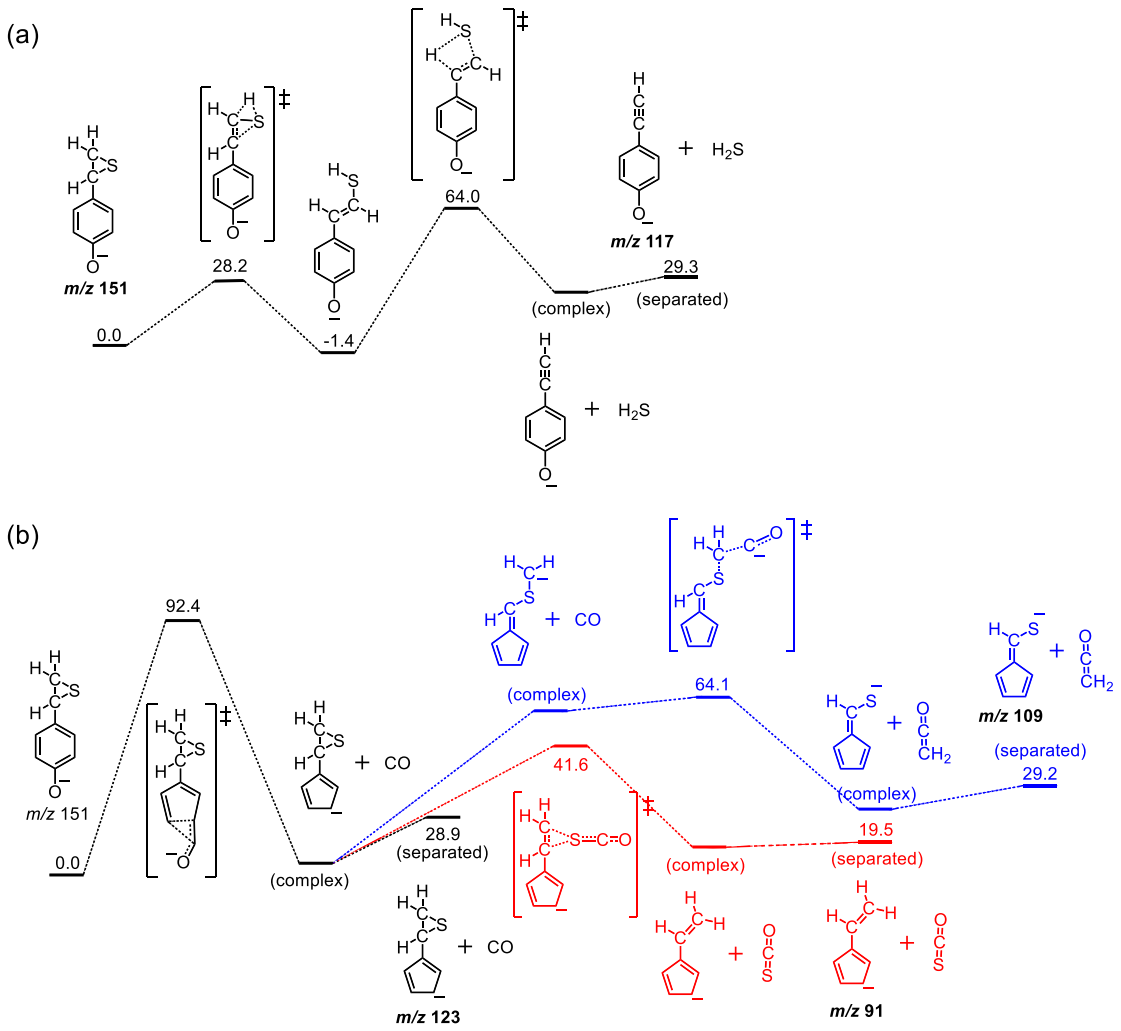

Figure 6.11. Potential energy surfaces (enthalpies in kcal mol^{-1}) calculated at the M06-2X/6-311++G(d,p) level of theory for the generation of fragment ions of (a) *m/z* 117, (b) *m/z* 123 (in black color), 109 (in blue color) and 91 (in red color) upon CAD of the ion of *m/z* 151. The ion of *m/z* 151 was generated upon the reactions of the distonic phenylcarbene anion **4'** with dimethyl disulfide (Figures 6.10a and 6.10b). Upon CAD, fragment ions of *m/z* 123, 117, 109 and 91 are generated via the elimination of CO, H_2S, $H_2C{=}C{=}O$ or $S{=}C{=}O$, respectively.

6.4 Conclusions

The phenylcarbyne anions **1 – 5** were generated in a linear quadrupole ion trap upon two consecutive CAD experiments to cleave two nitrogen molecules from the tetrazole precursors **P1 – P5**. MCSCF calculations indicate that the phenylcarbyne anion **1** and its three derivatives **3 - 5** have a triplet electronic ground state whereas the cyano-substituted phenylcarbyne anion **2** has a singlet ground state. MCSCF calculations also indicate that the proton affinities of **1** and **3 - 5** (375 – 380 kcal mol^{-1}) are substantially greater than that of **2** (346.1 kcal mol^{-1}). Therefore, it is not

surprising that the phenylcarbyne anions with triplet ground states were found to be so basic that they abstracted a proton even from reagents that are not considered to be Brønsted acids, such as acetone and acetonitrile. In sharp contrast, the 4-cyanophenylcarbyne anion (with a singlet ground state) only abstracted a proton from acetic acid.

All phenylcarbyne anions abstracted a •$SSCH_3$ group from *dimethyl disulfide*, which likely occurs via a radical mechanism and therefore probably involves the excited triplet state of the singlet phenylcarbyne anion **2**. Calculations also suggested that the formation of SCH_3^- upon reactions of **1** and **3 - 5** with dimethyl disulfide occurs via a radical mechanism. The phenylcarbyne anions with triplet ground states (**1** and **3 - 5**) were observed to abstract an oxygen atom from *acetone* via a radical mechanism based on quantum chemical calculations. On the other hand, **2** with a singlet ground state was the only phenylcarbyne anion studied that abstracted a H_2O or a $H_2C{=}C{=}O$ molecule from *acetic acid*, likely via a concerted C=O double bond insertion followed by the elimination of $H_2C{=}C{=}O$ or H_2O molecule, respectively. The phenylcarbyne anion **1** displayed a greater overall reactivity towards the four reagents than all of its derivatives (**2 - 5**), possibly because the π-orbitals of the substituents enable delocalization of the negative charge onto the substituents.

Hydroxy-substituted triplet phenylcarbyne anions (**4** and **5**) were demonstrated to partially isomerize to distonic triplet phenylcarbene anions **4'(T)** and **5'(T)** with the assistance of acetic acid, acetonitrile or acetone. The isomerization is initiated by a proton transfer from the reagent to phenylcarbyne anions, followed by another proton transfer from the so-generated neutral triplet phenylcarbene to deprotonated reagent. The distonic triplet phenylcarbene anions **4'(T)** and **5'(T)** are likely to undergo intersystem crossing to their singlet ground states due to their long lifetimes and many collisions with the helium buffer gas in the ion trap. These distonic singlet phenylcarbene anions abstracted an oxygen atom from acetone, which has been reported to be typical for singlet carbenes.[33,53] These singlet phenylcarbene anions can insert into a C-H single bond in acetonitrile[51,52] to form an adduct, followed by elimination of a HCN molecule to generate the final CH_2 abstraction product ion.

The above isomerization barely occurs upon interactions of the anions with *dimethyl disulfide*, likely because the deprotonated dimethyl disulfide decomposes to a thioformaldehyde molecule and a methylsulfide anion upon the deprotonation. The so-generated neutral distonic triplet phenylcarbenes then add to the thioformaldehyde molecule in a reaction that is exothermic by -

90.3 kcal mol^{-1} if intersystem crossing is involved. The methylsulfide anion can abstract a proton from the adduct to generate the final CH_2S abstraction product ion.

In conclusion, substitution was found to greatly impact the reactivity of the phenylcarbyne anion by altering the proton affinity and, for one phenylcarbyne anion, the ground state multiplicity. Triplet phenylcarbyne anions were found to react via radical mechanisms. For example, they abstract an oxygen atom from acetone and a proton and a $H_2C{=}S$ molecule from dimethyl disulfide to form the CH_3S^- anion. On the other hand, the singlet phenylcarbyne anion abstracts H_2O and $H_2C{=}C{=}O$ from acetic acid via non-radical mechanisms. Additionally, the reactivities of the isomeric, distonic phenylcarbene anions were found to be quite different from those of the phenylcarbyne anions. For example, singlet distonic phenylcarbene anions abstract CH_2 from acetonitrile, which is initiated by C-H insertion – a typical singlet carbene reactivity.

6.5 References

1. Do Minh, T., Gunning, H. E. and Strausz, O. P., Formation and reactions of monovalent carbon intermediates. I. Photolysis of diethyl mercuribisdiazoacetate. *J. Am. Chem. Soc.* **1967**, *89*, 6785-6787.

2. Strausz, O. P., Thap, D. M. and Font, J., Formation and reactions of monovalent carbon intermediates. II. Further studies on the decomposition of diethyl mercurybisdiazoacetate. *J. Am. Chem. Soc.* **1968**, *90*, 1930-1931

3. Strausz, O. P., Kennepohl, G. J. A., Garneau, F. X., DoMinh, T., Kim, B., Valenty, S. and Skell, P. S., Formation and reactions of monovalent carbon intermediates. III. Reaction of carbethoxymethyne with olefins. *J. Am. Chem. Soc.* **1974**, *96*, 5723-5732.

4. Rydbeck, O.E.H., Elldér, J. and Irvine, W.M., Radio detection of interstellar CH. *Nature* **1973**, *246*, 466-468.

5. Smith, P. P. K., Buseck, P. R., Carbyne forms of carbon: do they exist? *Science* **1982**, *216*, 984-986.

6. Zabarnick, S., Fleming, J. W. and Lin, M. C., Kinetics of methylidyne (CH X 2Π) radical reactions with ammonia and methylamines. *Chem. Phys.* **1989**, *132*, 407-411.

7. Ruzsicska, B. P., Jodhan, A., Choi, H. K. J., Strausz, O. P. and Bell, T. N., Chemistry of carbynes: reaction of CF, CCl, and CBr with alkenes. *J. Am. Chem. Soc.* **1983**, *105*, 2489-2490.

8. LaFrancois, C. J. and Shevlin, P. B., Formation of both CCl and CF in the reaction of atomic carbon with chlorofluorocarbons. *J. Am. Chem. Soc.* **1994**, *116*, 9405-9406.

9. Wang, J., Ding, Y.H. and Sun, C.C., Cyanomethylidyne: A reactive carbyne radical. *ChemPhysChem* **2006**, *7*, 710-722.

10. Wang, Z., Herraiz, A. G., Del Hoyo, A. M. and Suero, M. G., Generating carbyne equivalents with photoredox catalysis. *Nature* **2018**, *554*, 86-91.

11. Strausz, O.P., Kennepohl, G.J.A., Garneau, F.X., DoMinh, T., Kim, B., Valenty, S. and Skell, P.S., Formation and reactions of monovalent carbon intermediates. III. Reaction of carbethoxymethyne with olefins. *J. Am. Chem. Soc.* **1974**, *96*, 5723-5732.

12. Hou, Z. and Bayes, K.D., Rate constants for the reaction of methyne (a4. SIGMA.) with nitric oxide, dinitrogen, nitrous oxide, carbon monoxide, carbon dioxide and water. *J. Phys. Chem.* **1993**, *97*, 1896-1900.

13. Li, W. L., Zhang, Q., Chen, M., Hu, H.S., Li, J. and Zhou, M., Formation and characterization of a BeOBeC multiple radical featuring a quartet carbyne moiety. *Angew. Chem., Int. Ed.* **2020**, *59*, 6923-6928.

14. Seburg, R. A., Hill, B. T., Jesinger, R. A. and Squires, R. R., The phenylcarbyne anion. *J. Am. Chem. Soc.* **1999**, *121*, 6310-6311.

15. Zeng, T., Wang, H., Lu, Y., Xie, Y., Wang, H., Schaefer III, H.F., Ananth, N. and Hoffmann, R., Tuning spin-states of carbynes and silylynes: A long jump with one leg. *J. Am. Chem. Soc.* **2014**, *136*, 13388-13398.

16. Gutsev, G.L. and Ziegler, T., Theoretical study on neutral and anionic halocarbynes and halocarbenes. *J. Phys. Chem.* **1991**, *95*, 7220-7228.

17. Dunning Jr., T.H., White, W.P., Pitzer, R.M. and Mathews, C.W., The electronic states of carbon monofluoride: Low-lying valence states. *J. Mol. Spectrosc.* **1979**, *75*, 297-317.

18. Hall, J.A. and Richards, W.G., A theoretical study of the spectroscopic states of the CF molecule. *Mol. Phys.* **1972**, *23*, 331-343.

19. Cramer, C.J., Dulles, F.J. and Falvey, D.E., *Ab initio* characterization of phenylnitrenium and phenylcarbene: remarkably different properties for isoelectronic species. *J. Am. Chem. Soc.* **1994**, *116*, 9787-9788.

20. Mizuhata, Y., Sasamori, T. and Tokitoh, N., Stable heavier carbene analogues. *Chem. Rev.* **2010**, *110*, 3850.

21. Wanzlick, H.W., Aspects of nucleophilic carbene chemistry. *Angew. Chem. Int. Ed. Engl.* **1962**, *1*, 75-80.

22. McKellar, A.R.W., Bunker, P.R., Sears, T.J., Evenson, K.M., Saykally, R.J. and Langhoff, S.R., Far infrared laser magnetic resonance of singlet methylene: Singlet–triplet perturbations, singlet–triplet transitions, and the singlet–triplet splitting. *J. Chem. Phys.* **1983**, *79*, 5251-5264.

23. Tomioka, H., Persistent triplet carbenes. *Acc. Chem. Res.* **1997**, *30*, 315-321.

24. Matzinger, S. and Fülscher, M.P., Methyl substitution in carbenes. A theoretical prediction of the singlet-triplet energy separation of dimethylcarbene. *J. Phys. Chem.* **1995**, *99*, 10747-10751.

25. Hall, J.H., Fargher, J.M. and Gisler, M.R., Substituent effects on spin delocalization in triplet phenylnitrenes. 1. Para-substituted phenylnitrenes. *J. Am. Chem. Soc.* **1978**, *100*, 2029-2034.

26. Rau, N.J., Welles, E.A. and Wenthold, P.G., Anionic substituent control of the electronic structure of aromatic nitrenes. *J. Am. Chem. Soc.* **2013**, *135*, 683-690.

27. Akhlaghinia, B. and Rezazadeh, S., A novel approach for the synthesis of 5-substituted-1H-tetrazoles. *J. Braz. Chem. Soc.* **2012**, *23*, 2197-2203.

28. Dunning, T. H. Gaussian basis sets for use in correlated molecular calculations. I. The atoms boron through neon and hydrogen. *J. Chem. Phys.* **1989**, 90, 1007–1023.

29. Andersson, K., Malmqvist, P.A., Roos, B.O., Sadlej, A.J. and Wolinski, K., Second-order perturbation theory with a CASSCF reference function. *J. Chem. Phys.* **1990**, 94, 5483-5488.

30. Frisch, M.J., Trucks, G.W., Schlegel, H.B., Scuseria, G.E., Robb, M.A., Cheeseman, J.R., Scalmani, G., Barone, V., Petersson, G.A., Nakatsuji, H. and Li, X., **2016**. Gaussian 16, Revision A. 03, Gaussian. *Inc.*

31. a) MOLCAS 7.4: F. Aquilante, L. De Vico, N. Ferré, G. Ghigo, P.-Å. Malmqvist, P. Neogrády, T. B. Pedersen, M. Pitonak, M. Reiher, B. O. Roos, L. Serrano-Andrés, M. Urban, V. Veryazov, R. Lindh, J. *Comput. Chem.* **2010**, *31*, 224–247; b) Code Development : V. Veryazov, P.-O. Widmark, L. Serrano-Andrés, R. Lindh, B. O. Roos, *Int. J. Quantum Chem.* **2004**, *100*, 626–635; c) MOLCAS 7: G. Karlstrçm, R. Lindh, P.-a. Malmqvist, B. O. Roos, U. Ryde, V. Veryazov, P.-O. Widmark, M. Cossi, B. Schimmelpfennig, P. Neogrády, L. Seijo, *Comput. Mater. Sci.* **2003**, *28*, 222–239.

32. Liu, W., Guo, Y., Han, C. and Huang, X., Characteristic fragmentation behavior of 5-[1-aryl-1*H*-pyrrol-2-yl]-1*H*-tetrazole by electrospray ionization tandem mass spectrometry. *Life Sci. J.* **2008**, *5*, 25-29.

33. Hu, J., Hill, B.T. and Squires, R.R., New approach to carbene chemistry via distonic carbene ions: a case of spin-forbidden proton transfer and carbene-biradical tautomerism. *J. Am. Chem. Soc.* **1997**, 119, 11699–11700.

34. Kotha, R.R., Yerabolu, R., Aqueel, M.S., Riedeman, J.S., Szalwinski, L., Ding, D., Nash, J.J. and Kenttämaa, H.I., Quinoline triradicals: a reactivity study. *J. Am. Chem. Soc.* **2019**, *141*, 6672-6679.

35. Ma, X., Feng, E., Jiang, H., Boulos, V.M., Gao, J., Nash, J.J. and Kenttämaa, H.I., Protonated ground-state singlet *meta*-pyridynes react from an excited triplet state. *J. Org. Chem.* **2021**, *86*, 3249-3260.

36. Vinueza, N.R., Jankiewicz, B.J., Gallardo, V.A., Nash, J.J. and Kenttämaa, H.I., Effects of hydrogen bonding on the gas-phase reactivity of didehydroisoquinolinium cation isomers. *Phys. Chem. Chem. Phys.* **2018**, *20*, 21567-21572.

37. Arnold, B. R., Scaiano, J. C., Laser flash photolysis studies on 4-oxocyclohexa-2,5-dienylidenes. *J. Org. Chem.* **1992**, *57*, 6469-6474.

38. Cumming, J.B. and Kebarle, P., Summary of gas phase acidity measurements involving acids AH. Entropy changes in proton transfer reactions involving negative ions. Bond dissociation energies D (A—H) and electron affinities EA (A). *Can. J. Chem.* **1978**, *56*, 1-9.

39. Sheng, H., Ma, X., Lei, H. R., Milton, J., Tang, W., Jin, C., Gao, J., Wittrig, A. M., Archibold, E. F., Nash, J. J. and Kenttämaa, H. I., Polar effects control the gas-phase reactivity of *para*-benzyne analogs. *ChemPhysChem* **2018**, *19*, 2839-2842.

40. Jin, C., Feng, E., Ma, X., Tang, W., Sheng, H., Wittrig, A., Gao, J. and Kenttämaa, H.I., Reactivity of *para*-benzynes in solution and in the gas phase. *Tetrahedron Lett.* **2021**, *74*, 153161.

41. Nourbakhsh, S., Liao, C.L. and Ng, C.Y., A 193 nm laser photofragmentation time-of-flight mass spectrometric study of CH_3SSCH_3, $SSCH_3$, and SCH_3. *J. Chem. Phys.* **1990**, *92*, 6587-6593.

42. Kotha, R. R., Nash, J. J. and Kenttämaa, H. I., An oxygen-peri-bridged quinolinium cation and its monoradical counterpart. *Eur. J. Org. Chem.* **2017**, *11*, 1407-1412.

43. Campbell, J.L., Yang, A.M.C., Melo, L.R. and Hopkins, W.S., Studying gas-phase interconversion of tautomers using differential mobility spectrometry. *J. Am. Soc. Mass Spectrom.* **2016**, 27, 1277-1284.

44. Penfold, T.J., Gindensperger, E., Daniel, C. and Marian, C.M., Spin-vibronic mechanism for intersystem crossing. *Chem. Rev.* **2018**, *118*, 6975-7025.

45. Cavaleri, J.J., Prater, K. and Bowman, R.M., An investigation of the solvent dependence on the ultrafast intersystem crossing kinetics of xanthone. *Chem. Phys. Lett.* **1996**, *259*, 495-502.

46. Noda, H., Nakanotani, H. and Adachi, C., Highly efficient thermally activated delayed fluorescence with slow reverse intersystem crossing. *Chem. Lett.* **2019**, *48*,126-129.

47. Audier, H. E., Leblanc, D., Mourgues, P., McMahon, T. B. and Hammerum, S., Catalysed isomerization of simple radical cations in the gas phase. *J. Chem. Soc., Chem. Commun.* **1994**, *20*, 2329-2330.

48. Van der Rest, G., Nedev, H., Chamot-Rooke, J., Mourgues, P., McMahon, T. B. and Audier, H. E., "Proton-transport" catalysis in the gas phase. Keto-enol isomerization of ionized acetaldehyde. *Intl. J. Mass Spectrom.* **2000**, *202*, 161-174.

49. Cacace, F., Crestoni, M. E. and Fornarini, S., Proton shifts in gaseous arenium ions and their role in the gas-phase aromatic substitution by free Me_3C^+ and Me_3Si^+ cations. *J. Am. Chem. Soc.* **1992**, *114*, 6776-6784.

50. Bartmess, J.E., Scott, J.A. and McIver Jr, R.T., Scale of acidities in the gas phase from methanol to phenol. *J. Am. Chem. Soc.* **1979**, *101*, 6046-6056.

51. Zuev, P. and Sheridan, R. S., Tunneling in the C−H insertion of a singlet carbene: *tert*-butylchlorocarbene. *J. Am. Chem. Soc.* **1994**, *116*, 4123-4124.

52. Birchall, J. M., Haszeldine, R. N. and Tissington, P., Carbene chemistry. Part IX. Some CH insertion reactions of dichlorocarbene in the gas phase. *J. Chem. Soc., Perkin Trans. 1* **1975**, 17, 1638-1640.

53. Kovacs, D. and Jackson, J.E., $CH_2 + CO_2 \rightarrow CH_2O + CO$, one-step oxygen atom abstraction or addition/fragmentation via α-lactone?. *J. Phys. Chem. A* **2001**, *105*, 7579-7587.

VITA

Erlu Feng was born on October 26th, 1994 in Karamay, China. After he obtained his bachelor's degree from Fudan University in China in 2017, Erlu Feng joined Professor Hilkka I. Kenttämaa's research group at Purdue University. In Professor Kenttämaa's group, his research focused on development of mass spectrometric methods coupled with HPLC for the identification of specific functionalities from mixtures. His research interests also include the gas-phase reactivity of extremely reactive species, such as polyradicals and carbyne anions, toward small organic molecules. Erlu Feng is also experienced with exploring mechanisms of gas-phase reactions by using quantum chemical calculations. He defended his thesis in January 2022 and accepted a position as a Process Development Scientist in Amgen.

LIST OF PUBLICATIONS

1. **Feng, E.**, Ma, X., Kenttämaa, H. I. Identification of Protonated Urea Derivatives with Gas-Phase Ion-Molecule Reactions Followed by Collision-Activated Dissociation in Tandem Mass Spectrometry Experiments. *Anal. Chem.* **2021**, 93(22), 7851-7859.

2. Ma, X., **Feng, E. (equal contribution)**, Jiang, H., Boulos, V., Gao, J., Nash, J. J., Kenttämaa, H. I. Singlet meta-Benzyne Cations That Can React from an Excited Triplet State. *J. Org. Chem.* **2021**, 86(4), 3249–3260.

3. Ding, D., **Feng, E.,** Kotha, R. R., **(equal contribution)**, Chapman, N. C., Jiang, H., Nash, J. J., Kenttämaa, H. I. Spin-Spin Coupling Controls the Gas-Phase Reactivity of Aromatic σ-Type Triradicals. *Chem. Eur. J.* **2021**, 28(1), e202102968.

4. Jin, C., **Feng, E.**, Ma, X., Tang, W., Sheng, H., Wittrig, A., Gao, J. and Kenttämaa, H.I., Reactivity of para-benzynes in solution and in the gas phase. *Tetrahedron Lett.* **2021**, 74, 153-161.

5. Zhang, J., **Feng, E.,** Li, W. **(equal contribution)**, Milton, J. R., Sheng, H., Easterling, L. F., Nash, J. J., Kenttämaa, H. I. Studies of the Fragmentation Mechanisms of Deprotonated Lignin Model Compounds in Tandem Mass Spectrometry. *Anal. Chem.* **2020**, 92(17), 11895-11903.

6. Niyonsaba, E., Easton, M.W., **Feng, E.,** Yu, Z., Zhang, Z., Sheng, H., Kong, J., Easterling, L.F., Milton, J., Chobanian, H.R. and Deprez, N.R., Differentiation of Deprotonated Acyl-, N-, and O-Glucuronide Drug Metabolites by Using Tandem Mass Spectrometry Based on Gas-Phase Ion–Molecule Reactions Followed by Collision-Activated Dissociation. *Anal. Chem.* **2019**, 91(17), 11388-11396.

7. Tan, Y., **Feng, E. L.**, Sun, Q. S., Lin, H., Sun, X., Lin, G. Q., & Sun, X. W., Enantioselective Synthesis of Spirooxindole Benzoquinolizines via Organo-catalyzed Cascade Reactions. *Org. Biomol. Chem.* **2017**, 15(4), 778-781.

8. **Feng, E.**, Yu, Z., Jiang, H., Milton, J., Hoang, T. G., Nash, J. J., Kenttämaa, H. I. Gas-phase Reactivity of Phenylcarbyne Anions. *Submitted.*

9. **Feng, E.,** Ma, X., **(equal contribution)**, Jiang, H., Kenttämaa, H. I. Differentiation of Protonated Sulfonates and Sulfites via Gas-Phase Ion-Molecule Reactions in Tandem Mass Spectrometry. *Manuscript under preparation.*

10. Ma, X., **Feng, E.**, Johnson, E., Nash, J. J., Kenttämaa, H. I. Oxyquinoline Radical Cations React as Electrophiles in the Gas Phase. *Manuscript under preparation.*